UNIVERSITEIT VAN PRETORIA
UNIVERSITY OF PRETORIA
YUNIBESITHI YA PRETORIA

Department of Mechanical and Aeronautical Engineering
Clean Energy Research Group

Investigation of wind patterns on Marion Island using Computational Fluid Dynamics and measured data.

by

Kyle A. Goddard 14035066
Supervised by Prof. K.J. Craig, Mrs. J. Schoombie

In partial fulfilment for the degree of
Master of Engineering (Mechanical)

Dissertation

2021-02-12

© University of Pretoria

Investigation of wind patterns on Marion Island using Computational Fluid Dynamics and measured data.

Student:	Kyle Goddard 14035066
Supervisor:	Prof K.J. Craig
Co-supervised:	Mrs. J. Schoombie
Degree:	Master of Engineering (Mechanical)
Institution:	University of Pretoria, Department of Mechanical and Aeronautical Engineering

Abstract

There have been countless research investigations taking place on Marion Island (MI), both ecological and geological, which have reached conclusions that must necessarily neglect the impacts of wind on the systems under study. Since only the dominant wind direction of the general atmospheric wind is known from weather and satellite data, not much can be said about local wind conditions at ground level. Therefore, a baseline Computational Fluid Dynamics (CFD) model has been developed for simulating wind patterns over Marion and Prince Edward Islands, a South African territory lying in the subantarctic Indian Ocean.

A review of the current state of the art of Computational Wind Engineering (CWE) revealed that large-scale Atmospheric Boundary Layer (ABL) simulations have been successfully performed before with varying degrees of success. With ANSYS Fluent chosen as the numerical solver, the Reynolds-Averaged Navier-Stokes (RANS) equations were set up to simulate a total of 16 wind flow headings approaching MI from each of the cardinal compass directions. The standard k-ε turbulence closure scheme with modified constants was used to numerically approximate the atmospheric turbulence. A strategy was devised for generating a reusable mesh system to simulate multiple climatic conditions and wind directions around MI.

In conjunction with the computational simulations, a wind measurement campaign was executed to install 17 wind data logging stations at key locations around MI. Raw data output from the stations were cleaned and converted into an easily accessible MySQL database format using the Python scripting language. The Marion Island Recorded Experimental Dataset (MIRED) database contains all wind measurements gathered over the span of two years. The decision was taken to focus on validating only three of the 16 cardinal wind directions against the measured wind data; North-Westerly, Westerly and South-Westerly winds.

An initial interrogation of the simulation results showed that island-to-island wake interactions could not be ignored as the turbulent stream from MI could definitely be intercepted by its neighbour under the right conditions, and vice versa. An underestimation of the true strength

© University of Pretoria

of the Coriolis effect led to larger wind deflection in the simulations than originally expected, thus resulting in the wind flow at surface levels having an entirely different heading to what was intended. The westerly and south-westerly wind validation cases did not seem too badly affected by the lapse in judgement but the north-westerly case suffered strong losses in accuracy.

Significant effort was put into quantifying the error present in the simulations. After a full validation exercise, it was finally resolved to apply a conservative uncertainty factor of 35 % when using these simulations to predict actual wind speed conditions. Similarly, the predicted wind direction can only be trusted within the bounds of a 35° prediction uncertainty. Under these circumstances, the baseline CFD model was successfully validated against the measured wind data and can thus be used in further research. In terms of post-processing, all the wind direction simulations have been combined into a single wind velocity map, generated by weighting each of the simulations by the frequency of wind prevalence measured in the corresponding wind sector. A second turbulence intensity combined map has been provided using similar techniques. These maps, as well as the individual wind maps showing all 16 cardinal wind directions, are believed to be helpful to many future biological studies on MI as well as any possible forays into wind energy generation on the island.

Despite the encountered deficiencies, this project offers significant value to academia by providing a reliable method of predicting fine-scale wind patterns in a location previously devoid of any accurate data. Furthermore, it has highlighted where future CFD attempts can be improved in order to produce a compelling approximation of the realistic atmospheric phenomena occurring in the Marion Island territory. While error cannot be avoided when modelling such complex systems, it has been well quantified and discussed here so that any further research may make informed judgements in future studies.

Keywords: Atmospheric Boundary Layer,Computational Fluid Dynamics, k-epsilon Turbulence Model, Marion Island, Prince Edward Island, Wind Pattern Simulation

© University of Pretoria

Acknowledgements

The following individuals and institutions are thanked for their help and support throughout the course of the study:

- The financial assistance of the National Research Foundation (NRF) towards this research is hereby acknowledged. Opinions expressed and conclusions arrived at, are those of the author and are not necessarily to be attributed to the NRF.
- Prof. K.J. Craig for his excellent guidance and overall supervision.
- Janine Schoombie for her council and keen insights concerning Marion Island.
- Dr. Pete Le Roux for all the hard work and advice given regarding ecological aspects of this study.
- The South African National Antarctic Programme (SANAP) for providing the funding and affording me the opportunity to travel to Marion Island.
- The Centre for High Performance Computing (CHPC) in Cape Town for providing the computational resources.
- The South African Weather Service (SAWS) for providing any historical climate data from the Marion Island Base station.
- Special thanks to the field assistants Elsa van Ginkel, Dineo Mogashoa, and Jenna van Berkel for their valued support during the Marion Island over-wintering expeditions.
- And finally, to my dear parents and sister. Without their tremendous love, patience and support I would not be where I am today.

Thank you all.

© University of Pretoria

Table of Contents

© University of Pretoria

© University of Pretoria

© University of Pretoria

© University of Pretoria

List of Figures

© University of Pretoria

© University of Pretoria

© University of Pretoria

© University of Pretoria

© University of Pretoria

© University of Pretoria

© University of Pretoria

List of Tables

© University of Pretoria

© University of Pretoria

List of Abbreviations

ABL	Atmospheric Boundary Layer
AGL	Above Ground Level
ASL	Atmospheric Surface Layer
CFD	Computational Fluid Dynamics
CWE	Computational Wind Engineering
DEM	Digital Elevation Model
DES	Detached Eddy Simulation
DNS	Direct Numerical Simulation
DTU	Technical University of Denmark
HHTSL	Horizontally Homogeneous Turbulent Surface Layer
LES	Large Eddy Simulation
MAE	Maximum Absolute Error
MI	Marion Island
NS	Navier-Stokes equations
NWP	Numerical Weather Prediction
PDE	Partial Differential Equation
PEI	Prince Edward Island
RANS	Reynolds-Averaged Navier-Stokes
RKE	Realizable k-ε turbulence model
RMSE	Root Mean Squared Error
RNGKE	Re-Normalisation Group k-ε turbulence model
SANAP	South African National Antarctic Programme
SANSA	South African National Space Agency
SAWS	South African Weather Service
SKE	Standard k-ε turbulence model
SQL	Structured Query Language
SST	Shear Stress Transport
TDR	Turbulent Dissipation Rate
TI	Turbulence Intensity
TKE	Turbulent Kinetic Energy

© University of Pretoria

Physical and Empirical Constants

g	Gravitational Acceleration	$= 9.81\ \mathrm{m\,s^{-2}}$
R	Universal Gas Constant	$= 8.314\ \mathrm{J\,mol^{-1}\,K^{-1}}$
κ	von Kármán constant	$= 0.4187$
E	Empirical constant	$= 9.9793$
Ω	Earth's rotational speed	$= 7.292 \times 10^{-5}\ \mathrm{rad\,s^{-1}}$
A_c	Charnock constant	$= 0.018$

© University of Pretoria

List of Symbols

Latin Symbols

z	Altitude	[m]
f	Body force	[N]
$\mathbf{x} = \langle x, y, z \rangle$	Cartesian coordinates	[m]
L	Characteristic length	[m]
F_c	Coriolis Force	[N]
C	Denotes a constant value, Pearson Correlation Coefficient	
S	Denotes a source term	
G	Denotes energy generation	
n	Lag number	
M	Molar mass	[kg/mol]
P	Pressure	[Pa]
Re	Reynolds number	
k	Sand grain roughness height	[m]
c_p	Specific Heat Capacity	[J/kg-K]
T	Temperature	[K]
t	Time	[s]
k	Turbulent Kinetic Energy	[m^2/s^2]
R	Universal gas constant, Auto-correlation coefficient	
V	Velocity magnitude	[m/s]
$\mathbf{u} = \langle u, v, w \rangle$	Velocity vector	[m/s]

Greek Symbols

ρ	Density	[kg/m^3]
Γ	Dry Adiabatic Lapse Rate	[$^\circ C$/m]
μ	Dynamic viscosity	[Pa.s]
ω	Earth's rotational speed	[rad/s]
δ_{ij}	Kronecker delta	
σ	Prandtl number, Standard Deviation	
τ	Reynolds Stress	[Pa]
φ	Scalar placeholder	
ω	Specific disspation rate	[1/s]
ε	Turbulent disspation rate	[m^2/s^3]
μ_t	Turbulent viscosity	[Pa.s]
κ	von Kármán constant	
ϕ	Latitude	radians

© University of Pretoria

Subscripts

$*$	Denotes friction
μ	With respect to viscosity
ω	With respect to specific turbulent dissipation rate
ε	With respect to turbulent dissipation rate
0	Denotes a reference value
b	With respect to buoyancy
i, j, k	Denotes Cartesian coordinate directions
k	With respect to turbulent kinetic energy
n	Denotes a discrete number/counter
p	With respect to wall adjacent cell (perpendicular)
w	With respect to an adjacent wall

Superscripts

$(.)'$	Fluctuating component
$\overline{(.)}$	Mean component
$+$	Non-dimensional quantity

© University of Pretoria

1 Introduction

A Computational Fluid Dynamics (CFD) model is required for simulating wind patterns over Marion and Prince Edward Islands, a South African territory lying in the subantarctic Indian Ocean. The model must account for the atmospheric interactions within a large domain surrounding the islands and sufficiently simulate the fine-scale wind patterns close to ground level. Simulated results will be compared to physical data captured at the site as a validation exercise.

1.1 Motivation

1.1.1 Context

Atmospheric flow patterns over complex landscapes are of great interest in worldwide engineering studies since they are crucial to the success of wind energy generation projects and safety in design of structures and buildings carrying human lives. Atmospheric flows also have engineering importance in urban climate and pollutant transport applications. There is non-engineering related interest in other scientific fields such as ecological studies and biodiversity, where it is believed winds can hold a strong influence over the behaviour of living organisms and geological landforms.

Marion Island is one such landscape in which it is known that high wind velocities have a significant impact on both the biotic and abiotic systems around the island. Marion Island is located at 46°54′45”S 37°44′37”E, some 1769km south east of the South African coast and in the heart of the southern latitudes known as the ”Roaring Forties”. Marion Island (MI) and its close counterpart, Prince Edward Island, are small volcanic Islands in the sub-Antarctic Southern Ocean. Although there are very few human inhabitants on MI (none on Prince Edward), the sites are important meteorological and biological conservation landmarks for the South African National Antarctic Programme (SANAP) and the South African government.

This study aims to use the current state of the art of Computational Fluid Dynamics (CFD) to model complex wind patterns down to a fine spatial scale over the island topography. CFD is an engineering tool developed for solving complicated fluid dynamics problems numerically, although typically only used for much smaller domains than the current subject.

Aside from the CFD implementation, common industry practice requires that any models need to be successfully validated by comparing the numerical results with physically captured experimental data. In this regard, a campaign was recently performed on Marion Island where more than 30 sonic anemometers were deployed to sample the wind at strategic locations around the island.

This Masters study is focused on the computational aspects of wind engineering rather than on the biological and ecological impacts, which are beyond the scope of an engineering-centred

© University of Pretoria

investigation. The study results will, however, be used as input to other ecological studies and further follow-up masters and PhD studies.

1.1.2 Research Gap

There have been countless research investigations taking place on Marion Island, both ecological and geological, which have reached conclusions that must necessarily neglect the impacts of wind on the systems under study. Since only the dominant wind direction of the general atmospheric wind is known from weather and satellite data, not much can be said about local wind conditions at ground level.

Up until now, it has been postulated that many organisms and structures on the island tend to conform with the strong dominant wind direction. It is possible, however, that topographical features may influence the wind in such a way that the dominant winds in nearby localities deviate significantly from the measured mean atmospheric wind speed and direction, which leads to disagreement between observed data and scientific hypotheses. Since such a study has never before been performed on Marion Island itself, there are no available data regarding sub-mesoscale weather patterns in the region. Due to their isolation from other landforms, the Prince Edward Islands offer the perfect subject for a CFD study where important boundary conditions can be assigned.

Furthermore, the current project is subject to strict environmental constraints. The study will attempt to fully validate a CFD model using only sparsely available validation data. The challenges and shortcomings of this process, known and unknown, must be addressed before any trust can be placed in the model.

1.2 Aim

This research project aims to systematically simulate and validate fine-scale wind patterns on Marion Island under any plausible prevailing atmospheric wind conditions using CFD techniques.

1.3 Objectives

In essence, the research aims to use a CFD model of wind over the Prince Edward Islands as a means of predicting local wind changes resulting from topographical interference. The simulations predict average overall wind conditions by design and, thus, are merely an approximation to reality. However, the model would offer the opportunity for greater insights into local wind conditions at ground level and aims to provide a tool for researchers to design more wholesome experiments in future studies.

The following research questions capture the nature of this project:

© University of Pretoria

- Does the local dominant wind near topographical features deviate significantly from the atmospheric average wind speed and direction?

- Can a computational wind model be used to predict local fine-scale wind patterns?

- Are the retrieved numerical results from the CFD model a valid approximation to reality with application in future studies?

To answer these questions, a systematic approach to atmospheric boundary layer modelling must be followed. The listed objectives below offer a roadmap to a successful project and must be met in order to achieve satisfactory results:

- Review available literature on the subject of Atmospheric Boundary Layer (ABL) modelling, gathering a theoretical foundation for performing realistic CFD simulations of the atmosphere and validating any output results.

- Understand how other researchers in the field have approached similar problems and build on their insights to develop a strategy for modelling the atmosphere in ANSYS Fluent 2019R3.

- Test various aspects of the CFD model independently such that an understanding of the interaction between program settings and their subsequent outputs can be ascertained. Since the Marion Island simulations are bound to be exceedingly large and lethargic, test any settings on smaller and simpler problems first.

- Identify any shortcomings in the developed model through performing case studies with published datasets and comparing the results to those of other researchers. Find where the model can be improved or where caution should be taken to reduce the chance of producing invalid results.

- Simulate the wind patterns on Marion Island using the CFD insights gained thus far. Critically asses any results, comparing them with realistic measurements to validate the models.

- Use the CFD results to generate useful colour maps of flow variables around the island. Any maps generated as a consequence of this study can be used by researchers in future studies.

© University of Pretoria

1.4 Overview

This thesis begins by reviewing all the currently available literature concerning wind modelling in the ABL. Chapter 2 takes a deep dive into topics such as atmospheric stability, Computational Wind Engineering and all things concerning the numerical solution to the Reynolds-Averaged Navier-Stokes (RANS) Equations.

Chapter 3 takes all previously learned information and applies it to a set of example problems. This chapter can be viewed as practice and numerical fault finding before performing the actual simulations which form the final subject of this study.

Chapter 4 defines the physical wind capturing equipment and procedure used to generate a database of experimental wind data. The full MI wind measurement campaign is explained herein, as well as the pre-processing of incoming data streams.

Chapter 5 gives a thorough overview of the simulation strategy. Aspects such as requirements and limitations are discussed before proceeding with an explanation of the CFD setup. Mesh generation procedures as well as a grid convergence study have been documented here.

Chapter 6 presents the results and findings of the study. This is a longer chapter devoted to explaining and fully understanding the simulations as well as discussing any errors.

Chapters 7 and 8 conclude the study by summarising any findings and offering suggestions pertaining to future work.

© University of Pretoria

2 Literature Review

This section presents a collation of all the relevant available knowledge regarding CFD specifically tailored towards wind modelling over complex terrain. The governing flow equations and mathematical notation used throughout the report are detailed here, making information in this section crucial to understanding the rest of the study.

2.1 A Brief Introduction to Marion Island

Marion Island (MI) and Prince Edward Island (PEI) are a set of volcanic islands, together referred as the Prince Edward Islands, located in the Southern Ocean between South Africa and Antarctica. Marion Island, the larger of the two islands and the main subject of this study, can be found at 46°54'S 37°45'E while its neighbour is a mere 19km away at 46°38'S 37°57'E (Chown and Froneman, 2008). The next nearest occurrence of land is 950km away.

For orientation, a satellite view of the area is shown in Figure 2.1.

Figure 2.1: Geographical orientation of Marion Island and Prince Edward Island, Google Earth (2019)

While PEI is completely uninhabited by humans, MI is occupied in yearly cycles by teams of about 20 scientists at a time from all backgrounds including ecology, geography, climatology and astronomy. The islands are visited annually by the SA Agulhas II, a research vessel carrying the replacement team of overwinter scientists, supplies to restock MI for a further year of habitation, and a larger crowd of auxiliary researchers who only perform work while the ship is in the island vicinity (the author formed part of the 2018 crew of auxiliary researchers).

© University of Pretoria

The Islands are subjected to characteristically high wind speeds as a result of their location in an area known as the "Roaring Forties". Their climate and isolation from continental land make these islands the perfect candidate for conservation efforts; many indigenous sea birds and mammals are found cohabiting on the islands in relative exclusion from the rest of the world. These uncommon animals are the subject of intense biological studies which, among other things, aim to assess the progression of life in the absence of human interference. The PE Islands are home to a small yet incredibly sensitive ecosystem; it is comparatively easy to study this remote habitat and draw accelerated conclusions. Oftentimes, the environmental trends documented in this location eventually find themselves being repeated on a larger global scale (Chown and Froneman, 2008). This predictive property is especially advantageous under the current so-called climate crisis.

MI features as a prominent South African Weather Service (SAWS) outpost since its location allows meteorologists to capture useful information regarding approaching polar frontal systems before they reach the mainland. As a further outcome of its seclusion, MI is the ideal spot for the South African National Space Agency (SANSA) to study solar weather. There is little to no radio noise interference in this unpopulated part of the world and the atmosphere is significantly thinner than at the equator, allowing astronomers to erect delicate radio equipment and gain unique insights into the behaviour of our solar system.

To conclude, the PE Islands have become known as a diverse breeding ground for plants, animals and scientific disciplines alike; an environment which offers a mine of potential discoveries that are applicable not only to the local area but to the world at large.

2.2 The Atmospheric Boundary Layer (ABL)

A short discussion concerning the Atmospheric Boundary Layer (ABL) is necessary to give basic insight into the processes which the CFD models in this study try to imitate.

The ABL refers to the lower portion of the Earth's atmosphere which is responsible for the majority of the interactions (i.e. thermal and mechanical) with the surface topology. The ABL typically accounts for about the lowest 10-20 % of the free atmosphere, with a maximum height of $\sim$3 km, and is defined more explicitly to have a boundary layer height at which turbulence drops below 5 % of the surface value (Wallace and Hobbs, 2006). The ABL is separated from the rest of the free atmosphere by a temperature inversion cap, where the air temperature increases with height rather than decreasing. The capping inversion is not a strict boundary but rather a region where upward moving thermals from the ABL are suppressed by the air above. Turbulent mixing occurs between the two fluids in what is called the entrainment zone.

The Atmospheric Surface Layer (ASL) occupies the lowest portion of the ABL, very close to the ground. Turbulent fluxes in the ASL are directly influenced by the surface roughness of the ground covering (grass, trees, buildings, etc.) and steep vertical wind speed and temperature

© University of Pretoria

gradients. Heat and momentum fluxes in this layer are assumed to be constant and the effects of the Coriolis force are deemed negligible when compared to other factors. Higher up in the ABL, above the surface layer, the flow is not as dependent on surface conditions but the influence of the Earth's rotation (Coriolis Effect) becomes more dominant. The discussion up until this point can be graphically summarised as shown in Figure 2.2.

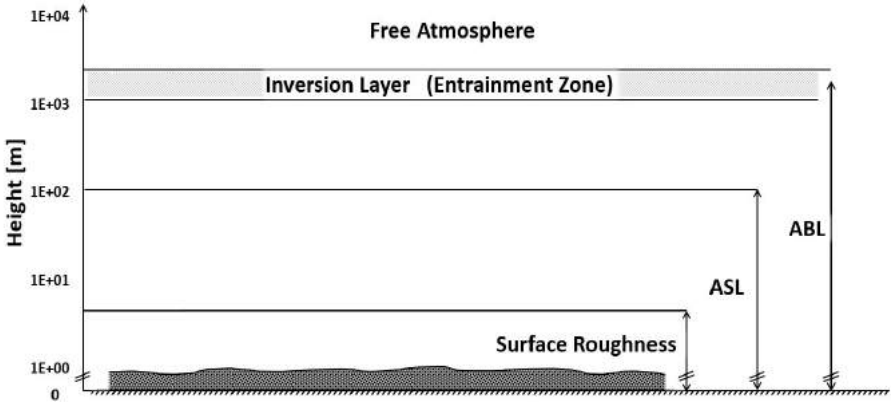

Figure 2.2: Diagram showing the vertical profile of a typical Atmospheric Boundary Layer at near-neutral stability. Adapted from Garratt (1994)

Turbulence in the flow is responsible for transmitting heat and surface friction effects from the ground upwards throughout the rest of the ABL at relatively quick response times (Garratt, 1994). The ground temperature is largely influenced by incoming solar radiation and so the atmospheric stability on land is continuously changing depending on the time of day or night. The ground is heated by the sun during the day and cools at night via the emission of long-wave radiation (Wallace and Hobbs, 2006). Depending on the weather conditions at different times in the 24 hour diurnal cycle, the ABL can be categorized into three different states: Unstable, Neutral, and Stable.

2.2.1 Atmospheric Stability

Stable conditions occur predominantly at night when the ground becomes cooler than the air above while unstable conditions occur in the day when the ground is being heated by the Sun. On a fair weathered day starting at sunrise, rising thermals due to buoyancy forces result in greater turbulence generation and form what is called the mixed or convective boundary layer. The convective layer continues to grow throughout the day until a maximum height is reached around the afternoon, followed by neutral stability of the ABL. Neutral conditions are characterised by a constant potential temperature with height above ground level; turbulence is generated mechanically (wind over a rough surface) rather than as a result of surface heating.

Night time cooling of the surface suppresses turbulent scales from the bottom up and is hence the reason for the formation of a stable boundary layer close to the ground. A residual layer of near-neutral air persists (from the late afternoon) above the nocturnal stable layer and is

© University of Pretoria

capped by the temperature inversion layer. Figure 2.3 presents a graphical summary of the discussed evolution of the ABL through a typical diurnal cycle.

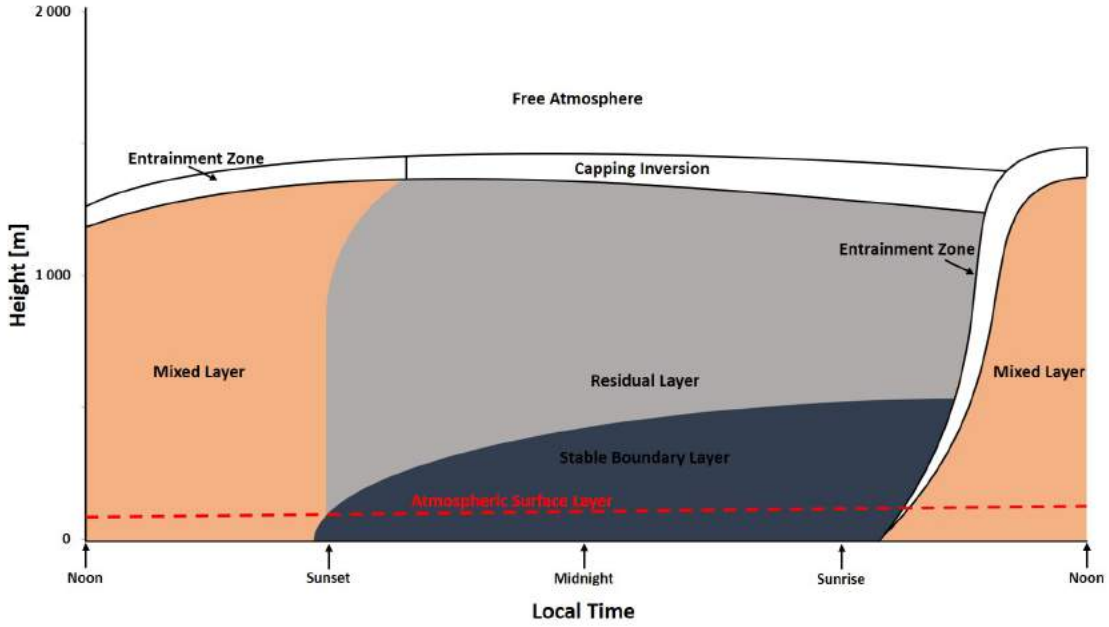

Figure 2.3: Evolution of the ABL through a diurnal cycle during fair weather conditions. Adapted from Wallace and Hobbs (2006)

Due to the no-slip wall condition along the surface, there must exist some profile in the wind speed going from 0 m/s at ground level to the full geostrophic wind velocity in atmosphere above. This profile is generally approximated by a logarithmic law, however, in reality the profile is sensitive to atmospheric stability conditions and can vary significantly from the standard law (Wallace and Hobbs, 2006; Monin and Obukhov, 1954).

Figure 2.4 shows the theoretical deviations of the wind profile from the standard log law as affected by the stability conditions of the atmosphere. These different profiles are used as boundary conditions to simulations further in the study.

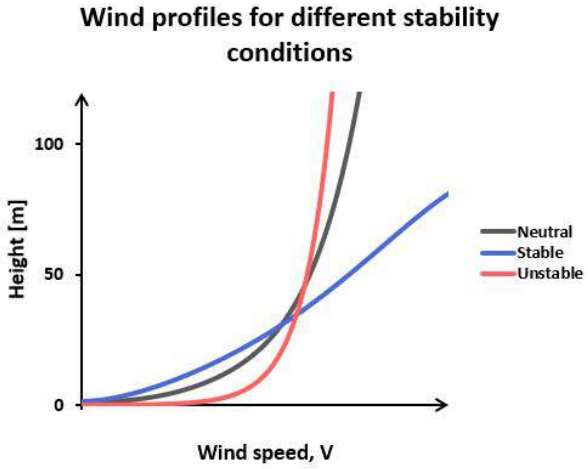

Figure 2.4: Wind speed profiles as a result of different atmospheric stability conditions. Adapted from Garratt (1994)

© University of Pretoria

The wind profile is strongly dependent on the ratio between the buoyancy forces and the shear force (Meissner *et al.*, 2009). To explain, stable conditions are characterised by suppressed turbulence which implies that mixing is diminished and that drag from the surface layer is not communicated upwards as effectively. This allows the wind to reach a higher velocity closer to the ground without being slowed down (wind shear is increased). Unstable conditions are contrarily characterised by high turbulence and large amounts of mixing between the thermal stratification layers, also mixing momentum, which leads to a quick wind speed increase very close to the ground but then smaller wind speed gradients further away where the flow is well mixed (wind shear is decreased). Neutral conditions fall somewhere in between these two extremes as seen in Figure 2.4.

A useful metric for classifying cases of atmospheric stability is the dry adiabatic lapse rate, Γ. If a parcel of air rises through the atmosphere its temperature will decrease as a result of the pressure decrease (Wallace and Hobbs, 2006). If that same parcel is lifted rapidly enough with minimal heat exchange to the environment, its temperature, T, will drop according to the lapse rate

$$\Gamma = -\left(\frac{\partial T}{\partial z}\right)_{adiabatic} = \frac{g}{c_p} \tag{2.1}$$

where z is altitude, g is the gravitational constant and c_p is the specific heat at constant pressure. The vertical temperature gradient tends to follow the lapse rate during neutral conditions. Deviations from the standard lapse rate imply differences in thermal stratification; $\partial T/\partial z < \Gamma$ implying stable conditions and $\partial T/\partial z > \Gamma$ implying unstable (Bechmann *et al.*, 2007b). The conventional value for the adiabatic lapse rate is specified as $\Gamma \approx 1$ °C/100m.

Thermal stratification is also responsible for lifting or blockage behaviour of air when it runs over topographical features (Meissner *et al.*, 2009). Unstable conditions result in rising air continuing to rise since it is now warmer than the surrounding air (more buoyant). Stable suppressed air is more likely to split and flow around a hill rather than go over it, while neutrally stratified air would pass smoothly over. A similar blockage effect is also well documented where the temperature inversion layer strongly inhibits vertical mixing (Wallace and Hobbs, 2006), thus forcing air to move around a high enough geographical feature rather than passing over it. Knowing that the temperature inversion in the atmosphere is commonly characterised by clouds, we can see an example of the thermal inversion blockage effect in Figure 2.5.

Figure 2.5a) shows a higher inversion layer, allowing air to flow over Marion Island while Figure 2.5b) shows air being forced around the highest portion of the island where mountain peaks break through the temperature inversion.

© University of Pretoria

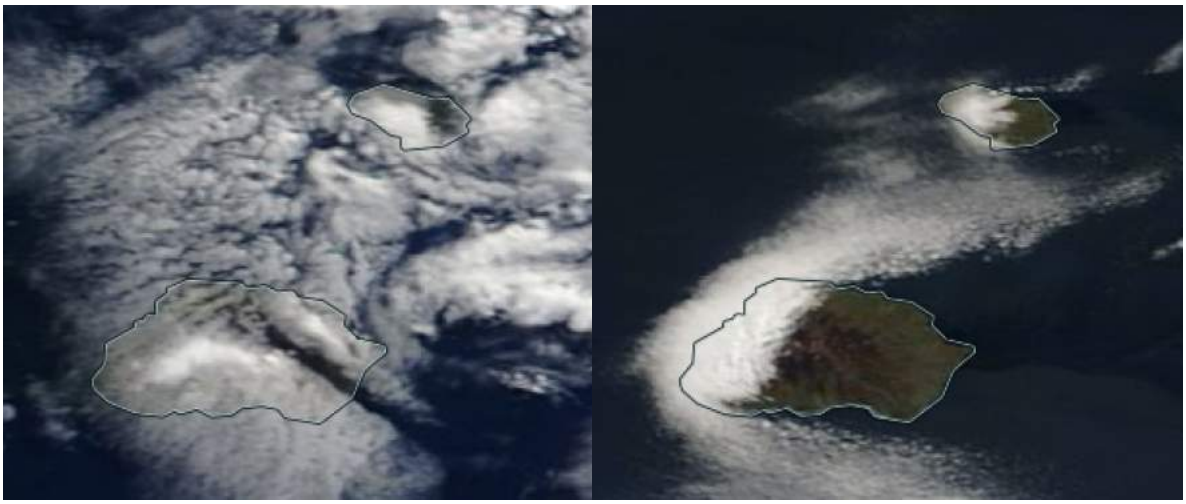

(a) **(b)**

Figure 2.5: A comparative example of the temperature inversion blockage effect over Marion Island. a) High cloud layer and therefore no vertical blockage, b) low inversion layer suppresses vertical air movement over high mountain peaks. *Imagery from the NASA Worldview application (2000-2018) operated by the NASA/Goddard Space Flight Center Earth Science Data and Information System (ESDIS) project*

2.2.2 Prevailing Climate on Marion Island

Bearing the previous discussion in mind, it should be noted that the climate around Marion Island is termed hyper-oceanic; meaning that, as a result of the island's geographic isolation, the atmospheric behaviour is predominantly determined by the marine boundary layer rather than thermal stratification effects over land mass (le Roux, 2008). The surrounding waters have a much higher thermal inertia than land and, in conjunction with the strong influence of passing frontal systems from the polar region, the island is subject to moderate to small daily temperature fluctuations, high humidity and precipitation (Smith and Steenkamp, 1990). As a consequence of its sub-Antarctic latitude, Marion Island also regularly experiences gale force winds and low incident radiation (le Roux, 2008). This information leads the author to believe that the ABL around the Island can be effectively modelled by neutrally stable conditions, neglecting the possibility of a stable or unstable atmosphere since thermal effects are minimal.

2.3 Computational Wind Engineering Review

Computational Wind Engineering (CWE) has enjoyed rapid growth as a topic of engineering study in recent decades, successfully establishing itself as one of the branching disciplines of mechanical and environmental engineering (Blocken, 2014). The ABL, and atmospheric modelling in general, is the focus of this section. The current state of the art is discussed and an attempt is made to compile an overview of the most commonly applied techniques. The review is by no means exhaustive but rather tries to remain within the scope of the current document.

© University of Pretoria

CWE is the broad term used to describe the use of CFD principles in wind engineering applications. The idea so far has been to visualise and study the spatial and temporal behaviour of wind fields numerically rather than erecting swathes of meteorological masts across an area of interest. The CWE method supplements sparse measurement campaigns since masts are expensive to erect and their location is limited by various factors, especially where complex terrain is concerned (Berge *et al.*, 2006). Together with measured wind data, wind fields are effectively estimated with CFD over terrain where no masts are erected.

The weather has been modelled on large scales for Numerical Weather Prediction (NWP) purposes and global climate modelling, although at resolutions too large to be of much use to engineers interested in detailed flow fields over complex domains (Wood, 2000). With this in mind, Castro *et al.* (2008) and possibly countless other researchers have developed methods for overlapping and coupling NWP mesoscale domains with traditionally smaller CFD microscale domains, essentially bridging the gap between climate models and useful CWE simulations at specific locations. The scope of this work does not extend as far as NWP or mesoscale weather simulation. However, it is an interesting avenue that could be explored at a later stage.

Micrositing is the strategy used when placing wind turbines and other man-made structures in optimal locations based on the wind climate. CWE is especially important for micrositing in complex terrains where wind variability is increased and becomes highly three-dimensional in nature as a result of the topology. Linear simplifications of the Navier-Stokes equations have been developed and implemented in various software packages such as WAsP, WinPro, MsMicro and others based largely on the work of Jackson and Hunt (1975). While these packages offer adequate results with minimal computational effort, the linearised governing equations are severely limited in terms of modelling highly complex terrain and climate.

Full three-dimensional (3D) CFD solvers are available commercially and publicly (e.g. ANSYS Fluent, Star CCM+ and OpenFOAM) which have grown in popularity for simulating ABL flows with the recent advances in computing power. The required effort in setting up full CFD simulations is much greater, but comes with the benefit of higher result accuracy and the ability to resolve significant non-linear effects over complex terrain, such as flow separation and the turbulent kinetic energy field. Koblitz (2013) successfully validated a non-neutral ABL model using an in-house CFD solver developed by the Technical University of Denmark, EllipSys3D (DTU, 2015). Similarly, Bechmann *et al.* (2007b) were able to develop and test a more advanced Large-Eddy Simulation (LES) code to integrate with EllipSys3D for modelling unsteady ABL flows over complex terrain.

Bechmann *et al.* (2007a) performed a preliminary CFD simulation of an ABL flow across the small peninsula of Bolund Island, Denmark. The results of this simulation went into predicting a suitable experimental design for a wind measurement campaign on the island (Bechmann *et al.*, 2009). The campaign aimed to capture the experimental data necessary for validating ABL flow models over complex terrain. Vladut *et al.* (2016); Yeow *et al.* (2014), amongst others,

© University of Pretoria

made good use of the reported Bolund Island experimental data for evaluating their own ABL models against a known base case. A similar procedure is followed by most researchers in the field of CWE who need to verify their novel solution implementations, namely:

- test any new algorithms or boundary conditions in an open domain to ensure continuity and correct fluid behaviour, including horizontal homogeneity.
- test the same approaches on a complex geometry that has been thoroughly documented in previous works and can be easily compared as a case study (e.g. Bolund Island).
- finally perform a full simulation on the new and unknown terrain given that the previous steps have resulted in a valid model.

The same process will be followed in this study.

2.4 Governing Equations

At the base of any CFD simulation is the set of governing fluid mechanics differential equations which need to be solved numerically. The Navier-Stokes (NS) partial differential equations are used to describe the three physical aspects and behaviours of fluid dynamics: conservation of mass, conservation of momentum, and conservation of energy. These governing equations were originally derived for general unsteady and compressible Newtonian fluid flows as Versteeg and Malalasekera (2007) explain. Although it is possible to solve these equations fully with Direct Numerical Simulation (DNS) methods (Schlatter and Örlü, 2010), the computational costs and necessary modelling constraints would be remarkably high for models at the large atmospheric scale with which the present study is concerned.

Hence, a number of simplifying assumptions have to be applied to ensure the computational feasibility of the simulations. This section reports the basic governing equations for ABL flows which will be expanded upon further in Section 2.6 to include buoyancy and Coriolis effects. The starting assumptions are as follows:

- Atmospheric air is a homogeneous mixture of gases which together obey the Ideal Gas law and behave as though they are one gas with measurable thermophysical properties (Çengel and Ghajar, 2015).
- Although air in the ABL is definitively turbulent (Blocken *et al.*, 2007), the instantaneous responses can be time- or ensemble-averaged to reduce the computational cost of resolving small turbulence scales (see Section 2.5 for more details).
- Natural wind speeds are relatively slow and do not approach the speed of sound in air, validating the assumption that atmospheric gases can be modelled as an incompressible Newtonian fluid. Pressure changes due to density changes are by definition small enough to be considered negligible (Manwell *et al.*, 2009).

© University of Pretoria

- Density changes as a result of temperature changes result in shifting atmospheric stability. For the remainder of this study, only a neutral ABL is considered and so buoyancy thermal effects are excluded (see Section 2.2.2).

- The focus is on microscale ABL interactions with the surface. As such, atmospheric radiation effects are neglected along with clouds and precipitation.

The Reynolds-averaged Navier-Stokes (RANS) equations for continuity (Eq. 2.2) and momentum (Eq. 2.3) given the preceding assumptions are expressed below using Einstein summation notation:

Continuity:

$$\frac{\partial(\rho u_i)}{\partial x_i} = 0 \tag{2.2}$$

Momentum:

$$\frac{\partial \rho u_i}{\partial t} + \frac{\partial \rho u_i u_j}{\partial x_j} = -\frac{\partial P}{\partial x_i} + \frac{\partial}{\partial x_j}\Big[\mu\Big(\frac{\partial u_i}{\partial x_j} + \frac{\partial u_j}{\partial x_i}\Big)\Big] + \frac{\partial(-\rho\overline{u_i' u_j'})}{\partial x_j} + f_i \tag{2.3}$$

Here, $u_i = \langle u, v, w \rangle$ are mean velocity components in the three Cartesian directions $x_i = \langle x, y, z \rangle$. t refers to the time domain, ρ is the density of air , P is the pressure at a point $\langle x, y, z \rangle$, μ is the dynamic viscosity of the fluid and f_i is an internal body force acting on the fluid. The quantity $-\rho\overline{u_i' u_j'}$ is known as the Reynolds stresses and is discussed further in Section 2.5. The Reynolds stresses in these equations are a direct result of time-averaging the instantaneous fluid behaviour.

© University of Pretoria

2.5 Turbulence Modelling

A complication arising in CFD is the accurate modelling of turbulence in a fluid. Turbulence is inherently random and chaotic so a fully deterministic solution of such flows would be extremely difficult to model. Since fluid mixing and energy dissipation in a wind field are highly influenced by turbulence and wall roughness boundaries, a lot of effort has been put into modelling the ABL using both RANS and LES turbulence closure approaches while paying particular attention to correct boundary condition enforcement (Blocken *et al.*, 2007; Vasaturo *et al.*, 2017; Parente *et al.*, 2011).

To date, the RANS approach has been the preferred method for solving typical engineering problems, with the $k-\varepsilon$ model being the most well known and implemented (Versteeg and Malalasekera, 2007). Technological advances have allowed for renewed interest in modelling turbulence using LES, which numerically resolves the largest turbulence scales while still approximating the small scales using spatial filtering (Abkar and Porte-Agel, 2015). The discussion is limited for now to the RANS approach and the more simple available turbulence models therein.

2.5.1 Reynolds Averaging

The RANS approach does not solve turbulent velocity fields directly but rather offers a steady-state solution to the governing equations where the turbulent fluctuations (often across a wide range of magnitudes and frequencies) have been time-averaged to reduce the complexity and computational expense of the problem at hand. Reynolds averaging involves decomposing instantaneous variables into mean values with fluctuating components, as shown below for velocity as an example:

$$u_i = \bar{u}_i + u_i' \tag{2.4}$$

where $\bar{u}_i$ is the average velocity and u_i' is the fluctuating (i.e. turbulent) component. The same decomposition is applied to all scalar variables such as temperature, pressure, energy, etc. Time averaging these components is mathematically defined as

$$\bar{\varphi} = \frac{1}{\Delta t}\int_0^{\Delta t} \varphi dt \qquad \text{and} \qquad \bar{\varphi'} = \frac{1}{\Delta t}\int_0^{\Delta t} \varphi' dt \equiv 0 \tag{2.5}$$

where φ can be any scalar quantity. Note that the time average of the fluctuations is always zero by definition. When these equations 2.4 and 2.5 for all velocity components are substituted into the incompressible Navier-Stokes equations (see Section 2.4), a new set of terms appear scattered throughout the fluid momentum equations which represent six additional turbulent stresses, or Reynolds stresses, taking the form:

$$\text{Normal stresses: } \tau_{ii} = -\rho\overline{u_i'^2} \quad \text{Shear stresses: } \tau_{ij} = \tau_{ji} = -\rho\overline{u_i' u_j'} \tag{2.6}$$

© University of Pretoria

where τ_{ij} represents the Reynolds stress tensor components in a fluid. Versteeg and Malalasekera (2007) treat the derivation of these stresses in greater detail. The objective of any RANS turbulence model is to close the Navier-Stokes equations by approximating the Reynolds stresses above. There are a variety of closure schemes available, each with their own advantages and disadvantages.

2.5.2 RANS Closure Schemes

When working with turbulence it is often necessary to quantify the instability in a fluid using the derived turbulence kinetic energy (TKE) value, k, given in Equation 2.7:

$$k = \frac{1}{2}\left(u'^2 + v'^2 + w'^2\right) \tag{2.7}$$

The Reynolds Stress Model (RSM) has been applied to ABL models in the past (Gibson and Launder, 1978) and is typically one of the more complex closure models, solving six transport equations for the Reynolds stress components and an additional equation for turbulent energy dissipation, ε. Although the RSM is well suited to predicting complex flows accurately, it is still severely limited by some of its closure assumptions and often is not worth the leap in required computing time over other closure schemes (ANSYS, 2018). The RSM is justifiably used in highly swirling flows and stress-driven secondary flows such as cyclone models or secondary induced flows in ducting; flows where the stresses are not isotropic by nature.

Further simplifications have been made to the Reynolds stress formulation; namely the assumption of isotropic turbulent eddies. While this is not necessarily true, it is a valid approximation for most practical flows dominated by only one of the turbulent shear stresses (ANSYS, 2018). The high Reynolds external flows considered in this study fall into this category. Isotropic turbulence is mathematically captured by the Boussinesq hypothesis (Marshall and Bakker, 2004).

The Boussinesq hypothesis is a common method for relating the Reynolds stresses to the average velocity gradients (Marshall and Bakker, 2004). This is done by introducing two new variables, the turbulence viscosity and kinetic energy, into the RANS equations:

$$\tau_{ij} = -\rho\overline{u_i' u_j'} = \mu_t\left(\frac{\partial u_i}{\partial x_j} + \frac{\partial u_j}{\partial x_i}\right) - \frac{2}{3}\rho k\delta_{ij} \tag{2.8}$$

where μ_t is the turbulence viscosity, k is the TKE and δ_{ij} is the Kronecker delta. The Spalart-Allmaras Model, k-ε and k-ω closure schemes all take advantage of the Boussinesq hypothesis. The Spalart-Allmaras Model solves a single extra equation and was developed mainly for use in the aerospace industry. The k-ε and k-ω schemes are both two-equation models that are more suited to general purpose complex flows (ANSYS, 2018) and are of more interest to this study.

© University of Pretoria

2.5.3 The Standard k-ε Model

Launder and Spalding (1983) proposed the first variant of the k-ε model, also referred to as the Standard k-ε (SKE) model, which has since become the workhorse for most practical engineering purposes and given rise to other similar variants due to its robustness and computational efficiency. The Re-Normalisation Group k-ε (RNGKE) and realizable k-ε (RKE) models are such modified variants of the SKE that account for known vulnerabilities in the original formulation. Parente *et al.* (2011) also looked at improving the k-ε model and wall functions specifically for simulation of ABL flows.

k-ε models resolve two new transport equations for the TKE and the turbulent dissipation rate, ε, shown respectively in Equations 2.9 and 2.10:

$$\frac{\partial \rho k}{\partial t} + \frac{\partial \rho k u_i}{\partial x_i} = \frac{\partial}{\partial x_j}\left[\left(\mu + \frac{\mu_t}{\sigma_k}\right)\frac{\partial k}{\partial x_j}\right] + G_k + G_b - \rho\varepsilon + S_k \tag{2.9}$$

$$\frac{\partial \rho \varepsilon}{\partial t} + \frac{\partial \rho \varepsilon u_i}{\partial x_i} = \frac{\partial}{\partial x_j}\left[\left(\mu + \frac{\mu_t}{\sigma_\varepsilon}\right)\frac{\partial \varepsilon}{\partial x_j}\right] + C_{1\varepsilon}\frac{\varepsilon}{k}\Big(G_k + C_{3\varepsilon}G_b\Big) - C_{2\varepsilon}\rho\frac{\varepsilon^2}{k} + S_\varepsilon \tag{2.10}$$

The unknown quantities in Equations 2.9 and 2.10 are compiled in Table 2.1 and further elaborated upon in Equations 2.11-2.14. All the given default values have been experimentally determined from frequently encountered turbulent flows, although the option to tune the constants is available (ANSYS, 2018).

Table 2.1: Modelling quantities for the SKE model

Variable	**Symbol**	**Default value**
Turbulent viscosity	μ_t	see Eq. 2.11
Turbulent Prandtl numbers	σ_k	1.0
	σ_ε	1.3
Turbulence generation terms	G_k	see Eq. 2.12
	G_b	see Eq. 2.13
Modelling constants	$C_{1\varepsilon}$	1.44
	$C_{2\varepsilon}$	1.92
	$C_{3\varepsilon}$	see Eq. 2.14
	C_μ	0.09 (Eq. 2.11)
Source terms	S_k	User defined
	S_ε	User defined

© University of Pretoria

$$\mu_t = \rho C_\mu \frac{k^2}{\varepsilon} \tag{2.11}$$

$$G_k = \tau_{ij} \frac{\partial u_j}{\partial x_i} \tag{2.12}$$

$$G_b = -g \frac{\mu_t}{\rho Pr_t} \frac{\partial \rho}{\partial z} \tag{2.13}$$

$$C_{3\varepsilon} = \tanh \left| \frac{v}{u} \right| \tag{2.14}$$

G_k and G_b account for the generation of turbulence as a result of the TKE and buoyancy effects (as discussed in Section 2.2.1). $G_b = 0$ in the x and y directions since buoyancy is only applicable in the direction parallel to gravity.

A brief overview of the other available k-ε variants is given here for completeness, although it is by no means an exhaustive survey. The variant models described here can be further perused in the original literature referenced above and in the ANSYS Fluent Guide (ANSYS, 2018) if necessary.

Yakhot and Orszag (1986) derived a turbulence model using re-normalisation group theory from statistics. The model was termed the Re-Normalization Group k-ε (RNGKE) model since it bears a similar form to the SKE, but offers refinements. The RNGKE provides analytical formulae for the turbulent Prandtl numbers (constant in the SKE) and introduces a new term in its derivation which allows for higher accuracy when modelling swirling flows (ANSYS, 2018). The RNGKE is thus suitable to modelling a wider range of flows if the appropriate care is taken when posing the problem.

A second improvement over the SKE was developed by Shih *et al.* (1995) which bears a new dissipation rate transport equation and a new formulation for the turbulent viscosity. This new Realisable k-ε (RKE) model places constraints on the Reynolds stresses, enforcing positive stress at all times; an important concept overlooked by both the SKE and RNGKE models which could lead to unrealisable stress solutions under certain conditions.

2.5.4 The k-ω Model

The k-ω (Wilcox *et al.*, 1998) and k-ω Shear Stress Transport (SST) (Menter, 1994) models both solve a transport equation for the specific dissipation rate, ω, rather than the dissipation rate, ε. Specific dissipation can be regarded as the ratio of ε to k, as given below:

$$\varepsilon = C_\mu k \omega \tag{2.15}$$

The TKE transport equation 2.9 is exactly the same for both the k-ω and k-ε models while

© University of Pretoria

the specific dissipation rate is modelled by the following ω transport equation:

$$\frac{\partial \rho\omega}{\partial t} + \frac{\partial \rho\omega u_i}{\partial x_i} = \frac{\partial}{\partial x_j}\left[\left(\mu + \frac{\mu_t}{\sigma_\omega}\right)\frac{\partial \varepsilon}{\partial x_j}\right] + G_\omega - Y_\omega + S_\omega \tag{2.16}$$

This family of models intrinsically accounts for the fact that flow close to a surface is slower and therefore has a low Reynolds number; compared to k-ε model and its variants, which have to apply artificial damping factors in near-wall regions to model the slower moving flow. The standard k-ω model has a known sensitivity to high Reynolds freestream flows where the k-ε model is better suited, thus giving rise to the k-ω SST model: a k-ω formulation which transitions into a full k-ε form further away from the wall boundary with the use of a blending function (Menter, 1994).

The exact details regarding all coefficients in the turbulence production, source and sink terms in Equation 2.16 are expounded upon in the Fluent Theory guide (ANSYS, 2018). Only the features of the k-ω formulation relevant to atmospheric simulations are discussed in this document.

In the k-ω model, the turbulent viscosity is computed as

$$\mu_t = \alpha^* \frac{\rho k}{\omega} \tag{2.17}$$

where α^* is a dynamically changing value based on the distance of a cell's centroid from its nearest wall and the local Reynolds number. Comparing Equation 2.17 with Equation 2.11 we note that α^* plays the same role as the quantity C_μ does in the k-ε family of models. It is this dynamic nature that makes the k-ω formulation more suitable to wall-bounded flows than the SKE model.

2.5.5 Wall Treatment

The presence of wall boundaries and surface roughness have a profound effect on turbulent flows and so the near-wall treatment in CFD code is very important for result accuracy. This section aims to describe the fluid dynamics in the near-wall region and also explain the computational methods used to simulate these conditions.

Any realistic viscous fluid is not able to glide along a wall frictionlessly, hence the well-known "no-slip" wall condition enforcing a zero relative velocity between wall and fluid (White, 2011). The fluid shear stress in the near-wall region, τ_w, accounts for the dissipation of energy due to friction and the subsequent reduction of fluid velocity.

The no-slip condition at the wall surface slows the moving fluid down to a low Reynolds number, thus resulting in an almost laminar flow. Viscous effects dominate the heat transfer and momentum flux in the laminar region known as the "viscous sub-layer"(Launder and

© University of Pretoria

Spalding, 1983); slightly further away from the wall, however, solution variables have large gradients which are responsible for the main generation of vorticity and turbulence in the flow. There is also a transitional region between the viscous sub-layer and the fully turbulent log-law flow. The accurate representation of these flow layers determines the success of the numerical predictions.

There are two approaches to near-wall modelling, namely: the use of semi-empirical formulae to bridge the gap between the wall region (viscous sub-layer) and the fully turbulent region, or the modification of the turbulence models in the near-wall region along with a finer mesh resolution to sufficiently capture the viscous sub-layer. Figure 2.6 provides an illustration for understanding both approaches:

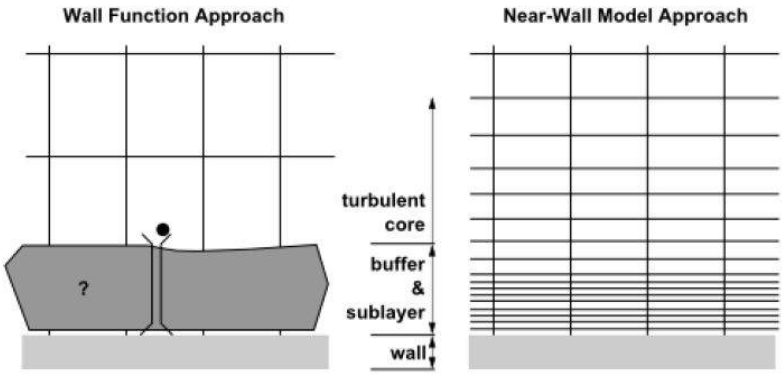

Figure 2.6: Two approaches to modelling fluid-wall interaction: The wall function approach applies separate equations to resolve near-wall fluid velocity, while the near-wall model approach still makes use of existing turbulence models with a finer mesh resolution. *Image from ANSYS (2018)*

Since ABL simulations already have quite large domain sizes with high cell counts by their nature, adding extra inflation layer cells as in the Near-Wall approach is deemed to be excessive. The Wall Function approach is a more economical use of computer resources for the current application. Rough surfaces are generally modelled by the standard smooth law of the wall with an extension to account for roughness (ANSYS, 2013):

$$\frac{u_p u_*}{\tau_w/\rho} = \frac{1}{\kappa} \ln\left(E \frac{\rho u_* z_p}{\mu}\right) - \Delta B \tag{2.18}$$

where: $u_p =$ mean velocity at the wall-adjacent cell centroid

$u_* =$ frictional velocity $= C_\mu^{0.25} k_p^{0.5}$

$k_p =$ TKE at the wall-adjacent cell centroid

$\tau_w =$ wall shear stress

$\kappa =$ von Kármán constant $= 0.4187$

$E =$ Empirical constant $= 9.9793$

$z_p =$ distance to the wall-adjacent cell centroid

© University of Pretoria

ΔB is the quantity used to adjust for roughness. ΔB has been shown to correlate fairly well with the non-dimensional roughness height, K_s^+, computed as (Zhang, 2009):

$$K_s^+ = \frac{\rho K_s u_*}{\mu} \tag{2.19}$$

K_s is the physical roughness height, typically defined as the equivalent sand-grain roughness, where it is assumed that roughness elements have a blockage effect roughly equal to half their height (Schlichting, 1979). There are three roughness regimes into which K_s^+ can be classified, and three corresponding ΔB relations as shown in Equations 2.20 - 2.22.
Hydrodynamically smooth regime, $K_s^+ \leq 2.25$:

$$\implies \Delta B = 0 \tag{2.20}$$

Transitional regime, $2.25 < K_s^+ \leq 90$:

$$\implies \Delta B = \frac{1}{\kappa} \ln\left(\frac{K_s^+ - 2.25}{87.75} + C_s K_s^+\right) \times \sin\Big(0.4258(\ln K_s^+ - 0.811)\Big) \tag{2.21}$$

Fully rough regime, $K_s^+ > 90$:

$$\implies \Delta B = \frac{1}{\kappa} \ln\left(1 + C_s K_s^+\right) \tag{2.22}$$

where C_s is a roughness constant that is dependent on the type of the roughness. The Fluent solver automatically assigns a value of $C_s = 0.5$, although it is possible to change (ANSYS, 2013).

Equation 2.18 modified for fully rough surfaces (Eq. 2.22) then becomes:

$$\frac{u_p u_*}{\tau_w/\rho} = \frac{1}{\kappa} \ln\left(\frac{E \rho u_* z_p}{\mu(1 + C_s K_s^+)}\right) \tag{2.23}$$

Noting that $\tau_w = \rho u_*^2$ under equilibrium conditions and applying the default setting $C_s = 0.5$ to Equation 2.23, we can rewrite the wall-function equations for smooth and rough walls in dimensionless form:

$$\text{Smooth:} \qquad u^+ = \frac{1}{\kappa} \ln\left(E y^+\right) \tag{2.24}$$

$$\text{Rough:} \qquad u^+ = \frac{1}{\kappa} \ln\left(\frac{y^+}{C_s K_s^+}\right) + 5.43 \tag{2.25}$$

$u^+ = u/u_*$ and $y^+ = \rho u_* z/\mu$ are the dimensionless velocity and distance from the wall, respectively.

© University of Pretoria

The turbulence boundary conditions enforced at the wall are discussed next. The k transport equation is numerically solved throughout the domain, including the wall adjacent cells, where the boundary condition is imposed as:

$$\frac{\partial k}{\partial n} = 0 \tag{2.26}$$

where n is the local coordinate normal to the wall.

The turbulence production, G_k, and dissipation rate, ε, are source terms in the k equation. These quantities are governed at the wall boundaries by:

$$G_k = \tau_w \frac{\partial u}{\partial z} = \frac{\tau_w^2}{\kappa \rho C_\mu^{0.25} k_p^{0.5} z_p} \tag{2.27}$$

$$\varepsilon_p = \frac{C_\mu^{0.75} k_p^{1.5}}{\kappa z_p} \tag{2.28}$$

It is worth highlighting that the turbulent dissipation transport equation is not solved throughout the domain like k transport equation, but rather by Equation 2.28 in wall adjacent cells.

Although a thorough treatment has been given here, the boundary conditions at the wall are well accounted for in the Fluent code and the modeller need only concern themselves with prescribing a realistic roughness height in order to achieve acceptable simulations (ANSYS, 2013).

One major drawback with the use of wall functions is that they tend to deteriorate if the mesh adjacent to a wall is too fine. As shown in Figure 2.6, the wall function equations were developed to numerically account for the deviation of a flow profile from the log law within the space of one cell, rather than explicitly resolving such a profile. For this reason, ANSYS (2018) recommend the use of scalable wall functions over the standard law of the wall in their Fluent solver.

Further details regarding wall boundary conditions can be found in Section 2.7.3.

2.6 Adaptation of Governing Equations for ABL Flows

In order to simulate full-scale ABL flows accurately, some important alterations are required to allow the RANS equations to reproduce atmospheric scale fluid dynamics. Changes will be necessary in the turbulence models which are often optimised to fit empirical data for the majority of industrial flows rather than for wind modelling applications. The Coriolis force must also be accounted for by including additional source terms to the Momentum Equation 2.3. ANSYS Fluent allows this effect to be introduced through source/sink terms and body forces, f_i.

© University of Pretoria

2.6.1 The Coriolis Effect

The Coriolis effect describes the induced inertial force in a parcel of air due to the rotation of the Earth (Manwell *et al.*, 2009). In most CFD studies, the Coriolis effect is barely noticeable and can be neglected; ABL simulations, however, need to take this effect into account due to their size approaching a meso-scale. In a frame of reference rotating on the Earth's surface, the Coriolis force always acts perpendicularly to the left with respect to the direction of wind travel (in the Southern Hemisphere). Coriolis forcing has a magnitude which is dependent on the wind speed and latitude (White and Bromley, 1995). Notationally, the Coriolis force is described by:

$$F_{c,i} = 2\Omega \sin(\phi)\iota_i \rho u_i \tag{2.29}$$

where F_c is the Coriolis force acting on the fluid, Ω is the speed of the Earth's rotation ($7.292 \times 10^{-5}\text{rad}\,\text{s}^{-1}$) and ϕ is the latitude in geographical radians. The Coriolis parameter, $f_c = 2\Omega \sin(\phi)$, is seen often in the literature, (e.g. Bechmann *et al.* (2007b)). The vector $\iota_i^T = \langle -1, 1, 0 \rangle$ implies that the Coriolis force is only applied in the horizontal x-y plane; gravitational acceleration far outweighs the Coriolis effect in the vertical z direction and thus renders it negligible (Manwell *et al.*, 2009). The force causes winds in the Northern Hemisphere to deflect to the right (with respect to the direction of travel), and those in the Southern Hemisphere to deflect to the left (Wallace and Hobbs, 2006).

2.6.2 k-ε and k-ω Model Constants

It has been noted throughout various pieces of literature that the SKE model with the components as shown in Table 2.1 has been adapted slightly by some authors. These modifications are slight but they do, nevertheless, affect the outcome of a solution.

Zhang (2009) notes that the typical value of $C_\mu = 0.09$ is a coefficient more suited to solving industrial flows whereas atmospheric research finds a value of $C_\mu = 0.03$ more applicable to ABL simulations, a value proposed by Katul *et al.* (2004). The other model constants are also adjusted to keep the model consistent in maintaining a Horizontally Homogeneous Turbulent Surface Layer (HHTSL). It should be noted here that the von Kármán constant is no longer a set value, but rather ranges between $0.4 \leq \kappa \leq 0.43$ depending on the other model constants:

$$\kappa^2 = (C_{2\varepsilon} - C_{1\varepsilon})\sigma_\varepsilon \sqrt{C_\mu} \tag{2.30}$$

The new model constants are chosen to fit experimental measurements or otherwise determined from Equation 2.30. Table 2.2 presents a modified set of SKE constants:

© University of Pretoria

Table 2.2: k-ε model coefficients used to model industrial and atmospheric flows (Launder and Spalding, 1983; Katul *et al.*, 2004)

k-ε model	C_μ	κ	$C_{1\varepsilon}$	$C_{1\varepsilon}$	σ_ε
Industrial (Launder and Spalding, 1983)	0.09	0.433	1.42	1.92	1.3
Atmospheric (Katul *et al.*, 2004)	0.03	0.4	1.21	1.92	1.3

In terms of the k-ω turbulence model, the numerical damping constant, C_μ, now becomes a dynamically changing factor as described by Equation 2.17. This effectively improves the near-wall treatment of the chosen turbulence model. Further away from the wall, where the k-ω model transitions into its k-ε cousin, the numerical constant β_∞ can also be altered from $\beta_\infty = 0.09$ to $\beta_\infty = 0.03$ to reflect the equivalent atmospheric alterations shown for the SKE model in Table 2.2 (Launder and Spalding, 1983; Katul *et al.*, 2004).

2.7 Boundary Conditions

Careful consideration of the boundary conditions surrounding the problem domain is an important aspect of CFD modelling. The idealised neutral ABL over a flat smooth surface is said to be horizontally homogeneous: air properties vary as a function of height, z, only and not of location, x, y. It has been the focus of many a research paper to correctly prescribe inflow boundary conditions which not only maintain this horizontal homogeneity requirement but also agree with experimental data as the solution is propagated throughout the computational domain (Yang *et al.*, 2009; Juretić and Kozmar, 2013; Balogh and Parente, 2015; Richards and Norris, 2015, among others).

This section is intended to compile the available literature into a clear set of modelling instructions to be used in ABL simulations going forward. In keeping with the theme of the document, only neutrally stable conditions have been considered.

2.7.1 Inlet Boundary Conditions

Inlet boundaries tend to receive the bulk of the attention since they are the main drivers of the solution and thus play the biggest role in a successful simulation. An inlet boundary condition for each of the solution variables (i.e. $\mathbf{u}$, T, k and ε) is required to solve all of the RANS equations and the temperature distribution.

As alluded to in Section 2.2, the wind velocity profile for a neutrally stable atmosphere follows the log law. The horizontal homogeneity assumption allows the incoming velocity to be specified as a one-dimensional function of height at the boundary given by (Zhang, 2009):

$$U(z) = \frac{u_*}{\kappa} \ln\left(\frac{z}{z_0}\right) \tag{2.31}$$

© University of Pretoria

with the direction of the driving velocity, U, being perpendicular to the boundary face. Defining an aerodynamic roughness length, z_0, as the height above ground where air speed is essentially zero due to roughness effects, the modeller can account for various types of realistic surfaces.

A pressure boundary condition does not need to be specified since the far-field pressure is already known to conform to the hydrostatic relation, $P(z) = \rho g z$, although it is necessary to set a reference pressure $P_0 = 101.3$ kPa. The influence of large-scale meteorological pressure systems has not been incorporated into the analysis. The temperature input is defined using the dry adiabatic lapse rate given in Equation 2.1 (Koblitz, 2013).

The turbulence parameters k and ε have analytical inlet profiles derived directly from the conservation equations by Richards and Norris (2011) under the assumption that the neutral ABL has a constant shear stress with height. These turbulence inlet profiles are given respectively by

$$k(z) = \frac{u_*^2}{\sqrt{C_\mu}} \tag{2.32}$$

and

$$\varepsilon(z) = \frac{u_*^3}{\kappa(z + z_0)} \tag{2.33}$$

The inlet boundary equations presented above can be successfully implemented with turbulence models other than the SKE model and, as such, have become common industry standards for ABL modelling (Blocken *et al.*, 2007). It should be noted that the TKE inlet profile described in Equation 2.32 above is applicable to only the lower surface portion of the ABL, typically no more than the first few hundred metres above ground level (Richards and Norris, 2011). When increasing height of the ABL is modelled, a smooth TKE profile needs to be established which maintains horizontal homogeneity while still accounting for higher turbulence close to the surface level and little to no turbulence in the upper part of the atmosphere; where geostrophic winds exhibit near-laminar flow.

Crasto (2007) derived such a TKE profile as shown in Equation 2.34:

$$k(z) = \frac{u_*^2}{\sqrt{C_\mu}}\left(1 - \frac{z}{z_h}\right)^2 \tag{2.34}$$

where z denotes the height above ground level and z_h is the depth of the boundary layer; taken to be the height at which actual and geostrophic winds coincide and above which the wind turbulence becomes minimal. While it is difficult to determine an exact boundary layer depth in reality, a value can be estimated for modelling purposes as:

$$z_h = C\left(\frac{u_*}{|f_c|}\right) \tag{2.35}$$

© University of Pretoria

The value for the constant C ranges from $0.2 - 0.4$ for a neutral ABL and is often given in the literature without a reference or derivation (Garratt, 1994).

2.7.2 Top Boundary Conditions

There has been contention over the correct modelling of the top ABL boundary, with academics struggling to find an all-encompassing formulation for a consistent boundary condition which does not lead to a decay in the ABL over long distances (Richards and Norris, 2015; Yang *et al.*, 2009; O'Sullivan *et al.*, 2011).

The original inlet conditions described in Equations 2.31-2.34 were derived with a constant shear stress in mind which led (Richards and Norris, 2011) to conclude that the top boundary requires the driving shear stress ($\tau = \rho u_*^2$) to be applied along with turbulent flux conditions

$$\left.\frac{\mathrm{d}k}{\mathrm{d}z}\right|_{top} = 0 \tag{2.36}$$

$$\left.\frac{\mu_t}{\sigma_\varepsilon}\frac{\mathrm{d}\varepsilon}{\mathrm{d}z}\right|_{top} = -\frac{\rho u_*^4}{\sigma_\varepsilon z} \tag{2.37}$$

The discussion by Hargreaves and Wright (2007) shed light on the fact that most modellers opt to neglect these recommendations and instead define the top boundary as a slip-free or symmetry boundary, which is the case with Koblitz (2013). While the symmetry boundary may provide a balance between simplicity and adequate results, it does run into shortcomings. In modelling the ABL this way, a decaying boundary layer is created which effectively changes by the time it reaches its intended solution target, so much so that numerical results could lose their meaning (Richards and Norris, 2011).

Unfortunately, the use of commercial CFD code (Fluent) is limited in that it does not allow all of these boundary conditions to be input without complex modifications. It is suggested that this and other similar limitations are what led to many engineers adopting the simpler slip-free/symmetry boundary approach in the first place (Hargreaves and Wright, 2007; Richards and Norris, 2015).

The closing comment for this discussion is that various easily implementable combinations of the top boundary conditions will be tested in later chapters and compared with each other to find a balanced approach for modelling a horizontally homogeneous ABL.

2.7.3 Terrain Boundary Conditions

While some aspects of wall treatment have already been investigated in Section 2.5.5, such as near-wall velocity and turbulence values, further details regarding the terrain (bottom wall) boundary are discussed here.

With regards to modelling the wind across Marion Island, a more complete description of slip is necessary to account for incoming airflow over the surrounding oceans. Wu (1975) performed

© University of Pretoria

some pioneering work in air-sea interaction with the main focus being on subsurface ocean velocity profiles as a result of winds. Conjugately, Veron *et al.* (2007) concluded that there is an equally complex air-sea interaction above, giving rise to wind-induced waves which can become large enough to introduce a new source of turbulence. Avoiding a model of such complexity, which is beyond the scope of this study, the approach taken by Longo (2012) is followed: simplifying air-sea interaction down to a simple drifting wall with velocity $u_s = 0.55u_*$ and a specified wave roughness height. The Charnock model (Peña and Gryning, 2008) can be used to approximate a roughness length, also as a function of wind friction velocity:

$$z_0 = A_c \frac{u_*^2}{g} \tag{2.38}$$

where g is the gravitational constant and $A_c \approx 0.018$ is the Charnock constant. It is common practice for CFD engineers to apply the aerodynamic roughness to the sea surface and neglect the drifting wall velocity as it adds an unnecessary layer of complexity without influencing the results significantly (Garratt, 1994).

The biggest concern with using a commercial CFD code to model flow over natural terrain is the discrepancies in modelling wall roughness. The user needs to be aware that the aerodynamic length, z_0, is essentially different from the sand-grain roughness, K_s, used by the wall functions in Fluent. The two roughness quantities are related by Equation 2.39 (Blocken *et al.*, 2007):

$$K_s = z_0 \frac{E}{C_s} \tag{2.39}$$

A range of typically used roughness lengths is given by Manwell *et al.* (2009) and is also available in Table A.1 in Appendix A. The wall functions used in Fluent were developed based on sand-roughened pipes and channels, which do not apply directly to terrain roughness, and so modelling errors could lead to unintended gradients in the velocity and turbulence flow directions (Blocken *et al.*, 2007).

To remove the confusion regarding wall functions and their roughness height sensitivity, a modified wall approach was derived by Parente *et al.* (2011) on the original foundation of Richards and Hoxey (1993) and can be seen as the direct extension of Equations 2.27 and 2.28 to include the influence of roughness length, z_0:

$$G_k = \frac{\tau_w^2}{\kappa \rho C_\mu^{0.25} k_p^{0.5} (z_p + z_0)} \tag{2.40}$$

$$\varepsilon_p = \frac{C_\mu^{0.75} k_p^{1.5}}{\kappa (z_p + z_0)} \tag{2.41}$$

© University of Pretoria

2.8 Wind Data Acquisition and Analysis

The final aspect of the Marion Island wind study is that of reliable physical measurements which are used to validate any CFD model. This short section focuses on the methods and instrumentation commonly used to gather wind data from the field, as well as an introduction to the statistical approach used to correlate obtained data with computer models.

From a wind energy perspective, wind data are important for determining the commercial viability of a potential wind farm location whereas from a CFD modelling perspective, that same data are crucial for solution validation exercises. At a glance the wind seems to behave erratically and without regard; however, there are underlying features that can be statistically analysed and manipulated for academic and commercial understanding (Manwell *et al.*, 2009). Hence, long-term wind data are crucial to understanding general trends rather than instantaneous measurements.

Kinetic wind energy is dissipated through the creation and destruction of successively smaller eddies. This well-documented energy cascade is easily seen in power spectral density plots (Aly, 2014). The time-averaged decomposition of wind speed has already been discussed in Section 2.5.1 and is helpful in determining real-world modelling quantities such as the Turbulence Intensity (TI) and integral length scales. Based on a time-series measurement of wind speed from an anemometer, the mean and standard deviation of the wind velocity can be computed over any length of time by

$$\bar{u} = \frac{1}{N_s} \sum_{n=1}^{N_s} u_n \tag{2.42}$$

$$\sigma_u = \sqrt{\frac{1}{N_s - 1} \sum_{n=1}^{N_s} \left(u_n - \bar{u}\right)^2} \tag{2.43}$$

where $\bar{u}$ is the time averaged velocity and σ_u is the standard deviation, both in a discretised sample form. N_s is the total number of samples in the data set and u_n are individual speed readings. The turbulence is not measured continuously, but rather sampled at an industry standard frequency of about 1Hz and then reduced down to average values ranging from 10 minute time periods to no more than an hour (Manwell *et al.*, 2009). The TI is defined by

$$TI = \frac{\sigma_u}{\bar{u}} \tag{2.44}$$

Higher turbulence intensities tend to occur during low wind speeds and vice versa. The surrounding terrain also has a significant effect on turbulence properties, which is partly the reason for performing such studies in the first place.

As with most naturally occurring phenomena, wind speed and direction typically fall into a probability density function rather than a clear deterministic distribution. Weibull or Rayleigh

© University of Pretoria

probability density functions tend to describe wind prevalence more aptly than the normal Gaussian distribution (Manwell *et al.*, 2009). However, for the purposes of the Marion Island wind project, the wind direction is also of importance along with the speed. The wind rose is an overall pictorial representation of these wind characteristics in an area (Crutcher, 1957). Figure 2.7 shows an example wind rose generated from raw Marion Island data (further discussed in Section 4.4).

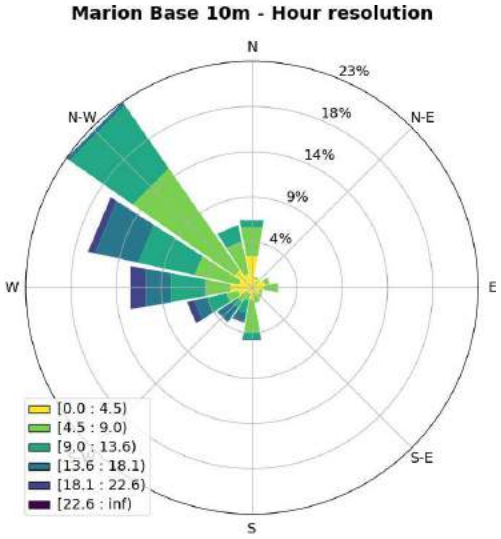

Figure 2.7: Wind speed [m/s] and direction prevalence depicted on a wind rose for the MI Base station sampled at 10m elevation

Autocorrelation is a powerful statistical method used to extract meaningful periodic interactions from the data such as turbulent length and time scales (Manwell *et al.*, 2009). Autocorrelation compares a signal with a delayed copy of itself in order to find the similarity between samples as a function of time delay. Essentially, the method returns a value of 1 when the lag is zero (i.e. every sample correlates 100% with itself, which makes sense) and successively smaller correlation values as samples further apart have less in common. The autocorrelation probability density function is given by

$$R(r\delta t) = \frac{1}{\sigma_u^2(N_s - r)} \sum_{n=1}^{N_s - r} u_n \cdot u_{n+r} \tag{2.45}$$

where R is the autocorrelation coefficient, r is the lag number and δt is the sampling time between points. Lag time, in Figure 2.8, is equal to the number of accumulated sampling time intervals ($r \times \delta t$). The integral time scale is determined by integrating the autocorrelation from $r = 0$ to the first point where $R = 0$ (refer to Figure 2.8). This time scale indicates the average time span over which wind speed fluctuations correlate.

© University of Pretoria

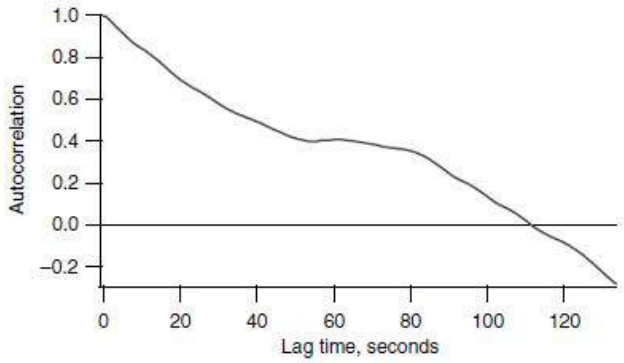

Figure 2.8: Simple figure to illustrate the calculation of the autocorrelation time scale

The integral length scale, L, is simply the mean velocity multiplied by the time scale. The integral length scale provides an indication of the average size of turbulent eddies in the mean flow. Cross correlation is a similar procedure, only performed on two different sets of data with the goal of determining the overall interactions and dependencies between values.

Last of the statistical analysis methods is the Power Spectral Density (PSD) function. If the wind turbulence fluctuations are thought of as multiple superimposed sinusoids with differing frequencies and amplitudes, the PSD function essentially transforms the turbulence data into the frequency domain via a Fast Fourier Transform (FFT), removing time dependence. Lower frequency turbulent eddies identified in the PSD are typically larger and contain far more energy than the higher frequency spectra (Manwell *et al.*, 2009). This technique finds useful application when modelling transient flows and comparing experimental data with the output from say a LES simulation.

2.9 Dimensional Analysis and Scaling

A main component of this project depends on data interpretation, specifically on comparison between large sets of experimental data against simulation outputs. Individuals in non-engineering disciplines, particularly in the biological or geographical sciences, may find this discussion helpful for explaining certain engineering conventions. This Chapter is aimed at acquainting the audience with the technique of dimensional analysis as well as any dimensionless parameters used throughout the rest of the report.

The technique of dimensional analysis is widely used throughout the science and engineering fields to reduce the complexity of a given problem as well as provide a compact means of presenting information (White, 2011). Of the vast number of dimensionless variables available to the CFD engineer, perhaps the most well-known and frequently encountered is the Reynolds number:

$$Re = \frac{\rho V_\infty L}{\mu} \tag{2.46}$$

© University of Pretoria

where V_∞ is the freestream velocity and L is a defined characteristic length inherent to a given problem. The Reynolds number can be viewed as the ratio of inertial forces to viscous forces within a fluid which is widely applied to determining the flow regime (White, 2011). For external flows, a Re number below the threshold value of 1×10^6 typically imply laminar flow while high Re numbers imply turbulent flow.

An explanatory discussion concerning non-dimensional parameters is available in Appendix B for the unacquainted reader.

The discussion thus far is of limited use without focusing on the non-dimensional quantities of direct importance in this project. Stull (1988) gives a full review for introducing dimensionless variables as a means of scaling most meteorological variables into a universal form. The following list of non-dimensional groupings in Table 2.3 will be used extensively throughout this report to discuss and compare various wind data.

Table 2.3: Table of important non-dimensional groupings used throughout this document (Balogh and Parente, 2015; Bechmann *et al.*, 2007b)

Parameter	Grouping	Definition
Velocity	$\frac{\lvert U\rvert}{u_*}$	The ratio of observed velocity magnitude against a reference velocity (taken to be the friction velocity). This scaling is also applied separately to u-, v- and w-components of velocity.
Turbulence (TKE)	$\frac{k}{u_*^2}$	The TKE scaled by a factor of u_*^2.
Height	$\frac{z}{\delta}$	The vertical coordinate, z, scaled by the a characteristic length. Typically, the boundary layer height, δ, is taken as the characteristic length. In cases where δ is not constant or non-deterministic (i.e. over complex terrain) a new characteristic length is chosen.
Turbulence Dissipation	$\frac{\varepsilon\delta}{u_*^3}$	The TDR scaled by a factor of u_*^3 and multiplied by a characteristic length to make the group dimensionless.

Since a majority of the dimensionless scaling groups rely heavily upon the friction velocity, u_*, Weber (1999) offer some remarks on calculating or estimating its value from data. Most of the experimental data in this project have been obtained from 2D sonic wind anemometers placed around Marion Island (further explained in Section 4.1), thus an accurate 3D definition

© University of Pretoria

of friction velocity is not possible. For 10-minute and 60-minute temporally-averaged wind measurements, Weber (1999) recommends using a linear estimator to define a value for u_* from simply determined 2D turbulence statistics. The use of this method has been generalised for flat terrains or open ocean and thus has limitations when estimating u_* over complex terrain (Weber, 1999); it is, however, the most viable option given the circumstances.

Table 2.4 gives the reported regression coefficients for estimating u_* as a function of either the scalar velocity magnitude, $|U|$, or the horizontal component of turbulence, σ_h, based on an extensive set of meteorological measurements (Weber, 1999). The horizontal turbulence is given by:

$$\sigma_h = \sqrt{\sigma_u^2 + \sigma_v^2} \tag{2.47}$$

Table 2.4: Regression coefficients, c, of a linear estimator for u_* under different atmospheric stability classes, for short (10-minute) and long (60-minute) sampling intervals. Adapted from Weber (1999)

Atmospheric	$\mathbf{u_* = c\|U\|}$		$\mathbf{u_* = c\sigma_h}$	
Stability	10'	60'	10'	60'
Slightly Stable	0.15	0.17	0.31	0.28
Neutral	0.15	0.15	0.33	0.28
Slightly Unstable	0.14	0.14	0.31	0.24

2.10 Summary

This literature review began by defining the Atmospheric Boundary Layer (ABL) and gave an in-depth treatment of the fluid physics taking place therein. Turbulent mixing in the atmosphere is a result of wind interactions with rough terrain in the lowest part of the ABL as well as of the buoyant forces causing air to rise when being heated or sink when being cooled by the ground below. The concept of thermal stratification is used to categorise the ABL into three main states of stability: unstable when turbulent mixing is at a maximum, stable when turbulence is suppressed by cooling effects and the neutrally stable when the atmosphere is in thermal equilibrium. Only neutral flows are considered in this study since it was deemed that Marion Island experiences neutral conditions most of the time as a consequence of its hyper-oceanic climate.

A review of the current state of the art of CWE revealed that large-scale ABL simulations have been successfully simulated before with varying degrees of accuracy and computational economy. A short discussion about the available CFD modelling software ensued where ANSYS Fluent was introduced as the package to be used throughout this study.

© University of Pretoria

The governing fluid mass and momentum conservation equations were explained and given in time-averaged RANS form. Turbulence modelling was also discussed, starting with the concept of Reynolds stress and moving on to the derivation and workings of the k-ε model and other variants in the family of two-equation models. The basic governing equations were adapted to suit ABL simulations by including the Coriolis Effect and buoyancy forces as new source terms.

Boundary conditions at the inlet, top and bottom (ground) surfaces are given based mostly on the constant shear-stress assumption through the height of the ABL (Richards and Hoxey, 1993). It was noted that there may be some trouble applying all boundary conditions due to software limitations in Fluent. Wall treatment and surface roughness were given more attention to include modelling a moving sea boundary as well as rough complex terrain.

A toolbox of statistical methods was put together to analyse real-world wind data and draw meaningful conclusions. In general, the wind data are reduced down to a mean and a standard deviation which can be used to calculate realistic model inputs. Autocorrelation offers a particularly interesting insight into the dominant turbulent length scale present in the data, while a Power Spectral Density (PSD) function extracts frequency and amplitude information from the measurements.

Finally, a brief treatment of dimensional analysis and scaling was given to acquaint the reader with methods used in this report to compare wind data from various sources. The necessary dimensionless parameters were listed for future reference when plotting scaled data in a compact universal form.

© University of Pretoria

3 Introductory Numerical Modelling

This Chapter focuses on prescribing and validating a numerical ABL model which was used for simulating the wind patterns across MI. Various aspects of the proposed wind model were tested and tweaked on simplified geometries/domains before being passed on for full MI wind simulations. These simplified experimental models are discussed and vetted for performance metrics which were crucial to understanding CFD solver behaviour when modelling the atmosphere. ANSYS Fluent 2019R3 software was used for all the CFD experiments in this study.

3.1 Model Setup

The objective here was to simplify the ABL model down to its core components without drastically reducing the accuracy of the results when compared to reality. Reducing the number of partial differential equations (PDEs) and other numerical elements at this early stage meant that more computational resources could be allocated towards achieving a finer resolution mesh and overall solution. Assumptions and engineering decisions made during the course of the CFD experimental procedure are presented below:

- Air as an incompressible homogeneous gas was used.
- Only neutral atmospheric conditions were considered since thermal turbulence effects are heavily superseded by the high wind speed turbulence effects.
- Since it is impractical to prescribe and maintain a thermal inversion capping layer at a predetermined height throughout the computational domain (other than at boundary nodes), these effects were neglected in the simulations. In the absence of these thermal effects, the decision was made to completely exclude solving the energy equation since temperature gradients were assumed to be negligible; thus reducing the computational requirements of the problem significantly.
- In the experiments performed in this Chapter, a reduced domain size was used thus rendering the Coriolis effect negligible. In the full Marion Island simulations performed in later chapters, however, Coriolis forcing was added as a momentum source term.
- Steady-state RANS simulations were performed with the modified atmospheric $k-\varepsilon$ turbulence model. Inlet velocity and turbulence profiles were applied as shown in Equations 2.31, 2.33 and 2.34.

Note that for all documented CFD experiments and results to follow in this study, the above simplifications have been applied unless specifically stated otherwise. To aid understanding, a table is provided at the beginning of each new case that discloses the full model setup.

© University of Pretoria

3.2 Empty Domain Testing

An empty domain test was performed in order to assess the validity of the applied inlet boundary profiles for velocity, TKE and dissipation rate. The goal was to achieve a horizontally homogeneous ASL starting at the inlet boundary with the same, or fairly similar, profiles being recovered at the outlet and throughout the domain.

3.2.1 Setup

A 100km long × 200m wide × 6 km high empty domain was created with the inlet profiles specified at one end and an outflow condition at the other end which simply extrapolates flow variables from the inner domain onto the outlet boundary with a constant gradient. Table 3.1 shows the full model setup parameters for simulation of the Horizontally Homogenous Turbulent Surface Layer (HHTSL).

Table 3.1: Model parameters for empty domain HHTSL simulations

Domain Size	100km x 200m x 6 km (L x B x H)
Mesh	
Cells:	4.25 Million Hex Cells
Horizontal Sizing:	20m x 20m
Vertical Sizing:	85 cells with constant growth factor
	0.05m first cell height
	growth rate: 1.1191
Inlet Boundary Profiles	
velocity	Eq. 2.31 with $U_* = 0.5ms^{-1}$ and $z_0 = 0.0005m$
TKE (k)	Eq. 2.34
TDR (ε)	Eq. 2.33
Other Boundary Conditions	
Outlet:	Outflow Boundary
Top:	a) Symmetry boundary
	b) Moving wall
Sides:	Symmetry Boundary
Bottom:	Wall Boundary
Model Settings	
Gravity:	-9.81 m/s^2 (z- direction)
Coriolis Parameter (f_c)	-1.06E-04
Coriolis Force:	No
Wall roughness:	$z_0 = 0.0005$m (rough sea)
Wall Functions:	a) Built-in scalable wall functions
	b) Parente *et al.* (2011) Improved wall functions

© University of Pretoria

A visual portion of the mesh is shown in Figure 3.1. The majority of cells are located at the bottom of the domain to capture surface layer interactions with the surface roughness whilst the higher parts of the domain are not expected to experience much change. This is in line with other wind research (See Section 2.3). Future analyses are dedicated to further focusing on the lower portion of the ABL. The results presented here were equally achieved by a coarser mesh of 50 m x 50 m horizontal and 75 cell vertical resolution; only the finer mesh results are shown and analysed since they were already calculated as part of the mesh independence exercise and readily available.

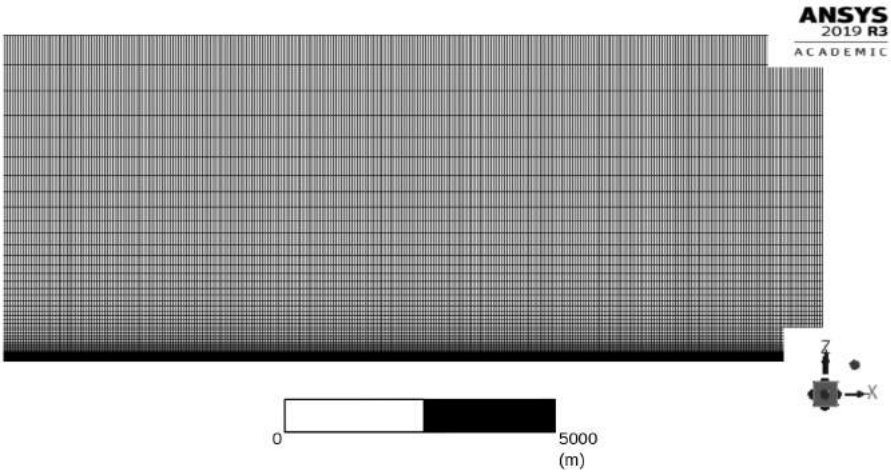

Figure 3.1: A small portion showing the Fluent mesh used in evaluating the inlet boundary profiles

3.2.2 Evaluation

As listed in Table 3.1, two boundary conditions for the top plane were attempted, namely: Symmetry and Moving Wall, as well as two wall-function formulations: the ANSYS built in Scalable wall functions and the Parente *et al.* (2011) improved wall function approach.

In terms of the top boundary plane options, the solution in the lower ABL exhibited no difference whatsoever. Since the only difference between a moving wall and a symmetry boundary type is a slight modification to the treatment of property gradients in adjacent cells, the solution becomes completely independent on the choice of boundary type if the boundary is placed sufficiently far away from the terrain (bottom wall).

As for applying the different wall function formulations at the terrain level, the plots in Figures 3.2 and 3.3 compare the ABL evolution for scalable wall functions and improved wall functions, respectively. Scalable wall functions were implemented in Fluent by converting the given roughness length, z_0, to an equivalent sand-grain roughness (see Section 2.7.3). A UDF was compiled and implemented to model the improved formulation and is available in Appendix C.

The quantities for velocity, TKE and turbulent dissipation in Figures 3.2 and 3.3 have been universally scaled with dimensionless quantities to remove dependence on the modelled wind

© University of Pretoria

speed. As explained in Section 2.9, Velocity and TKE are typically scaled by the corresponding wall-adjacent friction velocity, u_*, to give a dimensionless ratios, U/u_* and k/u_*^2 respectively. The non-dimensional height, h/δ, and dissipation rate, $\varepsilon\delta/u_*^3$, were calculated with the characteristic length as the modelled domain height, $\delta = H$, and the dissipation rate logarithmically scaled in Figures 3.2 and 3.3 to aid readability.

Wind "fetch" refers to the horizontal distance (x-direction) covered by the stream of air. The aim of Figures 3.2 and 3.3 is to visually present the degradation of the inlet profile with increasing fetch up to a maximum of 100km.

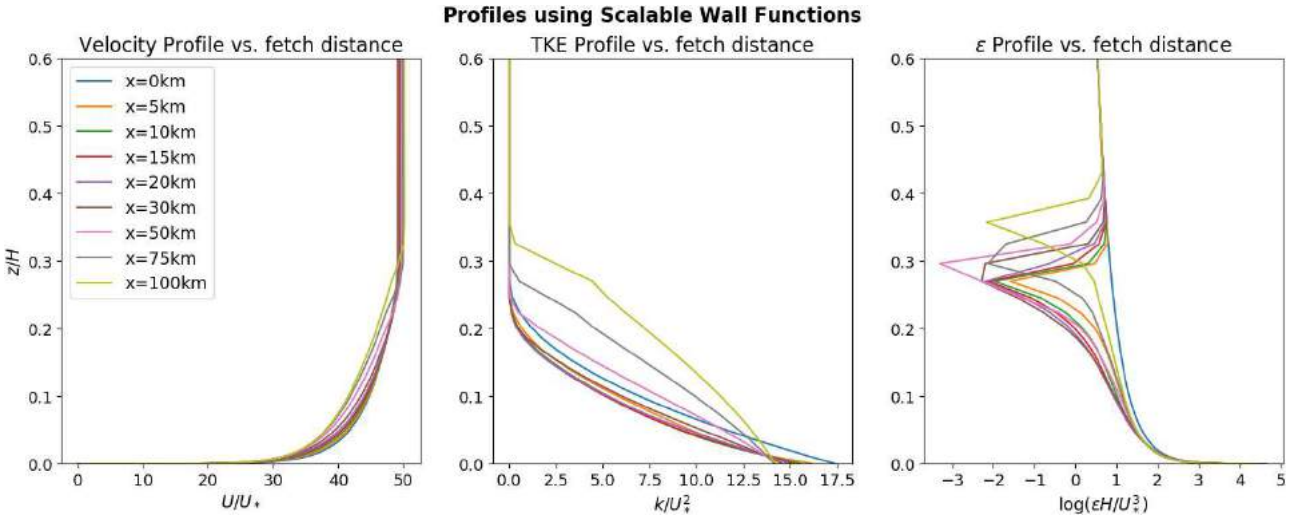

Figure 3.2: Inlet profile evolution through the 100km domain using scalable wall functions. Graphs have been made non-dimensional using model parameters $H = 6000m$, $U_* = 0.4m/s$

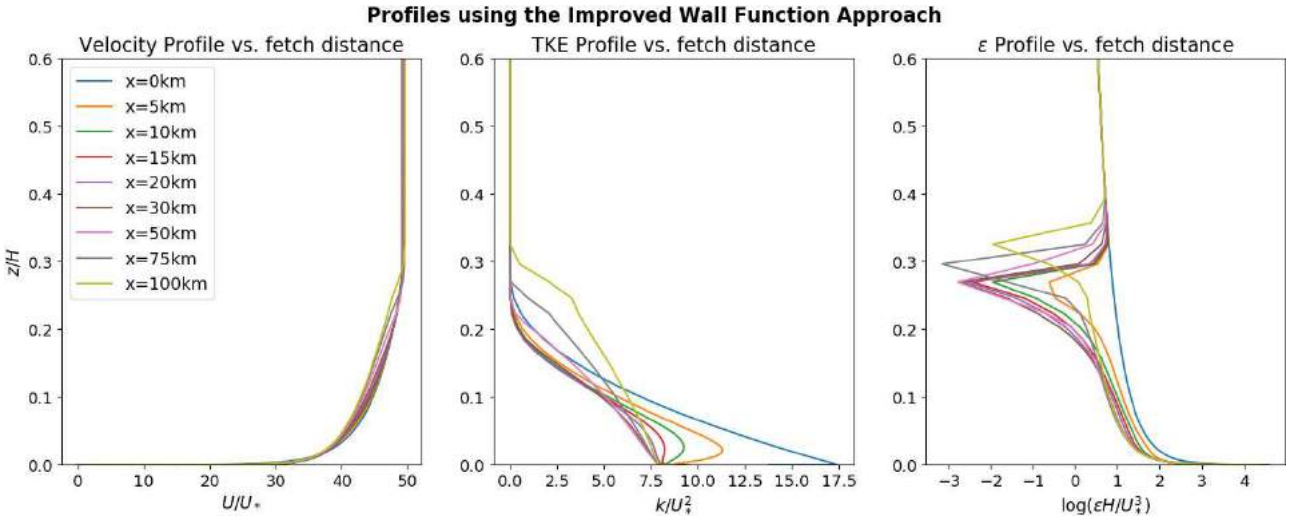

Figure 3.3: Inlet profile evolution through the 100km domain using the improved wall function approach of Parente *et al.* (2011).Graphs have been made non-dimensional using model parameters $H = 6000m$, $U_* = 0.4m/s$

© University of Pretoria

At first glance it would appear that the improved wall functions offer superior performance to the built-in scalable wall functions. The downwind profiles show less degradation over a longer fetch distance. However, two metrics are introduced to quantitatively evaluate the accuracy of the simulated wind profiles: namely, the Maximum Absolute Error (MAE) and the Root Mean Square Error (RMSE). These two metrics are calculated as follows:

- The MAE is calculated at each fetch distance, d, as

$$MAE = \max\left(|\phi_{dist=d} - \phi_{dist=0km}|\right) \times \frac{100}{mean(\phi_{dist=0km})} \tag{3.1}$$

- The RMSE is calculated at each fetch distance, d, as

$$RMSE = \sqrt{mean\left((\phi_{dist=d} - \phi_{dist=0km})^2\right)} \times \frac{100}{mean(\phi_{dist=0km})} \tag{3.2}$$

where ϕ is a placeholder notation for any velocity or turbulence array. The last term in both equations is a simple way of scaling the errors into an easily understandable percentage of the mean inlet profile. Figures 3.4 and 3.5 show the MAE and RMSE respectively, comparing both wall function strategies along the 100km fetch distance.

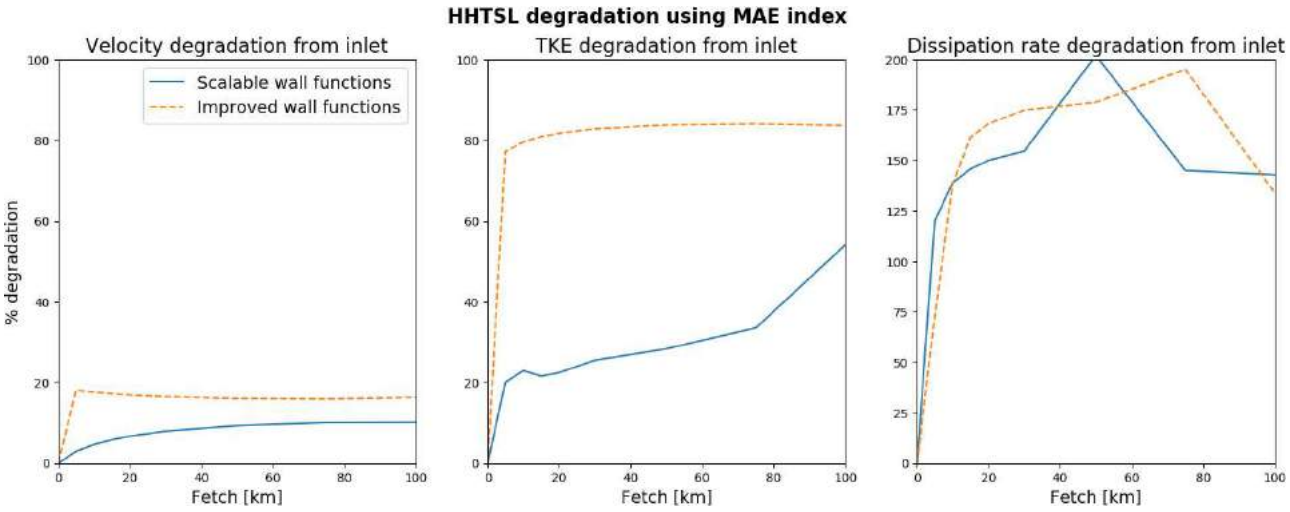

Figure 3.4: Degradation of the inlet profiles as they move through the domain subject to different wall functions, measured as a percentage deviation from the applied boundary condition

© University of Pretoria

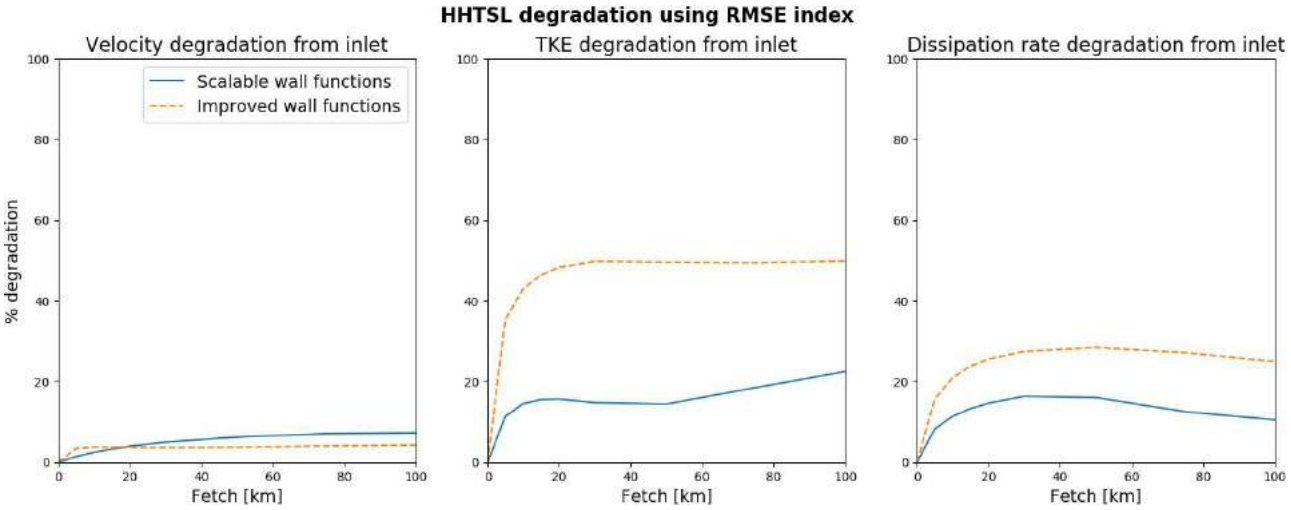

Figure 3.5: Degradation of the inlet profiles as they move through the domain subject to different wall functions, measured as a percentage deviation from the applied boundary condition

When looking at the MAE between the inlet boundary and each subsequent downwind profile (Figure 3.4), it becomes apparent that the improved wall function approach does a poor job of maintaining the inlet profile over distance. Similarly, the RMSE in Figure 3.5 shows that the improved wall functions only offer slightly better results for maintaining a velocity profile, but not for turbulence.

Up to a range of about 50km, the scalable wall functions outperform the improved wall function approach for all aspects. Both methods show equally poor performance regarding dissipation rate; reaching peaks of up to 250% maximum degradation. It should be noted, however, that the majority of this deterioration takes place in the upper part of the surface layer where the TKE and dissipation are really small; thus rendering a 250% error comparatively negligible to the turbulence quantities seen in the lower part of the surface layer.

Looking broadly at the solution contours for velocity and TKE in Figure 3.6 it is easy to see that horizontal homogeneity has been achieved to some degree. The length-wise dimension of the domain has been scaled to accommodate the full 100km domain within the width of a page. The velocity profile is seen to remain mostly consistent with fetch length while the TKE profile shows some degradation and change with distance. Scaling the length also helps to condense and show any degradation more prominently.

© University of Pretoria

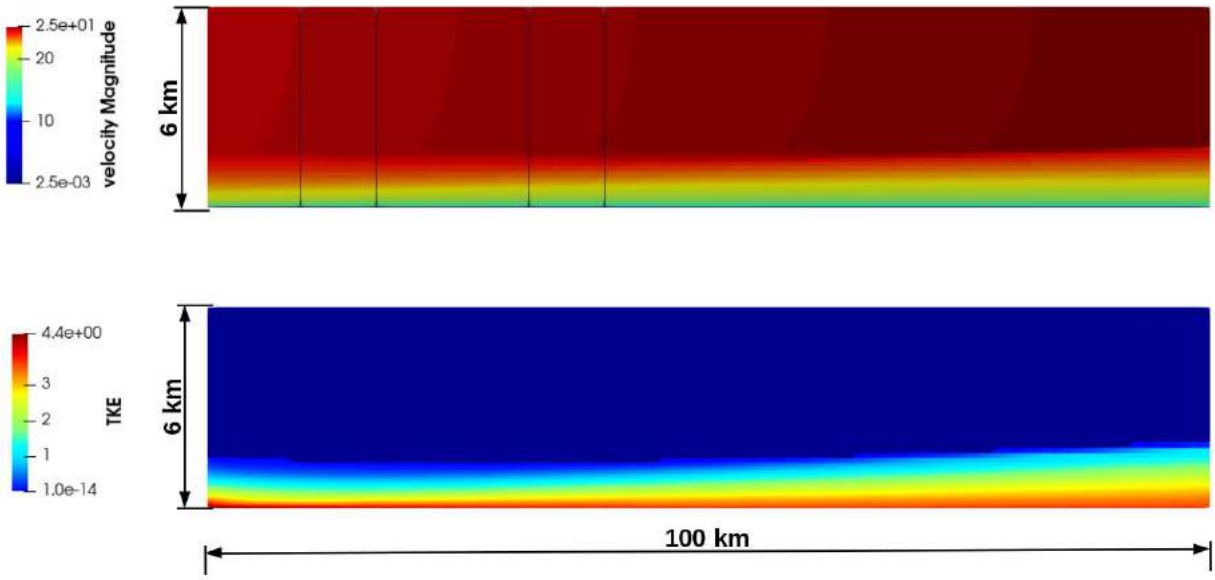

Figure 3.6: Contour plots of velocity magnitude [m/s](top) and TKE [m^2/s^2] (bottom) evolution throughout the 100km empty domain simulation. In both cases, horizontal homogeneity has been achieved until about the 50km mark

3.2.3 Deductions

The applied boundary conditions are conducive to simulating a horizontally homogeneous surface layer and will thus be introduced in all further simulations. The HHTSL degrades slightly over large distances, especially with respect to the TKE profile. With this in mind, it was determined that the ideal fetch length for future simulations would be 50km or less if excessive profile degradation is to be avoided. Also, referring back to Figures 3.4 and 3.5 again, it is seen that there is little to no benefit in using the improved Parente *et al.* (2011) wall-function approach if an upstream fetch of less than 50km is adhered to. While the scaled wall-function approach gives marginally better results in an empty domain, the topographical features in a non-trivial domain are expected to nullify any positive contribution once land-air turbulence interactions start to overpower the solution. The inconvenience of compiling a UDF across multiple computing cores and complicating the model can be avoided by simply using the built-in scalable wall functions which are proven to work and offer excellent results. The wall roughness height could be increased as a means of inducing more turbulent kinetic energy in the flow if needed, but this would be highly problem-dependent; an optimisation exercise beyond the scope of this investigation.

© University of Pretoria

3.3 Bolund Island Case Study

The current ABL model has been tested and verified for horizontal homogeneity in an empty domain; the next task is to validate its performance over a complex terrain, namely Bolund Island. Bolund Island is a small 12m high peninsula of land along the coast of Denmark near Risø DTU, pictured in Figure 3.7. Whereas the previous empty-domain case study focused on modelling the correct horizontally homogeneous atmosphere in the lower ABL, the current case study aims to validate the model performance over complex terrain using a well documented benchmark experiment. Rather than presenting a full, in-depth study of the Bolund Island experiment, the objectives of this section are:

- to evaluate and fine-tune the current ABL model for complex terrain simulations.
- to identify any shortcomings in the model which may need to be rectified at a later stage.
- to test various strategies, model parameters and settings on a smaller problem set before moving onto larger, computationally demanding ventures.
- to showcase the practical experience gained in wind modelling thus far.

Reaching these objectives have the end goal of finally simulating wind patterns across Marion Island.

Figure 3.7: Bolund Island in Denmark (Bechmann *et al.*, 2009), the subject of the current precursor case study

3.3.1 Setup

For the most part, authors of the original Bolund experiment (Bechmann *et al.*, 2009) fully describe an adequate modelling domain for simulating wind across the peninsula. For a more complete description of the Bolund wind measurement and experimental campaign, the original documents can be consulted (Bechmann *et al.*, 2007a, 2009; Berg *et al.*, 2011). While four wind direction cases were originally identified for modelling the most prevalent atmospheric conditions around Bolund Island, it was only necessary to model two such cases to reach conclusions on the validity of the ABL model; one with a direct westerly wind coming from a bearing of 270° and the second approaching from 239°. Table 3.2 shows the full model setup parameters for the experiments to follow. Polyhedral meshes were generated in ANSYS Fluent Meshing using the Bolund topographical data (Bechmann *et al.*, 2009) as input.

© University of Pretoria

Table 3.2: Setup parameters for Bolund Island simulations

Domain Size	1 km x 1 km x 200 m (L x B x H)
Mesh	
Cell Type:	Polyhedral
Horizontal Sizing:	0.25m at ground level
	15m at top boundary
Vertical Sizing:	0.1m first cell height
	1.1 growth rate for 20 layers
Cell count:	2.7 Million (Coarse); 5.9 Million (Fine)
Inlet Boundary Profiles	
velocity	Eq. 2.31 with $U_* = 0.4ms^{-1}$ and $z_0 = 0.0003m$
TKE (k)	Eq. 2.34
TDR (ε)	Eq. 2.33
Other Boundary Conditions	
Outlet:	Outflow
Top:	Moving Wall (same as inlet velocity)
Sides:	Symmetry Boundary
Bottom:	Wall Boundary
Model Settings	
Gravity:	-9.81 m/s^2 (in the z- direction)
Coriolis Parameter f_c	1.00E-04
Coriolis Force:	No
Sea wall roughness:	$z_0 = 0.0003$m (calm sea)
Land wall roughness:	$z_0 = 0.015$m (pasture)
Wall Functions:	Scalable with modified sand grain roughness

It should be noted here that the TKE formulation used in the simulations was different to that suggested by Bechmann *et al.* (2007a): namely, using Eq. 2.34 rather than the suggested constant value of $k/u_*^2 = 5.8$ through the domain height. For completeness sake, a coarse-mesh and a fine-mesh were generated and compared to ensure that mesh independence was achieved for this example problem. From a modelling perspective, land roughness of $z_0 = 0.015m$ was applied to cell faces that had a centroid height $z_c > 0m$ and to all faces with an x-component greater than $x > 327m$ (the start of the mainland); otherwise a wall roughness height corresponding to calm sea was specified. This is in accordance with the Bolund Experiment (Bechmann *et al.*, 2007a). The roughness lengths were converted into an equivalent sand-grain roughness (see Eq. 2.39) and used in conjunction with scalable wall functions. Iterations were stopped once all residuals were smaller than 1E-5.

© University of Pretoria

Figure 3.8 summarises the surface roughness modelling graphically and also shows the modelled wind directions and the positions of the wind measurement masts used to validate any CFD results.

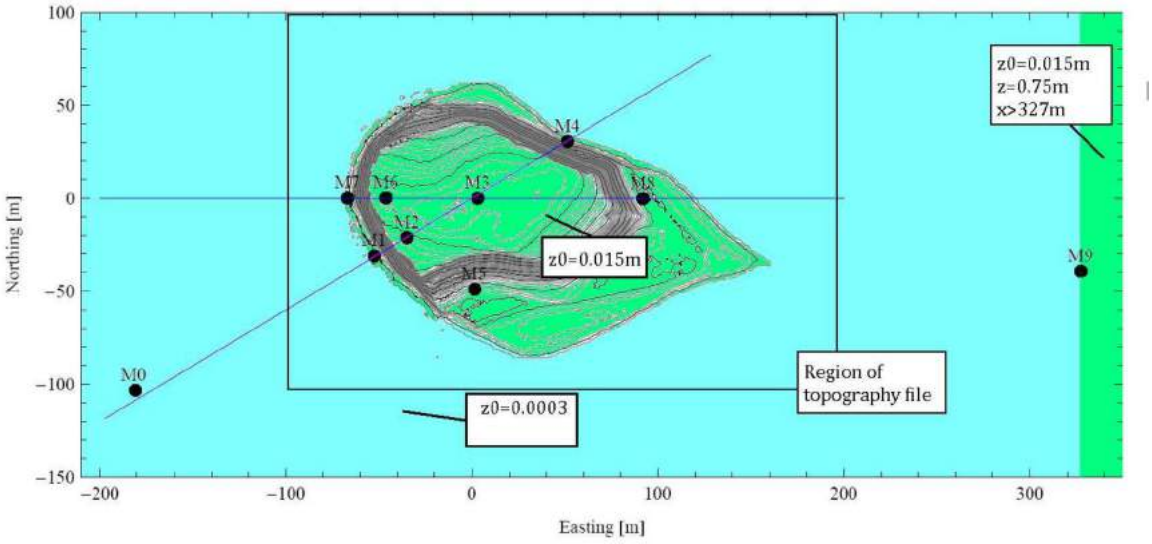

Figure 3.8: Definition of surface roughness as stipulated by Bechmann *et al.* (2007a). Mast locations M0-M9 are also labelled for future reference

The computational mesh used in these simulations is seen in Figure 3.9. The cell count was doubled by increasing the number of prism layers near the bottom wall surface as well as reducing the outward cell growth factor from the island; effectively adding more cells in areas critical to the simulations.

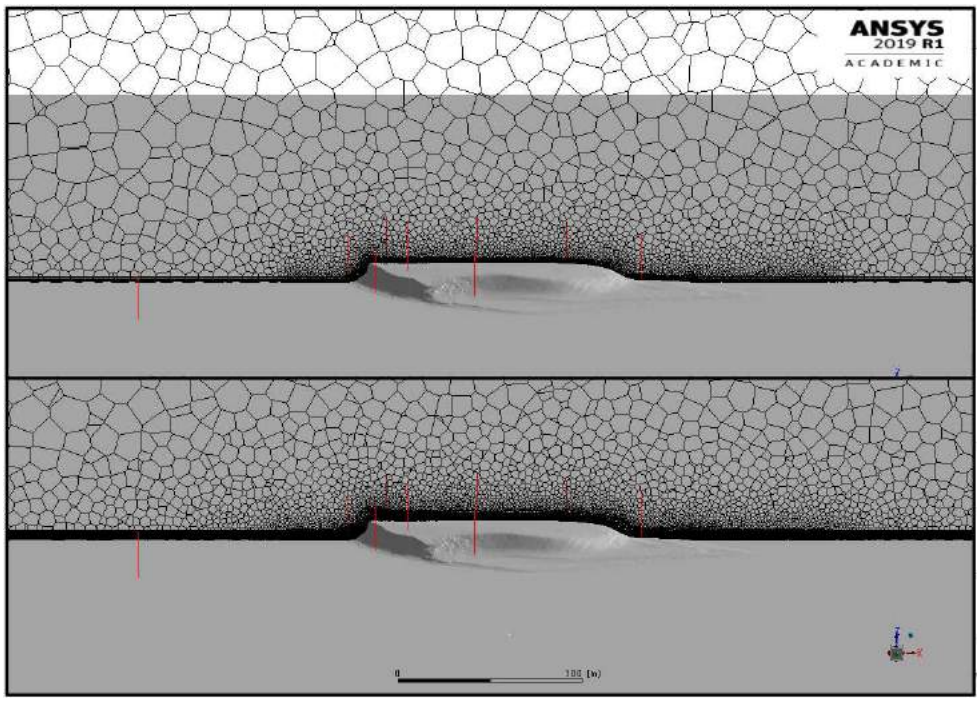

Figure 3.9: Coarse- (2.7 million cells, top) and fine grained (5.9 million cells, bottom) meshes used in the Bolund simulations. Cross sections taken in the $y = 0$ plane (270° direction). Red lines indicate mast positions M0 through M8 corresponding with those shown in Figure 3.8

© University of Pretoria

3.3.2 270° Wind Simulation

Evaluation of the ABL model is performed here by comparing the outcome of the simulations to the wind measurement statistics provided by Bechmann *et al.* (2007a) in the DTU Bolund Island dataset.

The vertical profiles in Figures 3.10 and 3.11 are the dimensionless velocity magnitude and TKE extracted from the CFD simulations for a wind approaching at 270°. Note that the order of the graphs in the profiles corresponds to the mast numbers following a direction of travel of the wind from West to East along the island; refer back to Figure 3.8 for clarification. Other masts are excluded for this direction of flow. The blue line indicates the coarse-mesh solution while the red line shows the fine-mesh solution. Data points from the given DTU Bolund Island dataset are indicated as black dots with standard deviation error bars obtained from Bechmann *et al.* (2007a). All data have been normalised such that the zero-reference height refers to local height Above Ground Level (AGL) rather than absolute altitude.

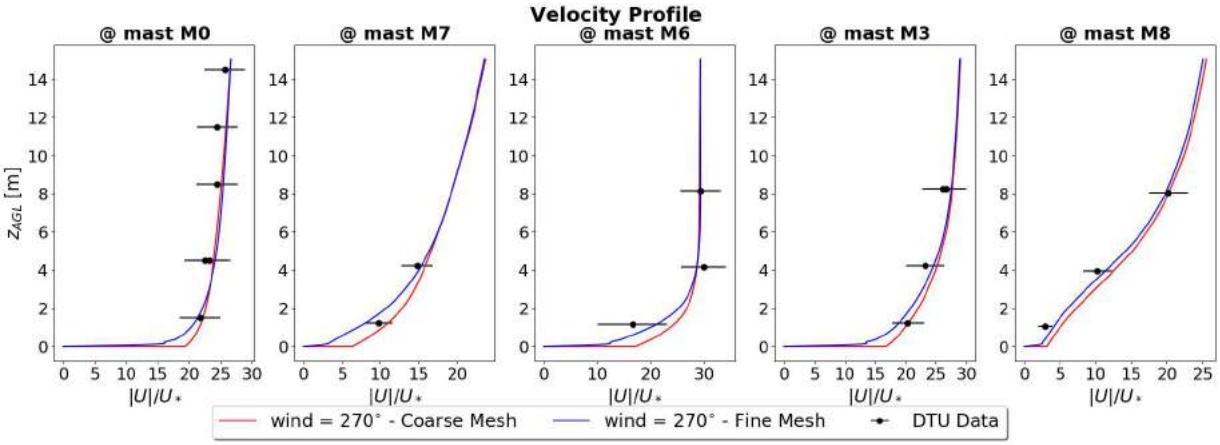

Figure 3.10: Simulated wind velocity profiles for an incoming wind from 270°. Results extracted from a coarse-mesh simulation as well as a fine-mesh simulation and compared with the DTU dataset

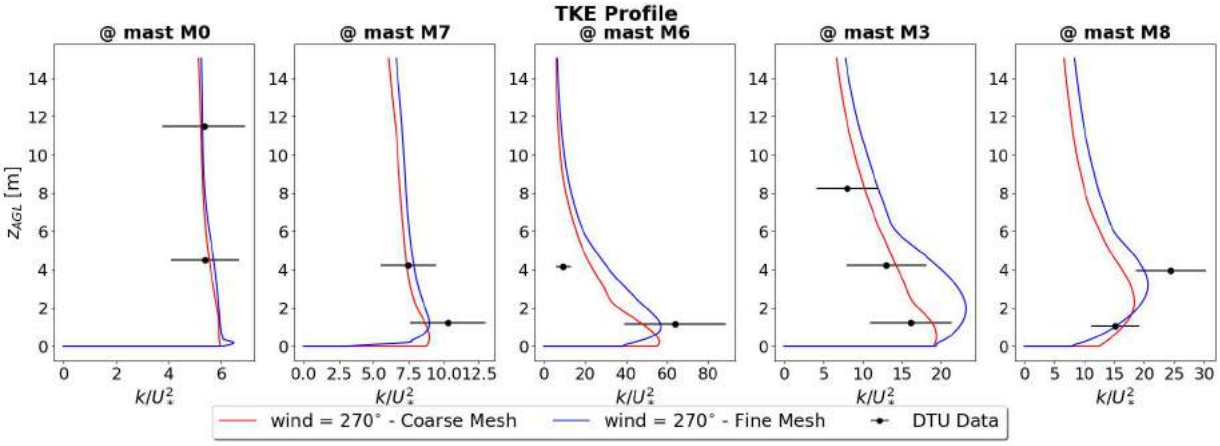

Figure 3.11: Simulated TKE profiles for an incoming wind from 270°. Results extracted from a coarse-mesh simulation as well as a fine-mesh simulation and compared with the DTU dataset

© University of Pretoria

A clear agreement is seen between the experimental data and simulated results in Figures 3.10 and 3.11. From a meshing density perspective it was noted that both granularities gave similar results for most masts despite the increase in cell count, implying a satisfactory mesh independence for the solution.

To better quantify this grid independence and also realise the model error, Figures 3.12 a) and b) plot the overall prediction errors between the respective simulations and the DTU provided dataset. The errors were calculated for every available sensor, including masts and sensors that were not directly in line with the oncoming wind. The concepts of a Maximum Absolute Error (MAE) and Root Mean Square Error (RMSE) have been adapted from Section 3.2 and applied again.

The error is calculated for each sensor:

$$error = \frac{|\phi_{sensor} - \phi_{simulation}|}{|\phi_{sensor}|} \tag{3.3}$$

where ϕ is any velocity or turbulence variable. The RMSE is then determined from the resulting set of errors and the MAE is simply the maximum of all the errors.

It was found that the maximum variation in velocity was small, $< 1\%$ between solutions, and a similarly small disagreement of $\sim 9\%$ between the TKE profiles throughout the analysed domain. Although a more rigorous mesh dependency study could be performed here, these statistics were deemed tolerable for the current case study application.

Figures 3.12 a) and b) show the individual error for each sensor vs. the sensor height AGL and coloured by ϕ. From the error data, a continuous average of the mean error vs. height AGL is shown along with the associated standard deviation of the error from the RMSE, marking a 95 % confidence interval for expected simulation error. The continuous error shown in the Figures is an interpolated function since the mast sensors and their associated errors are only given at discrete heights AGL. Viewing the continuous RMSE in the images, it is apparent that larger errors are incurred closer to the ground while the simulations become visibly more accurate at higher altitudes.

The significantly high proportion of green points lying outside of the highlighted 95% interval was also noted, indicating that the z-component of velocity is particularly responsible for high normalised error in the model. Since the z-component of velocity is generally quite small when compared to the dominating x- or y-velocity components, these high errors are deemed mostly negligible. This can be further confirmed by recognising that the velocity magnitude plots in Figure 3.10 still closely match the given DTU dataset despite some z-velocity component errors approaching as much as 300%.

In contrast, the blue and red points representing errors in the x-velocity component and TKE respectively, tend to fall well within the identified error envelope. Using only the fine-mesh

© University of Pretoria

results from Figure 3.12 b), it was concluded that most dominating errors should fall within 50% at ground level and $\leq 10\%$ at heights greater than 8 metres. While this result is perhaps not ideal for an ABL model aimed at achieving high accuracy near topographical features, it does present a unique insight into the behaviour of the ABL model. Only the simulation results concerning the fine-grained mesh domain are considered from this point forward.

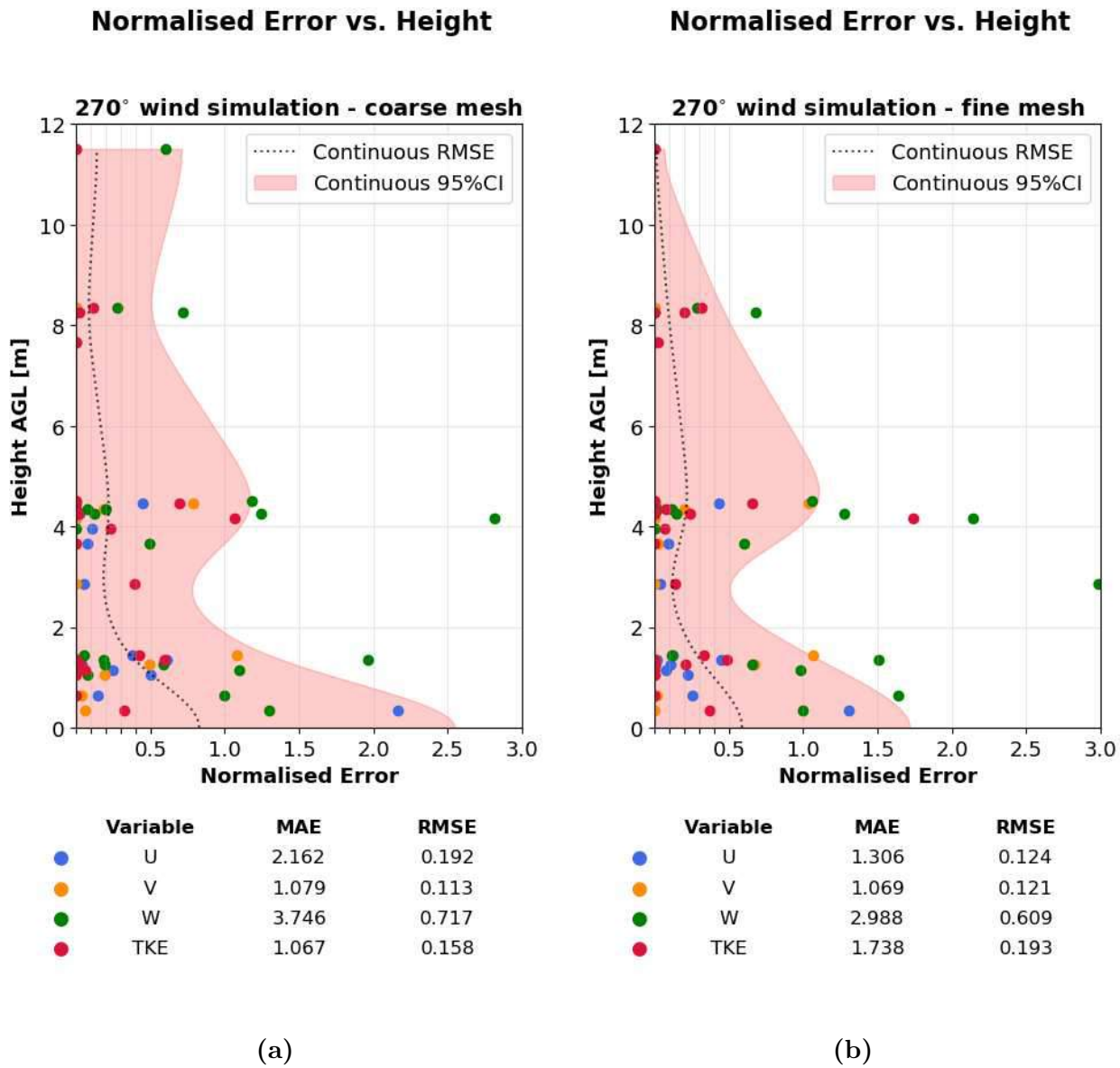

(a) **(b)**

Figure 3.12: Graphs presenting CFD simulation error as a function of height for the Bolund Island 270° wind case. The side-by-side figures indicate the prediction errors of a coarse-mesh simulation (a) against those of a finer mesh (b). Errors have been classified and coloured by u-, v-, and w-velocity components and the TKE to better understand which variables are responsible for larger error. A smooth and continuous error estimation and 95% confidence intervals have been interpolated from the discrete results. Tabulated maximum and average errors have been summarised for each flow variable in the colour legend. Note the axis inversion where the x-axis (Normalised Error) has been set as the dependent variable contrary to standard graphing etiquette; aiding visualisation.

© University of Pretoria

Three main deductions are available to explain why large errors are seen close to ground level, but reducing to almost zero at increasing height:

- Closer to the simulated wall boundary, surface roughness and wall treatment become high-level approximations rather than direct simulation. These approximations are clearly not adequate for modelling natural geographical surfaces since they were formulated with industrial applications in mind such as flows over manufactured surfaces with stricter shape and surface roughness tolerances. It is not numerically feasible to model exact landscape roughness and so the approximations must be kept.

- The sensors themselves are subject to high wind variability as a result of the increased turbulence intensity near to the ground roughness, producing internal measurement inaccuracy. This effect is further amplified near sharp topographical features that induce mechanical turbulence. Higher up, the air flow is less turbulent and data samples are accordingly more consistent.

- The chosen k-ε turbulence model does not fully accommodate turbulent separation and reattachment; a known flaw in the k-ε formulation when used to model external flows over bluff bodies. Whilst the k-ε constants have been altered in these simulations to better represent ABL turbulence behaviour, it should be noted that the said alterations were proposed primarily for industrial wind farm or pollution dispersal applications. Since it can actively be reasoned that wind turbine hubs or factory smoke stacks are designed for heights far exceeding 10 metres AGL, it is clear that the altered k-ε model is perfectly suited for those types of ABL simulations.

Figure 3.13 provides a visual means of assessing the accuracy of the ABL model in 3D space.

Figure 3.13: An island-wide view comparing all available experimental mast data (black vectors) with the Bolund Island 270°-wind simulation results (red vectors)

© University of Pretoria

Figure 3.13 brings mast M0 forward since it was used to confirm/calibrate the inlet profile for the CFD model. Consequently, the experimental vs. simulation data match up well for mast M0 as seen in the image. The perfect simulation should result in all vectors matching throughout the rest of the domain; however, this is not the case. To further highlight any strengths and shortcomings of the model, Figure 3.14 focuses only on the masts directly aligned with the incoming wind (i.e. masts 7, 6, 3 and 8). Note how well the vectors in the 270° case compare everywhere except the area directly downstream of the initial cliff face.

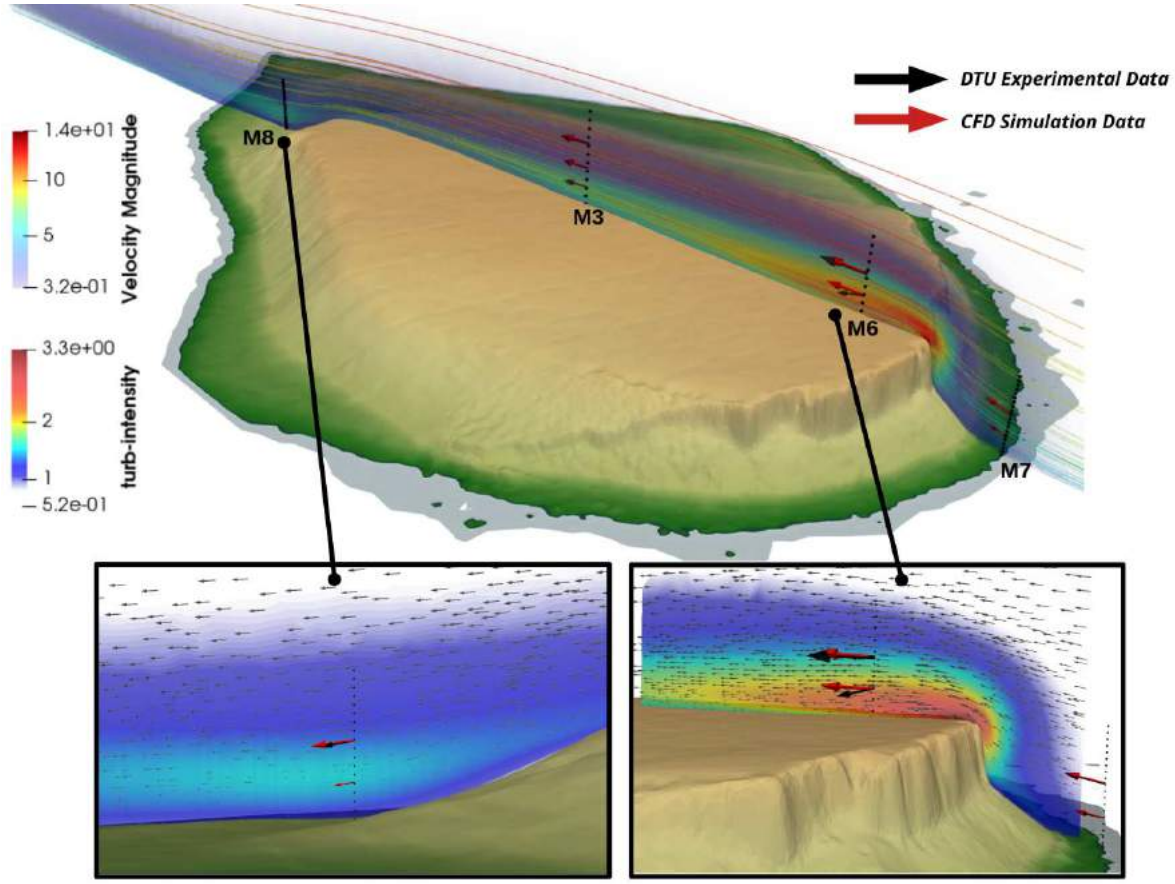

Figure 3.14: Bolund Island 270°-wind simulation results (red vectors) versus experimental data (black vectors). A cross-sectional view of a slice of data running directly along the 270° wind path is shown (top). Pathlines in the main image are coloured by velocity magnitude [m/s] while the semi-transparent contour plot is coloured by turbulent intensity (TI) [%]. The zoomed portions highlight areas of interest near masts M6 and M8, showing the same simulation vs. experimental results against a backdrop of the simulated velocity quiver plot and contours again coloured by TI

Seen in Figure 3.14, mast M6 is located inside the turbulent separation bubble caused by the topography. Only the lowest sensor on mast M6 seems to give unreasonably different results when comparing the physical data with simulations, once again confirming the poor resolution of turbulence close to the ground surface. In this case, it is possible that the chosen k-ε turbulence model is slightly over-predicting the length of the separation bubble behind the cliff face.

© University of Pretoria

Mast 8, situated behind Bolund Island, does not exhibit the same level of disagreement. This can be attributed to a number of factors:

- The turbulent detachment bubble behind the island is not as pronounced as the initial bubble.
- The trailing topography is not as sharp as the leading cliff face.
- The air movement is calmer and slower in the wake of the island.

All of these situations are helpful in allowing the numerical solver to recover some of the error produced at the leading edge of the island.

3.3.3 239° Wind Simulation

The second iteration of the Bolund Island wind simulation involved modelling an incoming wind approaching at 239°. In a similar fashion to the discussion above, the comparison between the simulation results and the DTU dataset is given here.

From the outset of this phase of the case study, it became clear that the inlet conditions in the 239° simulation did not match the experimentally determined data, despite applying an inlet condition in the advised wind direction. This deviation can be consistently noticed throughout the domain when looking at Figure 3.15; a compounding mistake which is a likely stem for any error. Based on the mean experimental data at mast M0, the 239° wind should actually be modelled at an incoming bearing of about 243° to keep the simulations consistent with the field measurements. For completeness sake, both a 239° and a 243° case were modelled and compared.

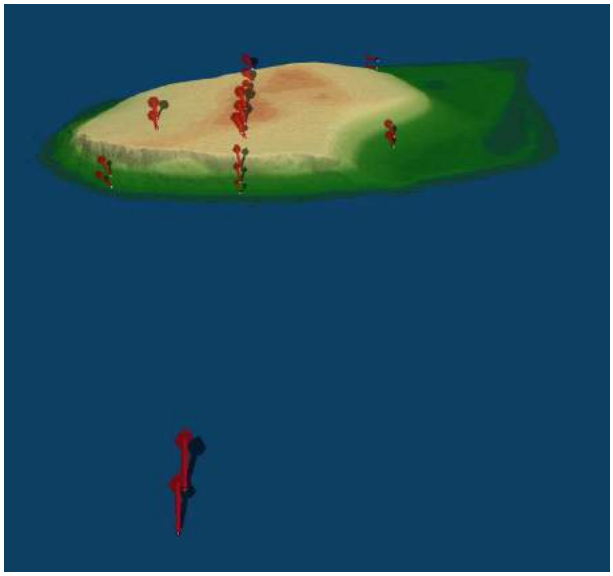

Figure 3.15: An island-wide view comparing all available experimental mast data (black vectors) with the Bolund Island 239°-wind simulation results (red vectors). The discrepancy between the modelled 239° wind and the DTU dataset at the inlet boundary was noted and accounted for by modelling a second 243° wind case

© University of Pretoria

The vertical profiles in Figures 3.16 and 3.17 are the dimensionless velocity magnitude and TKE extracted from the CFD simulations for winds approaching at 239° and 243°. Note that the order of the graphs in the profiles corresponds to the mast numbers following a direction of travel of the wind from West to East along the island; refer back to Figure 3.8 for clarification. Other masts are excluded for this direction of flow. The blue line indicates the 239° solution while the red line shows the 243° solution. Data points from the given DTU Bolund Island dataset are indicated as black dots with standard deviation error bars. Good agreement is seen between the simulation data and the experimental measurements throughout most of the domain, although a more rigorous evaluation has been performed in the discussion to follow.

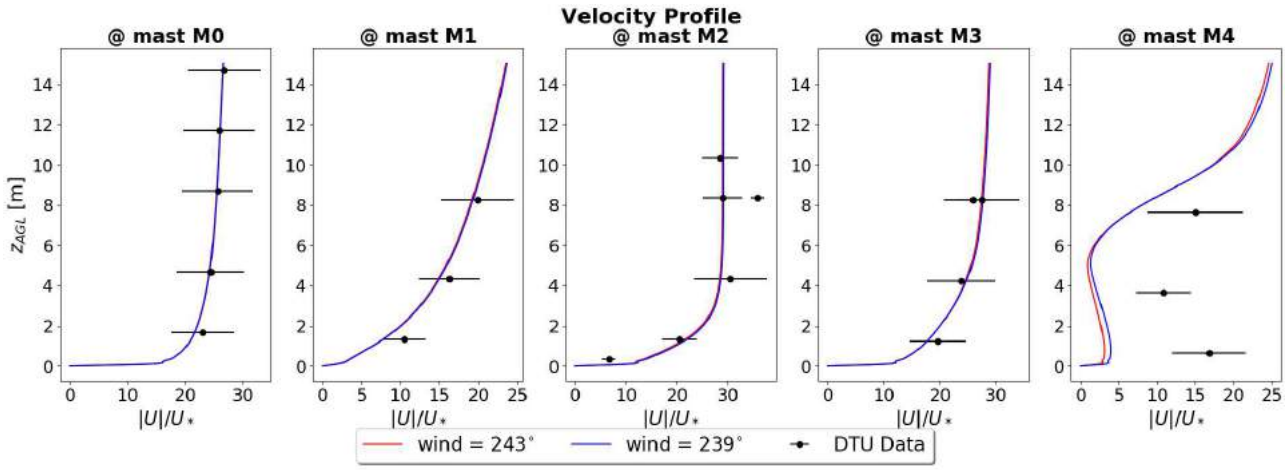

Figure 3.16: Simulated wind velocity profiles for an incoming wind from ≈ 239°. Results extracted from a 239° simulation as well as a 243° simulation and compared with the DTU dataset

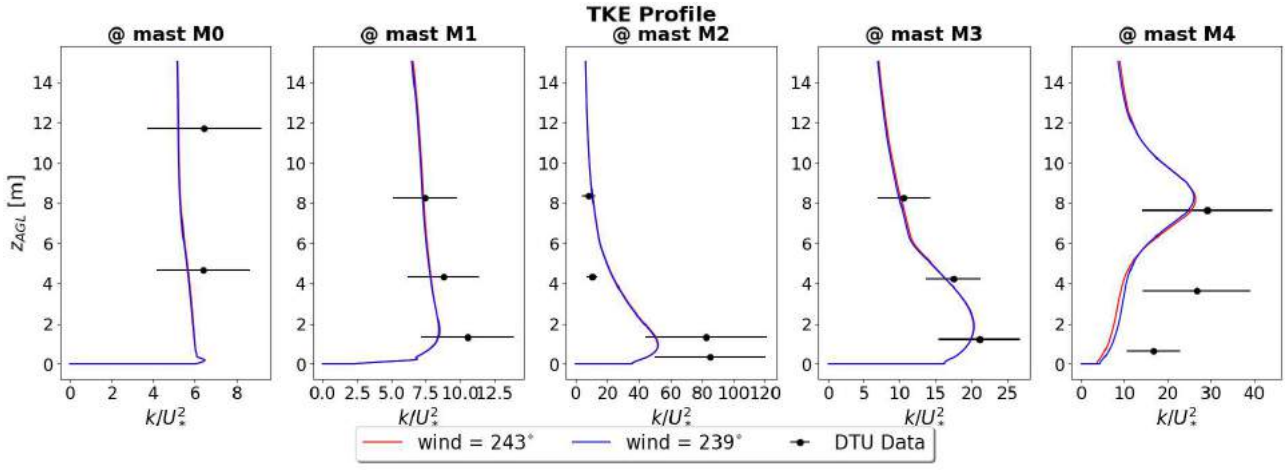

Figure 3.17: Simulated TKE profiles for an incoming wind from ≈ 239°. Results extracted from a 239° simulation as well as a 243° simulation and compared with the DTU dataset

Looking at the profiles in Figures 3.16 and 3.17, it is apparent that the solution is not as sensitive to input wind conditions as previously thought. The minimal 4° change from 239° to 243° had no significant impact on the wind profiles. Figures 3.18 a) and b) show the

© University of Pretoria

corresponding individual error for 239° and 243° wind cases, respectively. The error at each sensor vs. the sensor height AGL is shown and coloured by flow variable, ϕ. From the error data, a continuous average of the mean error vs. height AGL has been interpolated along with the associated standard deviation of the error from the RMSE, marking a 95% confidence interval for expected simulation error. From this point forward only the 239° case has been chosen for further study since both cases are almost equivalent.

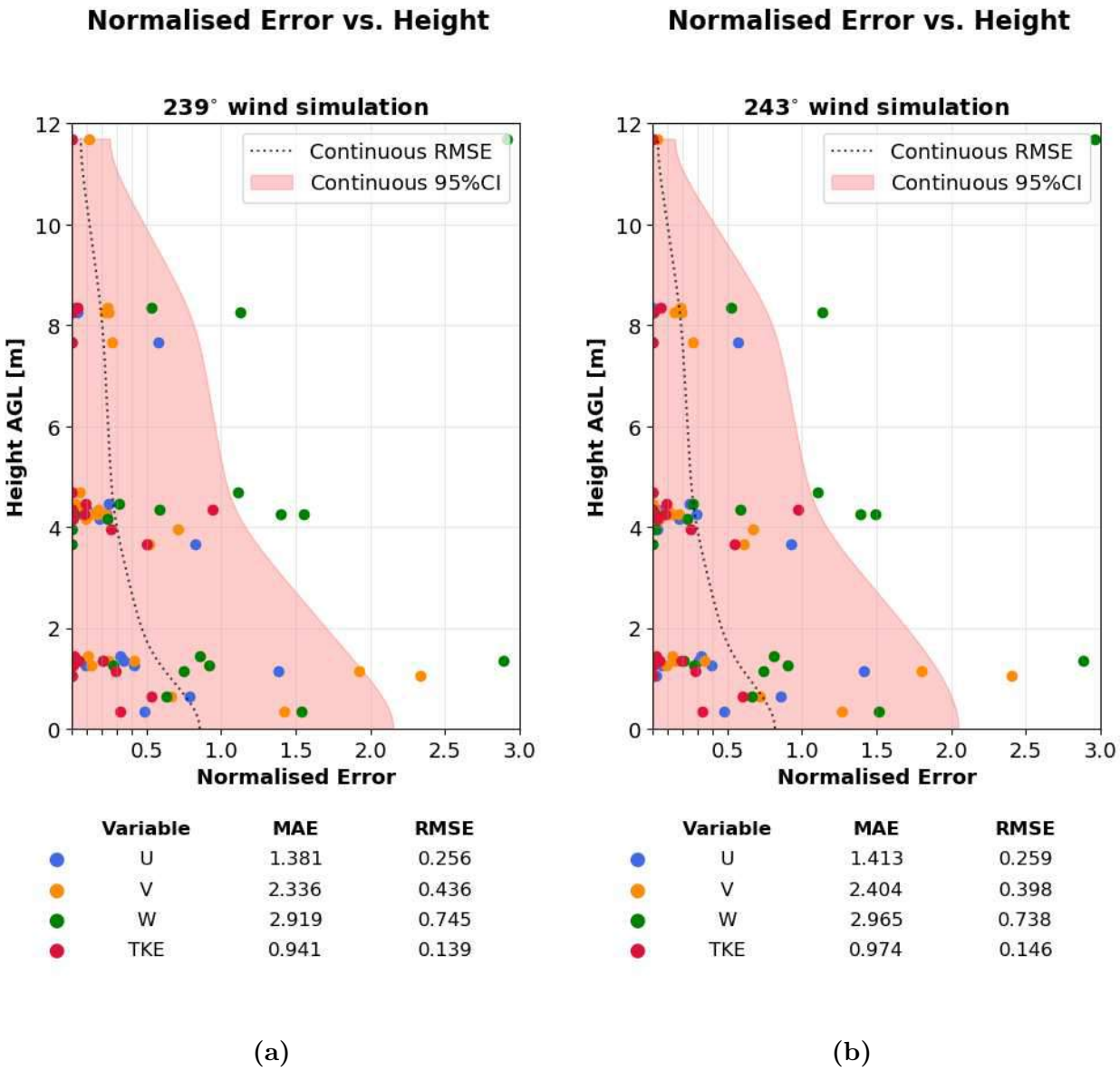

(a) **(b)**

Figure 3.18: Graphs presenting CFD simulation error as a function of height for the Bolund Island 239° wind case (a) against those of 243° wind case (b)in a side-by-side comparison. Errors have been classified and coloured by u-, v-, and w-velocity components and the TKE to better understand which variables are responsible for larger error. A smooth and continuous error estimation and 95% confidence interval has been interpolated from the discrete results. Tabulated maximum and average errors have been summarised for each flow variable in the colour legend. Note the axis inversion where the x-axis (Normalised Error) has been set as the dependent variable contrary to standard graphing etiquette; aiding visualisation

The same trends are noted in the 239° wind case as were seen in the 270° wind case; namely,

© University of Pretoria

a significantly high error close to ground level which decreases steadily with height AGL, and the w-velocity error being a root contributor to large overall prediction errors.

Comparing the normalised error for the 239° wind case against the 270° base case, the overall performance is slightly worse. Looking at the profiles in Figures 3.16 and 3.17, mast M4 is highlighted as a particularly poor region of prediction in the simulation domain. Considering all previous commentary, it should come as no surprise that mast M4 is located in a turbulent detachment bubble in the wake of Bolund Island.

Figure 3.19 focuses only on the masts directly in the line of the incoming wind (i.e. masts 1, 2, 3 and 4). Masts M2 and M4 are zoomed to show the areas directly downstream of topographical features in more detail.

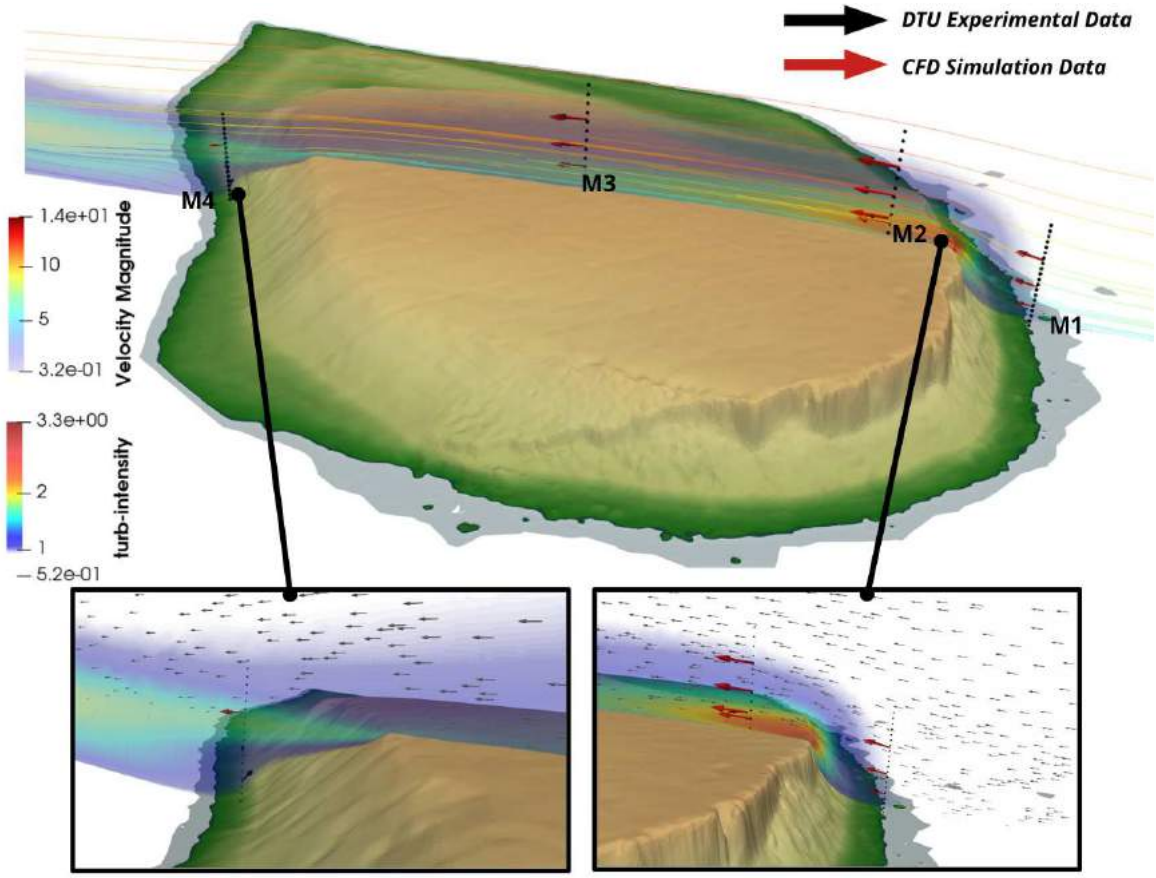

Figure 3.19: Bolund Island 239°-wind simulation results (red vectors) versus experimental data (black vectors). A cross-sectional view of a slice of data running directly along the 239° wind path is shown (top). Pathlines in the main image are coloured by velocity magnitude while the semi-transparent contour plot is coloured by turbulent intensity (TI). The zoomed portions highlight areas of interest near masts M2 and M4, showing the same simulation vs. experimental results against a backdrop of the simulated velocity quiver plot and contours coloured by TI

The combination of a slower wind speed behind the island and a steep drop-off leads to a calm - almost completely dead - wind zone surrounding the lowest sensors on mast M4. In Figure 3.19, the simulated flow vectors on the leeward side of the island are difficult to see due to their

© University of Pretoria

small magnitude. This observation once again confirms the fact that the CFD model cannot quite capture all the nuances of turbulence, especially near to any approximated topographical surfaces.

Figure 3.20 attempts to visualise the 3D nature of the flow solution. The vortical shapes seen in the image are a concern. As a consequence of using the k-ε turbulence model, all turbulence is simplified to be isotropic in nature. This isotropic assumption is not ideal for modelling complex vorticity and is thus largely responsible for the energy losses noticed in the simulations. It is a well-known deficiency of any simplified two-equation turbulence modelling scheme and the only methods of combatting such energy dissipation are to invest the use of more complicated turbulence modelling schemes like RSM or LES/DES.

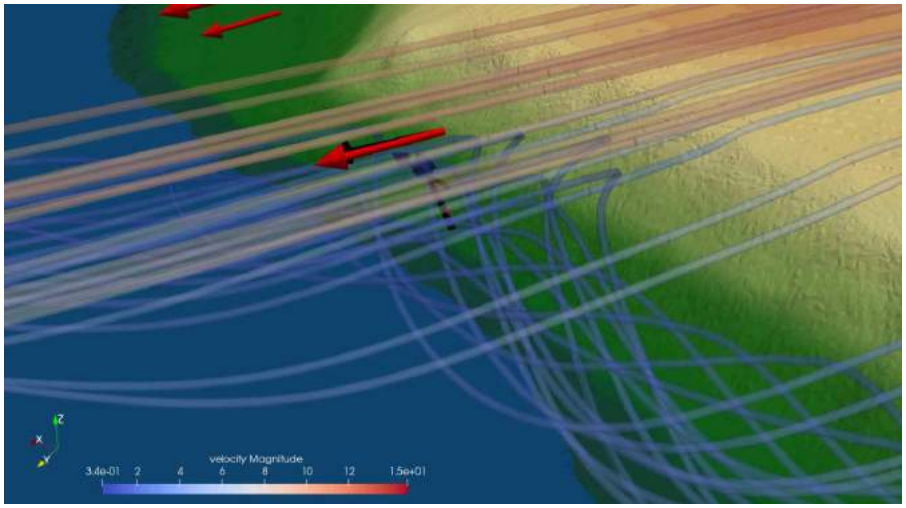

Figure 3.20: Streamline plot showing the 3D turbulent vortex behind Bolund Island

3.3.4 Deductions

The simulations in this section helped validate the chosen ABL modelling approach against a well documented case study. Moving forward, one can be reassured that the chosen approach for modelling the ABL over complex terrain reasonably captures the correct flow features in the lower part of the atmosphere. The current choice of boundary conditions yielded almost perfect approaching wind profiles over the short fetch distance ahead of the island. Turbulent detachment and recirculation has been brought forward as a possible cause for concern when using the k-ε turbulence model. Due to simplifications in the turbulence model and approximations in wall treatment near to the ground surface, the CFD model is prone to large prediction error in close proximity to any ground surfaces which reduces with height into the atmosphere. The simulations discussed in this section lead to the conclusion that any CFD predictions below a height of 10m AGL can only be trusted to an accuracy of about $\sim 50\%$ while predictions above 10m AGL reach accuracies better than 10%. Areas of high vorticity can also be used to identify regions which might benefit from further mesh refinement or possibly employing more complex turbulence modelling schemes to achieve more accurate simulations.

© University of Pretoria

3.4 Summary

The ANSYS Fluent solver calculates the solution to a standard set of partial differential equations (PDEs). There are a large number of input settings that can be applied beforehand to tweak the solver, greatly impacting the performance of any given model. This Chapter was aimed at developing and verifying the numerical modelling details for a CFD model of the atmosphere necessary for simulating wind patterns across Marion Island. The task at hand involved modelling orders of scales, from large atmospheric movements in the upper portion of the ABL right down to capturing fine flow details near the ground level of a complex terrain.

To confirm the workings of large-scale fluid mechanics in the atmosphere, an empty domain was used to verify the choice of inlet- and top-boundary conditions as well as wall modelling assumptions. The test results were positive, revealing that the inlet profiles described by equations 2.31 - 2.34 were sufficient for generating a neutral HHTSL over distances of up to 50 km. This gives an upper limit for the inlet boundary placement in all future wind simulation attempts. The decision was ultimately made to use the ANSYS built-in scalable wall functions to model surface roughness, naturally accompanied by converting any given aerodynamic roughness lengths to their equivalent sand-grain roughness heights using Eq. 2.39.

Regarding the fine scale, a complex terrain was modelled in a much smaller domain to test the model performance in close proximity to the ground. The details of a Bolund Island blind comparison test were implemented as suggested by the authors involved in the Bolund Experiment (Berg *et al.*, 2011; Bechmann *et al.*, 2007a, 2009) and served to highlight certain strengths and shortfalls of the numerical ABL model under study. In this case, the model was seen to agree with reality quite well, exhibiting acceptable performance. The model produced prediction errors of about 50% in areas of high turbulence/flow detachment, but mostly in the range of $\sim$ 10% or less. Turbulence modelling with the k-ε equations was brought forward as a possible area of improvement in the future.

Overall, while no specific optimisations were done to the CFD ABL model at this preliminary stage, it could be applied to the full-scale Marion Island problem with confidence. This Chapter concludes by defining a clear understanding of the relationships between the solver settings and the solver accuracy when simulating realistic wind patterns across a complex terrain.

© University of Pretoria

4 Experimental Wind Measurement Campaign

The next section reports on the work done in sorting and analysing physical wind data that have been collected from Marion Island (MI). A measurement campaign was carried out from April of 2018 until present (circa 2020) which involved setting out an array of sonic wind anemometers across the island terrain. The anemometers have since been providing continuous streams of wind speed and direction data for use in the project.

A brief discussion of the experimental procedure is given for context and then the analytical methods introduced in Section 2.8 are employed to extract reasonable modelling assumptions from the raw noisy data.

4.1 Experimental Setup

One of the most recent expeditions to the Prince Edward Islands included the wind measurement campaign already mentioned. A large cross-disciplinary team of biologists and engineers were involved in the design of this experimental campaign. The physical deployment of the initial set of data loggers was carried out over the course of April-May 2018 by the author and a team of three other researchers. The subsequent maintenance and data collection were taken care of by the over-wintering staff on MI.

The aim of the work was to set up as many as 34 Gill WindSonic ultrasonic wind anemometers around MI to gather wind data over the coming years. Due to cost constraints, more anemometers were not affordable and due to environmental conservation laws in the area, the anemometer stations were not to be mounted higher than 1 metre above the ground without due environmental impact studies. These severely limiting factors meant that the equipment needed to be located as efficiently as possible to enable reasonable wind sampling across the 290 km^2 land mass.

Bearing this information in mind, it was decided that 17 stations would be installed; each station consisting of two sonic anemometers, a solar panel and a portable logging device. Figure 4.1 shows a typical wind station layout. Care was taken to install each station in a relatively flat and open environment where possible. The stations could not be installed too close to a protrusion of land for fear of turbulence interference in the wake of the protrusion. Similarly, installing a station too close to the edge of a cliff was avoided since the anemometer would not be able to capture reliable data in a separation bubble. The Gill WindSonic ultrasonic wind anemometers are only capable of 2D readings so due attention was given to mounting them level and north-facing as accurately as could be achieved in the field. Note from Figure 4.1 that the two anemometers are offset; one capturing data at a height of 1 metre while the other is mounted at 0.5 metres high and off to one side. The reasoning behind such a setup is to improve on accuracy by capturing the wind gradient at the location with minimal interference from the centre mast on the lower anemometer. Upon receiving further funding in 2019, two 3D

© University of Pretoria

anemometer stations were also added to the campaign at a later stage. The equipment setup for these new stations copies the same layout as the original 2D stations already discussed.

Figure 4.1: Experimental setup of one of the 17 wind logging stations currently on Marion Island

The logging stations were set to sample the wind once every 2 seconds and save the data into three tables: one table with all the readings averaged over 10 minute intervals, one with hourly averaged data and the last with daily averaged data. Besides the wind speed and direction statistics the stations also logged information such as the ambient temperature, remaining battery voltage and a timestamp for each reading. A detailed sample of the raw data quantities available can be found in the Appendix, Table D.1. The Island is also home to a single 20 metre high weather station with a standard wind vane used to gather meteorological data for the South African Weather Service (SAWS). The SAWS station is located at the MI base and has been in constant operation since circa 1948. The geographical layout of the stations is shown in Figure 4.2.

Station Coordinates

© University of Pretoria

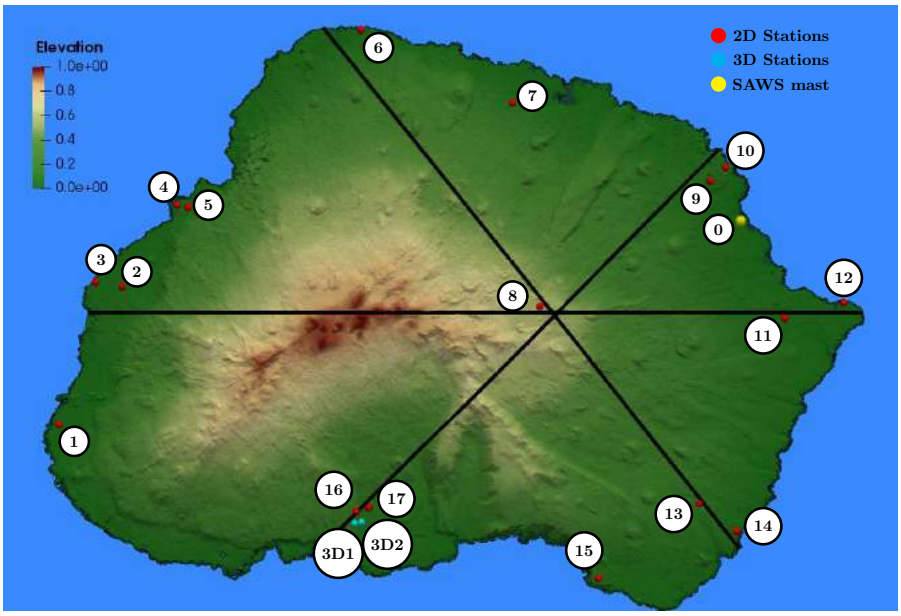

Figure 4.2: Experimental layout of wind measurement stations across Marion Island. Black lines show dominant wind directions, W, NW and SW. Multiple stations were placed in these dominant wind paths to provide the highest possibility of station correlation

The choice of location for each station was made according to various heuristics such that a maximum amount of data could be drawn across the entire island given the strict economical and environmental constraints. The exact GPS coordinates and corresponding station numbers for each station around MI is given in Table 4.1 for reference:

© University of Pretoria

Table 4.1: Station GPS coordinates

Station #	Name	Latitude	Longitude
0	MI Base	-46.8760	37.8580
1	Swartkops	-46.9333	37.5869
2	Kampkoppie Inland	-46.8954	37.6118
3	Kampkoppie Coastal	-46.8942	37.6009
4	Mixed Pickle Coastal	-46.8729	37.6331
5	Mixed Pickle Inland	-46.8737	37.6377
6	Cape Davis	-46.8247	37.7059
7	Repettos	-46.8444	37.7665
8	Katedraal	-46.8999	37.7777
9	Skua Ridge Inland	-46.8652	37.8456
10	Skua Ridge Coastal	-46.8614	37.8517
11	East Cape Inland	-46.9024	37.8759
12	East Cape Coastal	-46.8979	37.8995
13	Kildalkey Inland	-46.9530	37.8425
14	Kildalkey Coastal	-46.9607	37.8578
15	Puisie	-46.9738	37.8026
16	Grey Headed Ridge	-46.9560	37.7060
17	Santa Rosa Valley	-46.9551	37.7109
3D1	Grey Headed 3D	-46.9594	37.7052
3D2	Santa Rosa 3D	-46.9592	37.7080

The intuition behind the station placement is as follows:

- Most stations are placed near the coastal extremities of MI at lower altitudes to provide easier access for data gathering and equipment maintenance.
- Emphasis was held on keeping stations in relatively flat areas, away from any sharp geographical protrusions or valleys, where possible.
- Stations are often placed in pairs not too far from one another so that corresponding time series data can be related across short distances.
- A set of stations are placed at the island extremities in each compass direction such that an incoming wind profile might be sampled before it has been disturbed by the topography.
- Three dominating wind directions have been previously identified from historical weather data (Westerly, North-Westerly and South-Westerly). Stations have been placed roughly along lanes within these directions such that propagating wind eddies can be captured progressively and cross-correlated accordingly.

© University of Pretoria

- Six of the stations have been reserved for logging wind in areas of high ecological importance where a more accurate wind estimation would be preferred. Two of these stations lie in the north-eastern portion of MI, an area known as Skua Ridge, and the remaining four lie together in the southern portion, an area known as Grey Headed Ridge. The 3D measurement stations are both currently placed at Grey Headed Ridge.

4.2 Data Collection

There are a large number of factors at play concerning the efficient collection of wind data around MI. As is the case with most experimental endeavours, reality often stumbles even the most meticulous planning. This small section is devoted to discussing the nuances of collecting wind data on MI as well as listing the challenges experienced during the course of the campaign.

The incoming streams of data from the stations around MI were influenced by both physical and environmental factors. The physical challenges noted during the course of the project are listed as follows:

- installing the stations in the field, facing due North and standing completely level, is a precision exercise dictated by the accuracy of the tools used and the prevailing weather conditions. Practically, achieving suitable mast alignment was incredibly challenging when the cold and strong winds led to uncontrollable shivering and the rain-soaked surfaces were slippery. One should subsequently expect a large spread of mast alignment deviation.

- Similarly, when considering the large scale of MI and its weather patterns versus the small size of the masts, one could reasonably assume that accuracy is an issue. For instance, the location of a mast given in GPS coordinates can only be done up to a certain degree of precision. Even the best GPS equipment can only be trusted to an accuracy of about a 5 metre radius while a mast only takes up a roughly 1 metre diameter in floor space (translating to a $\sim 1\%$ positional accuracy).

- The stations themselves are incapable of any outward communication; the logged data is stored locally and must be retrieved in person before the memory storage space is depleted.

- The stations were separated from each other by vast distances, often in isolation from any other existing personnel or infrastructure on MI. Given the memory limitations, data collection intervals had to be balanced between stations: Collect data often, before storage runs out, but not so often that the personnel would be constantly running to get to the stations with no time to devote to other projects. A regular monthly schedule was implemented to ensure that each station received adequate attention.

- Mast components together with maintenance tools are bulky. Large lag times were experienced when identifying problems (since each station is only visited monthly) and then mobilising to attend to any consequent maintenance tasks. This challenge was aggravated

© University of Pretoria

when stations on the western side of the island, a two day hike from the MI Base, required attention.

- As explained earlier, masts are limited to a height of only 1 metre due to environmental conservation considerations. Many, if not all, of the CFD wind simulation projects around the world and articles referred to in Chapter 2 might scoff at this; successfully validating a wind simulation using masts so deeply entrenched in the turbulent boundary layer represents a unique challenge.

In addition to the logistics mentioned above, environmental concerns also played a large role in dictating when and how data would be collected. Due to the inhospitable climate and interactions with animal life, there are large gaps of missing data in the records that are explained in the following list:

- During the deployment phase, some ground conditions were not favourable for installing the anchors used to stabilise stations. In these cases, some masts were blown over by strong winds and had to be reinstalled or moved to a new location.

- Over the winter months, some masts had been completely snowed in on account of the fact that they are only one metre tall. During these months, the stations could not be accessed and data retrieval was deferred until the snow had melted.

- Cloudy weather is a staple on MI, presenting issues for the solar charging components. Some stations were also found to be unintentionally placed in the shade of surrounding geography. While the battery supply was designed to last up to two weeks without recharging, some gaps in data were still found as a result of low battery charge. Protocols were put in place to have spare batteries on hand for every station.

- Although every effort was made to waterproof and dehumidify the important components inside an enclosure, some moisture still managed to seep through into the loggers due to the high rainfall and strong gusts of wind.

- By far the most destructive force on the island was the rogue colony of mice. These animals are alien invaders on MI, introduced by the first fleets of human ships. With no natural predators on the island, these mice have multiplied exponentially and will look to eat or burrow in almost anything; including the wind measurement stations. No planning scenarios had ever anticipated the mice being so destructive, thus the stations had to be repaired and thoroughly "mouse-proofed" on a regular basis.

- The 3D anemometer stations were installed well after the initial set of 2D stations. Additionally, one of these 3D stations was found to be almost destroyed one day. The cause is unknown but suspected to be a rock- or bird-strike likely resulting from strong winds. Only small and inconsistent datasets were recovered from these stations over the short

© University of Pretoria

span of time, meaning that the 3D stations will mostly be ignored for most of the analysis taking place in later chapters of this document. Effort has been made to use the 3D anemometer data where possible to confirm certain findings rather than to prove or validate simulations.

- The SAWS station near MI Base was similarly removed from the set of viable validation results. After July 2018 (a mere 2 months after the start of this project), the wind speed measurement device was taken down for repairs and has not been replaced since. Wind direction and temperature data are still available for the project's duration but are of limited use.

These points represent the most urgent of the challenges faced when trying to collect useful CFD validation statistics around MI. The last hurdle to overcome is coordinating and reconciling the stream of data around the gaps and inconsistencies to find meaningful relationships in the wind patterns.

4.3 Database Structure

Processing the raw data from the various incoming streams into a single coherent database was done with the help of open-source technologies; namely Python 3.8 and MySQL 5.7.28. A description of the data preprocessing stage is given here, along with a guide to the overall wind sample database.

The 2D anemometer stations logged the wind using a speed-direction format, i.e. at every time interval, the positive magnitude of the mean wind speed was logged with a mean wind direction in degrees. Standard deviation statistics were also calculated for the wind speed and direction within a time interval. The raw data format for a 2D anemometer station can be perused in Appendix D.

To start, all data readings were cleaned of any glaringly erroneous data: negative wind velocity magnitudes, averaged speeds higher than 200 m/s or simple "NaN" values where the loggers failed to capture wind samples. This rudimentary filtering allowed for processing to proceed without any other difficulties.

The wind speed and wind direction were decomposed into equivalent u- and v-velocity vector components. Figure 4.3 shows this conversion from polar coordinates to rectangular coordinates necessary for CFD validation. The wind stations currently capture an incoming wind direction according to where the wind is coming from, conforming to standard convention in meteorology, while the decomposition to velocity component vectors refers to the origin as a starting point and typically describes the direction that the wind is flowing towards; the CFD convention for describing a fluid flow. The logged wind speed and direction standard deviations were also incorporated into the conversion to account for any time averaging and other measurement uncertainties. This process should become easier to grasp after viewing Figure 4.3. Note here

© University of Pretoria

that the 2D anemometers could not log a w-velocity component at each station and so these were all assumed to be zero since they were unknown.

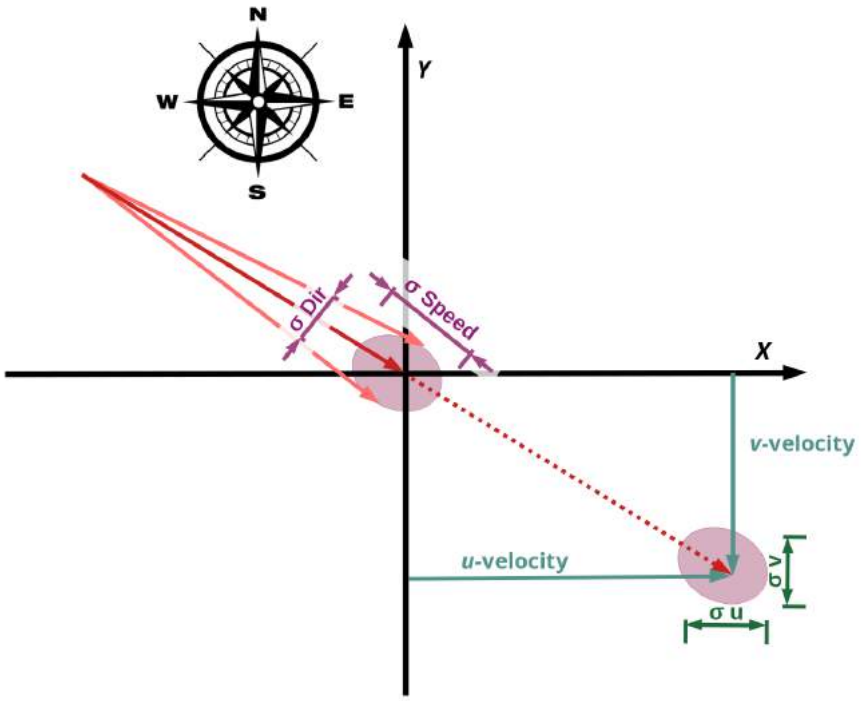

Figure 4.3: Diagrammatic representation showing how 2D anemometer measurements were converted from a mean wind speed and direction to the equivalent mean u- and v-velocity vector components. In effect, this is a conversion from polar coordinates to a rectangular coordinate system. Speed and direction standard deviations have also been converted to reflect standard deviations in the u- and v-velocity components. The probability distribution fields indicated by the purple areas are approximately equal. The global xy coordinate system aligns with the standard cardinal directions as shown in the image

A similar approach was not necessary for the 3D anemometer stations since these loggers already captured and stored the wind statistics in a rectangular coordinate scheme. In the case of 3D anemometer logging, w-velocity component measurements were available. Only the rudimentary filtering was performed to remove poor data.

As stated previously, the wind logging stations did not store every single reading due to memory constraints, but rather took measurements every 2 seconds and performed internal computations to average the data; only committing the averaged data to memory. The time-averaged data were calculated at 10-minute, 1-hour, and 1-day intervals. For simplicity, each subset of the stored data will be referred to as the 10M, 1H or 1D datasets respectively.

At this point, the following quantities were on hand for any anemometer:

- Global GPS coordinates.
- A date and timestamp for any averaged reading, taken at 10 minute, one hour, or one day intervals.

© University of Pretoria

- The installed height of the sensor above ground level. Keep in mind, there are two wind sensors per station (0.5 m and 1 m AGL).
- An averaged logger temperature reading throughout the time interval. This temperature reading is expected to be equal to that of the ambient air due to the influence of heat generated by the electronics and the logger being enclosed.
- Averaged battery voltage of the station logger throughout the time interval.
- Mean and standard deviation of the u-velocity, hereafter referred to as $\bar{u}$ and σ_u for the sake of brevity. This convention also corresponds to the naming scheme set out in Section 2.8.
- Mean and standard deviation of the v-velocity: $\bar{v}$ and σ_v.
- Mean and standard deviation of the w-velocity: $\bar{w}$ and σ_w. In the case of a 2D anemometer, the assumption is that $\bar{w} = \sigma_w = 0$.

From these known quantities, a few more derived values were calculated before full insertion into a database:

- The overall wind speed magnitude: $|U| = \sqrt{(\bar{u}^2 + \bar{v}^2 + \bar{w}^2)}$.
  - Note that velocity magnitude may be slightly underestimated for the 2D anemometers due to the assumption that $\bar{w} = 0$.
- The turbulent kinetic energy experienced by a sensor during any given time interval: $TKE = \frac{1}{2}(\sigma_u^2 + \sigma_v^2 + \sigma_w^2)$
  - Note that this is equivalent to Eq. 2.7. This is a crude measure since the sampling rate was necessarily low.
  - Note that TKE may be slightly underestimated for the 2D anemometers due to the assumption that $\sigma_w = 0$.
- The incoming wind direction was classified into one of the 16 possible sectors of a cardinal compass.

All the preprocessed data were compiled into a MySQL database. An overall layout of the said database is shown in the tree diagram in Figure 4.4. The database contains roughly 20 separate tables, increasing as the number of stations increases throughout the progression of this project. The first database table contains a list of all the stations installed to date, along with their corresponding GPS coordinates and installation dates. Each subsequent database table contains a running time series of the logged wind data discussed thus far. Figure 4.4 shows exactly what information has been kept and stored from this preprocessing stage.

This choice of storing the experimental data in a MySQL database makes it easy and convenient to load and analyse any subset of the data using Structured Query Language (SQL) at a later

© University of Pretoria

stage. For future reference in this document, the Marion Island Recorded Experimental Dataset is abbreviated to MIRED.

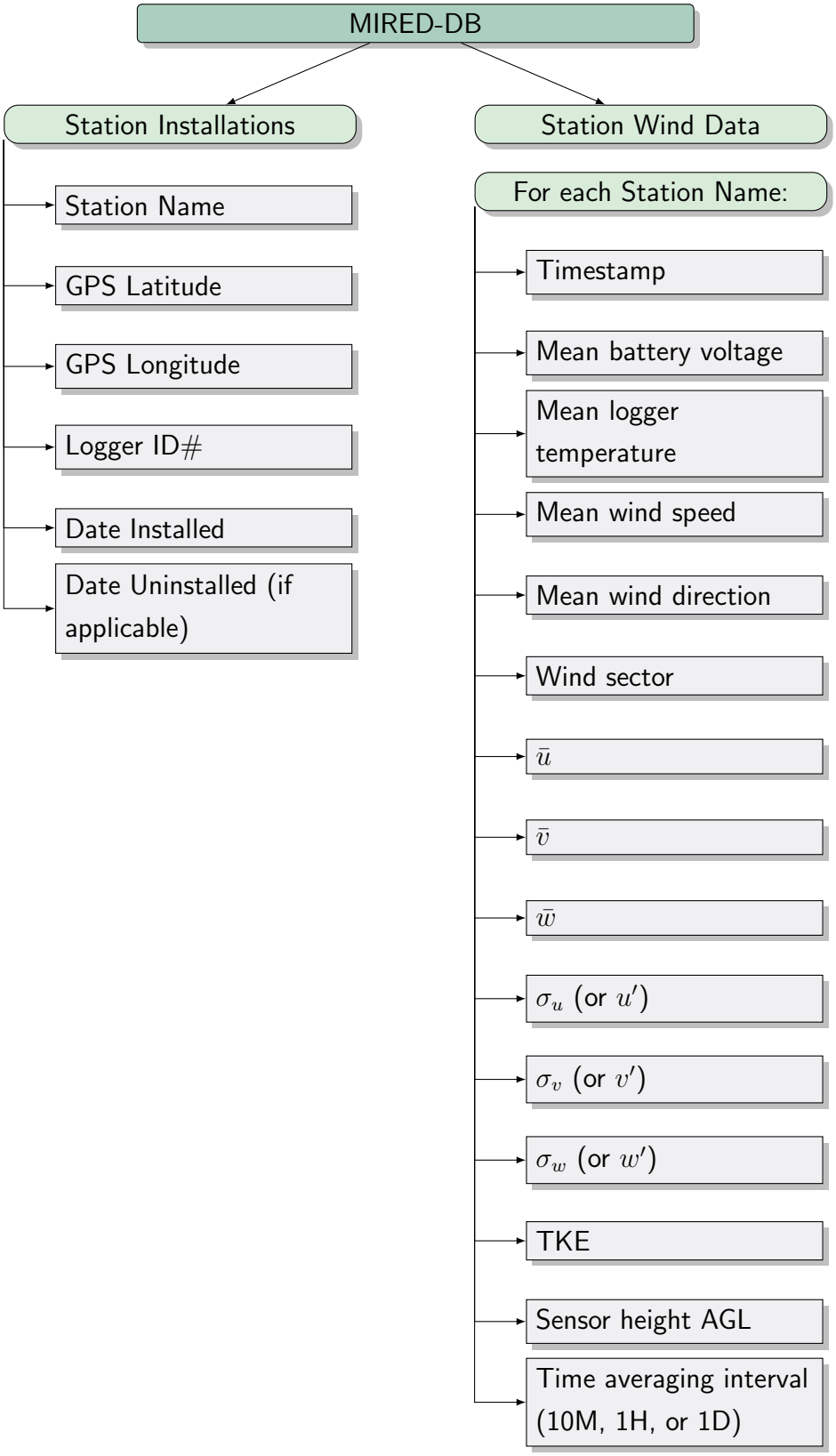

Figure 4.4: Database structure showing how and where all the known experimental data have been stored in a MySQL database, MIRED-DB

© University of Pretoria

4.4 Data Processing

This section describes how subsets of the full experimental measurement database were extracted and processed to reveal a set of clean statistics that would be useful in the validation stage of the MI wind simulation project.

This stage attempts to address the following questions:

- When can we be sure the prevailing wind around the island is blowing in a known direction?
- How can we extract only the relevant data from all stations during these known prevailing wind periods? Especially given the large distances between stations, some form of wind travel time needs to be incorporated.

For the purposes of data processing, the 1D daily time averaged statistics were not useful since the wind varies far too much throughout the course of a day to assume any single average speed or direction with any certainty. The 10M or 1H resolution data were naturally more suitable for this kind of statistical analysis. There was, nevertheless, some use to logging and maintaining the 1D dataset: due to its much smaller size, it was effective for first testing any processing strategies before applying them to the full 1H or 10M datasets. In this way, code debugging and performance validation were performed without wasting time.

As a first step, wind roses were generated for each sensor at each station. These graphs are essentially a frequency histogram of the 10M dataset, binned by wind speed and wind sector and subsequently plotted on a polar axis to better visualise where a wind is most likely to originate from at any location. The wind rose plots for all stations are available in the Appendix E.

Considering the wind roses in Appendix E and also taking previous historical weather observations into account, it is clear that there is a strong bias towards westerly winds on MI. In particular, Westerly and North-Westerly winds are known to be dominant directions in the region surrounding MI. There are various meteorological explanations for this phenomenon, beyond the scope of this study, but it means that some wind sectors are virtually empty of any data readings.

Due to the strong wind dominance, some wind sectors are easier and more meaningful to validate than others. Thus, the idea was that if three chosen wind directions showed good agreement between the CFD results and the experimental data, then all other sectors would follow suit within a margin of accuracy. With this strategy in mind, only three of the 16 wind sectors were chosen as candidates for experimental validation.

The three candidate wind directions were chosen based on high wind prevalence; i.e. wind sectors were chosen where the number of detected samples in that sector are comparatively high across all stations combined. Based on this criterion, the three chosen validation sectors are: West (dominant), North West, and South West.

© University of Pretoria

In order to extract meaningful data from the MIRED-DB, it was necessary to correlate data readings across all stations in time and geospatial location. Figure 4.5 explains how the MIRED-DB was queried to find suitable windows of time where the prevailing wind was flowing in a consistent direction.

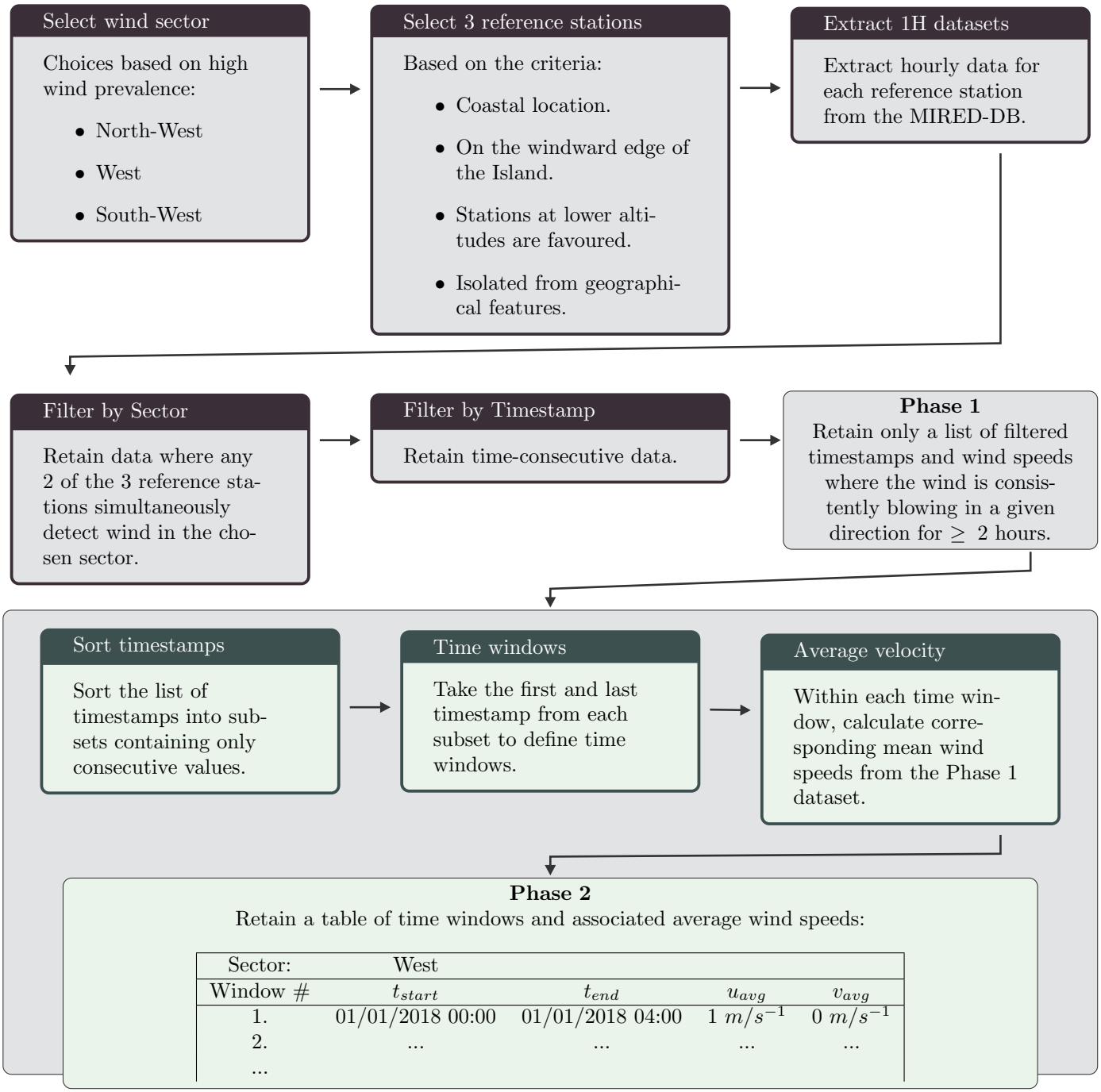

Figure 4.5: Workflow diagram showing how relevant date-time windows were extracted from the MIRED-DB to use in future processing steps. These windows are valid periods of time where the prevailing wind conditions surrounding MI follow a predetermined direction

A rather simplistic approach was taken to spatially and temporally correlate data between stations that are separated by some kilometres of natural landscape. Given a time window and average wind speeds, the known distance between stations was used to roughly infer the time

© University of Pretoria

delay that it would take for wind eddies to travel from one station to the next and be recorded. In layman's terms: "A station at point A detects a direct westerly gust of wind at time t. How long would it take a station at point B, further away, to register the same gust?"

This reasoning is not perfectly accurate since the way it was implemented only accounts for flow over a flat 2D map projection and does not fully capture the chaotic nature of wind. It was, however, deemed adequate to be taken a step further as seen in the chart in Figure 4.6. Figure 4.6 details the workflow used to extract relevant data readings from the MIRED-DB and calculate meaningful CFD validation statistics.

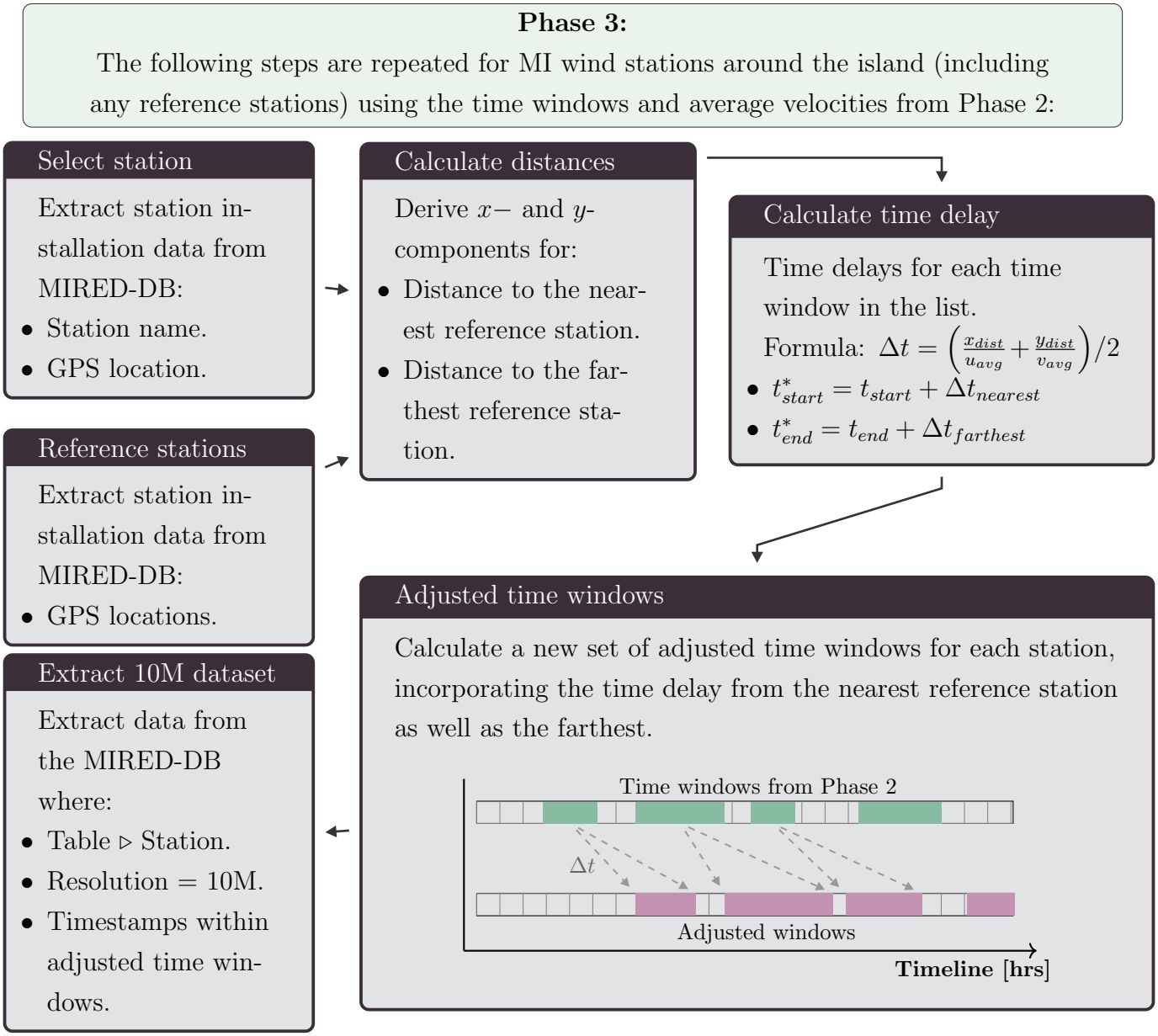

Figure 4.6: Workflow diagram showing how the relevant location- and time-correlated station data were extracted from the MIRED-DB. The resulting subset of data were useful for future CFD validation exercises

The chosen reference stations allured to throughout Figures 4.5 and 4.6 were chosen such that

© University of Pretoria

any given station would be at the coastal edges of the island and with an unimpeded view of any incoming wind. Priority was given to stations with no cliffs or sharp geographical features nearby. This ensured that the reference samples had minimal interactions with the island topography and thus offered a cleaner input case for CFD validation. Table 4.2 summarises the final choice of validation sectors and corresponding associated stations.

Table 4.2: Chosen wind sectors and reference stations for the MI CFD model validation

Sector	Wind	Reference Stations
West	270°	Swartkops
		Mixed Pickle Coastal
		Kampkoppie Coastal
North West	315°	Swartkops
		Mixed Pickle Coastal
		Skua Ridge Coastal
South West	225°	Kildalkey Coastal
		Puisie
		Kampkoppie Coastal

The resultant sensor time-series measurements after completing phase 3 were useful for further stages of data manipulation. In order to gain an overall perspective on how a consistent wind would interact with the island, it was possible to plot the average recorded velocities for every station under the influence of a strong prevailing wind.

The 2D-directional vectors of the average wind behaviour are shown in Figures 4.7-4.9, coloured by the average turbulence intensity values encountered. This average turbulence intensity colouring can also be viewed as a proxy for the measurement uncertainty due to high local wind variance. Note that some stations may report two vector arrows corresponding to the two anemometers present per station (at 0.5 m and 1 m heights). For convenience, the prevailing wind condition has been noted in each image and the correspondingly chosen reference stations have been highlighted in red.

In general, these averaged experimental results seem to strongly agree with one another; all stations exhibiting the same approximate direction of flow within a small tolerance. It is clear, however, that interior stations are often less predictable largely due to the local wind-land interactions taking place. In particular, the group of stations in the south-western section of MI show the largest deviation from the prevailing wind direction. This area is known locally as Grey-Headed Ridge and its renowned unpredictability has already marked it for more focused study from the inception of this MI wind modelling project.

© University of Pretoria

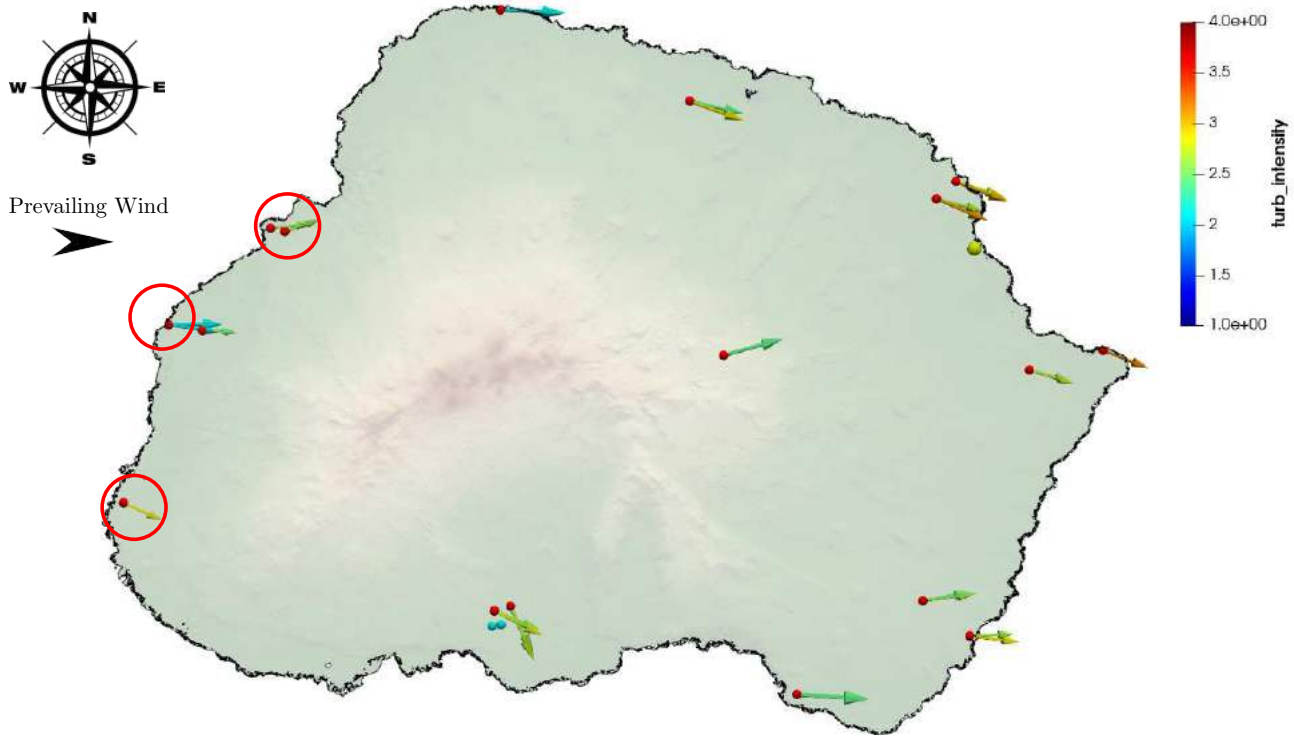

Figure 4.7: Average experimental measurements under a prevailing Westerly wind. 2D-direction vectors are plotted and coloured by average turbulence intensity [%] as a proxy for measurement variance. Reference stations circled in red were collectively used to deduce the time windows where the prevailing winds took place

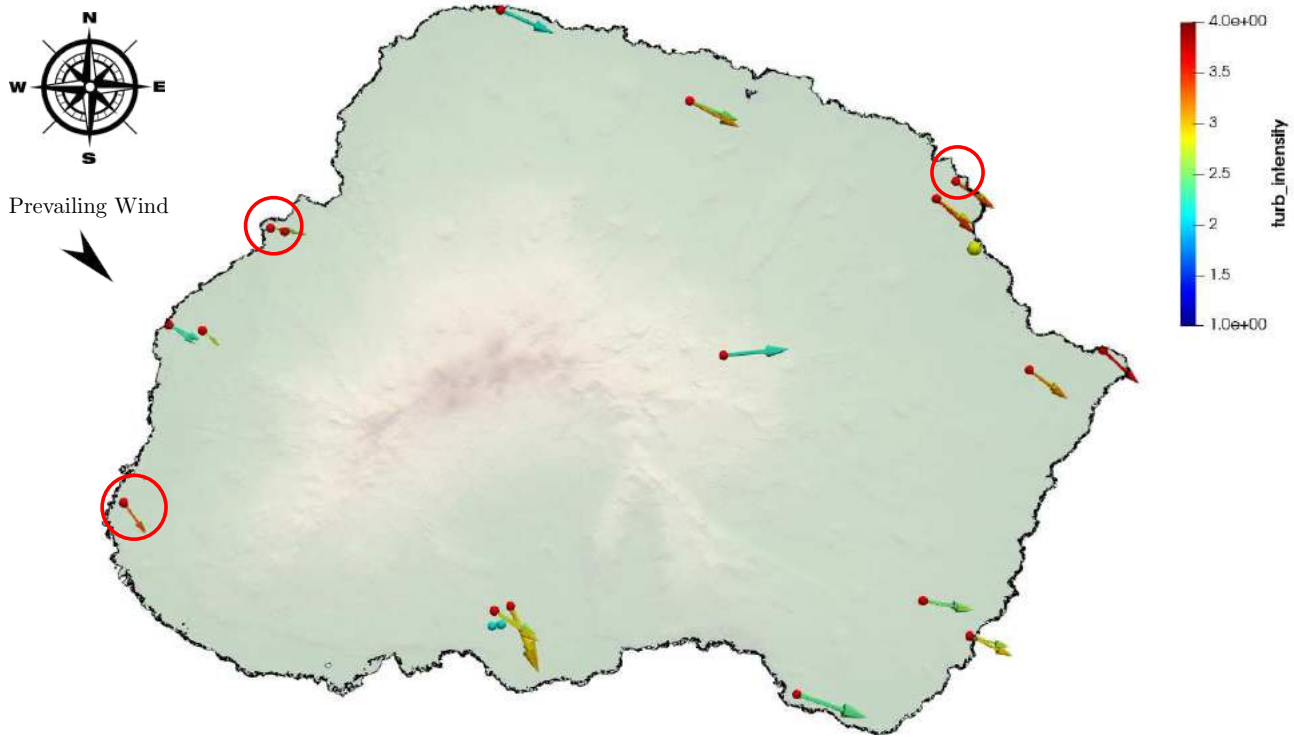

Figure 4.8: Average experimental measurements under a prevailing North-Westerly wind. 2D-direction vectors are plotted and coloured by average turbulence intensity [%] as a proxy for measurement variance. Reference stations circled in red were collectively used to deduce the time windows where the prevailing winds took place

© University of Pretoria

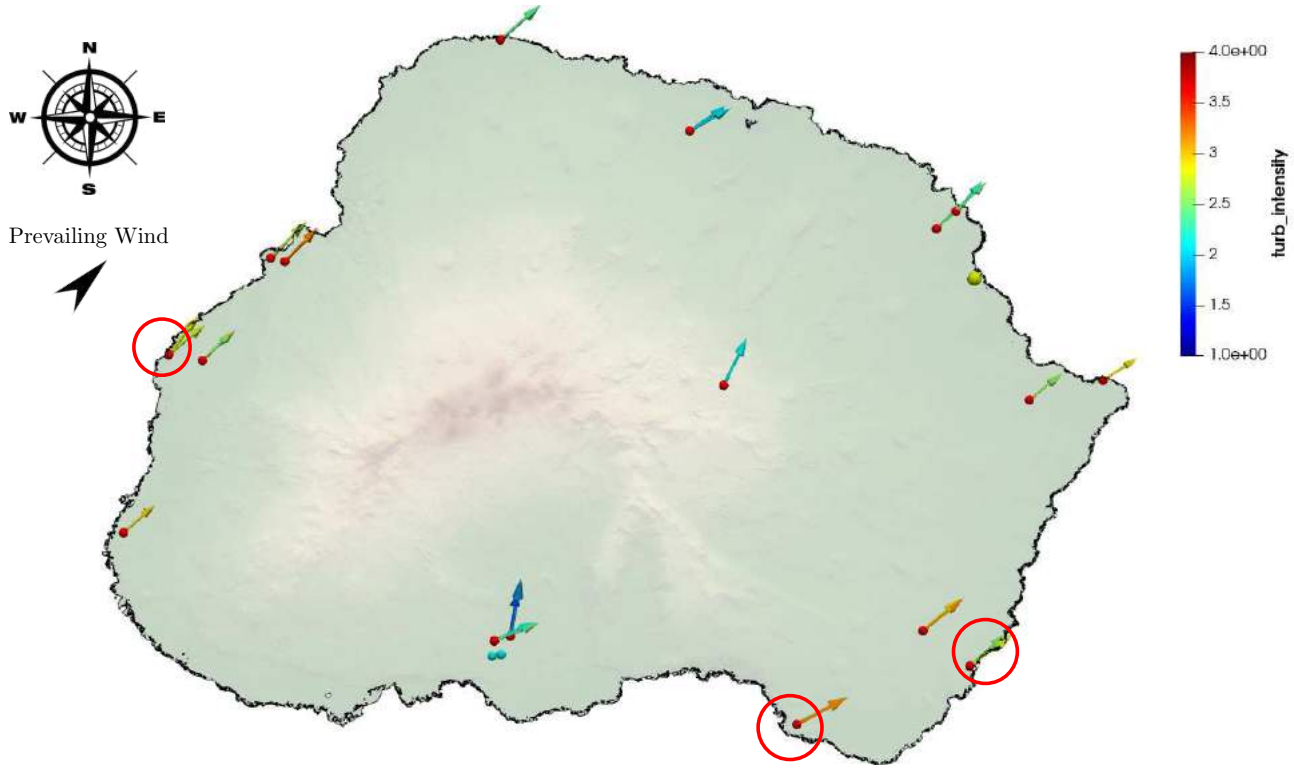

Figure 4.9: Average experimental measurements under a prevailing South-Westerly wind. 2D-direction vectors are plotted and coloured by average turbulence intensity [%] as a proxy for measurement variance. Reference stations circled in red were collectively used to deduce the time windows where the prevailing winds took place

Furthermore, the resultant sensor time-series measurements after completing phase 3 were cross-correlated to get an idea of any possible relationships between stations. Multivariate cross-correlation was performed across all stations, taking the average TKE and u-, v-velocity components as the model variables. A typical correlation heatmap is better for visualising such a large data manipulation. Figure 4.10 shows the coloured matrix output for the cross-correlation of the Phase 3 data series concerning a westerly prevailing wind. The aim is to visualise any relationships by means of coloured squares, with strong correlations depicted in darker colours.

A correlation value of $C = 1$ or $C = -1$ indicates that a pair of variables are perfectly synchronised such that a linear mathematical function could accurately be used to predict the fluctuations of one variable given its partner's behaviour. Conjugately, a correlation value of $C = 0$ indicates that 2 variables have nothing in common. The sign of the correlation value gives an indication of whether two variables increase/decrease in parallel (positive correlation) or if one variable decreases as the other increases (negative correlation). Note that the diagonal line of dark squares in Figure 4.10 simply means that every variable is directly and positively correlated to itself.

For convenience, correlations less than $|C| = 0.2$ in either direction have been hidden in Figure 4.10 so as to highlight stronger relationships.

© University of Pretoria

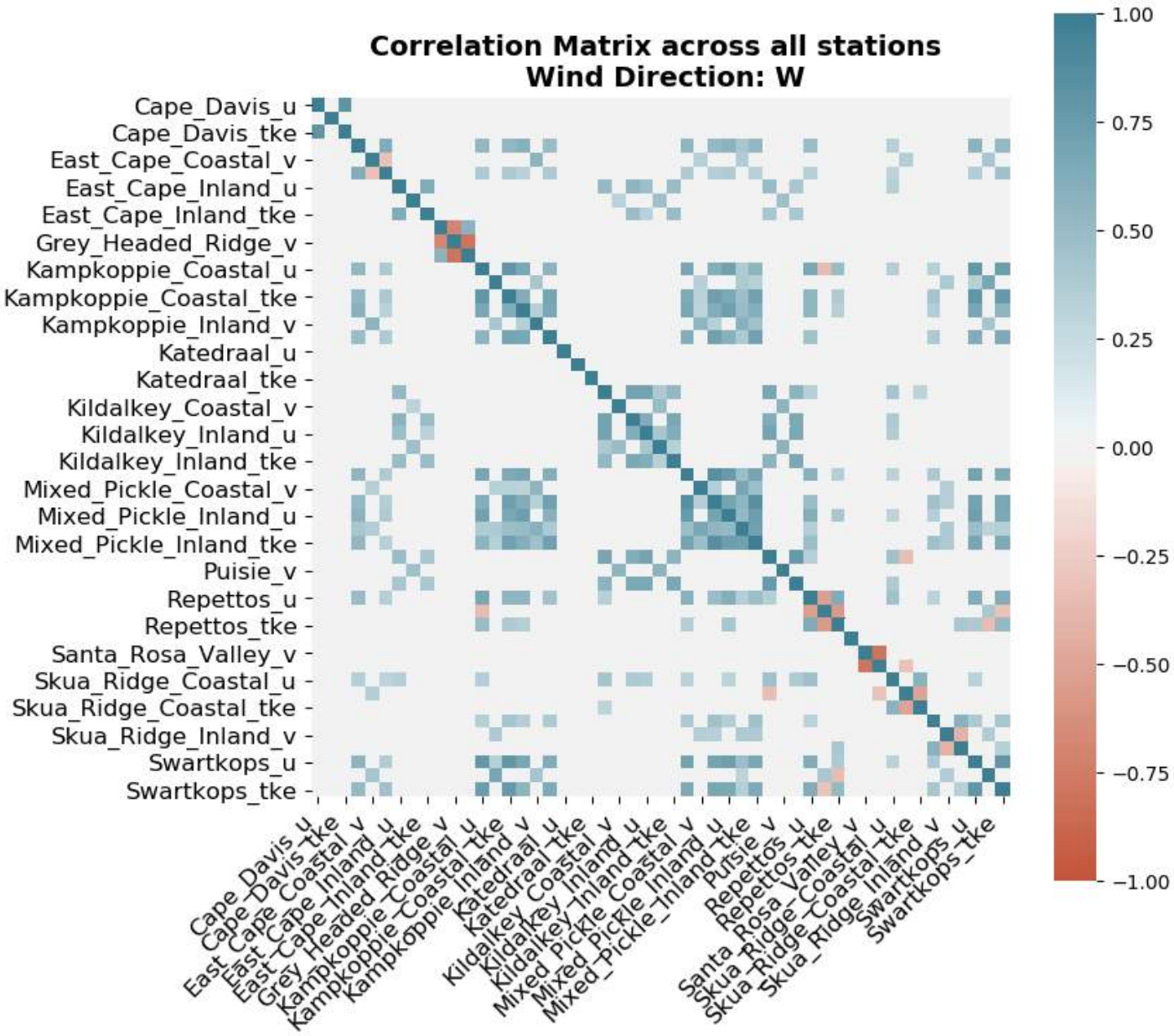

Figure 4.10: Correlation heatmap comparing the time-series data gathered by all stations during a prevailing westerly wind. Only the average TKE and u-, v-velocity component series' are compared. Strong positive correlations take a value of $C = 1$ while strong negative correlations take a value of $C = -1$. Variable pairs with correlation values $|C| \leq 0.2$ have been masked

To reduce the complicated correlation heatmap in Figure 4.10 down to an image that is easier to read and understand, certain filters were applied. Firstly, the 2-norm of every 3×3 sub-matrix was used to reduce the overall size of the heatmap, making it possible to focus on the average correlation between distinct stations rather than focusing on specific underlying wind variables. Next, the row-column ordering of the stations was changed to reflect the distance of any one station from its nearest reference station; thus, the reference stations would appear as the top- and left-most three names on the heatmap with the others ranked in order of increasing distance.

© University of Pretoria

Figure 4.11 shows the reduction process applied to the original heatmap. Note that this image now represents the absolute value of the average correlation between stations. Here, values of $|C| \leq 0.3$ have been masked to place visual emphasis on the stations exhibiting stronger statistical bonds.

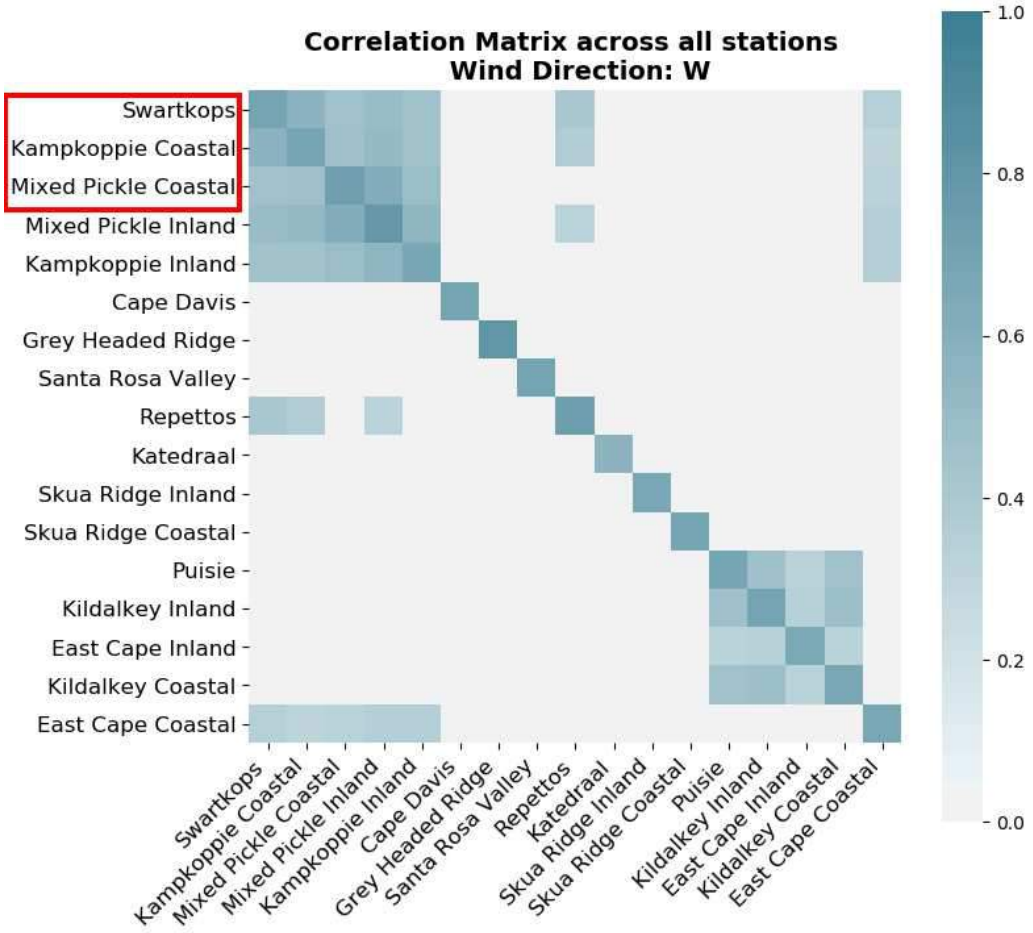

Figure 4.11: Absolute average correlation heatmap reduction comparing all measurement stations across MI for linear statistical relationships under a prevailing westerly wind. Weaker relationships have been masked while stronger relationships are coloured by darker squares. The ordering of the names on the axes indicates the distance of a station from its nearest reference point (marked in red). Correlation values $|C| \leq 0.3$ have been masked

The correlation and reduction process was repeated for prevailing wind cases in the North- and South-Westerly directions, shown in Figures 4.12 and 4.13 respectively. These correlation heatmaps are useful in proving that the chosen strategy for data extraction from the MIRED-DB yielded a high quality subset of results that could be used for future CFD validation efforts. Station pairs with particularly large cross-correlation coefficients would make good candidates for studying cause-and-effect relationships.

In general, it appears that stations located close to the reference stations relate quite well with one another. Stations further away are not as well connected to the reference set, but still have strong connections to their nearest neighbours.

© University of Pretoria

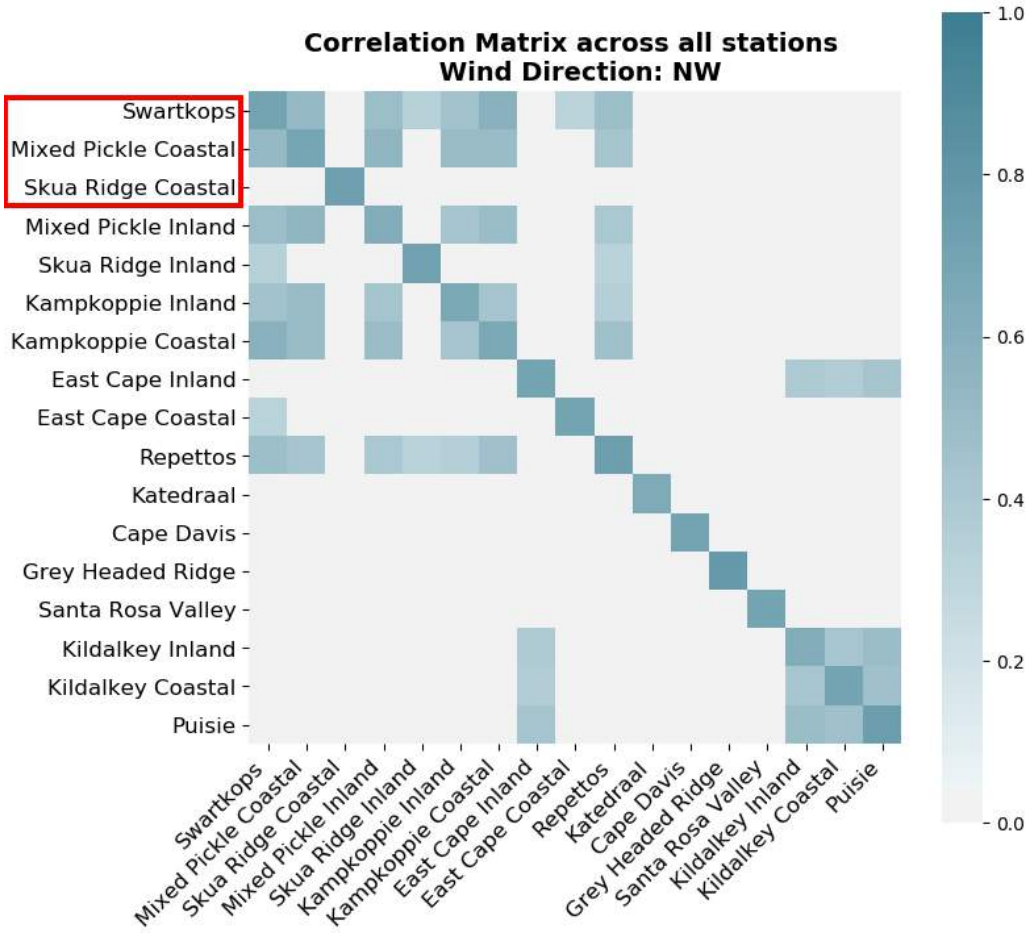

Figure 4.12: Absolute average correlation heatmap reduction comparing all measurement stations across MI for linear statistical relationships under a prevailing north-westerly wind. Weaker relationships have been masked while stronger relationships are coloured by darker squares. The ordering of the names on the axes indicates the distance of a station from its nearest reference point (marked in red). Correlation values $|C| \leq 0.3$ have been masked

Take note that the Pearson Correlation method (Pearson, 1896) was used to determine the correlation coefficients and subsequent heatmap colouring in Figures 4.11 - 4.13. While a rigorous explanation of the methodology is beyond the scope of this document and not entirely pertinent to the study at hand, some key take-aways from the discussion to this point are:

- The Pearson Correlation seeks out only linear mathematical relationships between variables; strongly non-linear functions cannot be represented accordingly.

- The Navier-Stokes equations for modelling fluids, not to mention wind interactions with the landscape and over vast distances, are inherently non-linear and are likely to slip through the net at this stage of processing.

- It is, nonetheless, encouraging to see linear patterns emerging from the dataset despite any underlying non-linearity.

© University of Pretoria

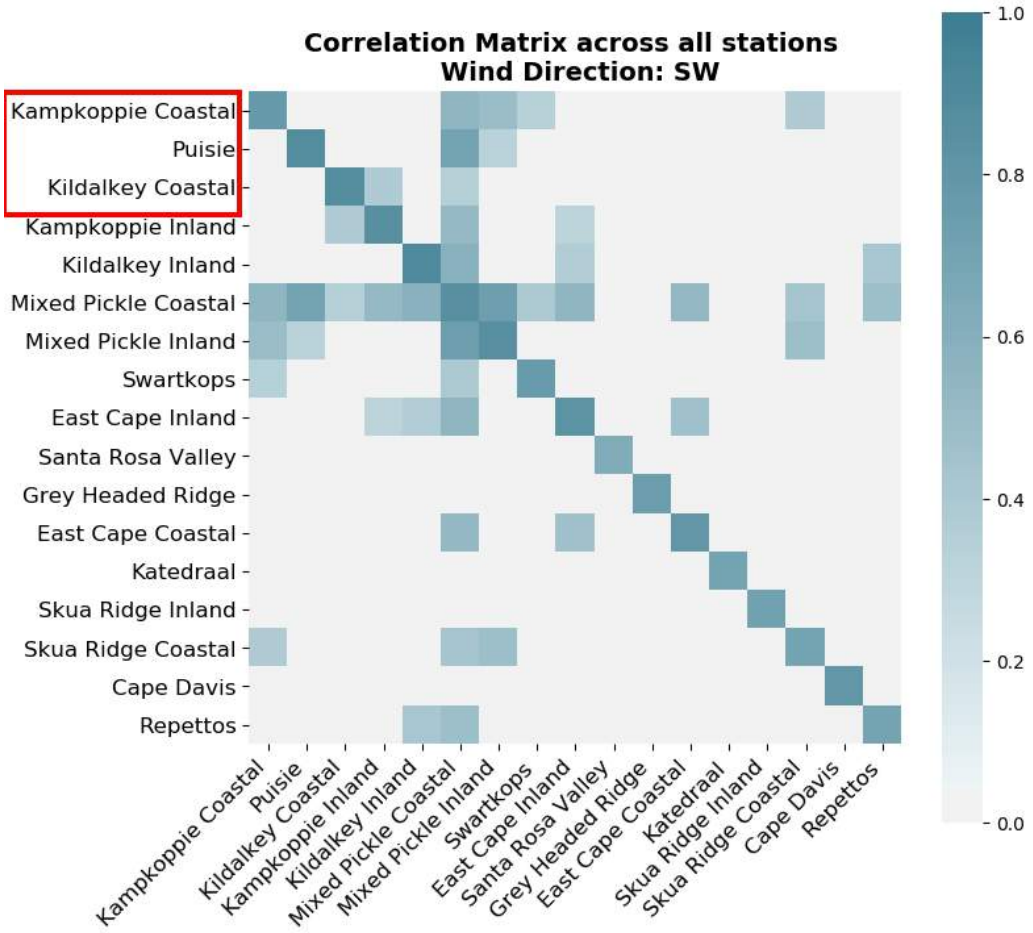

Figure 4.13: Absolute average correlation heatmap reduction comparing all measurement stations across MI for linear statistical relationships under a prevailing south-westerly wind. Weaker relationships have been masked while stronger relationships are coloured by darker squares. The ordering of the names on the axes indicates the distance of a station from its nearest reference point (marked in red). Correlation values $|C| \leq 0.3$ have been masked

Drawing inspiration from network modelling, the information in the correlation heat maps was combined with the geographical location of the stations to give the diagrams seen in Figures 4.14-4.16. These network diagrams provide a visual approach for selecting station sets that would make the best candidates for a CFD validation study based on simultaneously high statistical correlation and wide geographical spread.

A high correlation coefficient between a reference station and any other is desirable because it implies that the selected time windows and wind behaviour agree with one another. If a correlation is too small, it could either be due to poorly extracted data or due to erratic wind behaviour as a result of local geography or turbulence. Thus, the influence of poorly related stations should be minimised in any validation procedures.

A wide geographical spread is desirable when selecting validation stations to ensure that results dispersed around the island can be verified, specifically from regions on the leeward side. It is helpful to note that strongly correlated stations often exist on opposite sides of MI and also

© University of Pretoria

along the chosen lanes of dominant wind patterns as described and shown in Figure 4.2.

From Figures 4.14-4.16, the largest and darkest coloured nodes represent the best assortment of stations to use in a CFD validation study. These results are most likely to follow the prevailing realistic wind trends; a time-averaged CFD model will either match them with certainty or be disproved.

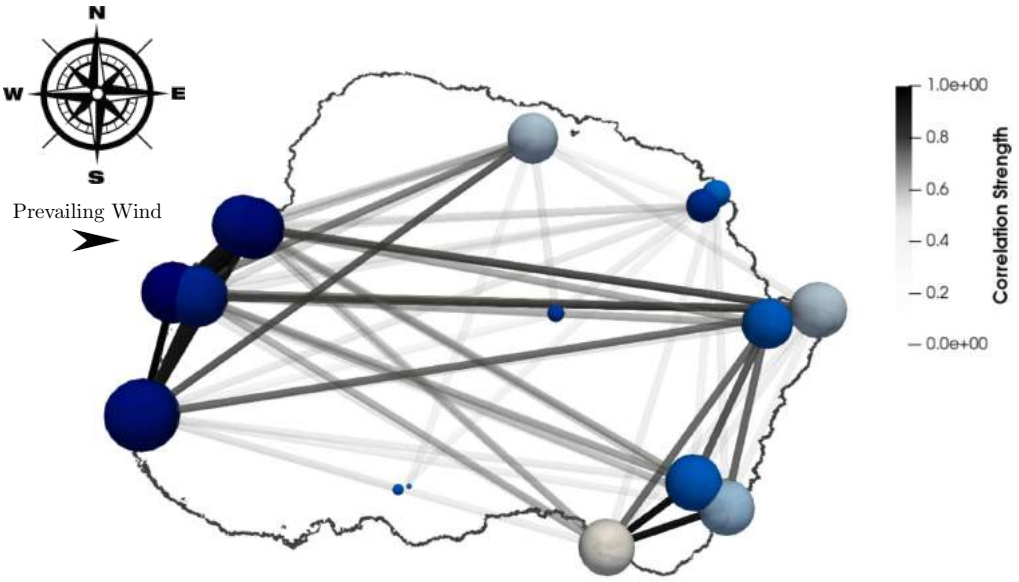

Figure 4.14: Correlation network diagram for the stations around MI under a prevailing Westerly wind. Nodes represent the GPS location of individual stations, sized and coloured by the sum and quality of their total connections. Each line connecting two nodes represents a correlation, with darker connections showing stronger pairs

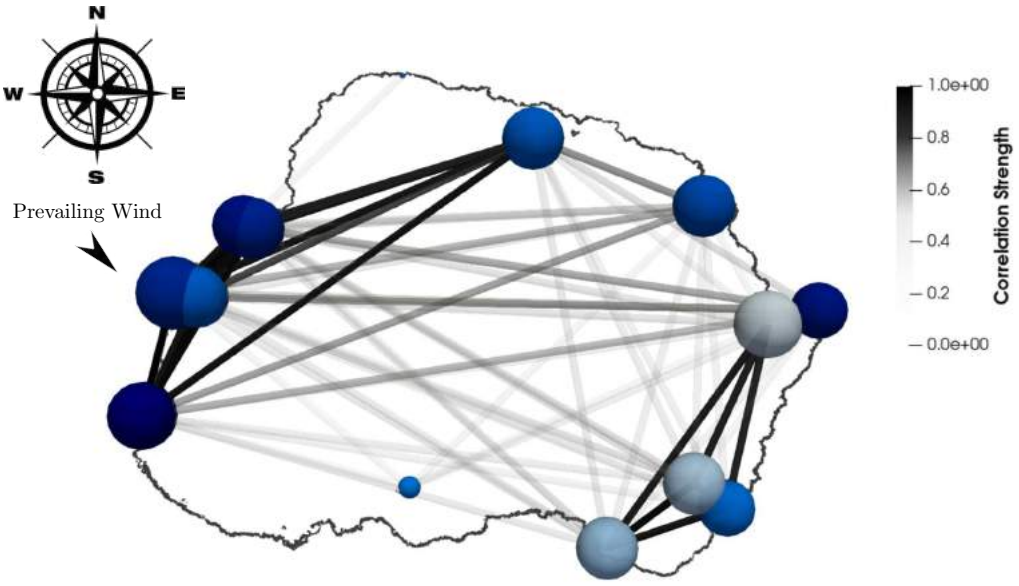

Figure 4.15: Correlation network diagram for the stations around MI under a prevailing North-Westerly wind. Nodes represent the GPS location of individual stations, sized and coloured by the sum and quality of their total connections. Each line connecting two nodes represents a correlation, with darker connections showing stronger pairs

© University of Pretoria

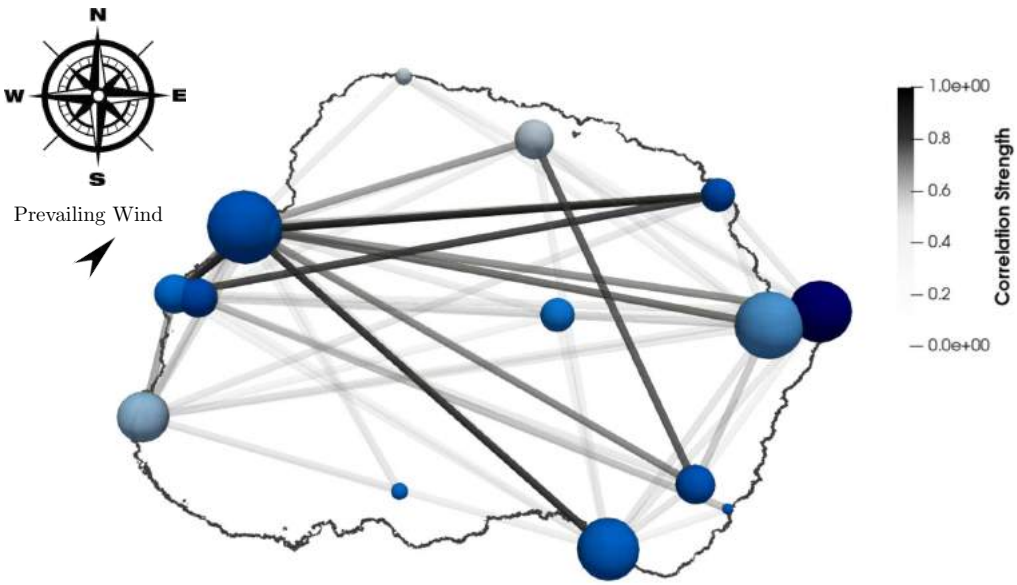

Figure 4.16: Correlation network diagram for the stations around MI under a prevailing South-Westerly wind. Nodes represent the GPS location of individual stations, sized and coloured by the sum and quality of their total connections. Each line connecting two nodes represents a correlation, with darker connections showing stronger pairs

Stations with little to no linear correlation do not offer a stable foundation for validation; with so few sampling locations around MI, there is no security in isolating the root cause of this statistical disagreement and thus no way of explaining why a CFD model may or may not be matching the physical measurements. Due to this, the stations with smaller and lighter coloured nodes in Figures 4.14-4.16 are given less weighting in any CFD validation procedures.

4.5 Summary

The Chapter focused on processing and distilling raw experimental wind measurements down to a format that can be used further on in the CFD modelling project pipeline. The experimental setup was explained and the intuition behind the recorded data management was clearly outlined.

The strategy for installing and maintaining wind monitoring stations includes posting 17 stations around MI, mostly near the coastal extremities with a small proportion in the interior. Stations are located at low altitudes and away from interfering geographical features to ensure a reduced noise environment. Each station supports a set of two ultrasonic anemometers programmed to store time-averaged wind data in series of 10 minute, 1 hour, and 1 day intervals.

Raw data output from the stations were cleaned and converted into an easily accessible MySQL database format using the Python scripting language. The Marion Island Recorded Experimental Dataset (MIRED) database contains all wind measurements gathered over the span of the two-year campaign.

© University of Pretoria

The decision was taken to focus on validating only three of the 16 cardinal wind directions; North-Westerly, Westerly and South-Westerly winds based on highest prevalence over the course of the two-year measurement campaign. To determine spans of consecutive time where the wind was blowing in these known directions, reference stations were chosen on the windward side of MI and their output data simultaneously compared to find matching timestamps.

Using the distance between stations and the average wind speed, wind travel times were used to add a time-delay to the reference time windows and subsequently extract correspondingly timestamped data from all 17 stations for statistical analysis.

Using statistical averaging, the mean wind speeds and directions were visually plotted for stations around MI to confirm that the correct prevailing wind conditions were indeed extracted from the full dataset. Furthermore, a Pearson Correlation procedure was applied to the extracted data and plotted in connected network diagrams. These diagrams served as confirmation that the stations were acceptably correlated in time and across vast distances. The network diagrams also allowed for visual identification of the best possible groups of stations to use in future CFD validation exercises.

© University of Pretoria

5 Marion Island Simulation Setup

A description of the full process is given here for setting up and running comprehensive wind simulations across Marion Island (MI) and its smaller neighbour, Prince Edward Island (PEI). Only the results pertaining to MI are relevant to this study. However, due to the subsonic and incompressible nature of the flow, atmospheric interactions between the two land masses were expected and thus both needed to be modelled in the same domain to maintain reasonable accuracy. The strategy outlined in the subsequent discussion was adopted in order to achieve suitably fine-scale results on MI whilst modelling a particularly vast domain; with computational resources being a chief limiting factor. In effect, this chapter provides an overview of the rest of the study to follow.

5.1 Requirements and Limitations

The following list of requirements formed the foundation of the decision-making process in this study:

- Simulate and validate wind patterns across the MI terrain that correspond as closely as possible with the experimental measurements discussed in Chapter 4.
- For completeness and for the sake of future academic endeavours, simulate multiple wind directions and wind speeds on MI once the original setup has been validated.
- Find a way of consolidating large, weather-scale atmospheric boundary conditions with micro-scale simulations at ground level of the MI terrain.
- Due to its proximity, include PEI in the modelling domain to account for any upstream/ downstream influences it may have on the MI CFD solution.

While the requirements for a successful project are not particularly strict, simulations were severely hindered by the following computational limitations:

- The Centre for High Performance Computing (CHPC) in Cape Town, South Africa, provides ample computing power. Compute nodes with 24 Intel Xeon 5th generation CPUs and 125GB RAM per node are available. The number of ANSYS Fluent licenses accessible by the University of Pretoria through the CHPC restricted the calculations to a maximum of 240 logical computing cores. If 10 nodes are used in parallel, using all available 240 licenses, the working memory is limited to 1.2 TB.
- For post-processing and visualisation purposes, final file sizes are limited. Only 125 GB RAM is available for collectively loading any relevant solution files and running post processing algorithms on the data.

© University of Pretoria

5.2 Topography Modelling

Geographical files for MI and PEI were provided in a Digital Elevation Model (DEM), a file format commonly used in Geographical Information Systems (GIS) to describe land coordinates and altitude but unrecognised by the Fluent Meshing software as a geometry descriptor. Converting the DEM to a usable Stereolithography (STL) geometry file is usually easily done with the help of freely available third-party software. However, due to the sheer size and scope of the landmass at hand, these conversions were not possible and a custom script had to be developed to reduce the problem to manageable proportions.

The provided DEM was generated using a combination of LIDAR and remote sensing techniques beyond the scope of this document; given in GeoTIFF format, a public domain standard which embeds georeferencing information into a simple picture format. Potential stored metadata includes map projections, coordinate systems and reference datums; everything necessary to describe the exact spatial reference of the subject. Pixels in the picture represent a structured grid matrix with the individual pixel colour values containing spatially dependent information. Table 5.1 summarises some important GeoTIFF attributes pertinent to this discussion.

Table 5.1: Marion and Prince Edward Islands DEM file attributes

Island	**# Pixels**	**Area Coverage**	**File Size**
Marion Island	700 Million	~ 700 km ^{2}	1.3 GB
Prince Edward Island	82 Million	~ 83 km ^{2}	170 MB

In the current case, the grid of pixels in the GeoTIFF format could be loaded and converted to an equivalent 2D array in a Python environment. After manipulation, each cell in the array matrix represents a horizontal 1 m$\times$1 m area on the Earth's surface with the numerical value of the cell taking on the average altitude above sea-level rounded off to the nearest 1m.

For ease of reference, each pixel in the matrix is referred to as a "point" from now on rather than a "cell" or "pixel". Each point has its own (i, j) index in the 2D matrix and a corresponding integer value for altitude. The natural ordering of a 2D array implies a rigid connectivity between neighbouring points which does not need to be explicitly defined when writing a GeoTIFF file. This structured ordering is responsible for the relatively small file sizes denoted in Table 5.1 despite the high number of sample points. However, the Fluent Meshing software is not able to interpret these files as a geometry and so the next simplest format would be the STL format common to many Computer Aided Design (CAD) programs.

Unfortunately, a valid STL file format requires an explicit set of Cartesian coordinates for every single point. Additionally, STL files require a separate connectivity matrix to group sets of points into defined geometric facets. These facets in turn make up the geometry which the

© University of Pretoria

software is able to interpret. Since the details of bitwise storage on computers is beyond the scope of this discussion, suffice to say that directly using this conversion process on the full GeoTIFF model results in a STL file size a factor of at least 64× larger than the original, depending on the number of resultant facets and how they are ordered.

Running third-party software with default settings to convert the GeoTIFF files to STL format on the CHPC cluster resulted in file sizes upwards of 180 GB and exceeded allowable computation time; it became abundantly clear that a custom approach was necessary to effectively reduce the total number of points before a useable STL geometry file was achievable. The objective of this exercise was to enable efficient modelling of the shape of the terrain while only using a fraction of the original sample points. The flow diagram in Figure 5.1 explains the full procedure behind the reduction process. A gradient-based approach was taken, meaning that areas with large sloping features were prioritised over flatter terrains when resampling points from the GeoTIFF model.

Following the resampling procedure from Figure 5.1, the list of $\langle x, y, Z \rangle$ points retained after processing each island was assembled into a long $N \times 3$ matrix where N is the total number of retained points. The list was then grouped into a connectivity matrix using a simple 2D Delaunay triangulation function. A complete description of the Delaunay triangulation is beyond the scope of this document. One only needs to note that the function outputs a matrix describing triangular facets; each facet made up from three points (vertices) found somewhere within the $N \times 3$ list and all facets are completely empty of any other points.

The resulting connectivity matrix was further reduced by eliminating any facets where all three defining vertices simultaneously had altitude values $Z = 0$. Figure 5.2 illustrates the final stages of the triangulation and conversion to STL format on a small portion of MI as an example.

Although a reduction of about 90% was applied to the portion of MI seen in Figure 5.2, it is still possible to visually reaffirm that the shape of the island was kept mostly intact; in practice, a reduction value far less extreme was used when resampling points from the GeoTIFF files. An attempt at quantifying any shape deviation was not performed as it is not applicable. One needs to keep in mind that both the GeoTIFF and the STL models are simple approximations of the topology, therefore neither will be entirely accurate. The STL geometry is a naturally coarser approximation but had to be used due to the fact that ANSYS Fluent does not recognise the GeoTIFF format.

© University of Pretoria

Load GeoTIFF into Python array and partition into subsets.

Read the GeoTIFF file into Python and convert to a 2D numerical array. Stored values represent altitude, Z, above sea level. Array $\langle i, j \rangle$ indices correspond to global $\langle x, y \rangle$ coordinates

Split the array into equal subsets. Only work with one subset at a time (processing the entire array at once is too demanding).

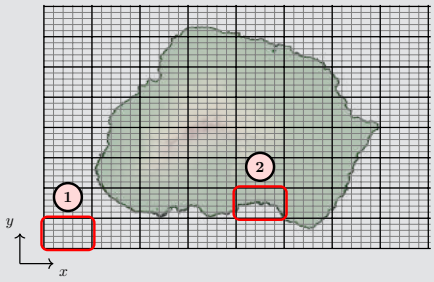

① If all Z values = 0

Delete any subsets containing only "Sea" points (redundant since we know $Z = 0$).

② If a subset contains relevant height data

Compute partial numerical derivatives in x- and y-directions. Central-differencing was used where possible.

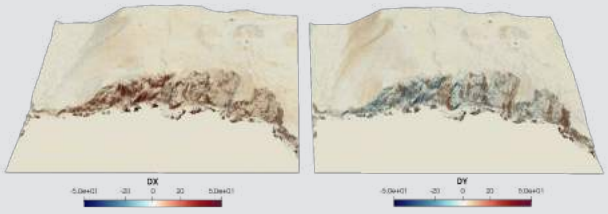

Combine gradients to find the geographical slope, S:

$$S = \arctan\left(\sqrt{\left(\frac{\partial Z}{\partial x}\right)^2 + \left(\frac{\partial Z}{\partial y}\right)^2}\right)$$

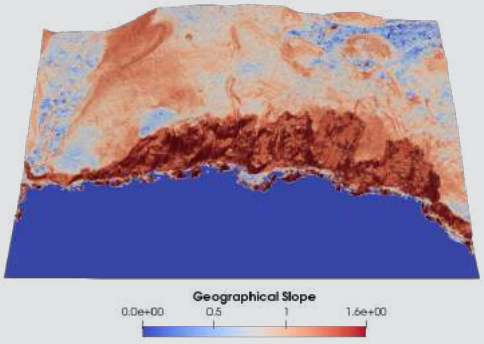

③ Convert to a smooth probability distribution.

The slope array, S, was converted to a 2D probability distribution function by:

- Applying Gaussian smoothing to suppress minor slope variations.
- Adding an arbitrarily small offset to all values (thus, a value may be small but never zero).
- Scaling all values by the sum total of the slope array: $P = \frac{S_{i,j}}{\sum_i \sum_j S_{i,j}}$

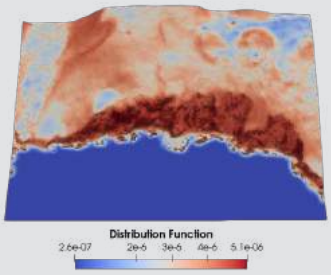

④ Draw a random sample from the PDF

Select a number of $\langle i, j \rangle$ points from the area based on the probability density function. The number of chosen points cannot exceed a user-defined value. Append the corresponding $\langle x, y, Z \rangle$ coordinates to a list.

Figure 5.1: Flow diagram explaining how the number of points in the GeoTIFF file were reduced before conversion to an STL geometry file format. A gradient-based slope detection method was used to identify the most important points for retention

© University of Pretoria

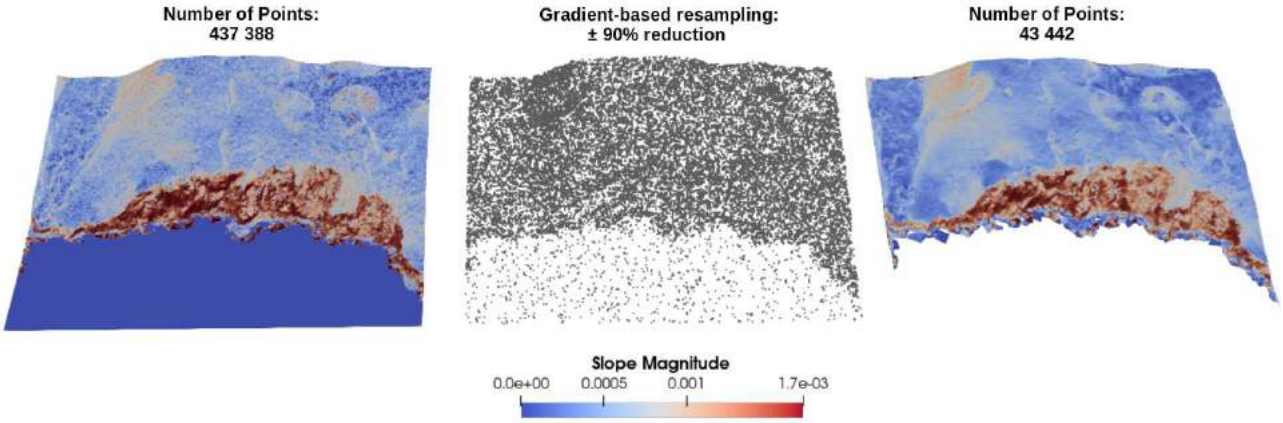

Figure 5.2: A small portion of MI is used for illustrative purposes to visually describe how the original GeoTIFF file (left), was randomly resampled according to a gradient-based Probability Density Function (middle) and the resulting set of points triangulated to form a geometry description of the island in STL format (right). Nodes and facets that were classified as "sea" areas were deleted from the model before saving

In the end, the final STL files for MI and its neighbour were reduced to the sizes shown in Table 5.2. Note that a large part of these reductions was simply the removal of buffer nodes surrounding the islands, all with a value of $Z = 0$ denoting sea level.

Table 5.2: Marion and Prince Edward Islands STL file attributes

Island	**# Points**	**# Faces**	**reduction [%]**	**File Size**
Marion Island	11.9 Million	23.7 Million	~ 63.7	1.2 GB
Prince Edward Island	0.46 Million	0.92 Million	~ 74.8	46 MB

Although the STL representations have been used extensively throughout many of the visualisations in this document, the unaltered files have been rendered in Figure 5.3.

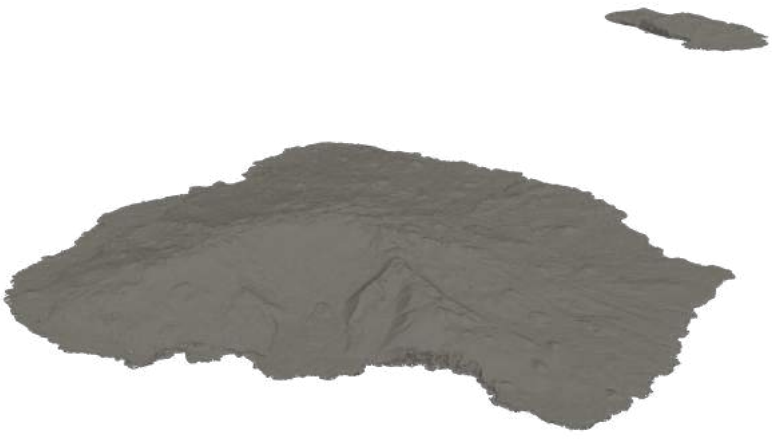

Figure 5.3: Oblique view of the rendered STL geometry files for both islands

© University of Pretoria

5.3 Modelling Strategy

Taking all requirements and limiting factors into account, it was clear that an intelligent simulation structure would be necessary to complete the project within CFD best-practice guidelines. The simulation approach was also developed with a sense of time management in mind. The setup was economised such that new wind speed/direction cases could be arranged without redoing work unnecessarily, especially with regards to the tedious process of mesh generation.

Without focusing on the full domain extents for now, the key idea behind achieving suitably fine-resolution results in the area of importance was to allocate more mesh cells nearer to MI and to decrease the mesh density further out; a common CFD practice. In order to maximise the number of cells in the domain and speed up overall solution time whilst remaining within computational limits set out previously, the decision was made to sacrifice double precision accuracy for the large-scale simulations.

A bird's eye view of the said solution strategy is presented below:

- Generate a near-field mesh encompassing both islands in a circle domain as shown in Figure 5.4. Using scoped sizing, the cell density on the ground surfaces of both islands is increased to accommodate a finer resolution result. Cell spacing further away from the islands is similarly adjusted to reduce the number of cells.

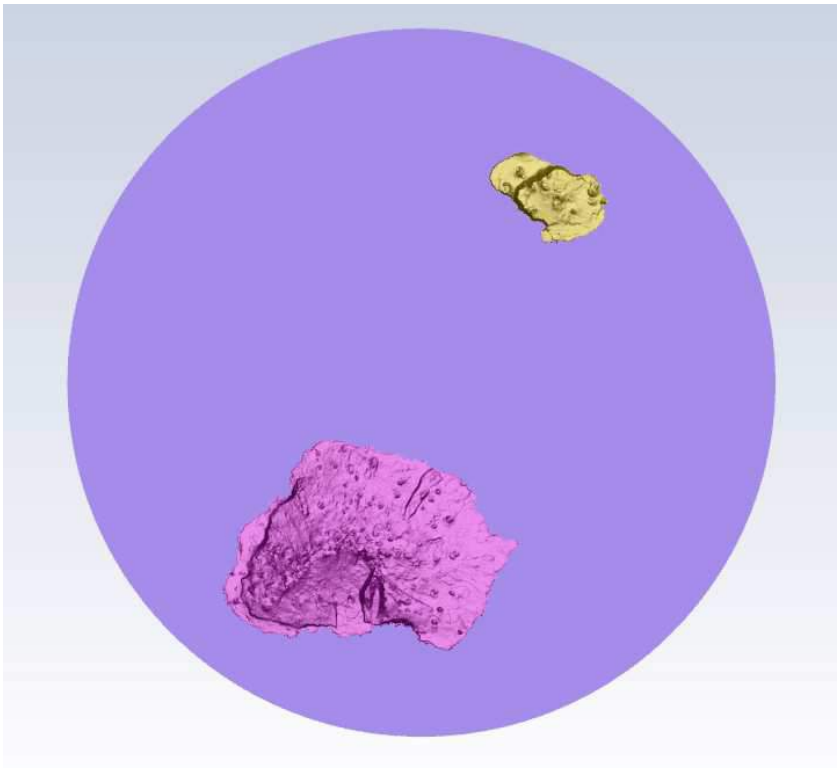

Figure 5.4: Near-field circle domain used in high level MI wind simulations

- Generate an outer rectangular domain with a corresponding circular hole cut out of it and non-conformally merge both meshes in Fluent. Consistent boundary conditions can

© University of Pretoria

be applied normal to the faces of the outer rectangle domain. Should the situation call for a different wind speed or wind direction, the inlet boundary conditions can simply be adjusted or the outer domain can be rotated respectively as depicted in Figure 5.5. Thus, the same mesh can be reused for multiple simulation cases and the boundary condition types never need to be changed once set. Validation against the measurement data set can be performed with the so-called full-scale simulations at this stage. More details are presented in Sections 6.1 to 6.7.

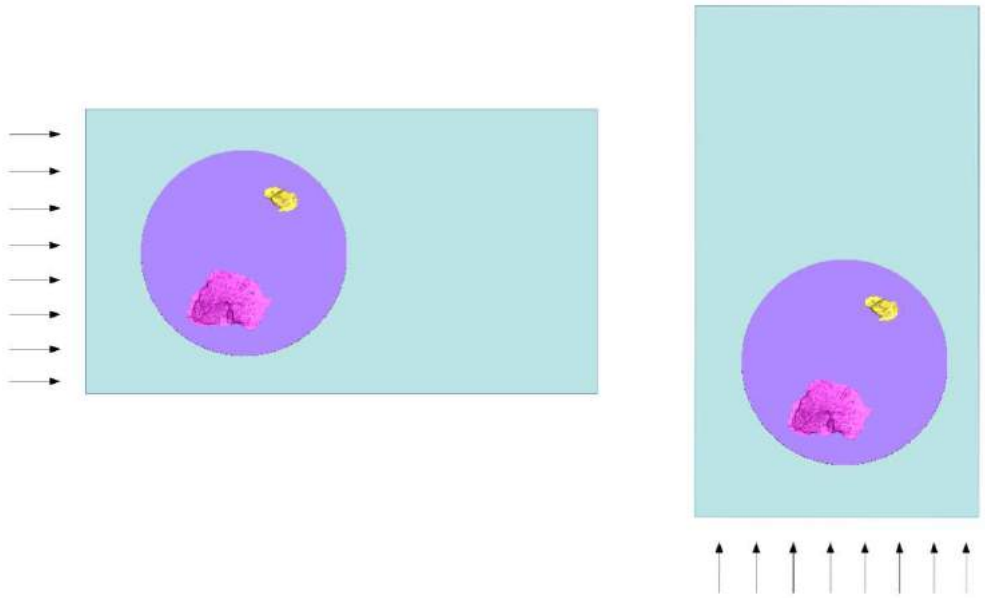

Figure 5.5: Illustration showing the basic strategy for altering the wind direction from 270° (left) to 180° (right) without regenerating an entirely new mesh or changing boundary conditions

- Define a sub-domain around only Marion Island which can be used to extract near-field simulation data from the area of interest as shown in Figure 5.6. For each simulated wind direction, save the converged data from the sub-region to a boundary file which is used in future modelling.

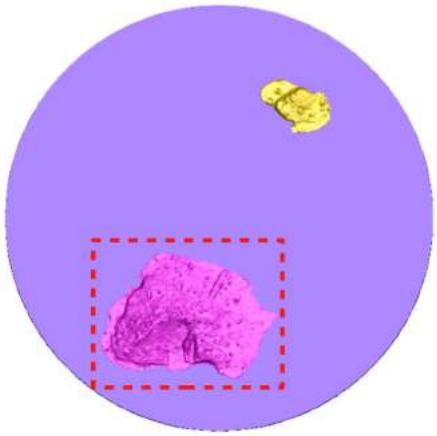

Figure 5.6: Depiction of the extent of the sub-global scale MI model

© University of Pretoria

- Generate a new mesh, reallocating all available cells within the memory limitation to a domain the size of the saved sub-domain from Figure 5.6. Any previously saved boundary files can be used as inlet boundary conditions and a starting point for a much finer grid simulation. This method should achieve similar results to embedding a finer scale mesh within the original grid, only without the additional computational burden. Disadvantages of the method include saving excess files to disk, spending extra time setting up sub-domain simulations and inducing possible errors when interpolating from a coarse grid to a finer grid. Although direct automation would not be possible with this refinement procedure, it duly saves time and computational effort when under constraints set by the requirements and limitations.

- The sub-domain models are validated against the experimental data once again to ensure simulation accuracy at a finer scale. These simulation results are then added to the final MI wind database for further use in MI related studies. More details are presented in Section 6.10.

- Repeat the task of defining and saving data from a sub-region of the MI fine-scale solution. This is not done for the entire island but only the specific areas where biological studies are concentrated. Possible locations for this refinement have been identified and highlighted in Figure 5.7. The regional models once again reduce the size of the computational domain whilst keeping a high cell count. In these cases, the grid should be fine enough to perform preliminary scale resolving simulations such as Large-Eddy Simulations (LES) or Detached-Eddy Simulations (DES). Completion of this exercise is dependent on all previous work.

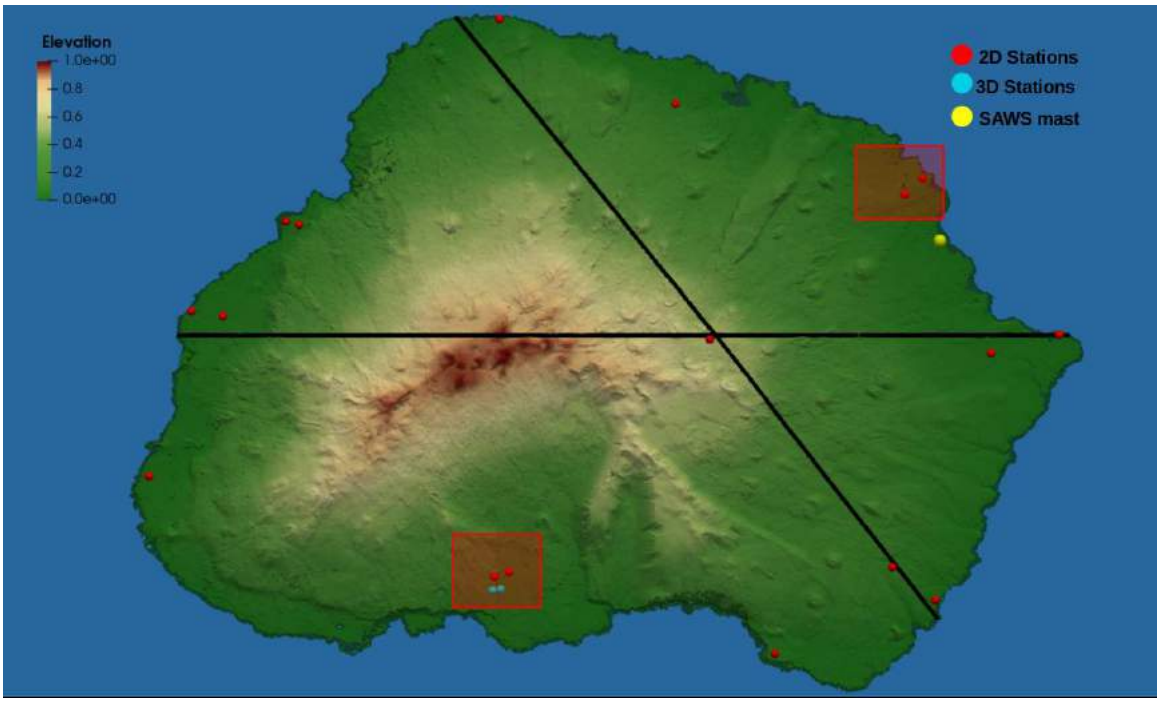

Figure 5.7: Highlighted zones of high biological importance on MI suitable for further grid refinement and Scale Resolving Simulations (SRS)

© University of Pretoria

5.4 CFD Model Settings

The default settings and CFD model parameters are described here with appropriate supporting arguments. The precursor simulations in Chapter 3 have culminated in this section to give an overall CFD modelling specification to carry forward throughout the rest of the project. Any alterations to these default settings will be explicitly noted where necessary in later sections.

5.4.1 Wall Boundaries

The ground is modelled using the STL geometry files with a uniform roughness height of $z_0 = 0.015m$; following the guidelines set out by Bechmann *et al.* (2009) and also in Table A.1 for a rough pasture. Vegetation on MI is dominated by mosses and grasses rather than trees or shrubbery due to the strong winds at play, so this assumption is seen as the most valid simplification of the land roughness. Figure 5.8 shows the typical surface conditions seen year-round on MI. The large volcanic rock structures seen in Figure 5.8 were largely ignored when making this decision because they would fall below the grid resolution of the simulation meshes. At higher altitudes, vegetation gives way completely to jagged rock and volcanic scoria cones. However, since there is no explicit aerodynamic roughness information for this material in Table A.1 and no clear boundary exists to define which areas are rocky or covered by vegetation, the idea of a variable roughness length was abandoned.

(a) **(b)**

Figure 5.8: The landscapes pictured around the masts show typical surface conditions in the summer months (a) and in the winter months (b). These conditions cover the majority of the MI surface area and can be modelled using the same aerodynamic roughness length, $Z_0 = 0.015m$

A similar approach is used to model the sea roughness, or wave height, as a function of wind speed. A completely flat geometry is used to model the sea surface, but the Charnock model (Eq. 2.38) will be applied as a wall boundary roughness to approximate a uniform wave height based on the wind speed at the inlet boundary. Varying roughness lengths and a moving sea wall boundary condition were ignored since they offer no significant improvement on the final solution (see the discussion in Section 2.7.3).

© University of Pretoria

Regarding vertical spacing, a first-cell height was chosen to ensure that the equivalent sand-grain roughness, K_s, would always be smaller than the height of the first-cell centroid, z_p; thereby eliminating non-physical wall boundary interactions. To determine the required first-cell height, Eq. 2.39 was used to convert the applied z_0 roughness to its sand-grain equivalent:

$$K_s = z_0 \frac{E}{C_s} = 0.015[m] \frac{9.9793}{0.5} = 0.07484[m] \tag{5.1}$$
$$\implies z_p \geq 0.07484[m]$$

To satisfy the constraint in Eq. 5.1, a minimum first-cell height of 0.2m was chosen throughout the domain.

5.4.2 Inlet Boundaries

The inlet and top boundaries are modelled using the standard neutrally stable log-law equations defined in Section 2.7.1. It is possible in ANSYS Fluent 2019R3 to define these inlet equations as mathematical expressions without resorting to programming and compiling User Defined Functions. This useful functionality meant that all inlet boundary conditions could be formulated to rely on a single user-input variable, namely u_*. I.e. the user simply needs to specify any practical value for the friction velocity, u_*, and the program will automatically interpret all other inlet functions and profiles. The inlet wind direction is defined perpendicular to the inlet face while the top boundary wind direction is defined parallel to the top plane and perpendicular to the inlet face.

The MIRED database was interrogated to get a reasonable estimate for a friction velocity. In this regard, the empirical linear approximations for friction velocity given in Table 2.4 were used to estimate the realistic value of the local friction velocity near the stations from limited mast data. In most cases, the masts had two ultra-sonic wind sensors at two different heights (0.5 m and 1 m) meaning that two possible friction velocity estimations were possible using this approach. An alternative method for approximating the experimental friction velocity given wind measurements at two different heights was to assume that the local wind follows a log-law profile; the analytical log-law relationship given in Equation 2.31 was then manipulated to find an estimate of the local friction velocity using the wind speed gradient:

$$u_* = \frac{\kappa}{2} \left(\frac{|U_{1m}|}{\ln(\frac{1}{z_0})} + \frac{|U_{0.5m}|}{\ln(\frac{0.5}{z_0})} \right) \tag{5.2}$$

where $\kappa = 0.4$ and $z_0 = 0.015m$ are assumed values. Neither estimation method is perfect, yet all tended to yield strongly similar results. Thus the average value of these estimates was taken as the experimental local friction velocity. Figure 5.9 presents the deduced friction velocity values from the experimental dataset. The overall average friction velocity anywhere on MI was determined to be $u_* = 0.1534$ m/s with a RMS difference of 0.033 m/s.

© University of Pretoria

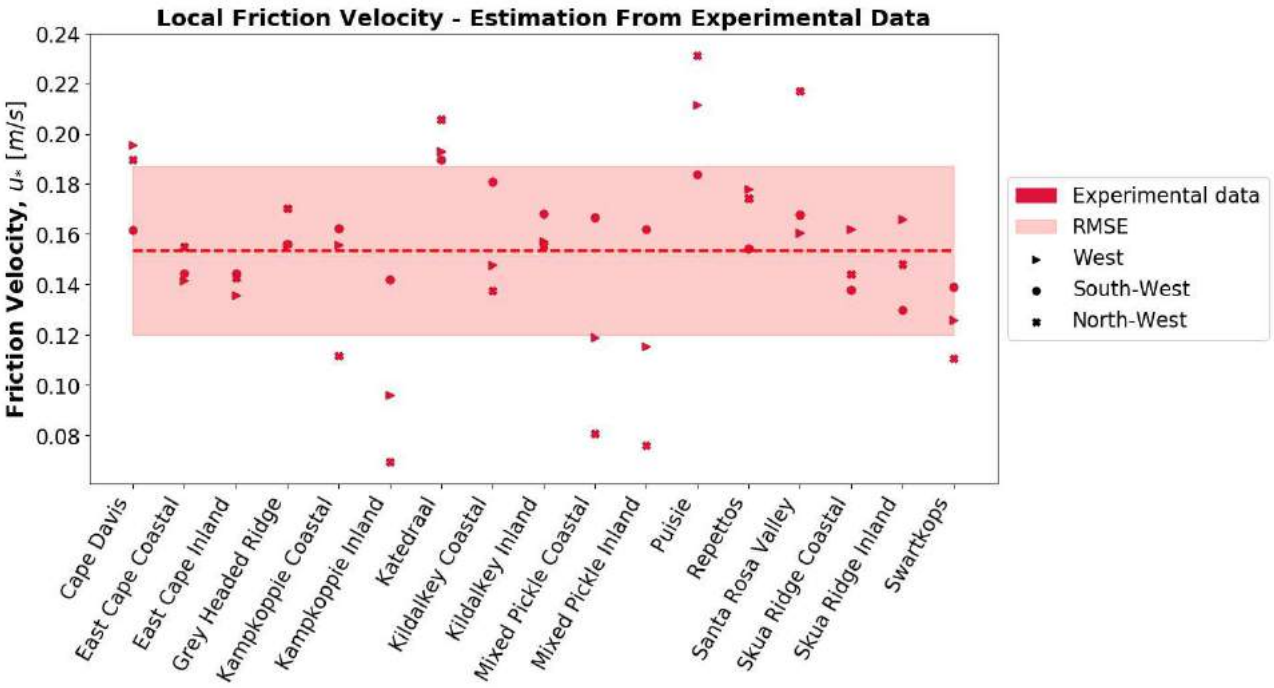

Figure 5.9: A scatter plot comparing the experimentally determined local friction velocity values for all three primary wind directions. The mean experimental friction velocity, $u_* = 0.1534$ m/s, is used as the input to any CFD simulations

A theoretical input value of $u_* = 0.15$ m/s has thus been chosen throughout most of the simulations described in this document. It should be noted, however, that this value is also used as a scaling value (see Section 2.9) when presenting results in universal form.

5.4.3 Outer-Domain Boundaries

The sides of the domain are modelled as symmetry boundaries while the outlet face is given a gradient-free outflow specification. Although care was taken to ensure that any boundary surfaces were placed far enough away so as not to influence the solution, it was clear that capturing the full wake behind the island at full-scale would not be possible without an excessively long domain. Thus, ignoring typical CFD practice, the domain was kept shorter but the outflow boundary was applied to minimise any negative effects of doing so.

5.4.4 Turbulence Model

Regarding the internal domain, the standard k-ε turbulence modelling scheme was used for all of the simulations unless otherwise stated. Despite the somewhat inaccurate behaviour of this scheme seen in the Bolund Island case study, the choice to keep using it was influenced by the fact that the majority of literature on this topic (see Section 2.5) preferred the k-ε turbulence model over other variants. Additionally, the modified k-ε constants from Table 2.2 were available to minimise the model's shortcomings. This being said, note that part of the work in this masters thesis involved testing and using other turbulence modelling schemes; the modified k-ε model was simply chosen as a default.

© University of Pretoria

5.4.5 The Energy Equation

Buoyancy effects, and the energy equation in general, have been neglected in the current study; although this represents an avenue worth pursuing in future studies. A neutrally stable atmosphere has been assumed since the strength of the wind in the MI region is sure to overpower any temperature interactions. The climate is also termed "hyper-oceanic", removing the need to model diurnal buoyancy fluctuations.

5.4.6 Coriolis Force

The Coriolis force has been implemented in all MI simulations from this point forward since the domain is too large to keep ignoring the Earth's inertial effects on fluid momenta. The Coriolis force is modelled in each case by calculating a new scalar equation (Eq. 2.29) in each cell and adding it to the Navier-Stokes momentum equations as an offset.

5.4.7 Convergence Controls

Due to convergence stability issues, the solver method has been changed to a SIMPLE solver as opposed to the current ANSYS Fluent default Coupled solver. Perhaps the most crucial settings to change within the Fluent interface are the internal convergence limiters. The viscosity ratio is limited to 10^5 for most industrial applications to stop the numerical solution from diverging. Flows in the upper atmosphere, by contrast, reach viscosity ratios orders of magnitude larger; in the range of about 10^9 - 10^{10}. Furthermore, the pressure-, momentum- and turbulence-relaxation factors need to be reduced to facilitate a more stable convergence of the solution. Leaving these terms at their default values may cause the solution to diverge if the quantities fluctuate too much between iterations. The cost of introducing these solver settings is a longer solution time; but far more stable.

5.4.8 Model Layout

The simulation settings discussed thus far have been combined with the large-scale domain selection discussed in Section 5.3 to give Figure 5.10: a summarised representation of the simulation domain tagged with its associated boundary conditions where possible. L_{up} and L_{down} denote the upstream- and downstream-lengths, respectively. H and W similarly correspond with the domain height and width, respectively. These dimensions have not yet been defined in Figure 5.10, since they are only completely determined after the mesh generation procedure in Section 5.5. Note that the interface condition between the near-field and far-field domains is not an exact fuse between the different meshes; it is kept as a standard mesh interface.

© University of Pretoria

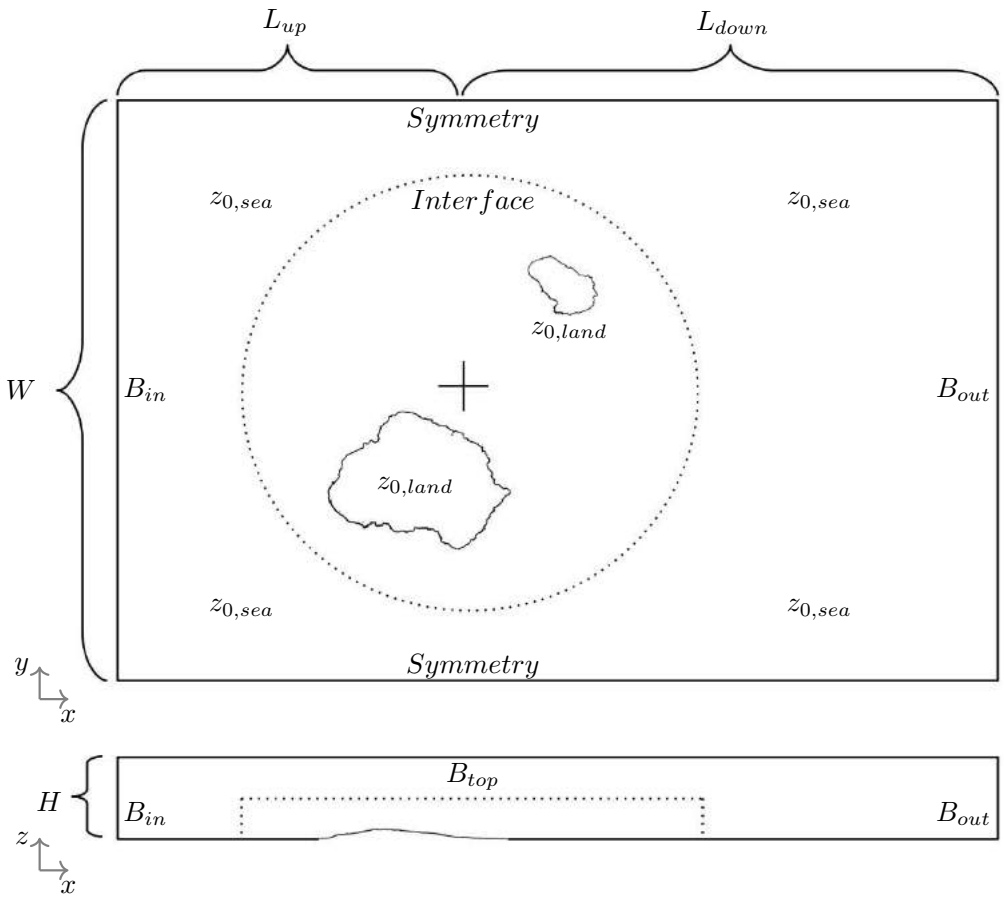

Figure 5.10: Graphic representation of the computational domain along with the tagged boundary conditions to be used throughout the CFD simulations. Table 5.3 contains further details regarding the boundary naming conventions used throughout the rest of this document. Domain dimension lengths have been left purposefully unspecified as these are subject to change

Table 5.3: Model parameters pertaining to Figure 5.10

Name	**Condition Type**	**Value/s**
B_{in}	Velocity inlet	Defined by Eqs. 2.31-2.34
B_{top}	Velocity inlet	Same as B_{in}
B_{out}	Outlet	Gradient free outflow
$z_{0,land}$	Stationary Wall	Roughness: $z_0 = 0.015m$
$z_{0,sea}$	Stationary Wall	Roughness defined by Eq. 2.38
Name	**Description**	
L_{MI}	Approximate length of MI	$\sim 20km$
H_{MI}	Approximate peak height of MI	$\sim 1.2km$
L_{up}	Upstream length	
L_{down}	Downstream length	
W	Domain width	
H	Domain height	

© University of Pretoria

5.5 Mesh Generation Procedure

Discretisation of the domain was primarily performed using the newly matured Fluent Meshing software in the ANSYS 2019R3 package. Since grid spacing is of utmost importance in a CFD analysis, due time was spent on mesh generation and grid independence studies to ensure that a model at this large scale was achieving the highest accuracy possible. For repeatability, these procedures are outlined in the discussion to follow.

5.5.1 Inner Domain

The circular inner domain described in Figure 5.4 was generated and discretised following a set of automated instructions in the Fluent Meshing program. These instructions were compiled into a journal file and executed at the CHPC to take advantage of parallel processing capabilities. Example journals are available in Appendix F although the process for generating the inner-domain mesh is described below:

- Create a cylinder primitive body in SpaceClaim with a radius of 30km and a height of 3km.

- Import the cylinder body, MI and PEI geometries (in STL format) into Fluent Meshing and rename all the surfaces to more meaningful alternatives.

- Apply scoped sizing to the important faces on the geometry:

  - 50m or greater horizontal spacing on the island surfaces (Provisions were made in the journal files to change this value as necessary). A growth rate of 1.2 was applied to this setting. Thus, allowance was made for cell sizing to vary slightly based on the surface gradient but this was not noticeable in practice.

  - 100m or smaller horizontal resolution on the sea surface. A growth rate of 1.1 was applied to this size setting; cells far away from the islands would be sized at 100m and steadily decrease to a size of 50m as they approach the islands.

  - 500m or smaller sizing on the top interface boundary of the cylindrical geometry. Again, cells approaching the islands would decrease down to a size of 50m according to a growth rate of 1.2.

- The "Material Point" is a defined coordinate/position within the domain that specifies which volumes the program is intended to mesh; typically inside a watertight geometry. Choose the so-called material point to be inside the cylinder body and above any of the island surface bodies.

- Wrap all the geometry into a single surface-mesh object which inherits the boundary-names and -condition types from its parent bodies. Surface-mesh sizing is dictated by

© University of Pretoria

the scoped definitions above or else linearly interpolated on faces where sizing was not explicitly stated.

- Apply prism/inflation layers to the sea- and island-surface boundaries. A first-cell height of 0.2m was applied with a growth rate of 1.3 in the vertical direction.

- Mesh the volume of the domain using a choice of tetrahedral or polyhedral elements. Polyhedral elements were primarily chosen because they offer the benefits of filling a greater volume per cell and therefore reduce the computational memory burden. Poly-cells are also better at approximating gradients since they have more neighbouring cells than other mesh types. However, localised mesh adaptation is not possible with poly-cells in post-processing so a compromise was made in this respect. Further details on the performance of polyhedral elements vs. other elements are beyond the scope of this study but can be pursued in a white paper published by ANSYS (2019).

Due to the size of the domain and the tightly-packed nature of its cells, it was not possible to view the entire inner-domain mesh within the resolution of a single screen frame on a computer. Therefore, a compilation of screenshots is presented in Figures 5.11-5.12 to show the relevant details of the inner-domain mesh.

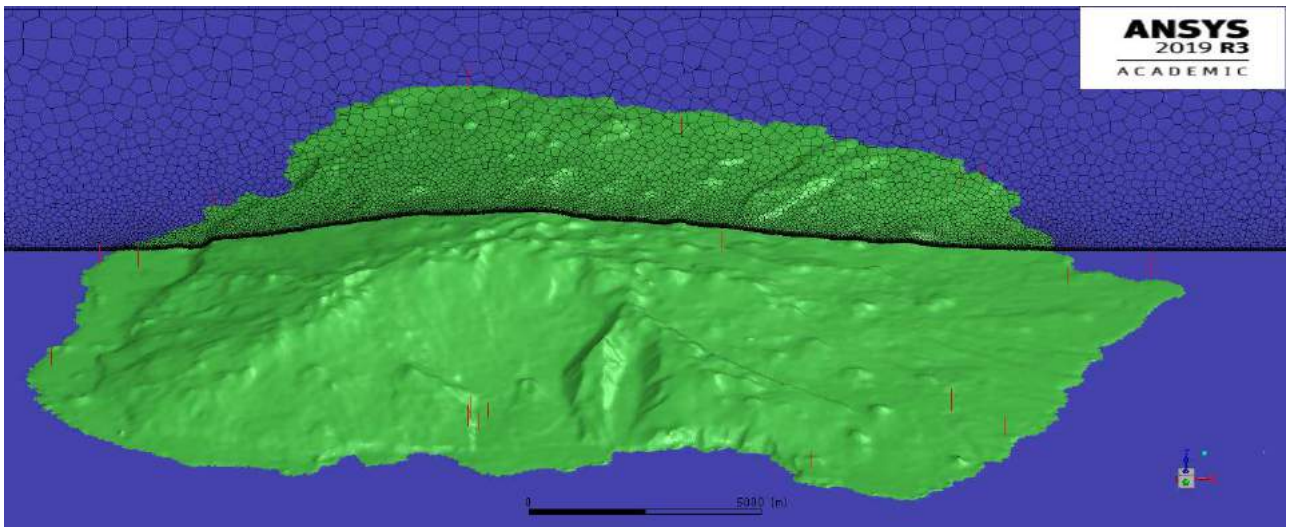

Figure 5.11: Polyhedral mesh cross-section going over MI in the 270° direction. Note how smaller cells simply disappear into a black mass due to the screen resolution; hence the reason why a screenshot of the entire domain could not be captured. Red lines indicate mast positions around the island where numerical CFD data are extracted for validation against the experimental statistics

© University of Pretoria

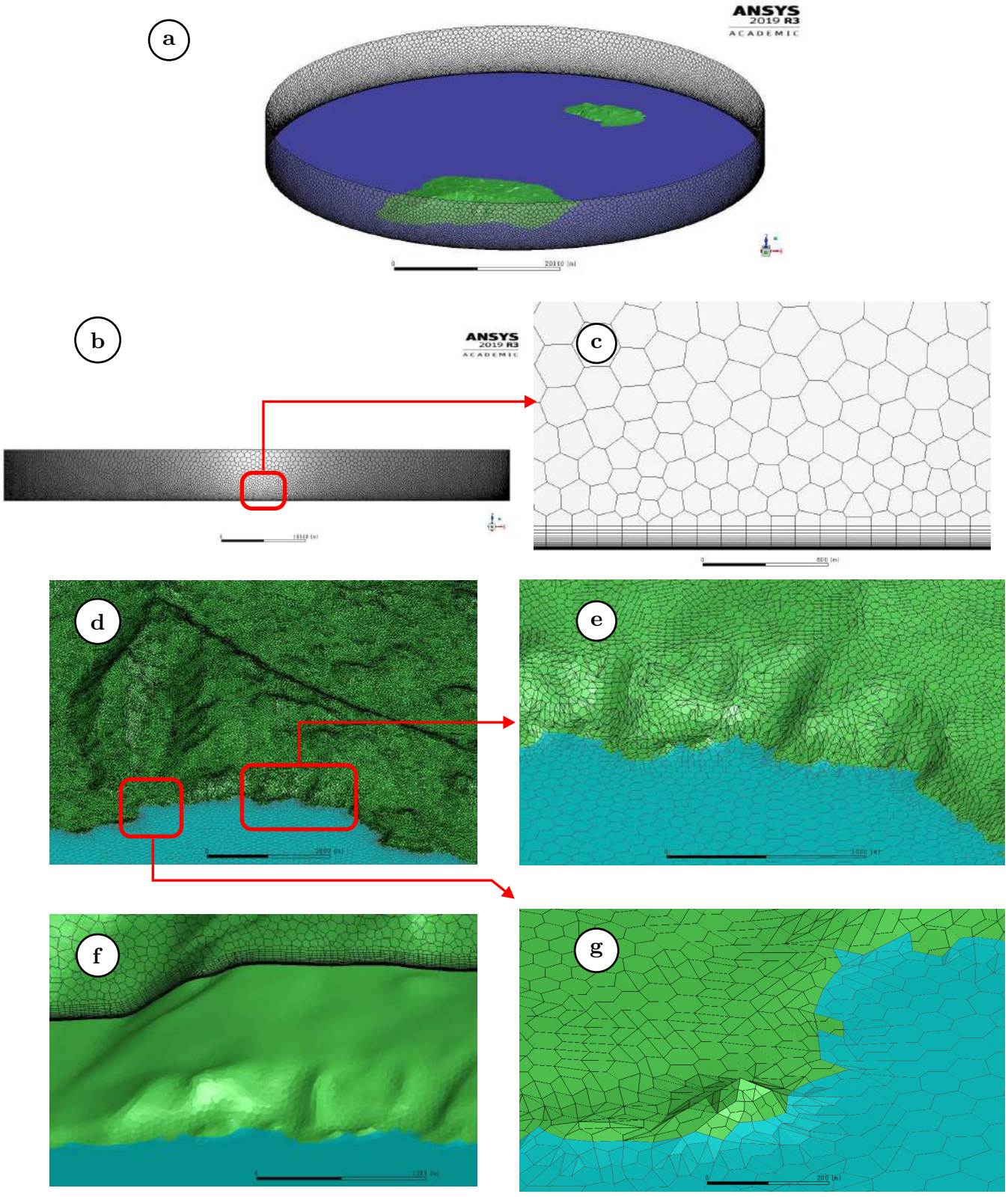

Figure 5.12: The images shown here attempt to highlight the characteristics of the MI near-field mesh (a) with the use of computer screenshots. An overall view of the vertical cell-sizing field (b) is shown on the outskirts of the cylindrical domain, with a close-up view of the sea-level inflation layers (c). A section of MI with 50m horizontal grid-spacing has been zoomed (d) and a closer detailed view of the coastline (e) shows cellular growth from a 50m grid on land to a 100m grid on the sea-surface. Inflation layers close to the island surface are shown (f). Possible problematic areas such as sharply pointed cell connections and a crudely approximated coastal bounding-edge (g) have been highlighted for further consideration in later discussions

© University of Pretoria

5.5.2 Outer Domain

Similar to the procedure described in Section 5.5.1, the outer domain and its accompanying boundary condition types were automatically generated using journal files in Fluent Meshing. The summarised instructions for the outer domain generation go as follows:

- Import the same cylinder body used when generating the inner-domain mesh. This geometry is now subject to surface meshing on the opposite faces so as to generate a smooth interface between the inner- and outer-domain meshes.

- Specify a bounding box geometry. The domain lengths L_{up}, L_{down}, H and W can be scripted into the journal as variables and used to size the bounding box as necessary.

- Create two more box geometries inside the outer bounding box; One upstream of the islands and one downstream. Each new box geometry is used as a Body of Influence (BOI) to exert a finer control on the grid sizing ahead of the islands or in the wake stream without influencing the rest of the domain. These BOI controls can be clearly seen in Figures 5.13 - 5.15.

- Apply scoped sizing to the important parts of the geometry:

  - A maximum 150m grid spacing on all the cylinder faces (interface boundaries between near- and far-field domains). A growth rate of 1.3 is specified throughout the domain so that cells can increase in size further away from the interface boundaries.

  - 250m grid spacing within the approaching-region BOI box (ahead of the islands).

  - 500m grid spacing within the wake-region BOI box.

  - Cell sizing anywhere else in the outer-domain is limited to 1000m.

- Choose the material point to be inside the bounding box geometry and above the cylinder body. BOI geometries are ignored by the meshing program other than to apply their scoped sizing controls to the cell-size field.

- Wrap all the geometry into a single surface-mesh object which inherits the boundary-names and -condition types from its parent bodies. Surface-mesh sizing is dictated by the scoped definitions above or else linearly interpolated on faces where sizing was not explicitly stated.

- Apply prism/inflation layers to the sea-surface boundary. A first-cell height of 0.2m was applied with a growth rate of 1.3 in the vertical direction to be consistent with the inflation layers present in the near-field mesh.

- Mesh the outer-domain volume using polyhedral cells as shown in Figure 5.13.

© University of Pretoria

The final product of these automated meshing journals can be seen in Figures 5.13 - 5.15. Since the interfaces between inner- and outer- domain meshes are non-conformal interface surfaces, particular attention has been given to keeping grid-spacing consistent on both sides of every interface pair.

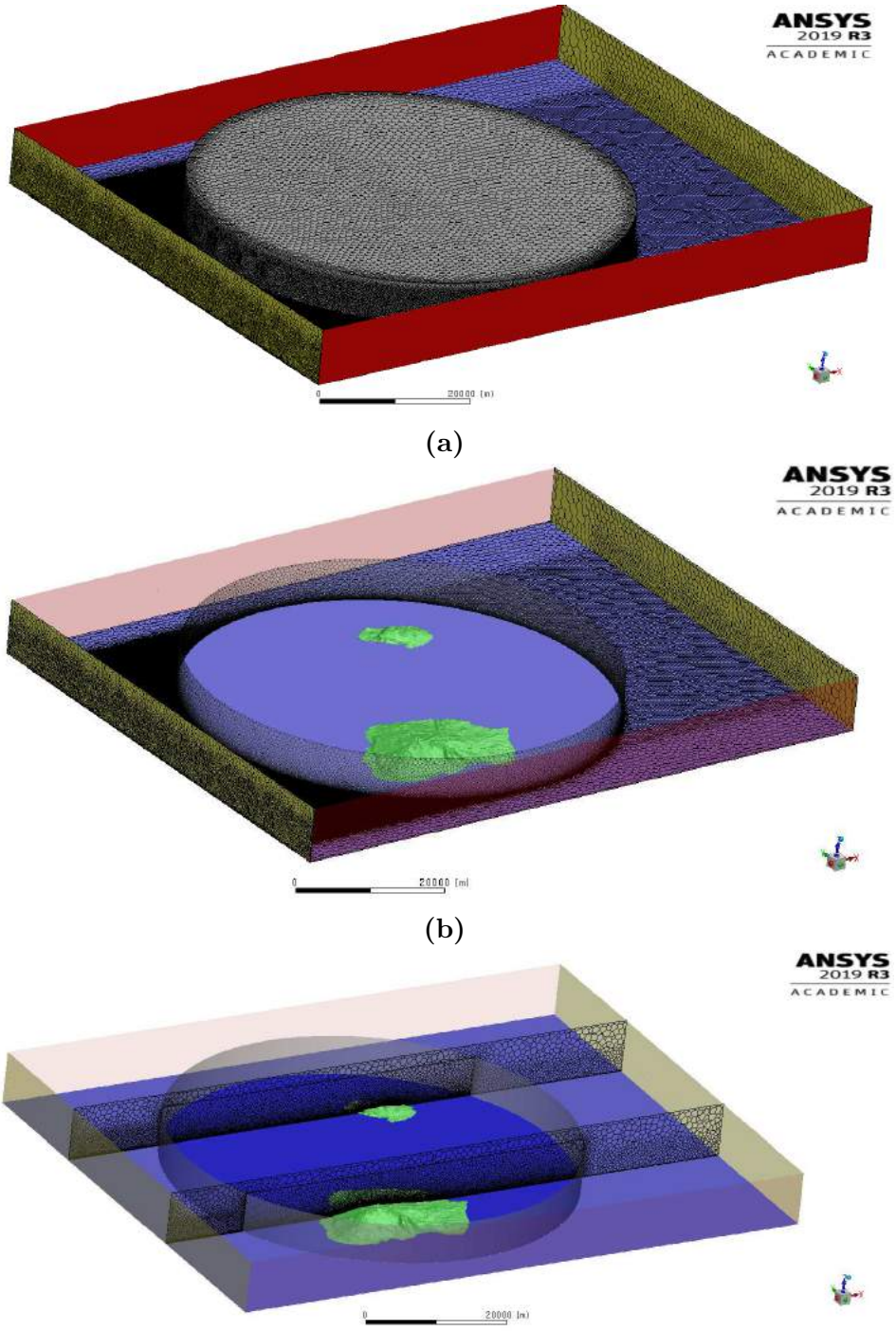

Figure 5.13: The screenshots of the outer-domain mesh (a) are shown after the mesh generation procedure. Inlet and outlet faces are coloured in yellow, symmetry faces in red, the sea-wall boundary in blue and the interface between inner- and outer- domains in grey. Employing colour transparency, the complete interaction between inner- and outer-domains can be seen (b). Cross-sectional views (c) show the cellular size-field from the inlet, over the islands, and towards the outlet

© University of Pretoria

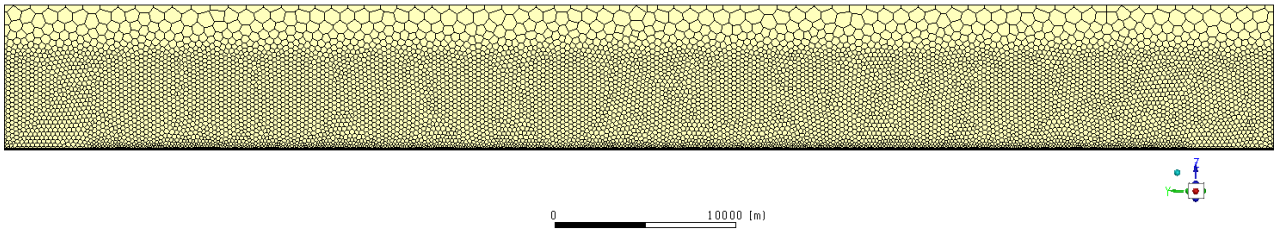

(a)

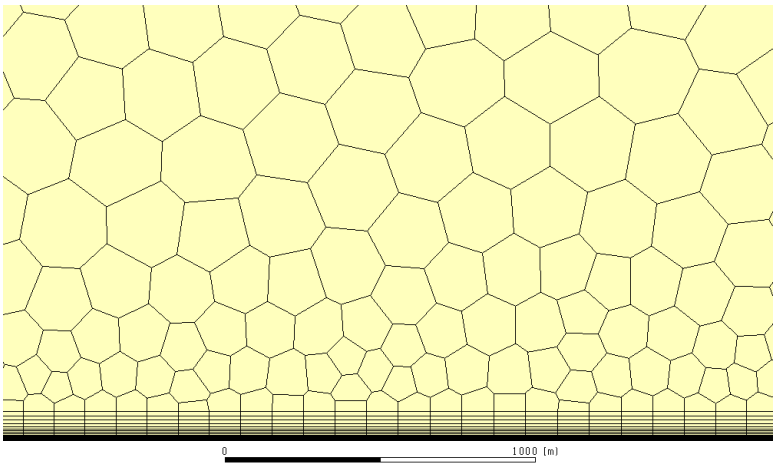

(b)

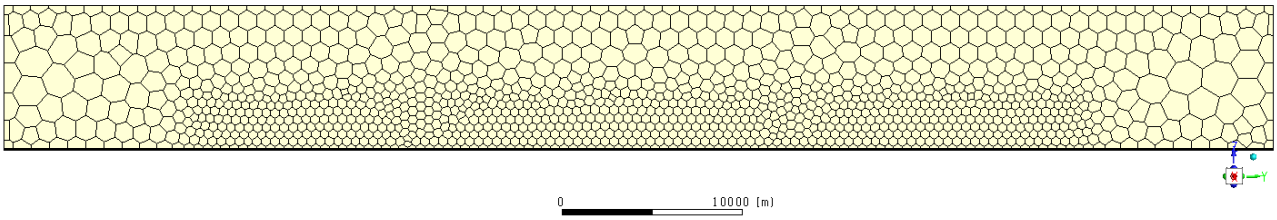

(c)

Figure 5.14: The surface mesh at the inlet (a) and outlet (c) boundaries of the outer domain; BOI sizing controls were used to limit the cell size in the approaching- and wake-regions, respectively. When zooming in on the inlet boundary (b), further detail is noted in the inflation layers

© University of Pretoria

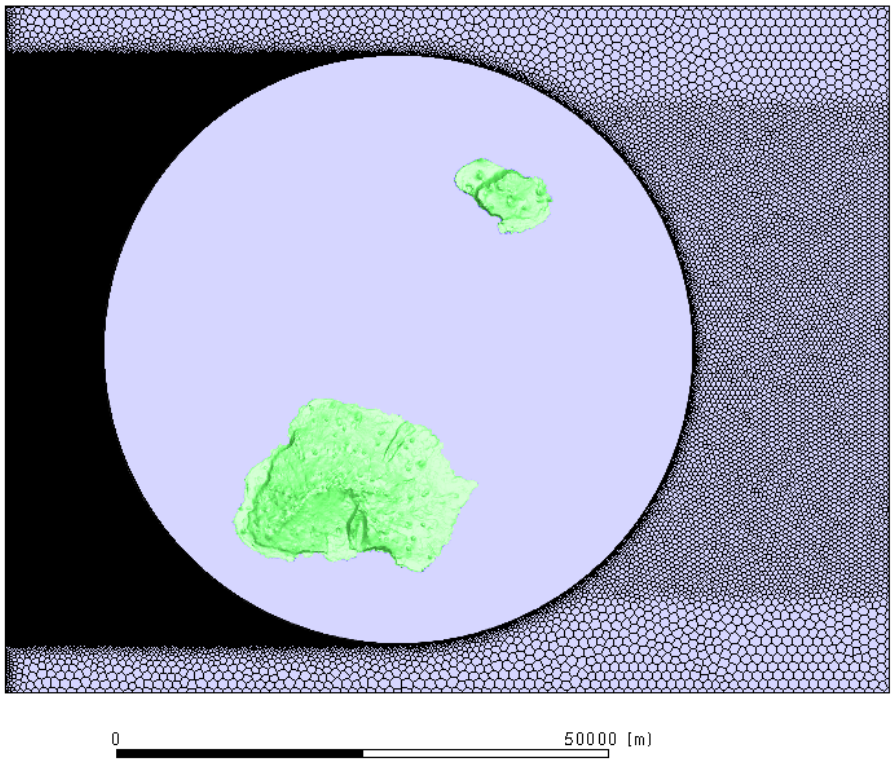

(a)

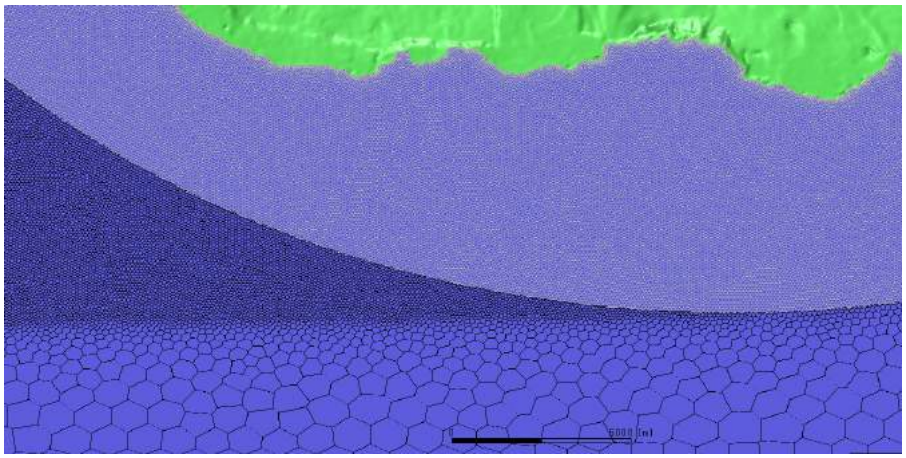

(b)

Figure 5.15: A screenshot of the outer-domain mesh viewed from the top (a) showing BOI sizing controls in the approaching- and wake-regions. Grid sizing is limited to a maximum of 250m ahead of the islands and 500m behind them. A zoomed shot of the area around the mesh interface (b) illustrates how grid sizing has been kept consistent to reduce the loss of accuracy when passing through the non-conformal surface between the inner- and outer-domain

© University of Pretoria

5.5.3 Grid Independence Study

Grid independence studies are performed in order to assess the error in a CFD simulation caused by discretising the domain; coarse meshes are naturally expected to incur larger error than finer meshes. The Grid Convergence Index (GCI) method (Roache *et al.*, 1986) was used in this study to estimate the solution of a grid with zero spacing by comparing the output CFD results from successively finer mesh resolutions. More details regarding the GCI method are provided in Appendix H.

To perform this mesh independence study, the outer domain was ignored and only the cells in the near-field circle (pictured in Figure 5.4) were refined. A very basic square outer domain was generated purely for the sake of applying boundary conditions to it in the same fashion as would be done for full MI simulations. Four different grid densities were used in this study, tied to four corresponding horizontal cell spacings: 1) 20 metres 2) 30 metres 3) 40 metres and 4) 50 metres. These different grids and their properties are summarised in Table 5.4.

Table 5.4: Increasing grid densities used to determine mesh independence

Grid #	Spacing	Cell Count	Refinement Ratio (r_*)
1.	20 m	214.1 Million	1.164
2.	30 m	135.9 Million	1.125
3.	40 m	95.5 Million	1.032
4.	50 m	86.8 Million	N/A

Note from Table 5.4 that further refinement after the 20m grid density was not possible due to computational limitations. If mesh independence had not been reached by this point, it would not be possible to simulate the full domain to the desired extent.

When assessing the cell counts and refinement ratios seen in Table 5.4, a basic mesh setup was used: only the cells in the circular near-field region (Fig 5.12 a) were refined while the outer domain with its associated grid spacing were held constant. It was not computationally viable to assess grid independence over the entire domain so focus was maintained on the areas of importance. In this case, the dimensions L_{up}, L_{down} and W were kept to a minimum. A more detailed analysis on the effects of moving the domain boundaries, and their impacts on the final solution, is left to Section 5.5.4. For this grid independence study, the domain dimensions were fixed as follows:

- $L_{up} = 35km \approx 1.75L_{MI}$
- $L_{down} = 50km \approx 2.5L_{MI}$
- $H = 6km \approx 5H_{MI}$

© University of Pretoria

- $W = 70km \approx 3.5L_{MI}$

As a quality assurance, the total wind-tunnel blockage ratio was calculated for the numerical wind domain. The blockage effect is less important in a numerical domain than for a physical wind tunnel, where a blockage of more than ~5% could lead to artificial flow acceleration with a decrease in cross-sectional flow area and thus cause unpredictable measurements. Nevertheless, the blockage ratio for this domain was calculated as a measure to minimise possible numerical error. The blockage ratio is calculated as:

$$\begin{aligned} B &= \frac{\text{(Frontal projected area of the subject)}}{\text{(Cross-sectional area of inlet face)}} \\ B &= \frac{L_{MI} \times H_{MI}}{W \times H} = \frac{20km \times 1.2km}{70km \times 6km} = 0.0571 \\ B &\approx 5.7\% \end{aligned} \tag{5.3}$$

Due to overestimating the frontal projected area of the islands slightly, the actual blockage ratio is expected to be below the calculated 5.7% and nearer to the 5% recommendation; therefore sufficient for performing CFD simulations.

Since the choice of performance metrics is arbitrary in the GCI method, the following data were extracted from the successive CFD simulations in order to evaluate the performance of a solution:

- The u velocity component and TKE at the MI Base station @ 10m height AGL.
- The u velocity component and TKE at the MI Base station @ 100m height AGL.
- The integrated wall-shear value over the entire MI land surface.

The intuition behind choosing these performance parameters rather than others was simple: two stationary points were chosen, one close to ground level and one further away, to confirm that the simulations were converging towards a distinct solution in the different flow regions. The integrated wall shear value was chosen since it is directly linked to the horizontal cell sizing and can thus show whether the changes in resolution have an impact on the overall solution, even though it has no particular physical meaning. Table 5.5 presents the performance metrics data extracted from preliminary CFD simulations. Note that these data are not considered working CFD results yet, as they have been used explicitly to evaluate the effectiveness of the chosen grid spacing scenarios. A detailed exploration of the CFD result set is left to Chapter 6.

© University of Pretoria

Table 5.5: Extracted performance parameters for a GCI analysis using four different grids

Grid	Cell Count	h = 10m		h = 100 m		Wall-Shear
	[Millions]	u [m/s]	k [m^2/s^2]	u [m/s]	k [m^2/s^2]	[MPa]
Very Coarse (4)	86.82	18.79	19.49	22.23	48.78	149.5
Coarse (3)	95.54	18.55	19.90	21.61	46.35	128.4
Medium (2)	135.9	18.13	20.85	20.91	40.67	117.6
Fine (1)	214.1	17.35	20.38	20.55	40.25	115.3

Given the order of convergence:

$$p = \ln\left(\frac{f_3 - f_2}{f_2 - f_1}\right) / \ln(r^*) \tag{5.4}$$

Richard extrapolation (RE) was performed to estimate the asymptotic limit of each performance parameter at zero-grid spacing according to:

$$f_0 = \frac{r^p f_1 - f_2}{r^p - 1} \tag{5.5}$$

The grid convergence statistics and the related best estimates for a zero-grid spacing are shown in Figure 5.16. A steady trend is seen in all the chosen performance parameters. In particular, it was noted that the medium mesh (30m ground resolution) offers comparable results to the finest mesh-sizing and estimated zero-grid solutions, presenting an opportunity to use the less computationally expensive mesh given that it passes the GCI criteria.

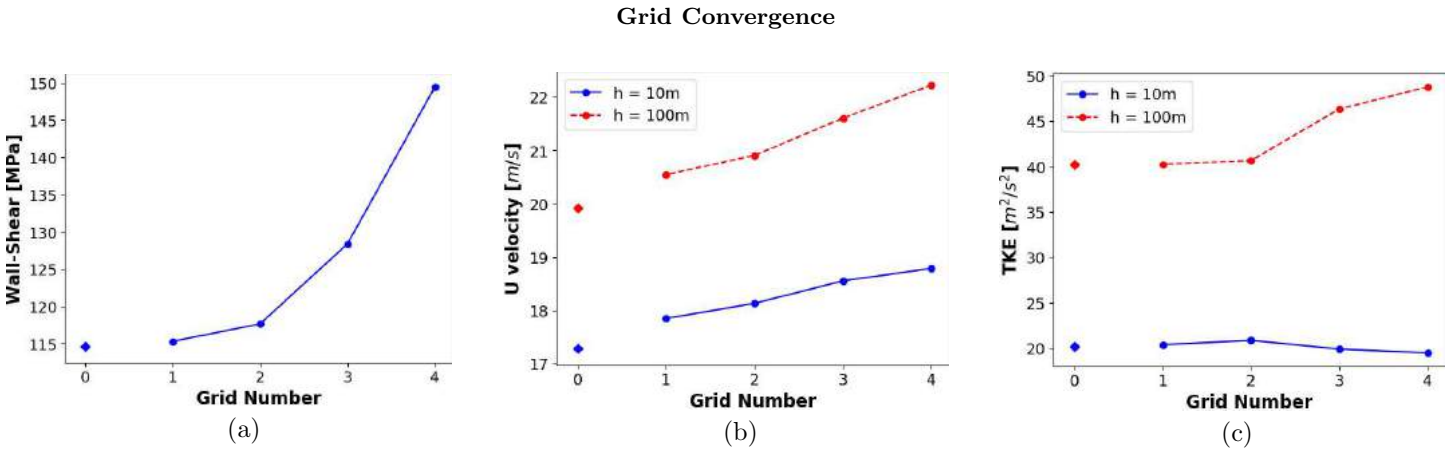

(a) (b) (c)

Figure 5.16: Convergence of integrated wall-shear stress (a), velocity (b), and turbulence (c) versus grid spacing. The single diamond markers represent the best estimate for the parameter at zero-grid spacing using Richardson extrapolation (f_0)

© University of Pretoria

Table 5.6 compares the medium and fine meshes against one another. The percentage error between the extracted performance parameters and the RE best estimate was computed using Equation 5.6:

$$\epsilon = \frac{|\phi_i - \phi_{RE}|}{\phi_{RE}} \times 100 \tag{5.6}$$

where ϕ denotes any of the performance parameters, subscript i denotes the grid number and subscript RE refers to the asymptotic Richardson extrapolated value.

These errors show that the medium grid always ranges within $\sim 5\%$ of the asymptotic value while the fine grid keeps within $\sim 3\%$; not a large increase in performance despite the significant difference in required computational resources. Next, the GCI method was completed in full for both the medium and fine grids using the procedure outlined in Appendix H considering only three successive solutions at a time (i.e. Grids 4-3-2 and grids 3-2-1). The final GCI scores in Table 5.6 are all sufficiently close to the required value of $GCI = 1$, implying that both grids are in the asymptotic range and are therefore equally capable of achieving accurate results.

Table 5.6: Comparison between the medium- and fine-mesh

Parameter	**Error [%]**		**GCI score**	
	Grid 1	**Grid 2**	**Grid 1**	**Grid 2**
Wall-Shear	0.571	2.617	0.980	0.916
u @ 10m	3.285	4.917	0.984	0.977
k @ 10m	2.338	4.702	0.977	1.048
u @ 100m	1.897	3.685	0.983	0.968
k @ 100m	0.087	1.151	0.989	0.877

Following this argument, the final decision was made to use a horizontal grid-sizing of 30m along the land surfaces in any simulations to follow. However, note that this outcome was anticipated to be heavily dependent on the spatial scale of the domain. The current grid cannot be expected to capture eddies smaller than ~ 30 metres in size, unless they are roughly accounted for in a time-averaged sense. If one should "zoom in" and simulate smaller regions with ever-finer grids, the fractal-like qualities of turbulence scales and rough terrain will surely result in different solutions; all still equally correct, just fluctuating as they capture smaller features within the flow. This inherently chaotic nature of the task at hand is the reason why multiple simulations need to be performed at successively finer spatial scales.

© University of Pretoria

5.5.4 Domain Extents

To determine a reasonable placement for the domain boundaries, a domain extent study was performed to see what configuration would be best for simulating the atmosphere without artificially affecting the flow around MI.

The inlet boundary is subject to one constraint: it should not be placed further than 50km away from the front edge of MI. Reasons for this are explained in Section 3.2.3. Similar restrictions do not apply to the other boundaries.

In this domain extent study, each of the dimensions for height, width, upstream-, and downstream-lengths were designated three testing values according to a "Low", "Neutral" and "High" length as shown in Table 5.7. When a low or high value for any dimension was being tested, all others were defaulted back to their neutral values.

Table 5.7: Sets of domain dimensional lengths used in the domain-extent study

Dimension	**Low**	**Neutral**	**High**
L_{up}	35 km	40 km	50 km
L_{down}	35 km	50 km	70 km
W	62 km	70 km	80 km
H	4 km	6 km	8 km

The testing dimensions above translate to nine possible combinations in total; an exploratory CFD simulation was performed for each. Three monitor locations were chosen along the length of the island to study the effects of a boundary surface placement on the general solution, namely: Swartkops station, Katedraal station and the MI base station. The u velocity component and TKE were extracted for each station at two heights, 10 metres and 100 metres, along the vertical wind profile. These monitor points and quantities all come to a total of 12 variables extracted per simulation. Figures 5.17 - 5.20 compare the monitored variables after changing each boundary surface to the low-, neutral- and high-length settings.

Figure 5.17 plots all variables as a function of the upstream boundary placement. The inlet boundary profiles are known to degrade slightly over large fetch distances, which is seen in the plot. A large sensitivity is noted in the results when manipulating the position of the inlet face nearer to or further from MI; largely thought to be attributed to the profile degradation. Considering all the information in Figure 5.17, the decision was made to keep the position of the inlet face fixed at L_{up} = 35km upstream of the islands to minimise profile degradation. Note, this value is approximate and is subject to change slightly when the incoming wind direction is rotated about the islands.

© University of Pretoria

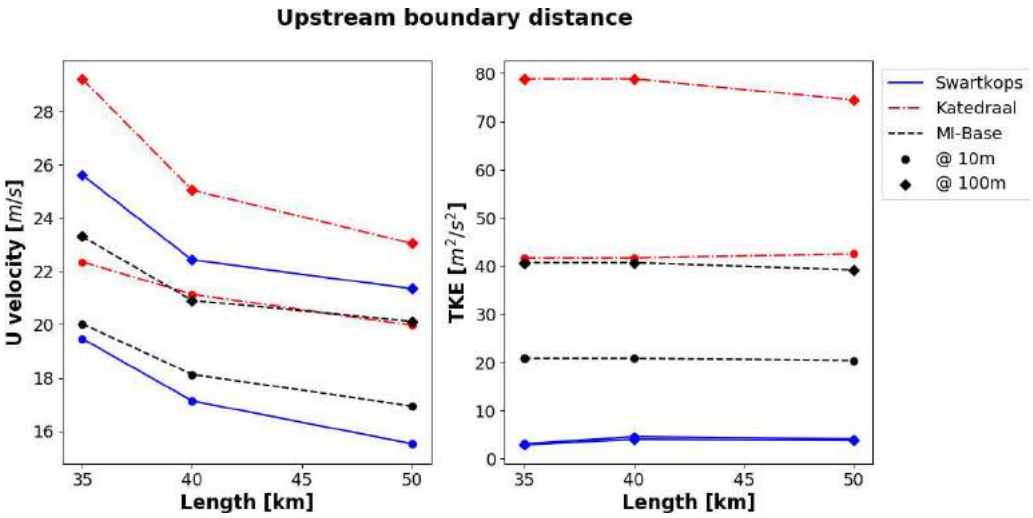

Figure 5.17: Comparison of monitoring points along the length of MI. u velocity (left) and TKE (right) values were extracted from exploratory CFD simulations where the upstream placement of inlet boundary was changed but all else kept constant

The downstream length and domain-width, plotted in Figures 5.18 and 5.19, respectively, displayed no clear trend in sensitivity to their corresponding boundary placements. All variables plotted in the images were relatively flat and unchanged no matter how far the boundaries were placed, implying independence. For this reason the minimum values were chosen such that the overall size of the domain was safely reduced, thus lifting some of the computational burden. The downstream distance of the outlet face and the width of the domain are therefore fixed at $L_{down} = 35$ km and $W = 62$ km, respectively.

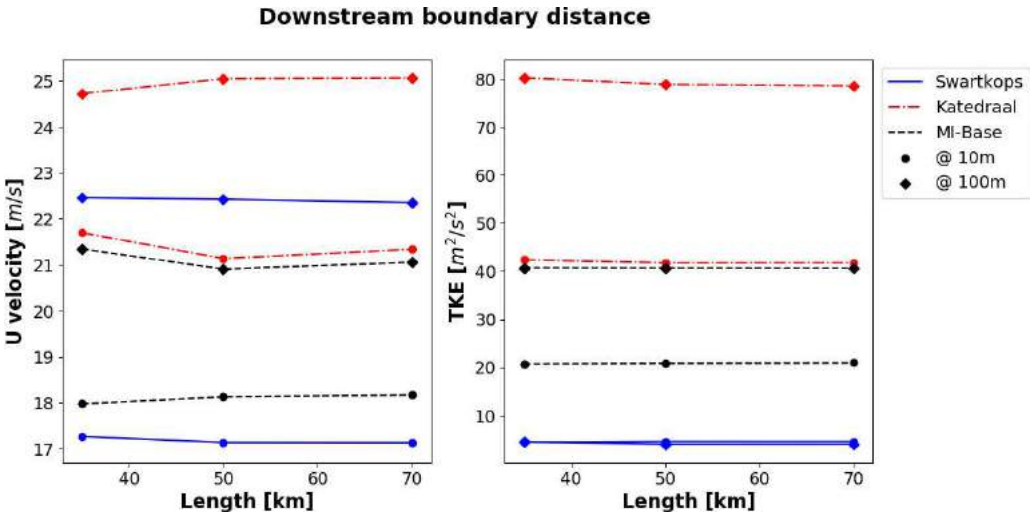

Figure 5.18: Comparison of monitoring points along the length of MI. u velocity (left) and TKE (right) values were extracted from exploratory CFD simulations where the downstream placement of outlet boundary was changed but all else kept constant

© University of Pretoria

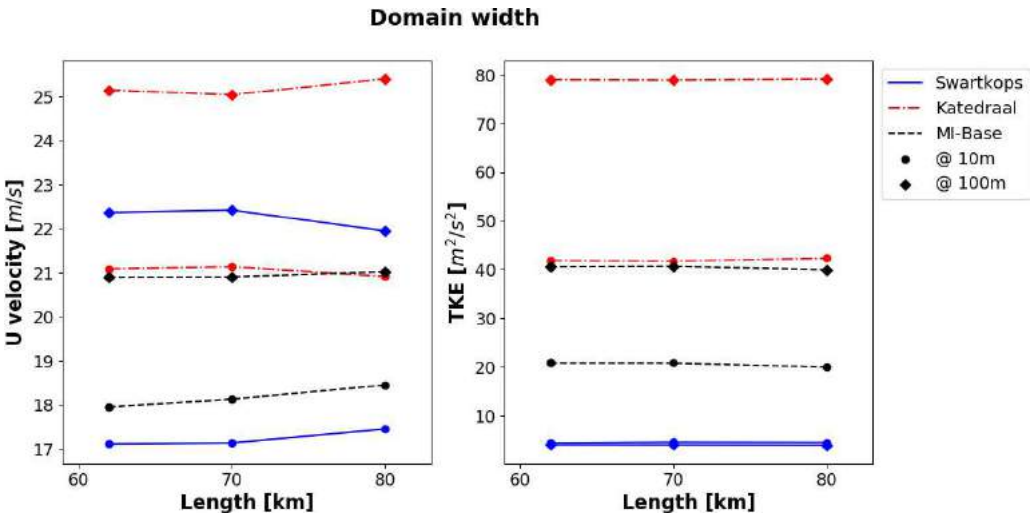

Figure 5.19: Comparison of monitoring points along the length of MI. u velocity (left) and TKE (right) values were extracted from exploratory CFD simulations where the width of the simulation domain was changed but all else kept constant

A sensitivity to the domain height placement, plotted in Figure 5.20, was noted. Reducing the domain height to a value of 4km led to overall increased wind-speeds in the domain, attributed to the likely artificial speed-up caused by reducing the cross-sectional flow area of the domain to a point where the blockage-ratio violates the suggested threshold of $\sim 5\%$. However, increasing the domain height to a ceiling of 8km high resulted in almost no change in velocity or turbulence when compared to a 6km domain height. Therefore, the height has been fixed at $H = 6$km for future simulation attempts.

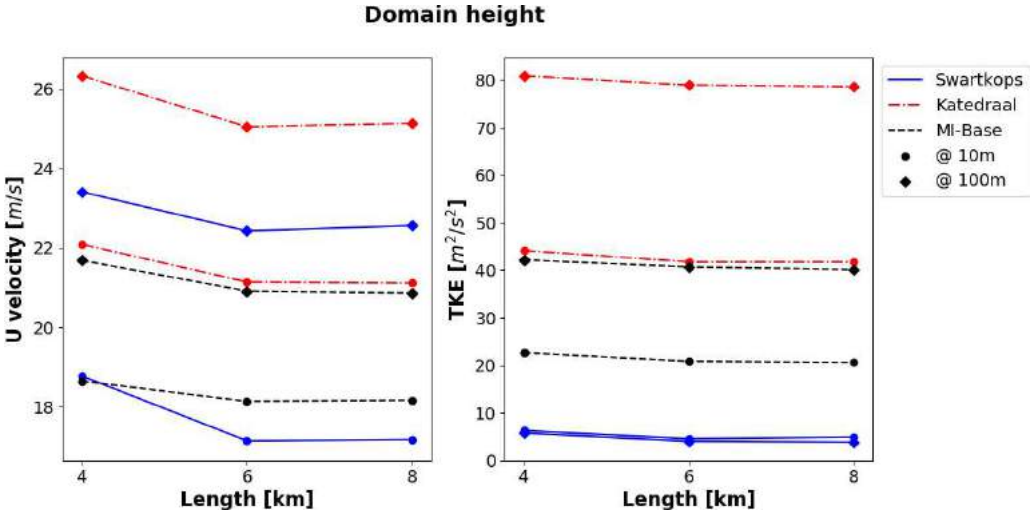

Figure 5.20: Comparison of monitoring points along the length of MI. u velocity (left) and TKE (right) values were extracted from exploratory CFD simulations where the height of the simulation domain was changed but all else kept constant

© University of Pretoria

5.6 Setup

Table 5.8 accumulates the details of the MI simulation setup into an easy-to-read format after the discussion so far. The details represented here should be taken as the standard configuration; if any changes were made, they have been explicitly stated. The screenshots in Appendix G show how these settings were achieved in practice when using the ANSYS Fluent Solver software.

Table 5.8: Setup parameters for Marion Island simulations

Domain Size	70 km x 62 km x 6 km (L x B x H)
Mesh	
Cell Type:	Polyhedral
Horizontal Sizing:	30m at ground level
	100m on sea-surface in the near-field region
	150m on sea-surface in the approaching-wind region
	500m on sea-surface in the wake region
	1000m at top boundary
Vertical Sizing:	0.2m first cell height
	1.3 growth rate throughout domain
Cell count:	$\sim$ 140 Million
Inlet Boundary Profiles	
velocity	Eq. 2.31 with $u_* = 0.15ms^{-1}$ and $z_0 = 0.0003m$
TKE (k)	Eq. 2.34
TDR (ε)	Eq. 2.33
Other Boundary Conditions	
Outlet:	Outflow
Top:	Moving Wall (same as inlet velocity)
Sides:	Symmetry Boundary
Bottom:	Wall Boundary
Model Settings	
Solver:	RANS
Gravity:	-9.81 m/s^2 (in the z- direction)
Coriolis Parameter f_c	-1.06E-04
Coriolis Force:	Yes
Turbulence model:	Standard k-ε turbulence scheme with modified constants.
Sea wall roughness:	$z_0 = 0.0003$m (calm sea)
Land wall roughness:	$z_0 = 0.015$m (pasture)
Wall Functions:	Scalable with modified sand grain roughness

© University of Pretoria

5.7 Summary

The focus of this Chapter was to pose the simulation problem and suggest a strategy and setup for completing the proposed task within time and computational constraints.

This project is aimed at producing useable simulation data across a vast domain, including and surrounding Marion Island, while being bound by some particularly strict computational constraints. The computational resource of any single simulation is limited to 240 cores and 1.2 TB of memory; imposed by the number of available ANSYS licenses at the CHPC. The final size of the solution files has been limited to 125 GB in order to facilitate interrogation, post-processing and visualisation of the data on a locally hosted machine at the University of Pretoria.

The topography of Marion and Prince Edward Islands has been given in a GeoTIFF format; a common file-type used in the geographical sciences to describe raster data but otherwise unrecognisable to ANSYS Fluent as a geometry descriptor. A gradient-based resampling algorithm was used to reduce the number of points stored in the GeoTIFF files before converting to compatible STL geometry files. The resampling effectively maintained the overall shape of the islands while using only a fraction of the number of points.

A strategy has been devised for generating a reusable mesh system which can be generated only once yet used to simulate multiple climatic conditions and wind directions around MI. The strategy calls for large-scale simulations to be performed; sections of the resulting solution can then be recast as input boundary conditions for sub-scale simulations at ever increasing mesh resolutions.

A group of default CFD simulation settings was discussed for MI simulations going forward. A uniform surface roughness value of $z_0 = 0.015m$ has been assigned to the MI landscape according to guidelines obtained from the literature. Input boundary profiles have been limited to the neutrally stable log-law equations given in Section 2.7.1 and rearranged to rely on a single user-defined friction velocity, u_*. The surrounding sea roughness value has similarly been set to rely on the input friction velocity. Coriolis forcing has been applied throughout the domain as a momentum source term. Buoyancy interactions and the general energy equation have been turned off by default since there is no evidence to show that these added complexities would perceivably benefit the solution. Internal solver convergence limiters have been tweaked where necessary to improve convergence stability, but at the cost of increasing solution times.

A complete description of the mesh generation procedure was given, including a grid independence study following the GCI guidelines and a domain extent study. A final mesh was settled upon for simulating the wind patterns on MI and greater surrounding regions.

© University of Pretoria

6 Results

6.1 Introduction

. The CFD simulation of the wind patterns across MI at the sub-mesoscale are presented in this chapter. The term "large-scale model" in this sense refers to modelling MI including much of its environmental surroundings. The neighbouring Prince Edward Island and hundreds of square kilometres of nearby ocean are included in the large-scale domain to ensure that any applied boundary conditions will not excessively influence the local flow patterns. The focus then shifts to a "island-scale model", a bounding-box model containing only MI and some of its immediate surrounding ocean. The boundary inlet conditions for the island-scale model have been extracted directly from the large-scale model simulations in an attempt to gain finer solution accuracy without resorting to fully embedding the island-scale mesh inside the large-scale domain. Focus was held on the primary wind directions (West, North-West and South-West) for the duration of the initial solution interrogation and validation procedures in this chapter. The post-processing section (6.11) has been set aside for further analysis of the other wind directions and possible data extrapolations.

A wide array of computed CFD data were retrieved from the large-scale simulation models and have been presented first. The solution data for the primary wind directions are then interrogated, initially from a broad perspective and then successively zoomed in to extract finer detailed information.

6.2 Turbulent Wake Streams

Looking at the turbulent wake interactions shown in Figures 6.1 - 6.2, some basic insights are gained regarding the overall performance of the Fluent solver and CFD model.

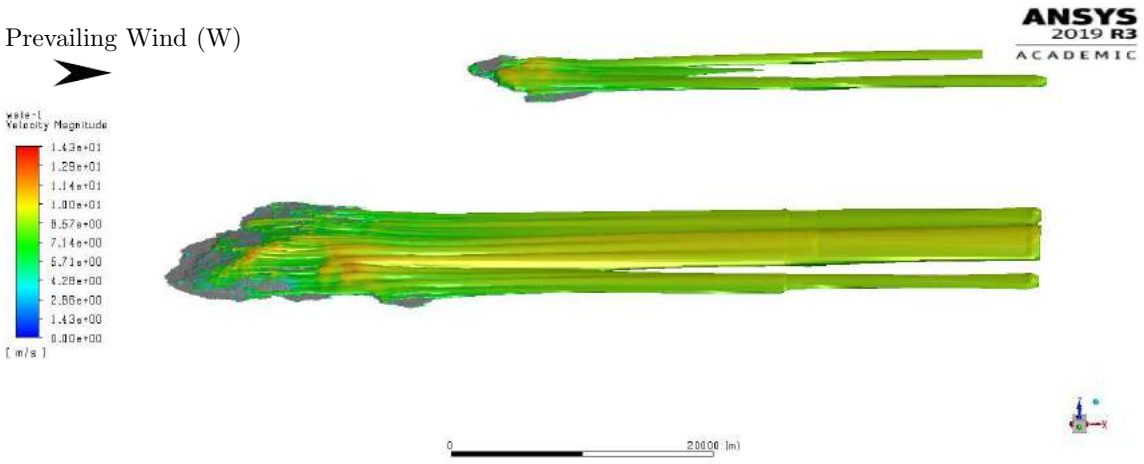

Figure 6.1: Turbulent wake iso-surfaces across MI and PEI for a Westerly prevailing wind. The iso-surface was calculated for an arbitrary TKE=1 m^2/s^2 throughout the domain and coloured by velocity magnitude. The wake is seen to terminate prematurely at the outlet boundary; bearing no significant influence on the immediate MI wind patterns. This same effect was noted when simulating all other wind-directions

© University of Pretoria

As stated in Section 5.5.4, the extent of the modelled domain would not be long enough to accommodate the full length of the wake behind MI. The premature termination of the wake at the outlet boundary is seen in Figure 6.1. Although it contradicts standard CFD practical guidelines, this shorter domain was found to have no significant impact on the solution immediately surrounding MI.

Similarly generated iso-surfaces for the South-Westerly prevailing wind case (Figure 6.2) indicate that the turbulent eddies emanating from MI upstream will interact with the neighbouring PEI since the islands are located close enough to one another. While this effect is not necessarily important for the South-Westerly wind case, it is surely going to play a large role when modelling winds approaching from other directions, e.g., North-Easterly.

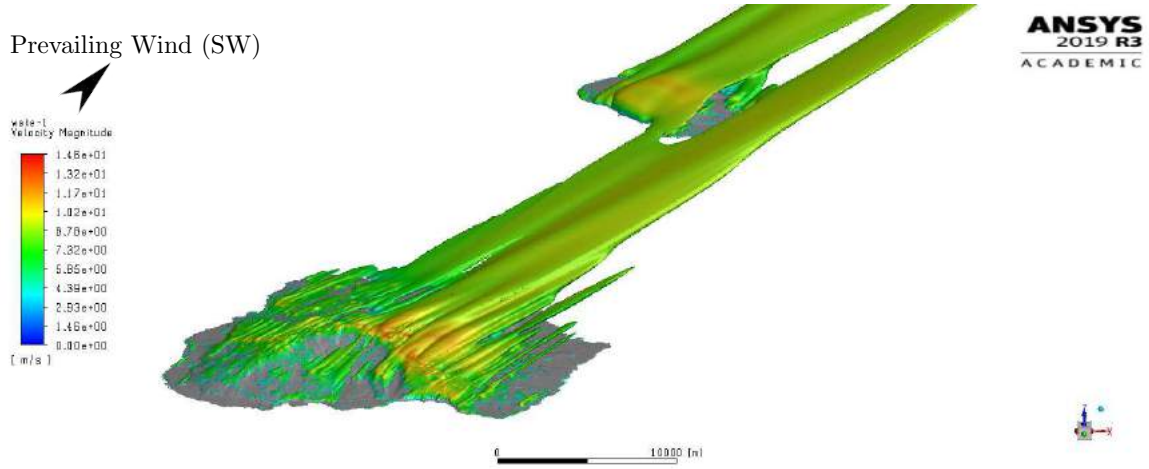

Figure 6.2: Turbulent wake iso-surfaces across MI and PEI for a South-Westerly prevailing wind. The iso-surface was calculated for an arbitrary TKE=1 m^2/s^2 throughout the domain and coloured by velocity magnitude. The wake from MI is seen to reach and interact with that of PEI, confirming the notion that both islands have to be modelled in order to capture significant incompressible fluid phenomena

The turbulent iso-surfaces in the images above also highlight the steady-state nature of the RANS solution. These smooth looking "bubbles" of turbulence would be seen as vortical structures or eddies in reality, were it not for the time-averaging. It was, however, not practical to simulate the entire domain at this scale with transient methods such as LES.

6.3 Surface Velocity and Wall Shear

Since the boundary node velocity on the MI surface is zero by definition, Figures 6.3 - 6.4 plot the surface wall-shear stress as a means of identifying regions of high or low velocity magnitude along the surface subjected to the primary dominating wind directions. Higher shear stress, and thus higher velocity magnitudes, are present near the peaks of topographical features as would be expected by reasoning that incompressible airflow would have to speed up to travel around such obstructions. An opposing trend is also noted for regions of low wind velocity over flatter portions of land and especially in the wakes behind topographical features.

© University of Pretoria

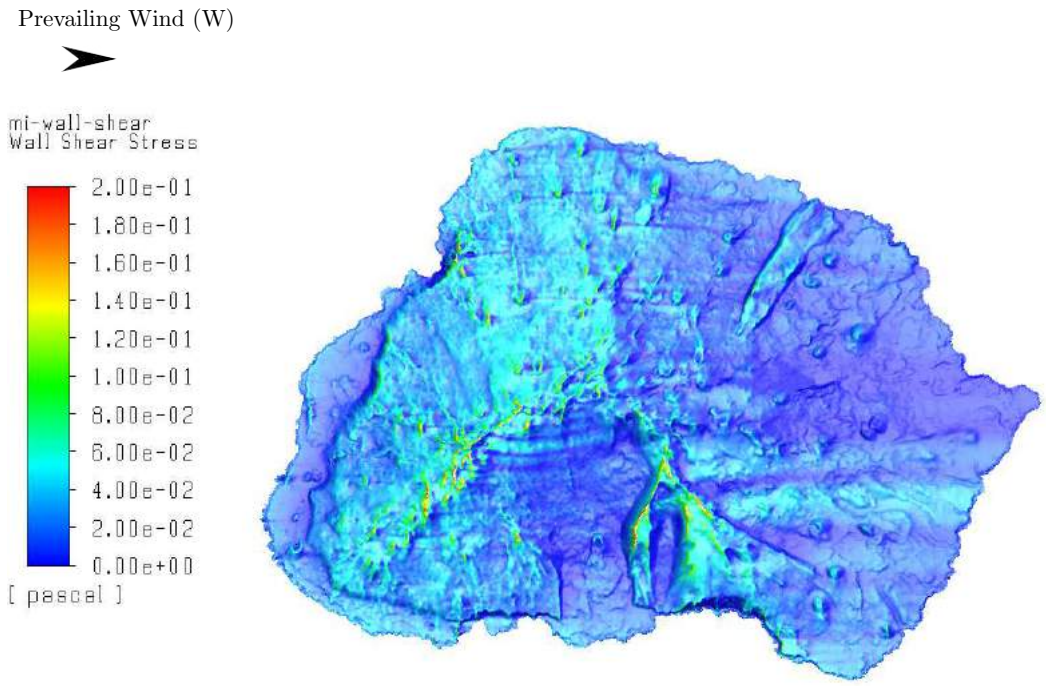

Figure 6.3: Wall-shear stress contours across MI for a Westerly prevailing wind. Wall-shear stress is plotted as it is directly proportional to the surface wind velocity magnitude. Values have been clipped to 0.2 Pa to enhance colouring of the contours although a true peak stress of 0.278 Pa was present. Here, regions of high or low surface-wind speed are easily identified

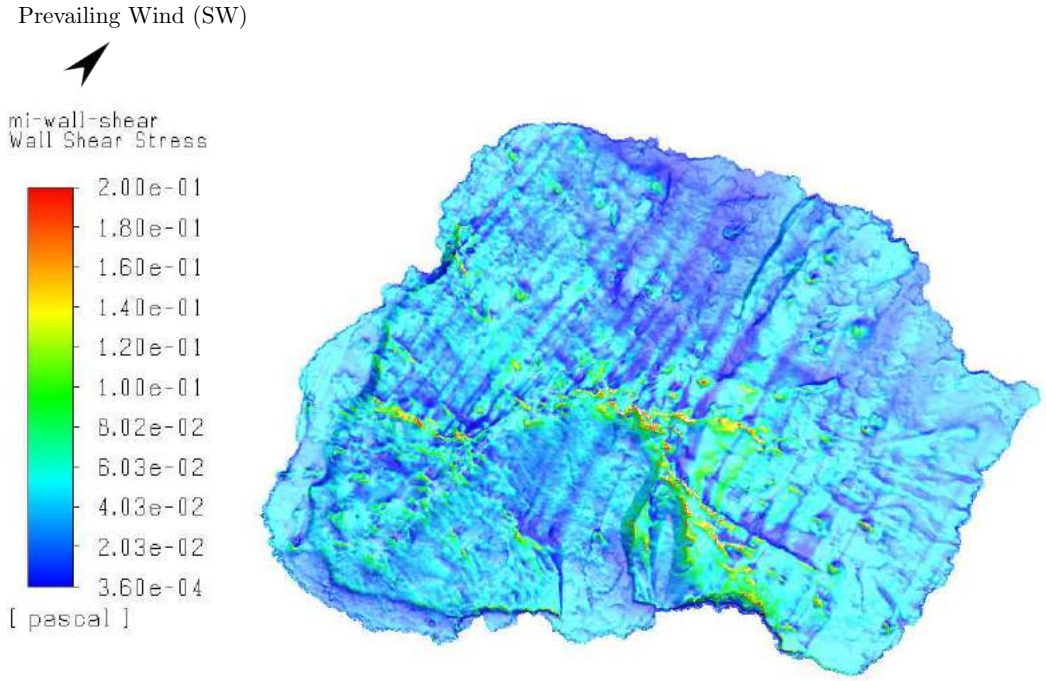

Figure 6.4: Wall-shear stress contours across MI for a South-Westerly prevailing wind. Wall-shear stress is plotted as it is directly proportional to the surface wind velocity magnitude. Values have been clipped to 0.2 Pa to enhance colouring of the contours although a true peak stress of 0.383 Pa was present. Here, regions of high or low surface-wind speed are easily identified

© University of Pretoria

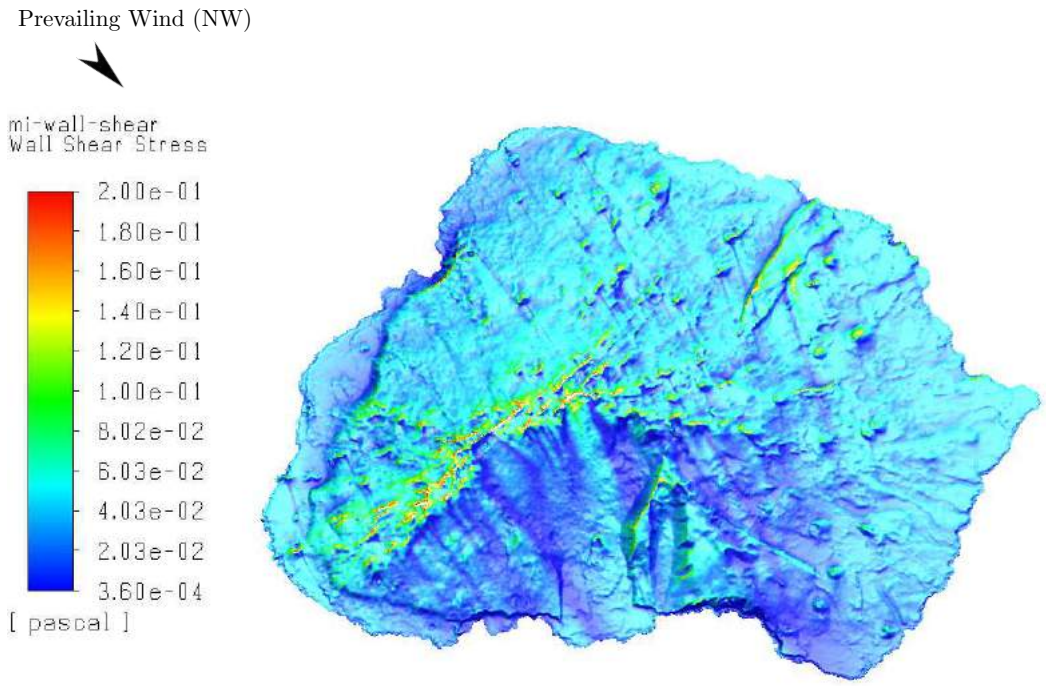

Figure 6.5: Wall-shear stress contours across MI for a North-Westerly prevailing wind. Wall-shear stress is plotted as it is directly proportional to the surface wind velocity magnitude. Values have been clipped to 0.2 Pa to enhance colouring of the contours although a true peak stress of 0.398 Pa was present. Here, regions of high or low surface-wind speed are easily identified

An important note here is that these images tend to show prevailing wind movement over the island when looking at wake patterns etc., but fine-scale wind direction vectors at the ground level are not immediately ascertainable from the wall-shear plots although they are available in the solution data.

6.4 Local Friction Velocity

In order to meaningfully compare the CFD results to the obtained experimental data, extensive efforts were made to scale the sets of data into a universal form. The local friction velocity is extracted from the CFD data by converting the local wall-shear stress according to Equation 6.1:

$$u_* = \sqrt{\frac{\tau_w}{\rho}} \tag{6.1}$$

The contour plots for local surface friction velocity are given in Appendix I, Figures I.1 - I.3, although they are not too different from the original wall-shear plots posted in Figures 6.3 - 6.5 since they have been calculated directly using those reported wall-shear values. Figure 6.6 presents the comparison between the experimentally determined local friction velocity values at the 17 measurement stations and those extracted from the CFD simulations at the corresponding locations; simply an amended version of Figure 5.9.

© University of Pretoria

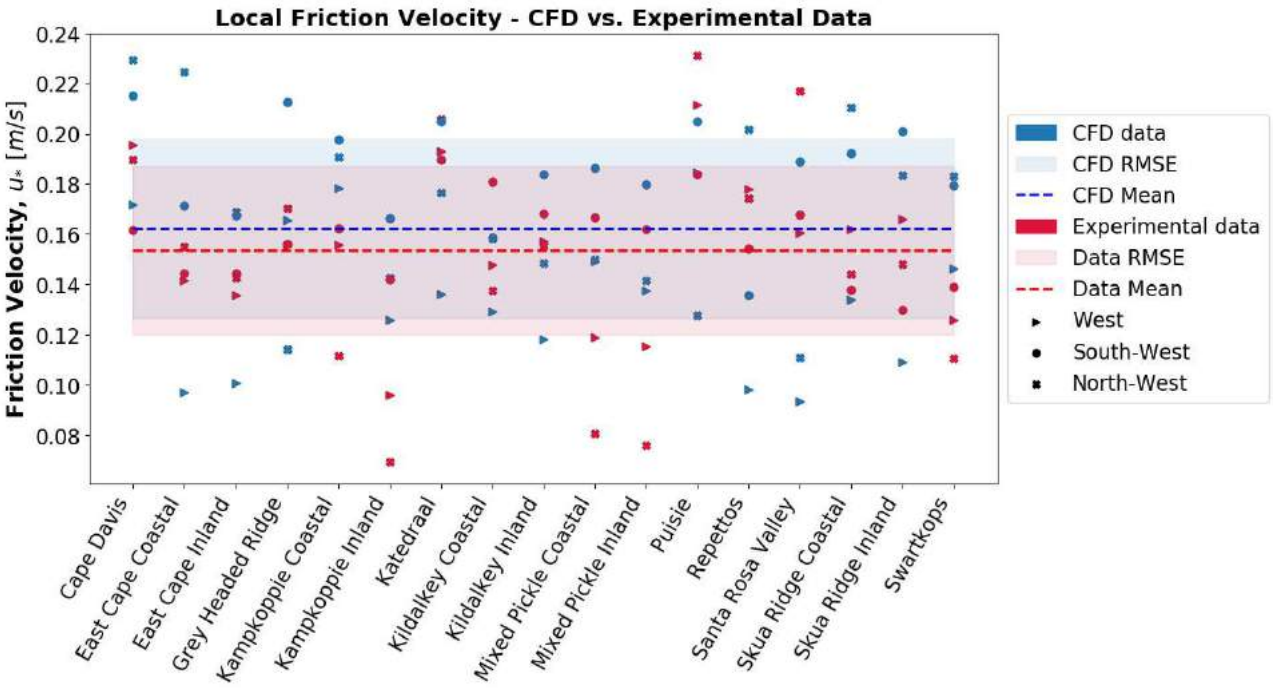

Figure 6.6: A scatter plot comparing the experimentally determined vs the simulated local friction velocity values for all three primary wind directions at the 17 stations. CFD Mean = 0.162 m/s, Experimental Mean = 0.153 m/s. CFD RMSE = 0.036 m/s, Experimental RMSE = 0.033 m/s

The minor discrepancy between the mean CFD and experimental results in the scatter plot of Figure 6.6 can be attributed to modelling the incoming wind at the inlet boundary with a characteristic friction velocity of $u_* = 0.15$ m/s *at sea level*. This does not account for the natural increase in wind speed as the air passes over the landscape at a higher altitude, resulting in the larger local average friction velocity seen in the CFD simulations.

6.5 Wind Vector Comparisons

The images in Figures 6.7 - 6.9 compare side by side the CFD simulated wind vectors vs. the experimental mean wind speed and direction as extracted from the MIRED-DB for each validation wind case. Note that the plotted CFD and experimental vector arrows only take the u- and v- wind velocity components into account. The w-velocity has been excluded since the 2D anemometer stations were not capable of measuring a vertical wind component.

While a more detailed analysis of the differences between the simulations and reality is left for discussion in further sections, it is possible to glean some broad conclusions from the birds-eye view of the information presented in Figures 6.7 - 6.9 before continuing:

- The westerly and south-westerly simulations compare favourably with realistic measurement data, while the north-westerly case appears to have deviated too much from reality.

© University of Pretoria

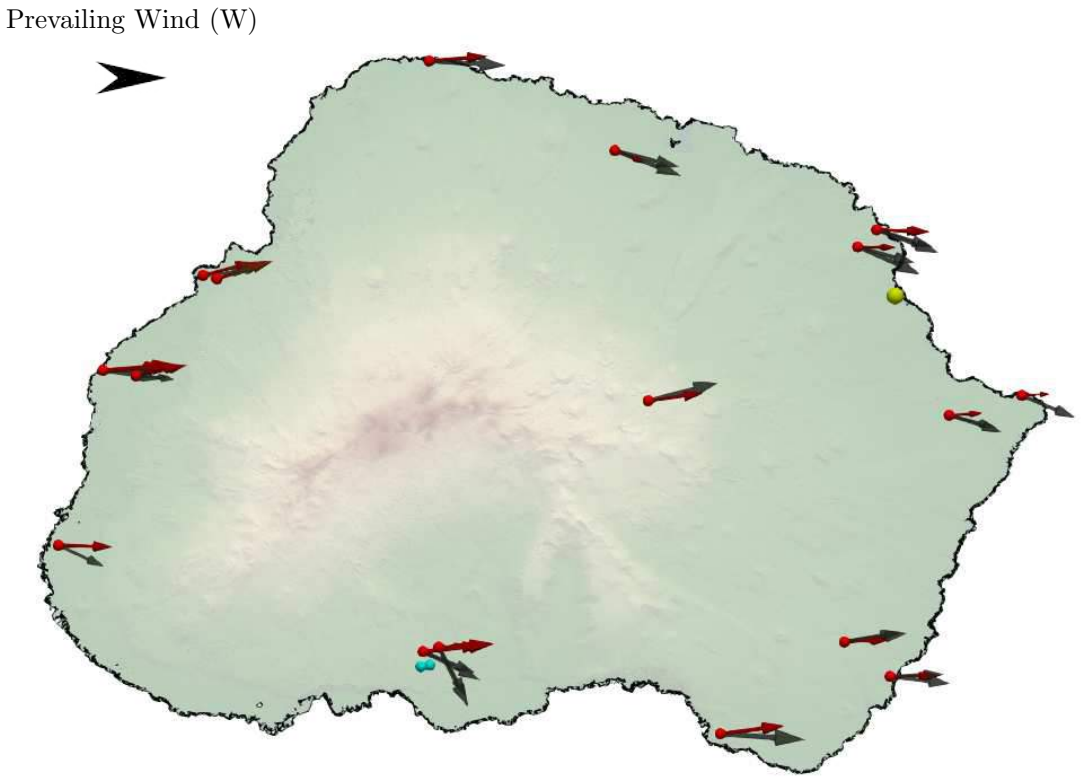

Figure 6.7: Simulated (red) vs. experimental (black) mean wind vectors across MI subject to a Westerly prevailing wind

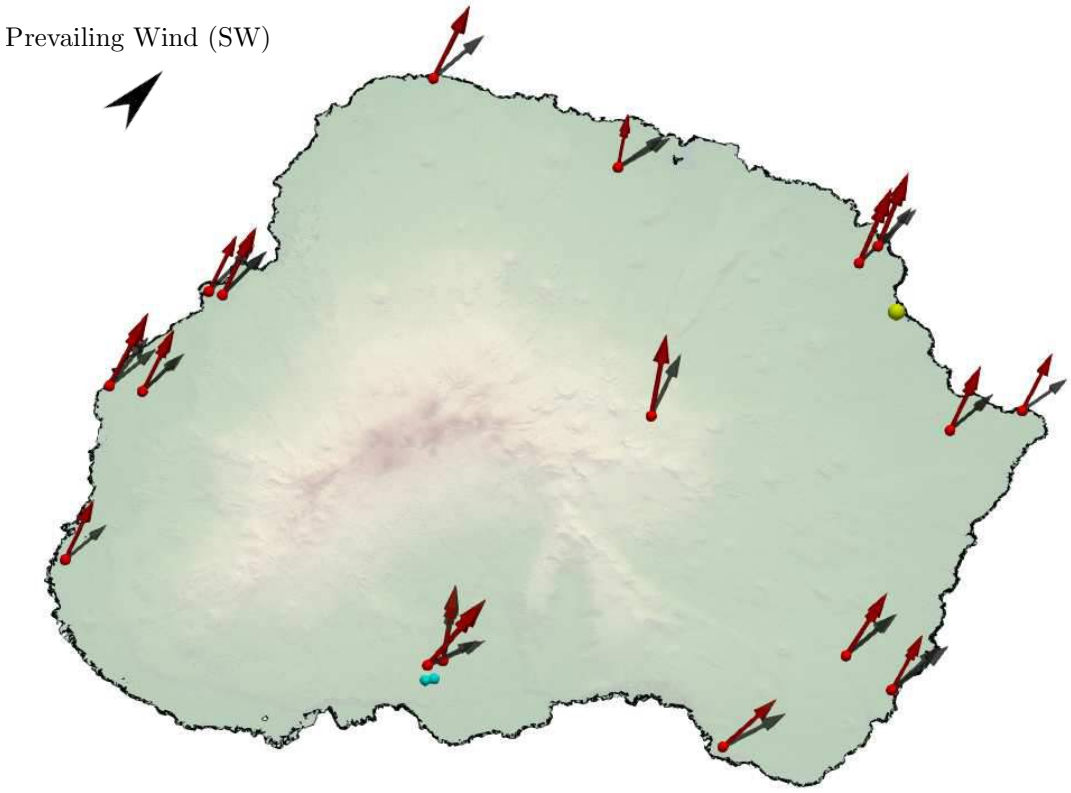

Figure 6.8: Simulated (red) vs. experimental (black) mean wind vectors across MI subject to a South-Westerly prevailing wind

© University of Pretoria

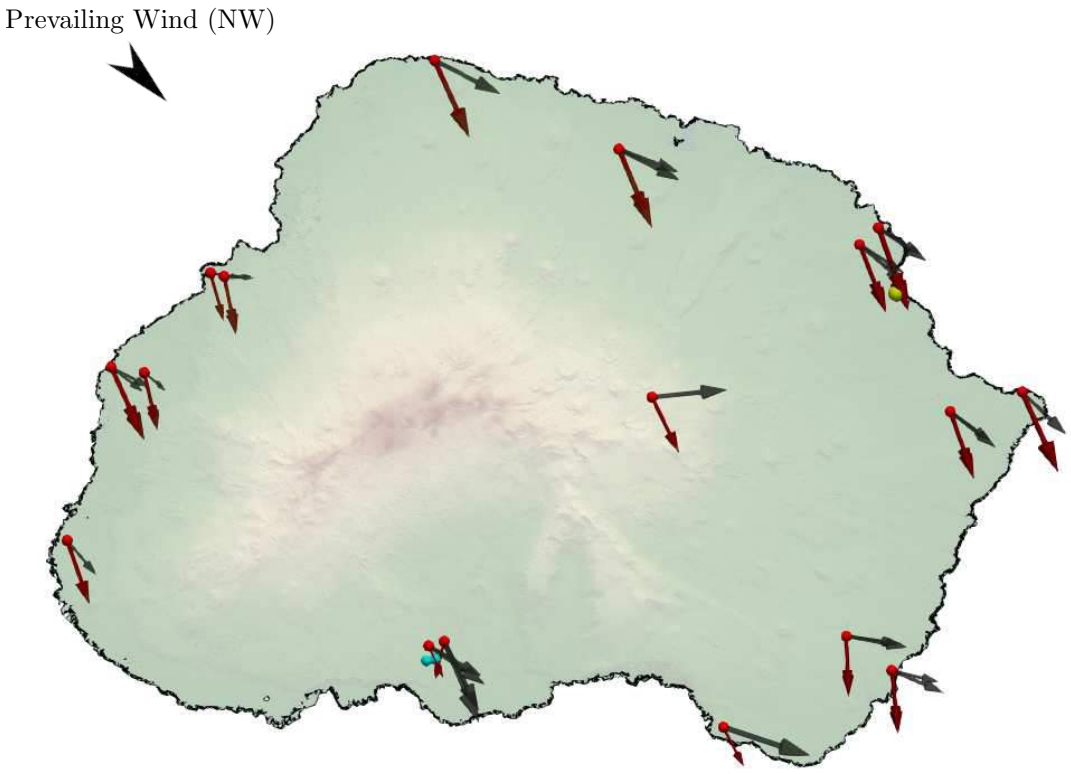

Figure 6.9: Simulated (red) vs. experimental (black) mean wind vectors across MI subject to a North-Westerly prevailing wind

- Experimental standard deviation/uncertainty has not been accounted for in these images; a factor which significantly impacts the CFD validation procedure. While the discrepancy between experimental and simulated results appears exaggerated on these maps, the reality may be much more accurate.

- The southern quadrant of MI (Grey-Headed Ridge and surrounds) is a source of particularly large disagreement across most of the simulated wind directions. This was to be expected due to the steep geographical features in the area being the cause of high turbulence.

- An arguable, although completely uncontrollable, source for error is simply the chaotic behaviour of the natural atmosphere at this large a scale. Where the numerically approximated winds have been specified in a straight, unidirectional pattern from one domain boundary to another, the realistic causes for the flow are actually complicated interactions between large weather pressure cells acting as sources and sinks for atmospheric energy. These interactions are definitely non-linear and do not act in a straight line as the simulated model has been constrained to do. However, the hope remains that these complicated pressure cell interactions would be "averaged out" by recording experimental data over the course of the two-year long wind measurement campaign.

- A plausible cause for the difference between mast and CFD data is the modelled Coriolis force. More specifically: the masts were interrogated to retrieve wind data com-

© University of Pretoria

ing from a given direction at the island surface level (surface winds), while the applied boundary conditions were specified in the same direction but at vastly different altitudes (upper-atmospheric winds). The so-called "Ekman Spiral" effect caused by the Coriolis force would thus cause the modelled airflow to turn slightly between the specified upper-atmospheric boundary and the surface level.

- It is possible that pockets of time-dependent flow develop in areas of high turbulence activity. This directly contradicts the steady-state assumption fundamental to the RANS approach, and could therefore be a source of deviation in the simulations.

- A further possible cause for disagreement is the overall GPS accuracy of the placement of the stations vs. their equivalent placement in the numerical domain. If the GPS tracker used to capture the location of a given station was only accurate to the nearest 5-10 m, there are any number of local geographical features within that area of uncertainty which could greatly impact the wind measurements. A similar argument can be made for pointing all the stations directly due north within the confines of human error and equipment accuracy.

At this stage, various ideas were put forward to attempt to address the flaws discussed above.

In terms of modelling accurate weather activity, such as high- and low-pressure cells in the atmosphere as sources and sinks for energy, there are methods of coupling two-dimensional Numerical Weather Prediction (NWP) models with the standard 3D Navier-Stokes solvers used in this study. Such a coupling, although achievable, would effectively mean modelling weather patterns only present on a designated day or under very specific sets of atmospheric conditions; the idea behind the current study is to model much broader atmospheric activity. Furthermore, the coupling procedure is fraught with complexity which makes fault-finding and debugging a laborious task even beyond what has been encountered here. As such, numerical coupling has been left outside the scope of this study and as a rich topic for future research.

Unfortunately, not much can be done to improve the accuracy of the GPS coordinates and orientation for the wind stations without investing in significantly more expensive equipment and much time. However, the deviation error attributable to poor location accuracy is minor when compared to the other identified sources of error. There is only a real benefit in updating the location/orientation accuracy of the mast stations after the numerical models have been studied, validated and tuned to the point where wind prediction is achieved within considerably fine tolerances. Since this project is only the first of its kind on MI, a somewhat introductory foray into the modelling of wind patterns in the region, such a costly step has been left to future research if the need ever arises.

© University of Pretoria

6.6 The Coriolis Effect in Simulations

In order to confirm the proposal that the Coriolis Effect is indeed the culprit for the large errors seen in Figures 6.8 and 6.9, further simulations were setup to run without the momentum source terms needed to compensate for the Earth's rotational inertia (termed "Non-Coriolis" simulations for the rest of this discussion). Since the non-Coriolis simulations completely neglect a significant portion of the atmospheric fluid momentum in the upper atmosphere, they cannot be interrogated or used in any way to determine realistically feasible results; they have simply been performed for the purpose of comparing their results to those of the fully described simulations.

The effects of "switching off" the Coriolis force can be seen clearly in Figures 6.10 - 6.12 below. The top boundary of the numerical domain is always specified in the same fixed direction pertaining to the chosen wind simulation case. Note the colours and sizes of the wind velocity vectors in all images: top-boundary vectors are naturally larger and coloured more red to denote faster winds in the upper atmosphere, while surface-level winds are slower due to interactions with the bottom wall and are thus represented by smaller blue arrows. Local wind vectors on the island surface itself have been ignored for now, focusing rather on the surrounding environmental wind conditions.

For the westerly wind case presented in Figure 6.10, the Coriolis force directly counter-acts the flow of wind. The overall colour of the arrows in Figure 6.10c. are darker than those in Figure 6.10b., implying that the wind speed has been decreased with the inclusion of Coriolis forcing while the direction remains unchanged. In other words: the air is moving from left to right in the same direction as the rotation of the Earth; thus the flow of air *relative* to the Earth's inertial frame of reference is perceived to be slower than if the Earth weren't rotating at all.

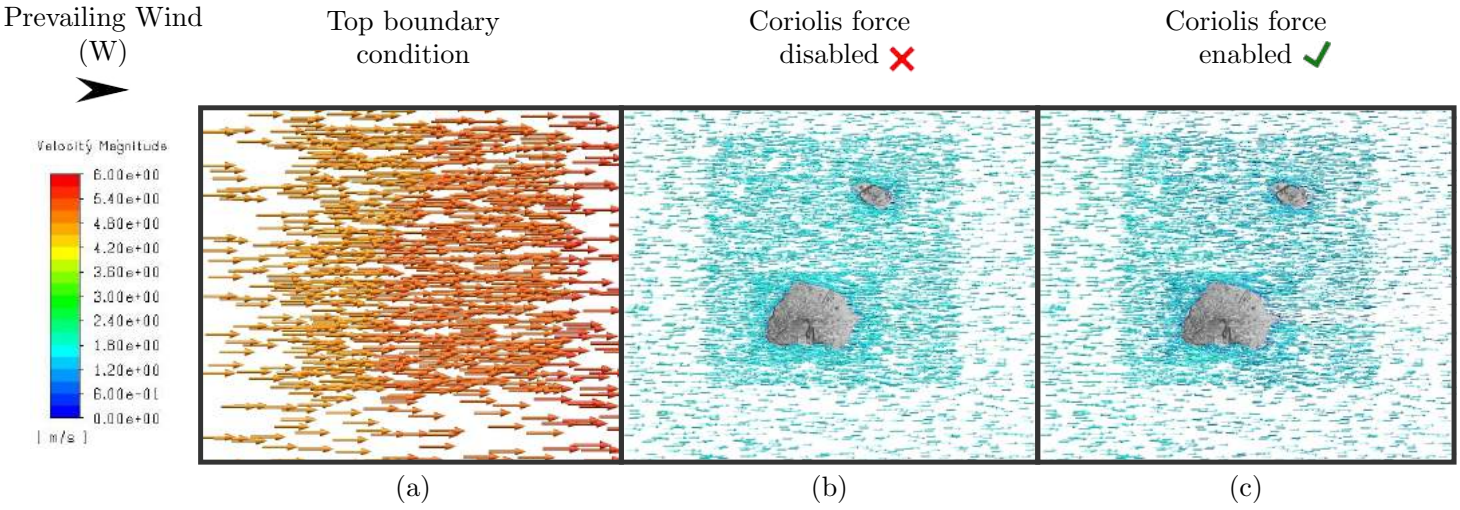

Figure 6.10: Vector plot comparing the effects of running a westerly wind simulation with and without the Coriolis force momentum source terms. The top boundary condition in the upper atmosphere (a) is consistent across both cases; the surface-level vectors around MI change due to the influence of the Coriolis force. The velocity scale has been kept constant throughout the images

© University of Pretoria

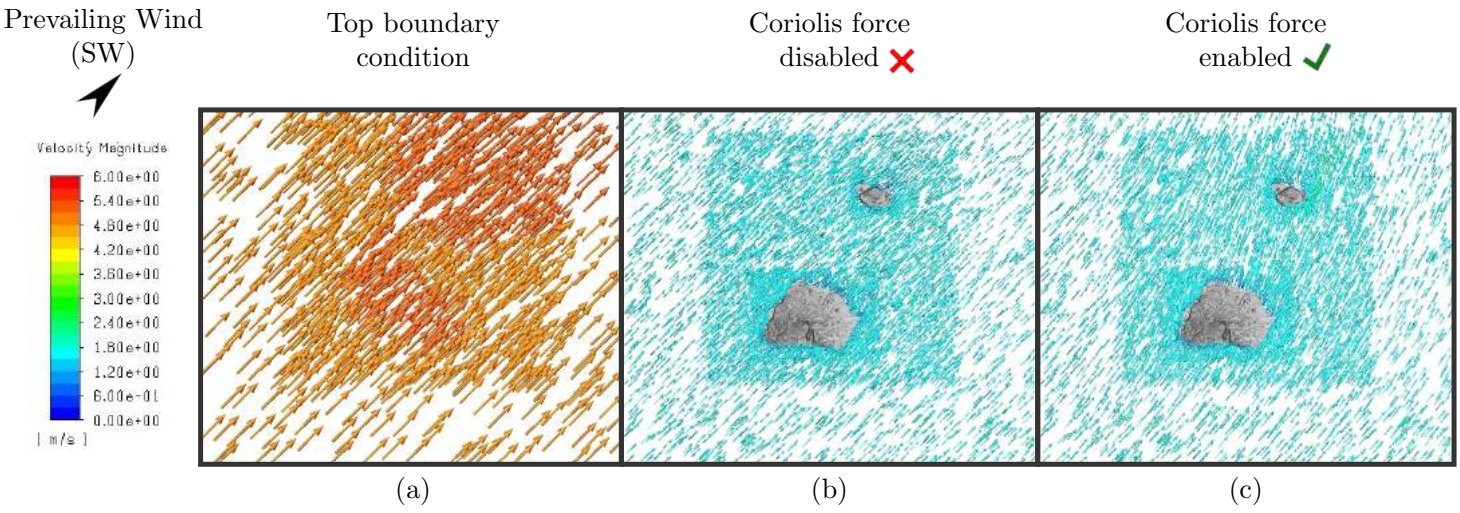

Figure 6.11: Vector plot comparing the effects of running a south-westerly wind simulation with and without the Coriolis force momentum source terms. The top boundary condition in the upper atmosphere (a) is consistent across both cases; the surface-level vectors around MI change due to the influence of the Coriolis force. The velocity scale has been kept constant throughout the images

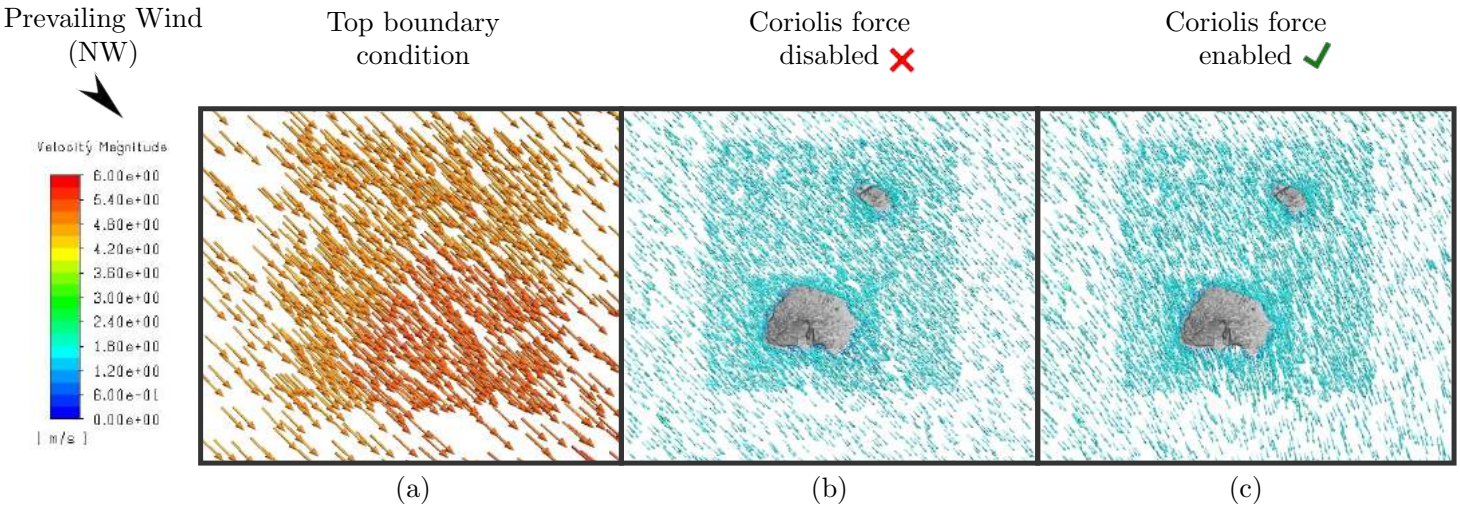

Figure 6.12: Vector plot comparing the effects of running a north-westerly wind simulation with and without the Coriolis force momentum source terms. The top boundary condition in the upper atmosphere (a) is consistent across both cases; the surface-level vectors around MI change due to the influence of the Coriolis force. The velocity scale has been kept constant throughout the images

In Figures 6.11 and 6.12, the inclusion of the Coriolis force momentum terms causes changes in the wind speed as well as its direction of travel. The twisting of the flow is a result of the wind moving in a direction that is not exactly aligned with the rotation of the Earth as was seen in the previous westerly case. In both the south- and north-westerly cases, wind deflection appears to become more exaggerated with farther distance from the inlet boundary. Since MI is slightly closer to the inlet boundary when a wind is approaching from the south, one would expect less wind deflection by the time the flow reaches the island. The deflected wind in Figure

© University of Pretoria

6.11c seems to still lie within the south-west sector, although not precisely centred, when it first strikes the island. By contrast, wind coming from a northern direction deflects more since MI is further away from a northern inlet boundary. By the time it reaches the middle of the numerical domain, the approaching north-westerly wind in Figure 6.12c has already deflected so much that it seems to be striking MI at an angle somewhere within the NNW wind sector.

While this high-level overview of the CFD simulations does not lend itself well to a more precise discussion yet, a closer interrogation of the CFD results set has been deferred to Section 6.7.

The discussion until now, concerning the Coriolis force effect seen in Figures 6.10 - 6.12, is consistent with what was noted previously when the simulation vectors were compared to experimental measurements in Figures 6.7 - 6.9:

- The westerly simulation case compares very well with measurements because there is little to no change in wind direction as a result of the Earth's rotational inertia.

- The south-westerly simulation case compares fairly well with measurements but is subject to a wind deflection. Since the inlet boundary is close enough to MI, wind deflection is not too much of a problem yet and the disagreement between CFD vs. experimental results is within the bounds of a reasonable uncertainty.

- The north-westerly simulation case breaks down and no longer shares much similarity with physical measurements. The Coriolis force has deflected the airflow too much by the time it reaches MI since it is slightly further away from the inlet boundary face than it was during the south-westerly simulation.

Thus, although the Coriolis force was correctly taken into account during simulations, its effect at such a large scale was greatly underestimated. The misjudgement of the Coriolis Effect comes as a consequence of not testing and evaluating its importance in the introductory case studies performed in Chapter 3; there was no indication that such testing needed to be done at that stage. This late discovery has become a hindrance to perfectly comparing and validating the CFD model against experimental data in any given wind sector.

6.7 Validation Against Experimental Data

A fully tabulated set of raw results is available in Appendix J for each of the three validation cases; summarising the experimental measurements, CFD results and non-Coriolis CFD results extracted for every 2D anemometer station around MI. These are the exact data that have been used in the current section in an attempt to validate aspects of the CFD simulations against reality.

© University of Pretoria

The method for validating these simulations is focused on first ensuring the accuracy of the vertical wind-speed profiles at the mast coordinates, then on local wind direction vectors as was previously done in the Bolund Island case study.

Due to the shortfalls discussed previously, regarding the stronger-than-anticipated influence of the Coriolis Effect, it should be apparent by now that a direct comparison between simulation and reality would not yield a convincing argument for CFD validation. The validation cases have been presented in order from best to worst.

6.7.1 Westerly Wind Case

The unscaled wind velocity profiles for a westerly approaching wind have been given in Figure 6.13 showing only the masts that lie nearest to the west-following lane. A normal deviation has been demarcated in the experimental mast data to include turbulence effects and measurement noise within a 95% confidence interval. Furthermore, the numerically simulated turbulence has been incorporated into the velocity plots to offer a complete one-stop visual comparison of the vertical wind profiles.

From the plots in Figure 6.13 it is clear that the CFD simulation has predicted a realistic westerly wind based on the comparison with sparse mast data. Although the CFD velocity magnitudes do not correspond exactly with their experimentally averaged counterparts, all profiles shown fit well within the experimental 95% confidence interval. It is impossible to tell whether or not this degree of accuracy is maintained in higher parts of the atmosphere due to the lack of wind sensors higher than one metre above ground level; highlighting room for improvement in future iterations of this project.

The scale of the axes has been kept constant throughout all plots in Figure 6.13. Note how the horizontal black lines, denoting experimental measurement deviation, become progressively longer on either side of the experimental mean (black dots) as the wind progresses across MI from west to east. This lengthening can be attributed to the fact that the Kampkoppie Coastal wind mast was taken to be a reference station during the experimental data extraction procedure for this wind direction; highlighted in Table 4.2. There is naturally less noise associated with such a reference station than with the downstream masts where vast distances and time lags have taken their toll on statistical precision. That is to say, stations further away from the Kampkoppie coastal reference were expected to include more measurement deviation, not because they were subjected to any more wind turbulence or topographical interference, but rather due to the filters that were applied to the full dataset when extracting relevant experimental recordings from the MIRED database.

One may note from Figure 6.13 that the blue CFD turbulence band also falls well within the experimental 95% confidence interval in all cases. This is a good sign indicating that the simulation and reality are in strong agreement. However, we need to remain aware of the

© University of Pretoria

fact that the chosen k-ε turbulence model is still likely to be under-predicting the TKE due to known deficiencies when assuming isotropic turbulence properties (already discussed in Section 3.3). Once again, the w component of velocity has been completely excluded from the CFD velocity profiles since it is not available in the experimental side.

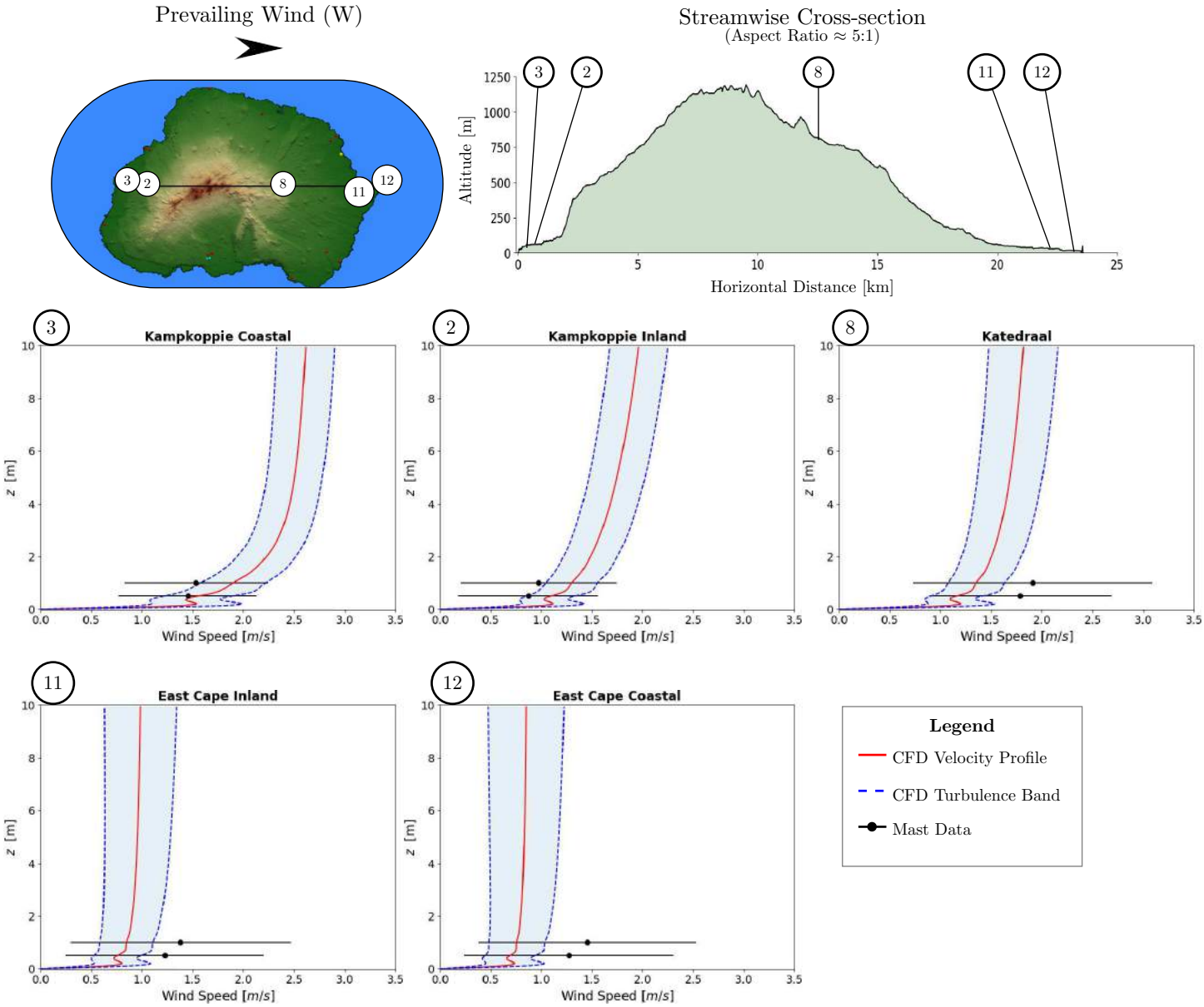

Figure 6.13: Pictorial representation of the wind velocity profile as it follows a westerly path across MI. The island thumbnail image and stream-wise cross-section give an indication as to the location and altitude of the stations, respectively. Focus is held on only the stations closest to the indicated lane of wind. Black dots indicate the experimentally determined mean wind velocity with the accompanying error bars to show measurement uncertainty. Red lines show the mean wind velocity profile with an accompanying band of blue uncertainty (due to turbulence) as extracted from the simulation

Moving on, Figure 6.14 plots much of the same information already discussed but the overhead perspective offers a means of assessing the accuracy of the modelled wind direction. The red and blue colour scheme has once again been reserved for illustrating the simulated wind velocity

© University of Pretoria

and turbulence, respectively. Similarly, black arrow vectors show the observed mean wind with the attached black balloons indicating the measurement deviation.

The ideal modelling result would thus be represented in Figure 6.14 as a blue CFD balloon exactly superimposed over a portion of its corresponding black experimental balloon. For the westerly wind simulation, this is the case for all of interrogated mast sensors. In particular, the 1-meter anemometer at the Kampkoppie Coastal station shows an almost exact match between the CFD simulation and the realistic measurements. This should be seen as an exception rather than the rule since the Kampkoppie station was used as a reference point to anchor the CFD simulation to a very specific subset of experimental observations, but it is still exciting to know that the numerical wind profile has reached its first contact with MI as intended. With this really good starting point in mind, it is no wonder the rest of the simulation yielded such promising comparisons with reality.

Prediction error equations 6.2 and 6.3 were devised to quantify the accuracy of the simulated wind velocity and direction when compared to the experimental results. Here, $\bar{V}_{EXP}$ denotes the average measured wind speed in metres per second while V_{CFD} refers to the extracted simulation value. Note that only the horizontal wind speed magnitude was used here; any vertical wind speed components had to be ignored since the anemometers on MI were only 2D sensors. Similarly, $\bar{D}_{EXP}$ denotes the average measured wind direction in degrees and D_{CFD} refers to the simulated equivalent.

$$E_{vel} = \frac{|\bar{V}_{EXP} - V_{CFD}|}{|\bar{V}_{EXP}|} \times 100 \tag{6.2}$$

$$E_{dir} = \min\left[360^\circ - |\bar{D}_{EXP} - D_{CFD}|, |\bar{D}_{EXP} - D_{CFD}|\right] \tag{6.3}$$

E_{vel} denotes the velocity magnitude error as a percentage while E_{dir} denotes the directional error in degrees. The Min operator used in Equation 6.3 simply accounts for the fact that, when measuring the angle between two vectors, there will always be two possibilities: one less than 180° and another greater than 180° to make up a full 360°. The smaller of the two angles is always chosen to represent the directional error. Table 6.1 reports the average and maximum error statistics found for the current validation case.

Table 6.1: Error statistics for the Westerly wind simulation

	Mean	Max	Location of Max Error
Velocity Error [%]	29.3	64.5	Santa Rosa Valley
Direction Error [°]	16.2	70.6	Santa Rosa Valley

© University of Pretoria

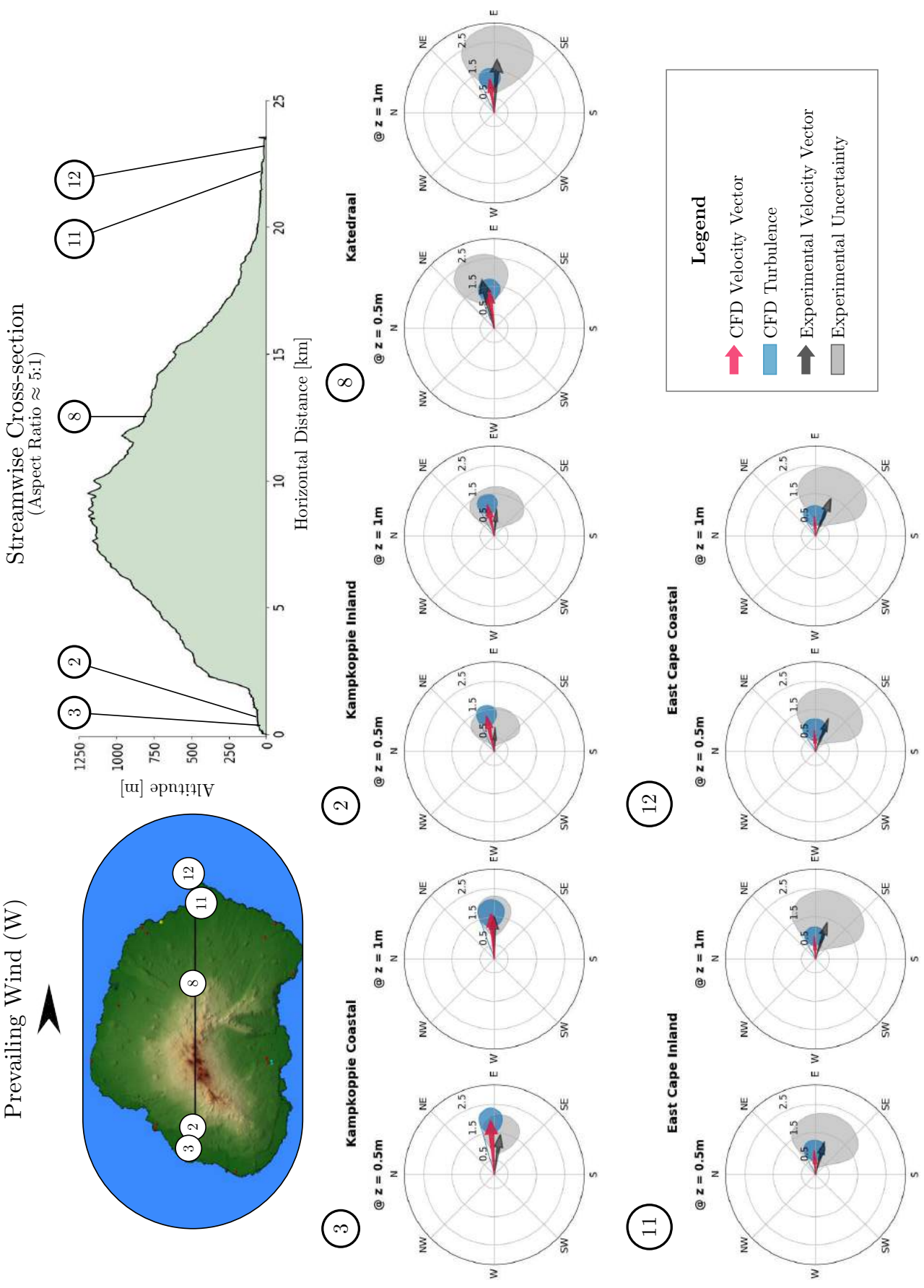

Figure 6.14: Pictorial representation of the wind velocity vectors following a westerly path across MI. Black vectors indicate the experimentally determined mean wind velocity with the accompanying error balloons to show measurement uncertainty. Red vectors show the CFD mean wind velocity with an accompanying blue balloon to represent turbulence fluctuations as extracted from the simulation

© University of Pretoria

The average velocity prediction error across all MI mast stations was found to be 29.3%. The maximum recorded magnitude prediction error was 64.5% at the Santa Rosa Valley station. The simulation results were also found to have wind bearing direction out by an average of 16.2° with a maximum directional prediction error of 70.6° at Santa Rosa Valley again. The results at Grey Headed Ridge were also subject to larger prediction errors, no doubt due to the strong influence of the steep topographical features in that area of the island. Figure 6.15 shows the stations with the worst error statistics.

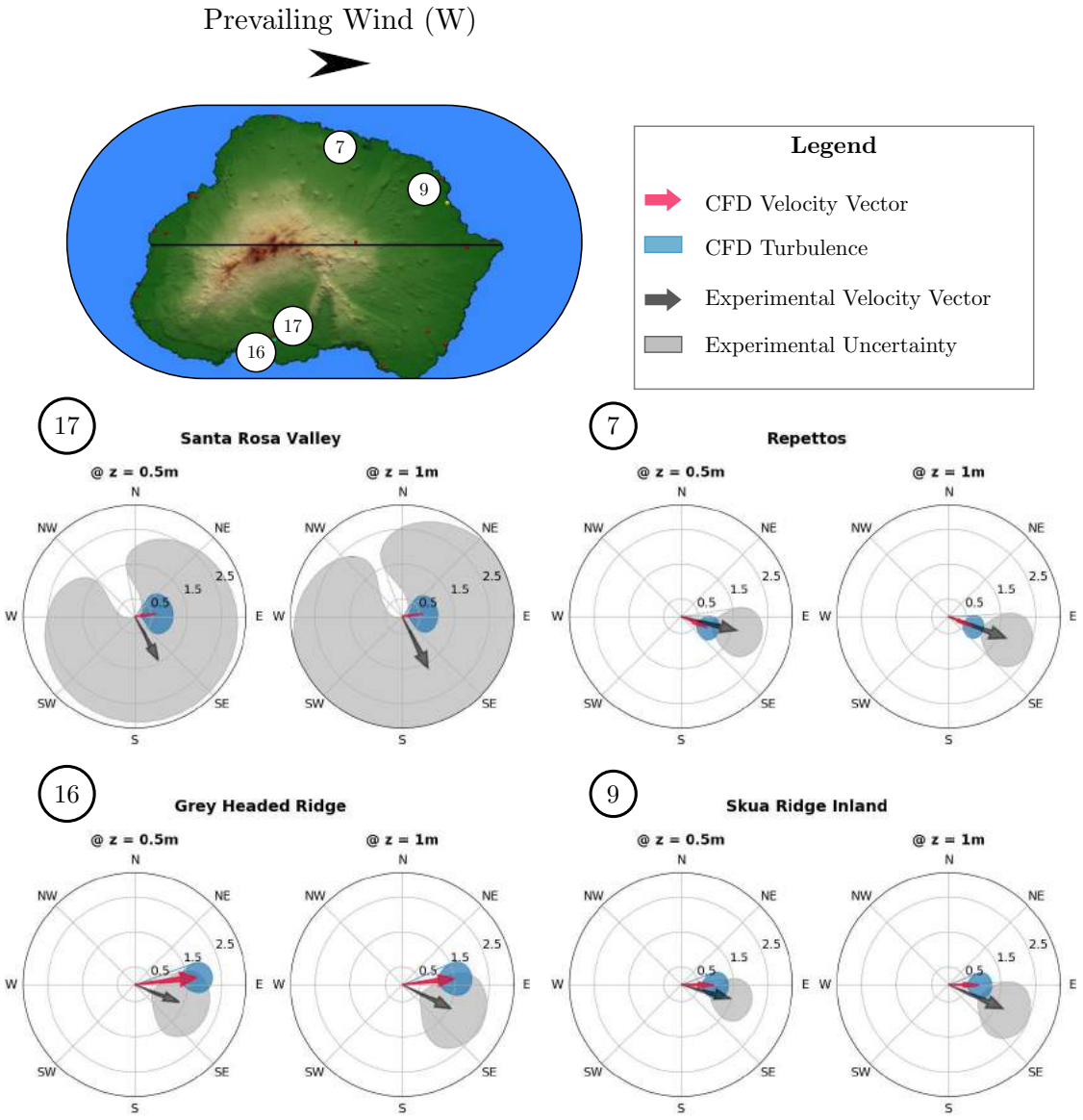

Figure 6.15: Pictorial representation of the wind velocity vectors at the stations exhibiting high prediction error. The island thumbnail image gives an indication as to the location of the stations

Note that this method of quantifying error compares experimental means directly to the CFD results without taking any measurement deviation into account. Santa Rosa Valley provides the perfect example: note in Figure 6.15 how widely the experimental dataset deviates from its simplified mean direction. The high experimental variance noted for the Santa Rosa Valley

© University of Pretoria

station can be attributed almost purely to the fact that it is located at the bottom of a steep valley, no doubt within the separation zone of any winds rolling over the cliff-edge, and is thus subject to wildly unpredictable wind loading. The Grey-Headed Ridge station can also be seen to have rather large experimental uncertainty, although not nearly as bad as was seen in Santa Rosa Valley located below it.

The simplest and most effective way to account for measured deviation is to reduce any error to zero where the CFD simulation predicts a wind anywhere within the corresponding experimental range. In colloquial terms: "Wherever the blue blobs fall exactly within the grey blobs" in Figures 6.14 and 6.15 we may assume a zero error. This line of reasoning is not without its own flaws but it safely removes any strong outliers (such as Santa Rosa Valley) from influencing the error analysis.

With measurement deviation accounted for, the reported error dropped dramatically as seen in Table 6.2. The average velocity magnitude error is now < 1 % with a maximum of 15 % seen at Repettos station. The wind direction error is so low as to be negligible. Under these conditions, the two worst results came from the Repettos and Skua Ridge inland stations seen in Figure 6.15.

Table 6.2: Error statistics for the Westerly wind simulation, accounting for experimental measurement deviation

	Mean	**Max**	**Location of Max Error**
Velocity Error [%]	<1	15.0	Repettos
Direction Error [°]	0.0	0.0	-

The results for this small case study have been better than expected given the limitations seen thus far in the study. Even a maximum wind magnitude error is not too bad considering the fact that those wind measurements have been taken at heights of only 0.5-1m above ground level; a tiny fraction of the scale of the modelled Marion Island and the atmosphere above it. It remains to be seen, however, whether or not these results have been maintained in higher reaches of the atmosphere. It has been left to future funders and researchers to install taller measurement masts around MI and assess the validity of these simulations or any further CFD simulation attempts.

6.7.2 South-Westerly Wind Case

With the Westerly wind case providing reasonably accurate comparisons with realistic measurements, the South-Westerly validation direction has been assessed here. Keep in mind that the Coriolis Effect has affected the CFD results more than originally anticipated, making for a less convincing validation case.

© University of Pretoria

Figure 6.16 presents the wind velocity profiles following a wind crossing MI from a south-westerly direction. The same plotting conventions from Figure 6.13 have been adhered to here, only the chosen station numbers have been changed to align with the new wind direction. For the most part, the CFD simulation seems to have predicted the wind velocity and turbulence accurately within the bounds of a 95% confidence interval.

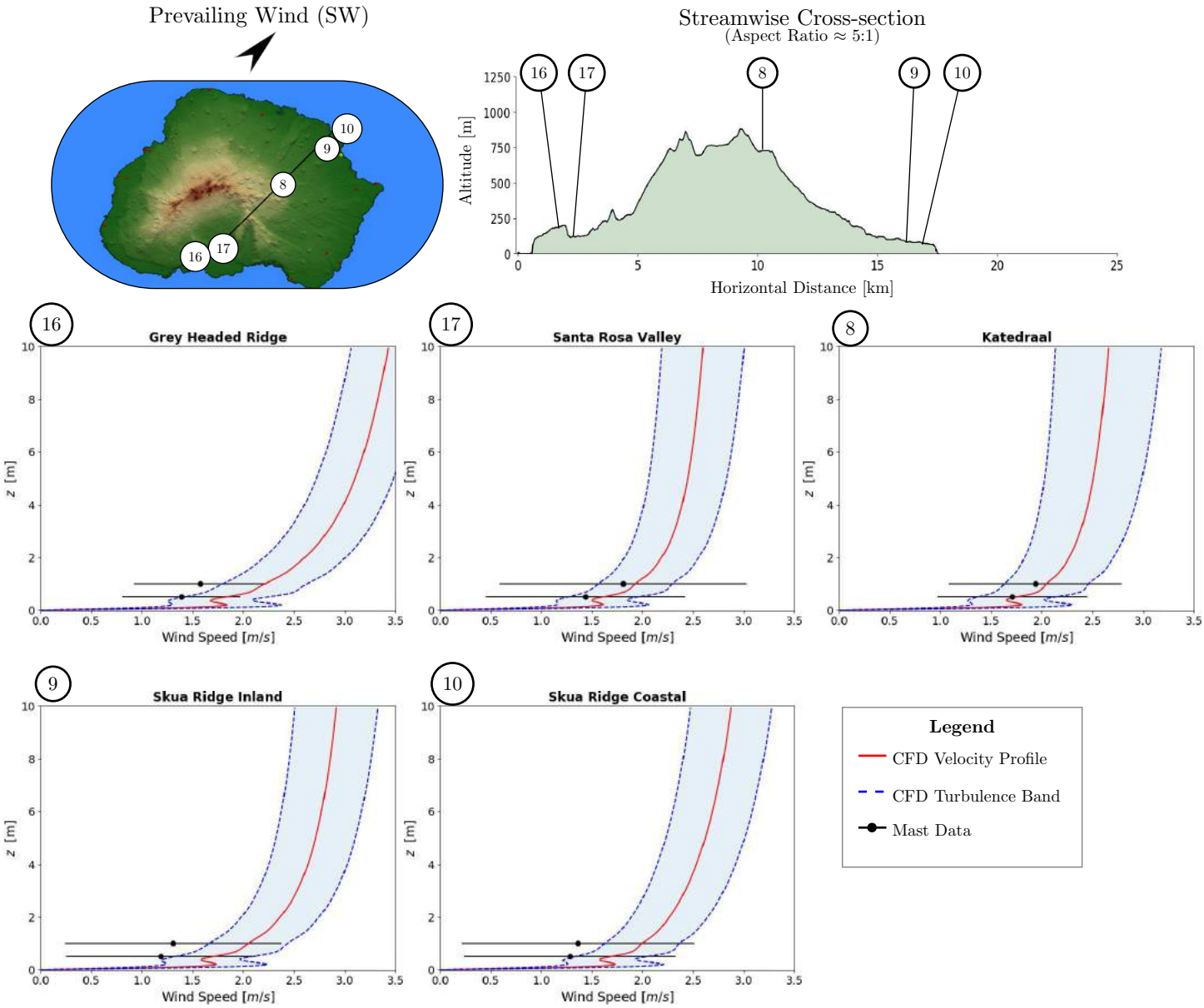

Figure 6.16: Pictorial representation of the wind velocity profile as it follows a south-westerly path across MI. The island thumbnail image and stream-wise cross-section give an indication as to the location and altitude of the stations, respectively. Focus is held on only the stations closest to the indicated lane of wind. Black dots indicate the experimentally determined mean wind velocity with the accompanying error bars to show measurement uncertainty. Red lines show the CFD mean wind velocity profile with an accompanying band of blue uncertainty (due to turbulence) as extracted from the simulation

One outlier in Figure 6.16 stands out in particular: the Grey Headed Ridge station. Since the Grey-Headed Ridge station is one of the first in line to acknowledge a wind coming from this

© University of Pretoria

direction, one question comes immediately to mind:

How can the first station bear inaccurate results but all other downstream stations seem to compare favourably with experimental measurements?

There are, of course, many reasons or plausible explanations for why this could have occurred; the obvious discretisation errors and the ever-looming Coriolis Effect form part of these. Nevertheless, a likely answer to the puzzle comes from looking carefully at the enlarged valley area shown in Figure 6.17. The black vectors in the image reflect the simulated wind speed and direction. Note the strong diversion of the arrows as they interact with the steep sides of Santa-Rosa valley and also the nearby landform known colloquially as the Sphinx. The strong influence of topographical features on the airflow was naturally expected as an outcome in this study so it is believed that the steep valley sides are responsible for funnelling any incoming wind into a single aligned direction. The station located at the bottom of the Santa Rosa Valley (Station 17) therefore shows an almost perfect match between experimental and CFD data as a result of its proximity to the valley wall. Other stations, like the Grey-Headed Ridge station (Station 16), do not benefit from such a funnelling effect and are thus more at the mercy of the prevailing wind.

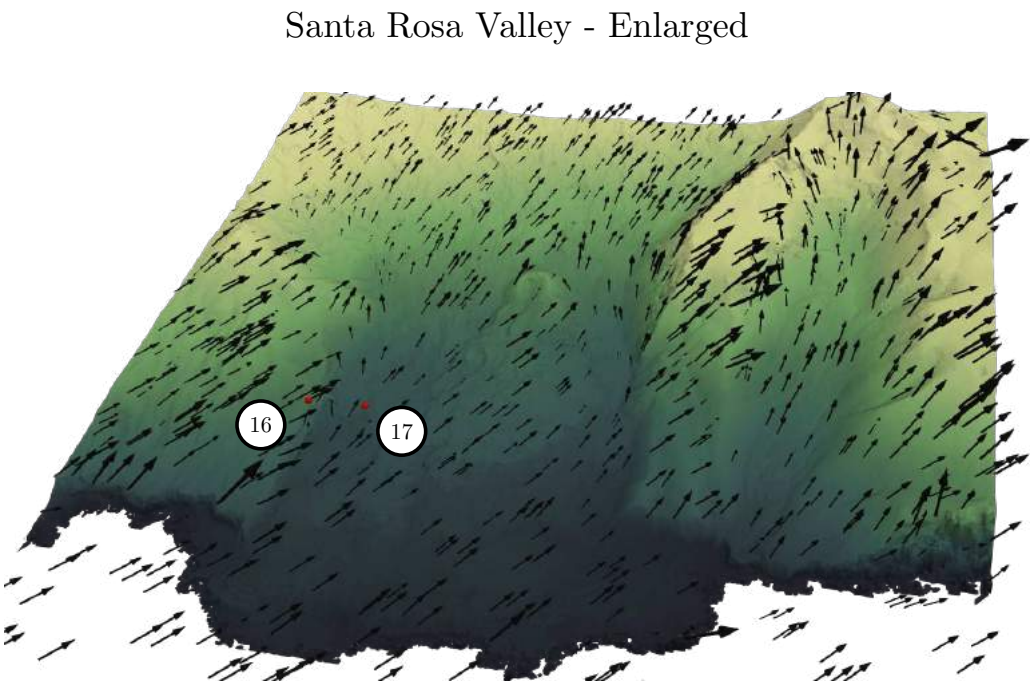

Figure 6.17: Enlarged view of the Santa-Rosa valley and Sphinx landforms subjected to a south-westerly incoming wind. Black arrow vectors indicate simulated wind flow. A strong influence of the topography on the wind has been noted here, causing the wind to be funnelled into a single direction aligning with the valley walls. Stations 16 and 17 have been highlighted

Furthermore, it is reasonable to expect that the aligned wind flow exiting from the top end of the valley has cascaded downstream and influences all subsequent monitoring stations. This would go a long way in explaining the favourable results seen at the downstream stations after

© University of Pretoria

Santa-Rosa valley. One must note, however, that this effect probably declines with distance from the valley and only follows a south-westerly lane directly in line with the prevailing wind. Stations outside of this scope are more likely to be affected by a vastly different, and unrelated, set of circumstances.

Figure 6.18 further dissects the south-westerly simulation results by looking at the 2D wind vectors seen from above. As before, the ideal result would look like a blue balloon completely overlapping a grey balloon; exactly as shown for the Santa-Rosa valley anemometers in this case. One notes from these plots that there is an almost constant disagreement in wind angle between experimental and CFD results; an average angular error of 21.2° was calculated for the south-westerly case across all stations. Since the experimental measurements (black vectors) in Figure 6.18 mostly correspond with a south-westerly surface wind, any angular error has therefore been fully attributed to misgivings in the CFD simulation.

Although it has been mentioned abundantly, the underestimation of the numerical Coriolis Effect is seen as the chief cause for such large prediction errors. Table 6.3 summarises the average and maximum error statistics found for the current south-westerly validation case using the same methods described in Section 6.7.1. While accounting for experimental measurement deviations, the mean and maximum wind velocity error was found to be 1.53% and 27.6%, respectively. This is a significant increase in error compared to what was noted in the westerly wind case. Similarly, the mean and maximum wind angle error have jumped to 1.34° and 17.4°, respectively.

Table 6.3: Error statistics for the south-westerly wind simulation, accounting for experimental measurement deviation

	Mean	Max	Location of Max Error
Velocity Error [%]	1.53	27.6	Cape Davis
Direction Error [°]	1.34	17.4	Repettos

Figure 6.19 plots the location and wind arrow diagrams for the two worst comparing stations as highlighted by the error analysis above. Note that Cape Davis and Repettos are both situated on the leeward side of MI, likely encapsulated within a turbulence separation zone.

© University of Pretoria

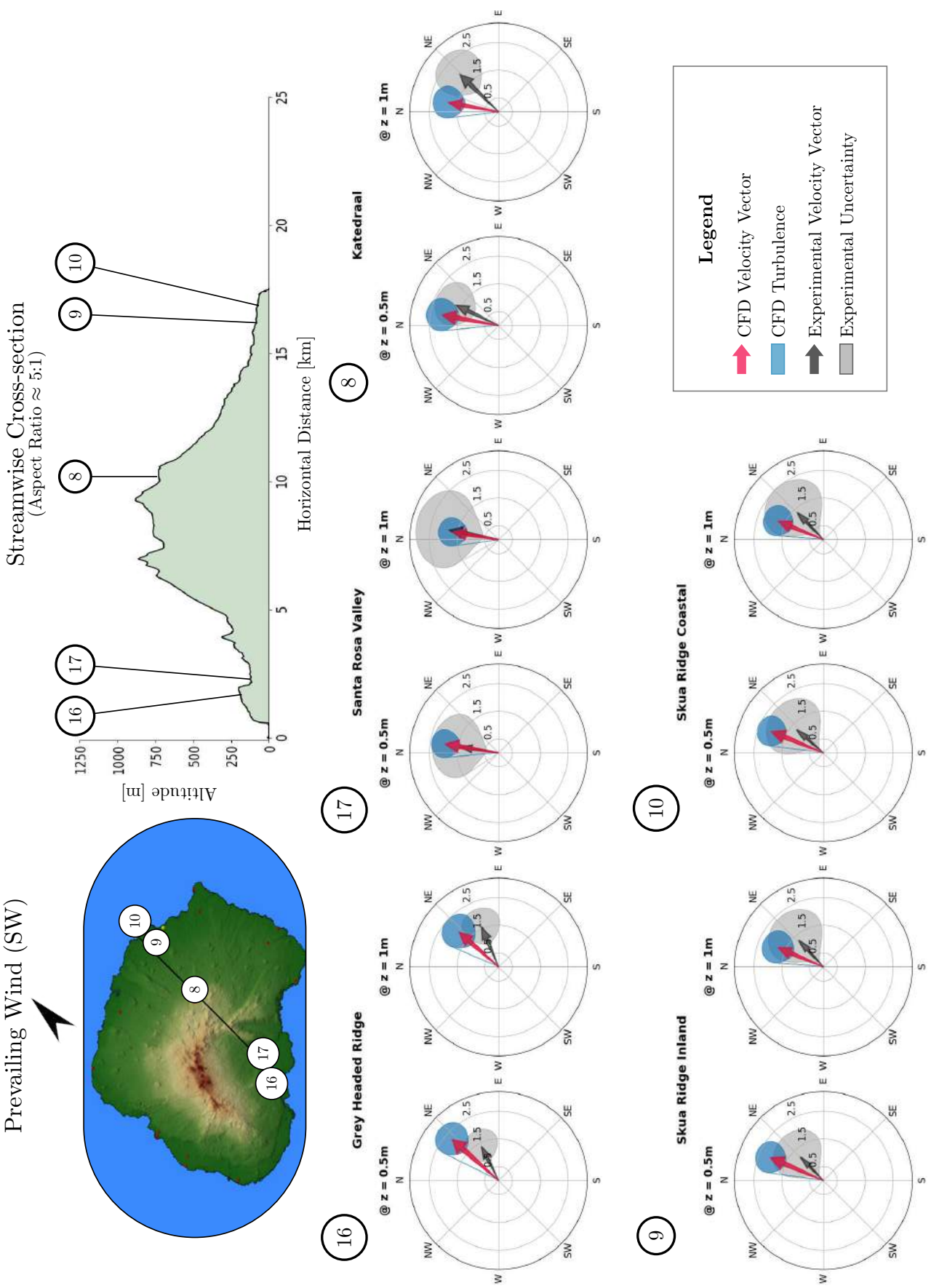

Figure 6.18: Pictorial representation of the wind velocity vectors following a westerly path across MI. Black vectors indicate the experimentally determined mean wind velocity with the accompanying error balloons to show measurement uncertainty. Red vectors show the CFD mean wind velocity with an accompanying blue balloon to represent turbulence fluctuations as extracted from the simulation

© University of Pretoria

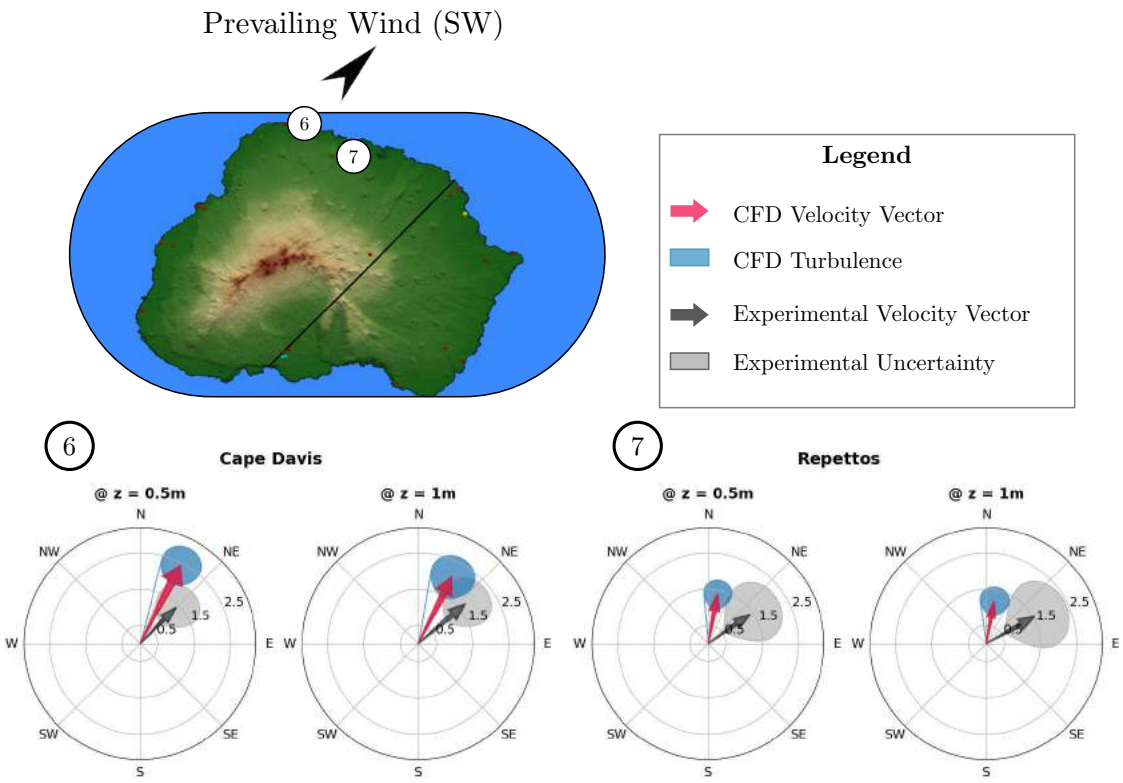

Figure 6.19: Pictorial representation of the wind velocity vectors at the stations exhibiting high prediction error. The island thumbnail image gives an indication as to the location of the stations

6.7.3 North-Westerly Wind Case

Possibly the worst-case scenario in this study, from a validation point of view, comes from simulating a north-westerly approaching wind. As already noted, the poor results here are a by-product of the simulation setup and a severe underestimation of the Coriolis Effect; not of any calculation defects in the ANSYS Fluent code.

Keeping with the theme so far, Figure 6.20 presents the wind magnitude profiles along a north-westerly lane on MI. Note that Repettos (station 7) has been included even though it is located relatively far out of the way of the designated lane.

Figure 6.20 shows that the wind velocity magnitude has been reasonably well approximated at stations across the island. This result is useful since all previous wind simulation cases have had similar outcomes, implying that the chosen inlet wind profile was perfect for modelling the yearly average wind conditions over MI. While simulations of average wind conditions have been successful to a certain degree, the current study has not accounted for characteristically "faster-" or "slower-than-average" wind conditions which could be encountered on any given day. For this to be achieved, the input boundary conditions would have to be modified slightly to reflect the required wind conditions. Furthermore, it should be kept in mind that an accurately predicted wind speed is only half the picture; wind direction has not yet been assessed for this north-westerly case.

© University of Pretoria

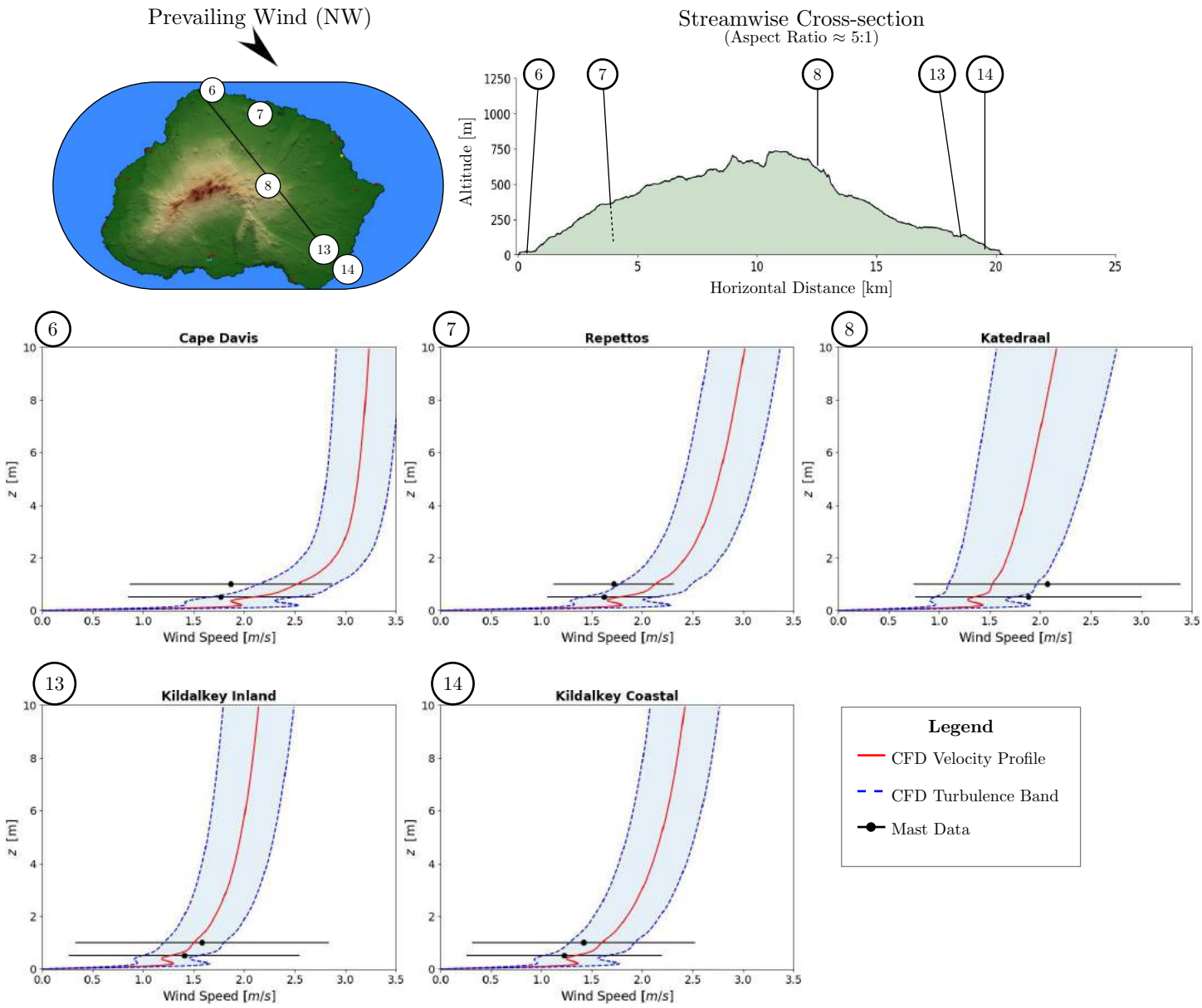

Figure 6.20: Pictorial representation of the wind velocity profile as it follows a north-westerly path across MI. The island thumbnail image and stream-wise cross-section give an indication as to the location and altitude of the stations, respectively. Black dots indicate the experimentally determined mean wind velocity with the accompanying error bars to show measurement uncertainty. Red lines show the CFD mean wind velocity profile with an accompanying band of blue uncertainty (due to turbulence) as extracted from the simulation

Figure 6.21 plots the black experimental vectors vs. the red CFD vectors as seen from above in a 2D sense. The large errors in this simulation become clearly visible in the plots, noting that not a single CFD vector across the board lines up with its corresponding experimental partner. The cause for this has already been rightfully attributed to the strong Coriolis Effect.

© University of Pretoria

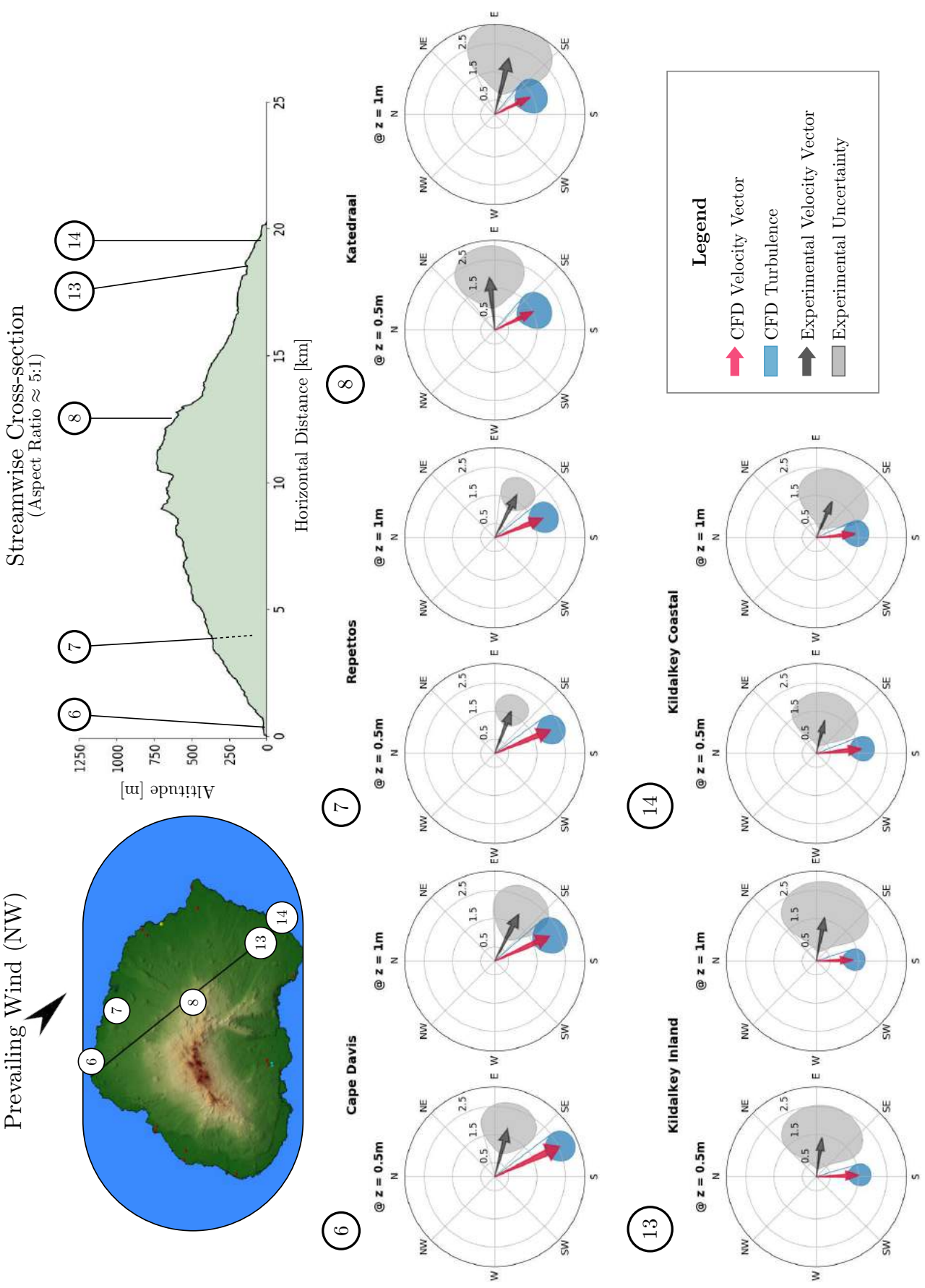

Figure 6.21: Pictorial representation of the wind velocity vectors following a westerly path across MI. Black vectors indicate the experimentally determined mean wind velocity with the accompanying error balloons to show measurement uncertainty. Red vectors show the CFD mean wind velocity with an accompanying blue balloon to represent turbulence fluctuations as extracted from the simulation

© University of Pretoria

Table 6.4 summarises the average and maximum error statistics found for the current north-westerly validation case. While accounting for experimental measurement deviations, the mean and maximum wind velocity error was found to be 3.86 % and 34.3 %, respectively. Similarly, the mean and maximum wind angle error have jumped to 8.80° and 34.6°, respectively.

Table 6.4: Error statistics for the north-westerly wind simulation, accounting for experimental measurement deviation

	Mean	Max	Location of Max Error
Velocity Error [%]	3.86	34.3	Swartkops
Direction Error [°]	8.80	34.6	Katedraal

Besides the obviously large error caused by underestimating the effect of the Coriolis force, there are other factors such as topographical interference and instrumentation accuracy which could be affecting these results. Keep in mind that the incoming wind direction has changed significantly from the input boundary conditions. By the time this "north-westerly" wind has reached MI, it has deflected significantly due to Coriolis forcing. Compounding error as a result of the deflected wind interacting with the topography in an unintended direction is to be expected.

Figure 6.22 plots the vector illustrations for the worst prediction stations presented in Table 6.4. It is worth noting that the prediction error recorded here is considerably higher than what was found in the south-westerly simulation case.

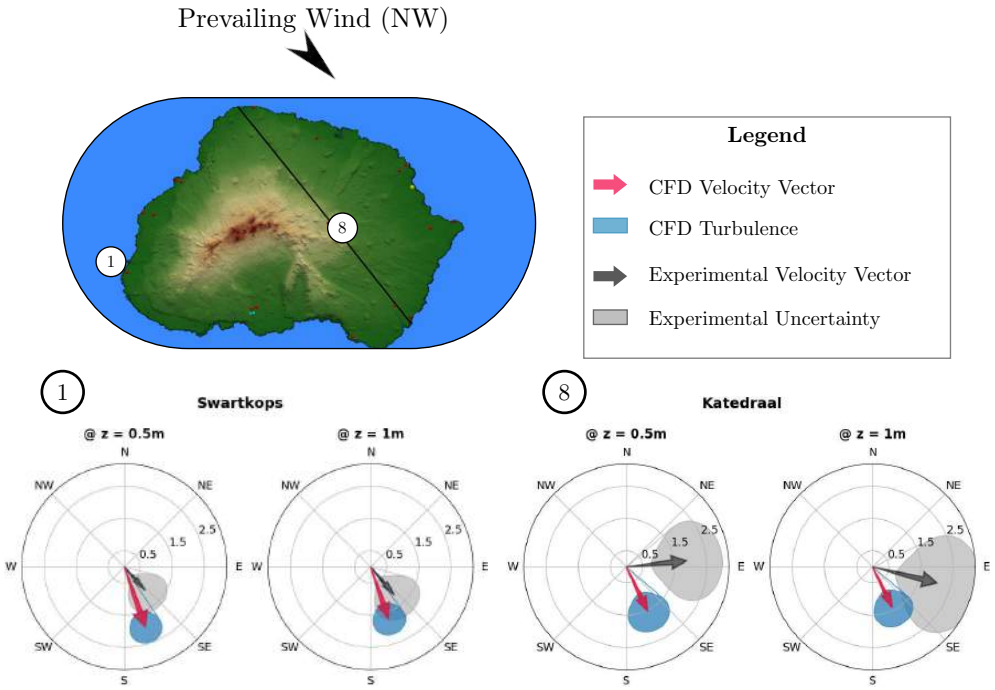

Figure 6.22: Pictorial representation of the wind velocity vectors at the stations exhibiting high prediction error. The island thumbnail image gives an indication as to the location of the stations

© University of Pretoria

6.8 Error Analysis

This section focusses on coagulating the all prediction errors discussed so far with the hopes of providing future readers with a broad understanding of any shortcomings in the CFD simulations.

For simplicity, the error statistics for each of the three chosen validation cases have been repeated here in Table 6.5 along with a new aggregated error score which combines results from all three cases before calculating the total error.

Table 6.5: Error statistics for all validation cases

Wind Case	**Type**	**Mean**	**Max**
West	Velocity Error [%]	< 1	15.0
	Direction Error [°]	-	-
South-West	Velocity Error [%]	1.53	27.6
	Direction Error [°]	1.34	17.4
North-West	Velocity Error [%]	3.86	34.3
	Direction Error [°]	8.80	34.6
Combined	Velocity Error [%]	2.04	34.3
	Direction Error [°]	3.38	34.6

The numbers presented in Table 6.5 are useful for drawing broad conclusions but they cannot, by design, show everything there is to show regarding the simulation prediction error. Figure 6.23 thus attempts to graphically show the extent to which individual stations were subject to prediction error.

Note that the size and colour of the circles in the plots have been based on averaged error. Wind velocity magnitude error and wind direction error have been blended into a single compound error per station to aid the visualisation. Further to this, each station has two anemometer sensors; the summed errors from both sensors were taken into account when calculating a final averaged error circle per station. The exact techniques used to do the error addition are not of importance since this is not a conventional way of quantifying error. Rather, the numbers have been recast to form a visually appealing plot for the reader to interpret with the eyes; a qualitative visual aid for the discussions to follow.

© University of Pretoria

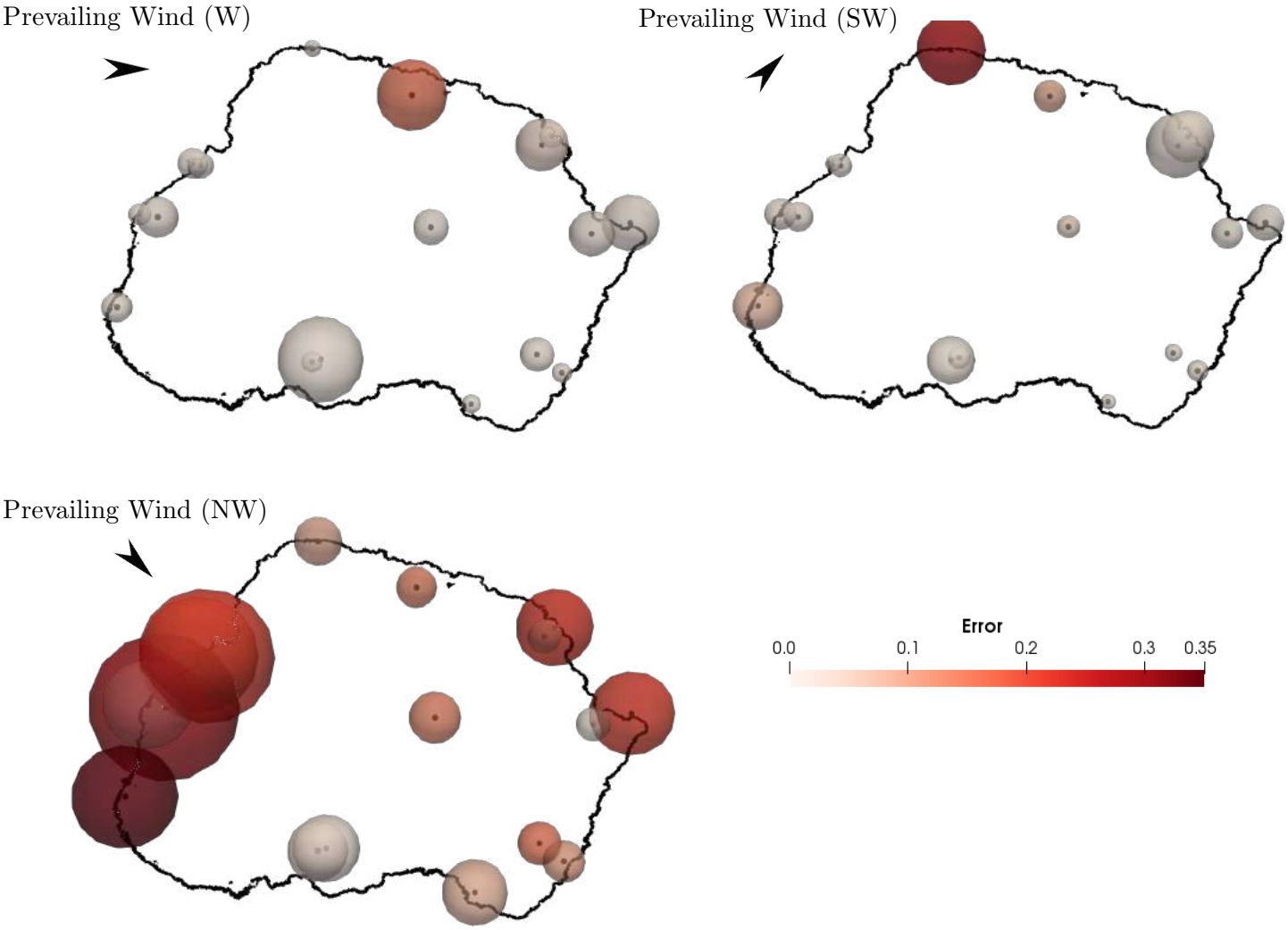

Figure 6.23: Graphical representation of the error at each station across MI under the various simulated wind conditions. Small circles indicate a small initial error between CFD vs. Experimental data. Circles have been coloured by the adjusted error; taking experimental measurement deviation into account. Table 6.6 gives an explanation as to the size and colouring of the circles

The size of each circle in Figure 6.23 corresponds to the direct error between the CFD vectors and the experimentally determined vectors without taking measurement uncertainty into account. The colour of each circle corresponds to the adjusted error, taking measurement uncertainty into account as explained in Section 6.7.1. In order to fully understand the plots in Figure 6.23, one may consult Table 6.6:

© University of Pretoria

Table 6.6: Table explaining the error plots seen in Figure 6.23

Circle Attributes	Explanation
Size	Corresponds with direct error between CFD and experimental vectors. Larger direct error leads to a larger circle size, smaller error leads to smaller circle size.
Colour	Corresponds with the error after adjusting for experimental measurement uncertainty. Darker reds imply large error after factoring in uncertainty.
Small, White	Imply that CFD and experimental data comparisons had little to no error. This is the ideal result.
Large, White	Imply that the experimental measurements are subject to high volatility/uncertainty. The initial error between CFD and experimental data was large, but was reduced to ~ 0 after accounting for the large fluctuations in the experimental dataset. These results may not be very trustworthy due to the highly volatile wind measurements.
Medium, Red	These stations lie somewhere in the spectrum from good to bad results, depending on size and colour.
Large, Dark Red	Imply that the station measurements exhibited little to no similarities with the CFD simulations, even after considering experimental uncertainty. This is the worst possible outcome.

One notes from the plots in Figure 6.23 that the lacklustre outcome of the north-westerly validation case heavily influences the combined total error. The especially large red circles on the western side of MI are a consequence of the incoming north-westerly wind having an entirely different flow direction in the simulations as opposed to reality. Not only has the incoming flow been deflected by the Coriolis force, but is also believed that the escarpment on the western edge of MI acts as a barrier to the air flow; causing the already deflected wind to deviate even further as a result of impingement on the "wall".

Figure 6.24 shows the effect of the escarpment barrier on the incoming wind flow from a south-westerly and a north-westerly direction. Since the escarpment wall is approximately in line with the direction of flow from a south-westerly direction there is understandably less flow

© University of Pretoria

diversion due to topography and hence less error in that simulation case. However, the wall is almost perpendicular to an incoming north-westerly wind and a likely contributor to the large error seen in that simulation case.

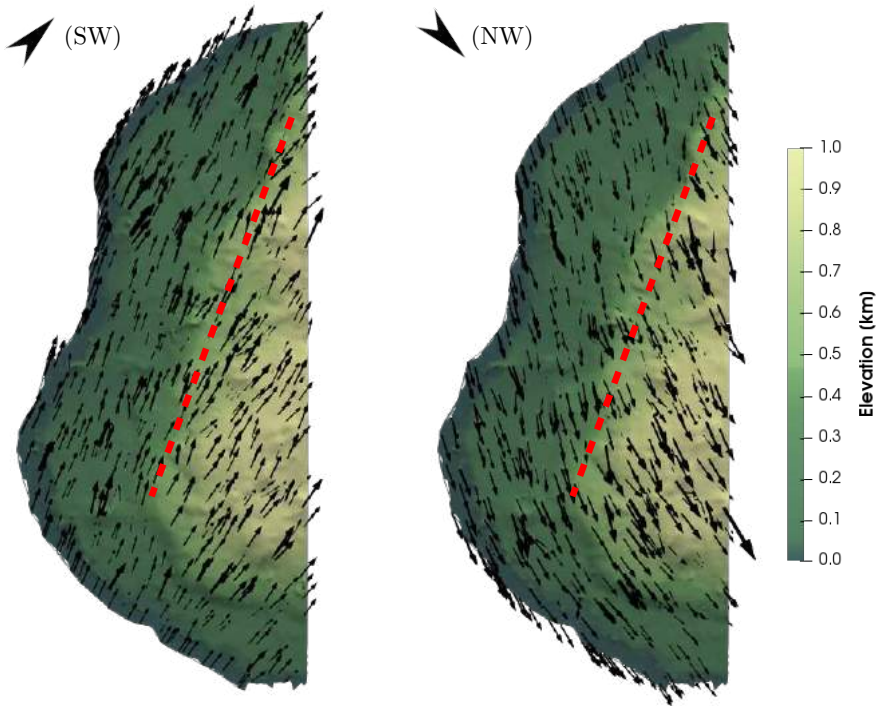

Figure 6.24: Plots showing the barrier-like effects of the western escarpment of MI on incoming wind flows. The escarpment wall is roughly aligned with a south-westerly wind, causing the wind to deflect slightly. The wall is almost perpendicular to an incoming north-westerly, causing large deflection and even aerodynamic dead-zones in some locations. The escarpment wall has been denoted by a dashed red line in these images.

It is likely that the westerly wind simulation exhibited little to no error as a result of flow impingement on the western escarpment wall. Recall that the westerly wind simulation was not drastically affected by the Coriolis force. Thus, any wind vectors in the simulation would have a good starting point to interact with the topography in a similar way to what realistic wind flow would do.

In general, stations in the south-eastern quadrant of MI seem to have a good track record despite the negative performance noted in the north-westerly simulation. This is likely a result of the gentle topographical gradients in that section of the island. Stations in that region were easily erected on flat land away from any large features, making for an ideal wind capture scenario that is easy to compare with simulation data. By contrast, the station at Cape Davis has been highlighted as an especially poor site. It is surrounded by sharp rocky outcroppings and located close to a steep cliff edge; both of which are likely to cause excessive wind turbulence. The station at Cape Davis has also been notoriously difficult to maintain over the years since it was erected, meaning that its poor performance could also be a result of other factors.

There is evidence in Figure 6.23 to suggest that the accuracy of the wind simulations degrades with distance travelled. It was often noted that stations on the leeward side of MI, relative to

© University of Pretoria

the incoming wind flow, would exhibit slightly more error than those on the windward side, plotted as larger error circles. The only real exceptions to this are the far western stations under a north-westerly prevailing wind (already discussed) and the stations located around the Grey-Headed Ridge area. The large white error circles in the Grey-Headed Ridge area imply that the physical sensor measurements are subject to high volatility, likely as a result of the steep geographical features interfering with the air flow and causing turbulent separation regions. That being said, the experimental readings and the CFD data coincide adequately after accounting for the volatility.

The uncertainty and error discussed in this section is far from ideal yet it may still be manageable if caution is applied when using the simulation data to predict realistic climatic phenomena. In short, with the simulations being validated to this extent, one could extract CFD data from other as-yet untested wind simulations and apply suitable factors to account for the documented uncertainty. The resulting predictions would have a reasonably high *accuracy*, but at the cost of having a low *precision*.

A conservative approach would thus be recommended to any future researchers making use of the wind simulation data from the current study: any wind velocity values extracted from the CFD dataset should factor in a $\pm 35\%$ uncertainty. Likewise, any wind direction data should only be trusted to within $\pm 35^{\circ}$ in either direction. Note that this highly conservative strategy uses the maximum error of 35% encountered during the validation exercise as a safety factor. It would be possible to reduce this factor if more risk of an erroneous prediction is allowable to the application.

6.9 Predicting Different Wind Speeds

An aspect of wind simulations that has not been fully addressed yet is that of simulating and predicting wind speeds which are faster or slower than the yearly average. This is an easily conceivable scenario, especially on MI where winds can gust much faster for days on end or go quiet and wind-still the next moment. These fluctuations have all been captured over the course of the two year project and melded into a broad spectrum statistical mean and standard deviation. However, this section is aimed specifically at explaining how the current wind simulations can be used to predict wind in statistically outlying situations.

The original full-scale simulations were set up to run such that all the boundary profiles would be automatically calculated based on a single input value for friction velocity, u^*, and applied to their respective boundary surfaces. As stated in Section 5.4, the chosen value for the simulated u^* amounted to $u^* = 0.15$ m/s. As an experimental exercise, the simulations were rerun again with the boundary profiles being changed based on an input friction velocity of $u^* = 0.3$ m/s. This higher input friction velocity would result in a faster overall flow field.

Figure 6.25 presents the extracted CFD wind velocity profiles at all 17 wind stations under

© University of Pretoria

an average-speed westerly prevailing wind and under a high-speed westerly prevailing wind. Further plots for the other two validation wind directions (SW and NW) are available in Appendix K.

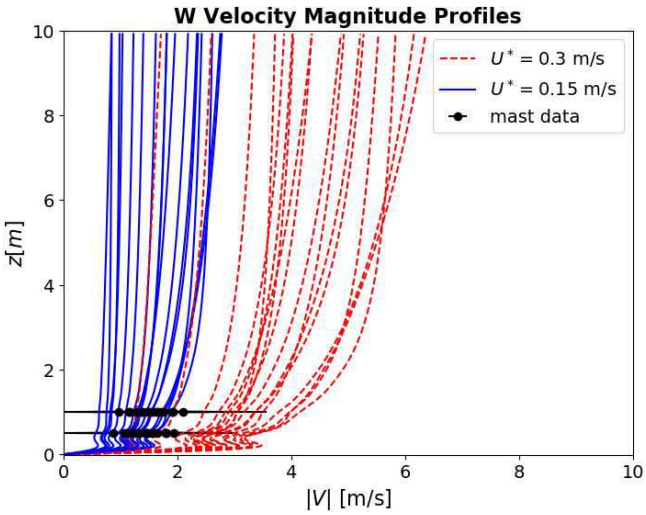

Figure 6.25: Wind velocity profiles extracted at 17 locations from an average-speed (blue) and a high-speed (red) CFD wind simulation. This plot is specifically for a westerly wind flow direction over MI

Note that the high wind speed scenario resulted in consistently faster velocity magnitude profiles as expected, just by changing the input value of the friction velocity. The plots in Figure 6.25 only show the first 10 metres above ground level, but the trend indeed carries on higher up into the atmosphere following a near-logarithmic law. It was seen that the black points denoting experimental mast data for this wind direction coincided very neatly with the mass of blue lines denoting the average-speed modelled wind. Meanwhile, the red dashed lines fell towards the higher end of of the experimental mast data range.

Figure 6.26 presents exactly the same data as before, only now the profiles have been scaled into a non-dimensional/universal form; dividing each line by its corresponding local friction velocity number as extracted from the CFD simulation. Further plots for the other two validation wind directions (SW and NW) are available in Appendix K.

© University of Pretoria

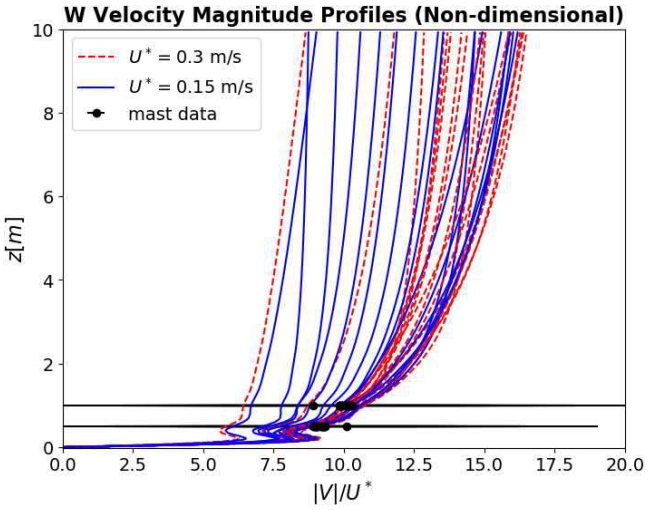

Figure 6.26: Non-dimensional wind velocity profiles extracted from an average-speed (blue) and a high-speed (red) CFD wind simulation. The lines are densely overlapped after being cast into universal form. The overlapping is more pronounced at lower heights and becomes progressively more spread out with increased altitude. This plot presents the same data seen in Figure 6.25

Note from Figure 6.26 how the plotted lines have become superimposed over one another in this universal form, implying that the use of the friction velocity as a scaling factor is a simple yet effective way of comparing completely different CFD solutions. Or better yet, using the results from a readily available CFD solution to predict the outcome of another closely related scenario without resorting to spending further time and computational resources to run a new simulation.

It is therefore suggested that future researchers making use of this study do not need to perform any new simulations in order to predict faster- or slower than average wind patterns. Rather, an easy way of predicting wind speed near ground level would be to extract the readily available average-speed wind simulation data and scale it up or down accordingly using an appropriate friction velocity as shown in Equation 6.4. A reasonable choice of friction velocity would be in the range of 0 - 0.3 m/s, with u^* =0.15 m/s being the average wind speed as originally modelled.

$$|V|_{prediction} = \frac{|V|_{CFD}}{u^*_{CFD}} \times u^*_{assumed} \tag{6.4}$$

where the subscript CFD denotes a quantity extracted from the simulation data, *prediction* denotes the approximate wind speed prediction and *assumed* denotes a reasonable guess at a scaling friction velocity. Note that this method is not perfect and will break down as one tries to predict wind speed higher up in the atmosphere. The method would only offer a good approximation within the first 10 metres above ground level, after which one would have to start factoring in a new source of error.

© University of Pretoria

6.10 Island-Scale Simulations

Attempts were made to simulate the same 16 wind directions in a smaller domain using extracted profiles from the full-scale domain as boundary conditions. The aim of this exercise was to achieve a higher resolution outcome by condensing the same number of cells into a much smaller region; focusing only on the immediate domain around MI and excluding the neighbouring island and much of the surrounding seas from calculations.

6.10.1 Mesh Generation and Procedure

The intention here was to generate a high-density mesh, using roughly the same number of cells as were used in the full-scale simulations but in a domain covering roughly 5 % of the original volume. During the full-scale simulation GCI exercise in Section 5.5.3, it was found that a 30m horizontal cell spacing was adequate for achieving a grid-independent solution. However, that part of the study only used the successive horizontal cell spacings: 50 m, 40 m, 30 m, and 20 m. In an effort to capture any truly sub-grid flow phenomena on a small scale, a new horizontal cell spacing of 10m was settled upon. Other aspects of the new mesh were left untouched, such as the vertical first-cell height and the overall cellular growth rate in the domain.

The new domain, termed the "island-scale domain" from here on, spans a volume of 28 km x 20.5 km x 2.5 km directly centred over MI. Figure 6.27 shows the island-scale domain as it was generated.

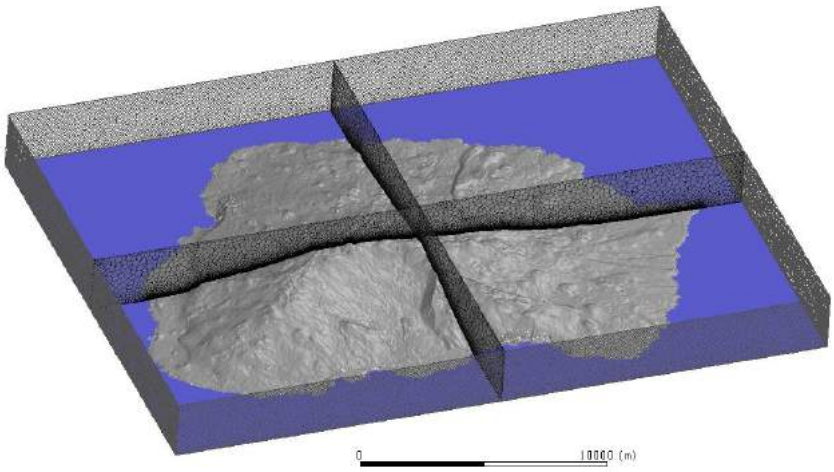

Figure 6.27: Island-scale mesh generated in Fluent Meshing, containing 126 million polyhedral cells

The island-scale mesh contains 126 million polyhedral cells, or roughly 90% of the number of cells found in the full-scale mesh. Unfortunately, the meshing process is complex and remains somewhat of a "black-box" enigma when using the ANSYS software. The process is inherently random every time and thus not easily controlled. Many complications arose during the generation phase which led to failed meshing attempts. The current mesh presented here is one of

© University of Pretoria

only a few successful versions which came about after considerable time spent tinkering with the software settings.

Wind velocity, turbulence and pressure profiles were extracted directly from the full-scale simulations and written to the disk. These profiles were taken at the exact location of the top-, side-, front-, and rear-inlet boundaries seen in the island-scale mesh seen in Figure 6.27. The boundary conditions were then simply read from file and applied directly to the corresponding boundary faces when needed. This method allowed the same mesh to be used for any required wind direction simulation; one simply had to keep track of the correct boundary profile files to go with a given simulation case.

6.10.2 Discussion

Due to unforeseen circumstances regarding the meshing and simulation times, the island-scale simulations did not converge to a valid solution. While it is believed that the methods used here were sound in principle, further refinement and testing are still required before simulations at this scale can be given any credit.

To give an example for why it was believed that these particular attempts at refining the solution had failed, Figure 6.28 has been provided to present the simulation data as it was retrieved. It was noted that the increased horizontal cellular resolution could have possibly resolved smaller features on MI and thus been responsible for the meandering wind velocity profiles seen in the plots. However, a far more likely reason for these plots being so different from those seen back in Section 6.7.1 is that the simulation had indeed failed due to any number of extenuating circumstances. The chief cause being that the meshes were vastly different between the full-scale and the island-scale simulation cases.

It is worth noting that the experimental vs. CFD data seen in the profile plots of Figure 6.28 correspond quite well with one another, although this is believed to be a happy coincidence. To discredit the apparent validity of these results, one may note that the simulated velocity profiles meander far too much and that the CFD turbulence in the plots took on a fixed constant value throughout the domain; i.e. the blue bands in Figure 6.28 maintain a fixed width throughout the height of the profiles, and across all the interrogated stations; a clear indication that something has not gone according to plan. Whatever the case, more investigation should be devoted to this subject of smaller scaled simulations.

© University of Pretoria

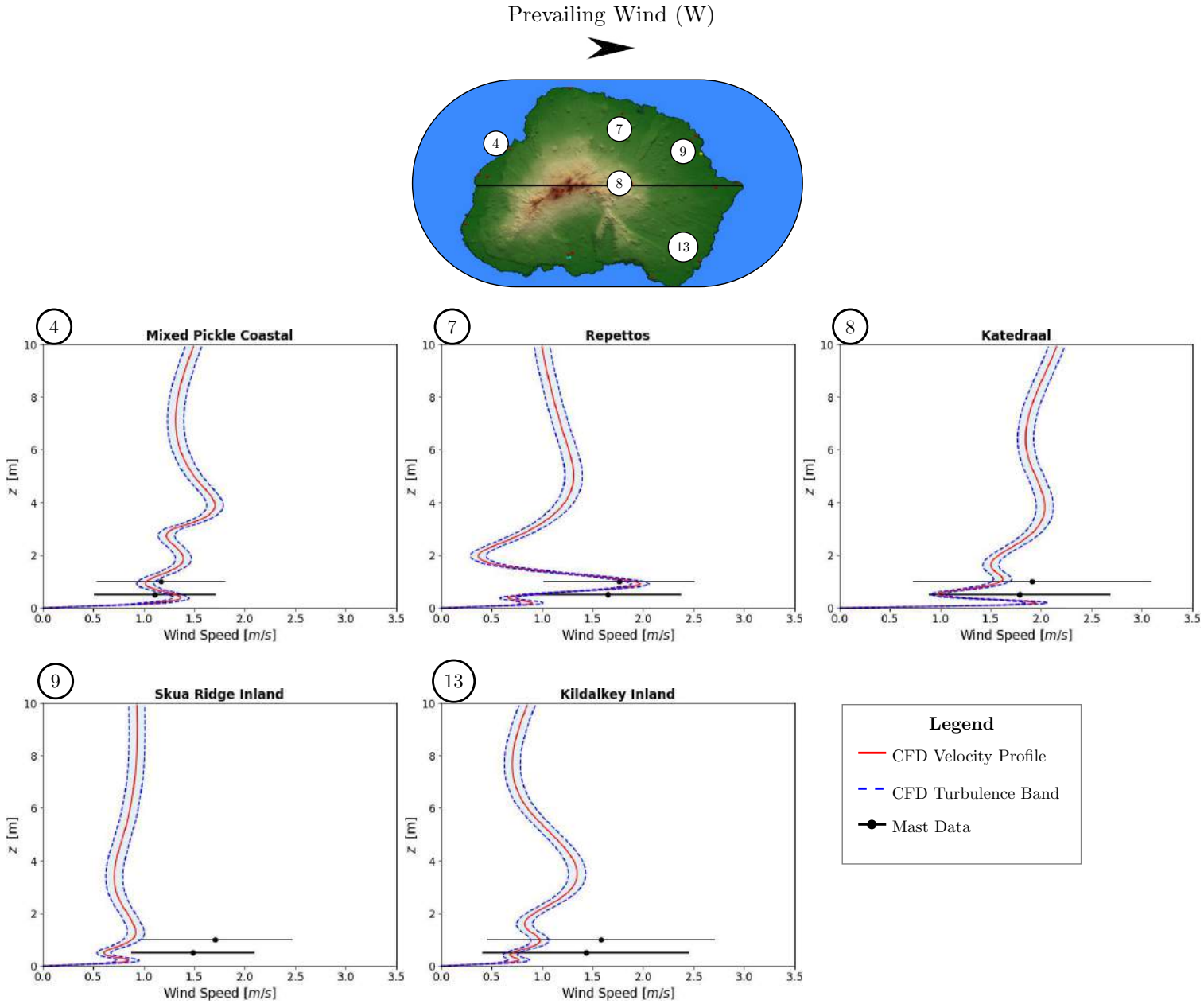

Figure 6.28: Example plots of the poor results extracted from the island-scale simulation of a westerly wind across MI. Various stations across the island were interrogated to be sure that this phenomenon was not an isolated event but had actually occurred everywhere in the domain

6.11 Composite Wind Maps

With the simulation results on hand and validated to a certain extent, further post-processing of the results is an easily achieved task. To remain within the scope of the current project, only limited use cases have been documented here but the possibilities for future users are endless. This section focuses on plotting island-wide wind maps for identifying regions of high- or low wind speed and turbulence. Furthermore, attempts have been made to use the simulation data to predict wind flow on one side of MI based on measurements retrieved from stations located on the opposite side. Since the island-scale simulations did not prove effective, only

© University of Pretoria

the full-scale simulations have been used here and thus all illustrations and conclusions relate to those results alone.

Remaining consistent with the scope of this study, Figure 6.29 shows a wind map plotted for the westerly wind simulation direction. The wind velocity magnitude has been logarithmically scaled so as to provide higher contrast in the image, highlighting areas of higher or lower wind speed for easy identification. The map was generated on an iso-surface placed exactly one metre above ground level over the island.

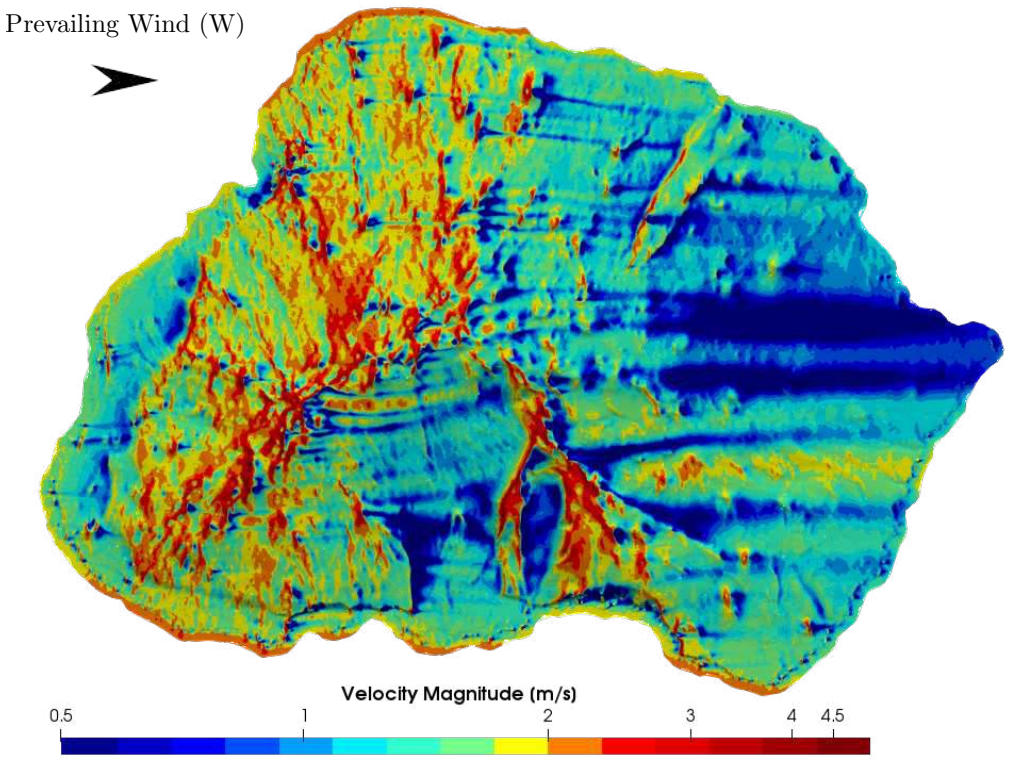

Figure 6.29: Wind velocity map at one metre AGL for MI subjected to a westerly prevailing wind

As expected, the windward side of the island is coloured a richer shade of red due to the incoming wind being unobstructed, and thus faster, on that side while the leeward half of MI displays more subdued colours since it is in the wake of the island. The region behind Grey-Headed Ridge was especially noted for having a large pocket of slow moving air.

Similarly to the previous plot, Figure 6.30 presents the wind turbulence intensity on an iso-surface placed one metre AGL for the westerly direction. The turbulence map has been clipped at a value of 60% TI to aid identification of high- and low turbulence regions. It was noticed that high turbulence was often concentrated behind the peaks of features, with turbulent wakes extending far beyond their points of origin.

Note that numerical TI values extracted directly from the Fluent case do not correspond to actual turbulence without a small adjustment. The default behaviour in ANSYS is to report

© University of Pretoria

all TI with respect to a fixed reference velocity, $u_{ref} = 1.0$ m/s. In order to achieve the correct TI values as they have been plotted in Figure 6.30, the following correction has been applied:

$$TI_{local} = \frac{TI_{Fluent}}{|V|_{Fluent}} \tag{6.5}$$

where TI_{local} denotes the TI calculated with the local velocity magnitude as a new reference rather than a fixed value. TI_{Fluent} denotes the TI values extracted directly from a Fluent case while $|V|_{Fluent}$ denotes the local velocity magnitude in the solution.

Maps for all 16 simulated wind directions are available in Appendices L and M. Although no discussion has been dedicated to each of these maps, the same trends explained until this point in the study can be applied there.

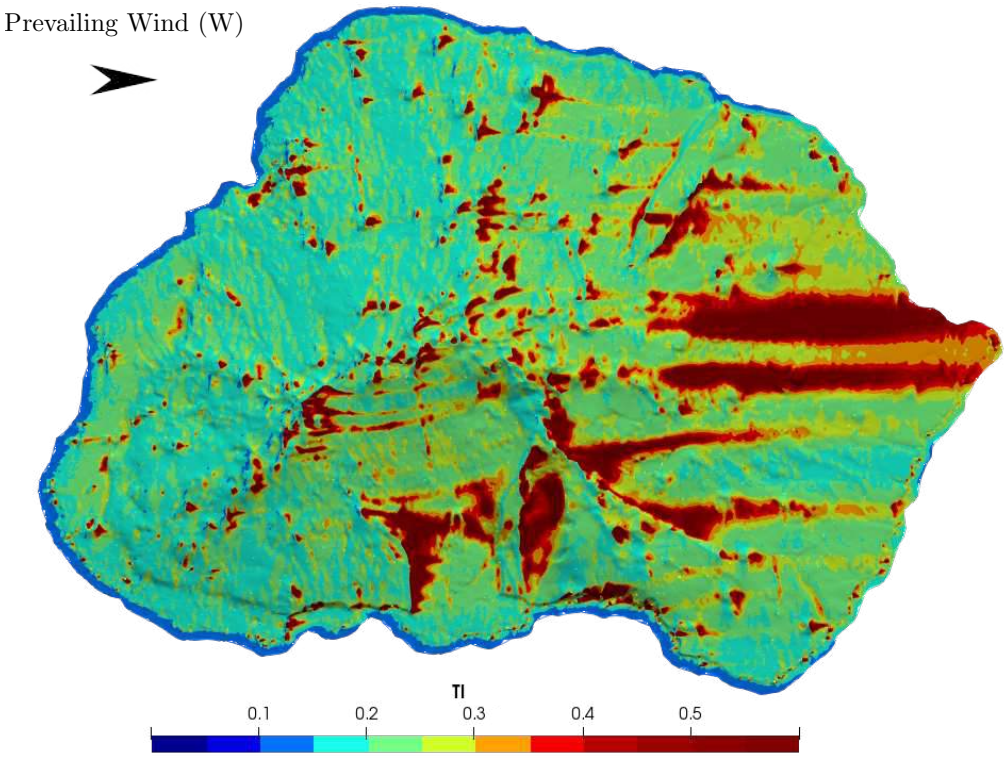

Figure 6.30: Wind turbulence map at one metre AGL for MI subjected to a westerly prevailing wind

One particularly interesting use of the wind simulation data is a yearly weighted-average wind map for MI. To achieve this, the MIRED database was interrogated to find the total frequency that each station registered wind across the spectrum of possible sectors; the sector frequency across all sensors and stations was normalised by the total frequency count to get a wind prevalence percentage graph as shown in Figure 6.31. The easiest way to understand the information presented in Figure 6.31 is by noting that the most common winds registered on

© University of Pretoria

MI come from a west-south-west direction, roughly 15 % of the time. Followed by a south-westerly direction about 14 % of the time, then westerly and so on. This graph was generated using all the experimental data gathered over the course of about two years across all 17 2D wind stations.

The wind prevalence information shown in Figure 6.31 was then used to give each corresponding wind simulation a weighting before combining their results into one average wind map according to Equation 6.6:

$$|V|_{avg} = \sum_{sector=WSW}^{sector=ESE} P_{sector} \times |V|_{sector} \tag{6.6}$$

where $|V|_{avg}$ denotes the weighted-average wind velocity magnitude, P_{sector} denotes the wind prevalence per sector as seen in Figure 6.31 and $|V|_{sector}$ denotes the extracted CFD wind velocity magnitude corresponding to the same sector.

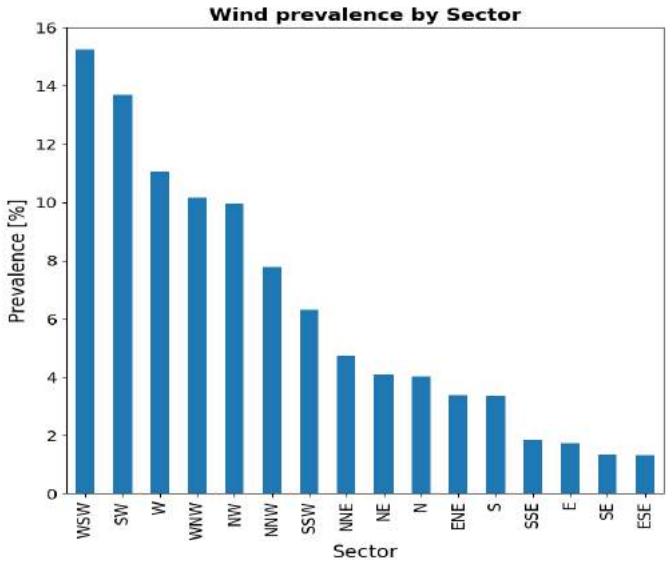

Figure 6.31: Bar plot showing the frequency of wind being registered in different sectors by all 17 wind stations over the course of two years. The frequency counts have been normalised by the total to give a wind prevalence percentage per wind sector

The wind map, shown in Figure 6.32, shows the 1 metre iso-surface above MI contoured and coloured by weighted-average velocity magnitude. This is the best possible approximation of the total wind climate on MI given the current state of the experimental setup and simulation results. It should be kept in mind that this map no longer contains any wind direction vectors; it is purely an evaluation of average wind speeds as a function of location on MI.

Such a plot could be used in future to predict the optimal location for wind turbine sites for power generation if the need should ever present itself. More importantly, the biological studies taking place on MI now have a reasonable approximation of wind climate on the island; if used

© University of Pretoria

in conjunction with known bird nesting patterns or plant distribution maps, this could bring about valuable insights that were never possible before.

Although it may not be apparent at this stage, it is highly likely that turbulent buffeting would have an effect on biological processes on MI just as much as pure wind speed does. Hence, the contour plot in Figure 6.33 has included the weighted-average turbulence intensity map.

The weighted-average TI map has been generated in a similar manner to the weighted-average velocity map and with similar objectives in mind. Equation 6.7 gives the expression used to determine the values seen in the map.

$$TI_{avg} = \sum_{sector=WSW}^{sector=ESE} P_{sector} \times TI_{local,sector} \tag{6.7}$$

One should keep in mind that all the maps generated thus far have only taken a single height into account, namely a one metre iso-surface above ground level. These plots serve as an example that the solution data can be manipulated to retrieve any data from other altitudes or locations within the modelled domain as necessary.

As a solution to predicting wind conditions on one side of MI given data readings from a station on the opposite side (or any other location on MI for that matter), a second mySQL database has been devised to store key parts of the full simulation dataset. A mySQL database has various advantages for storing this type of data:

- Users/researchers do not need to attain expensive ANSYS Fluent licenses in order to access and manipulate the simulation data. ANSYS Fluent or some other CFD software would only be required to run new simulations.

- Users/researchers do not need to load the full simulation datasets into memory when working with them. The mySQL language is built such that a well-structured query can extract only the required subsets of data.

- For now, only the 1-meter iso-surfaces and their corresponding flow variables have been extracted from the simulation cases and stored in the database. Any new sets of extracted data from the simulations can be easily appended and indexed in the database so that they can be readily accessed in the future.

© University of Pretoria

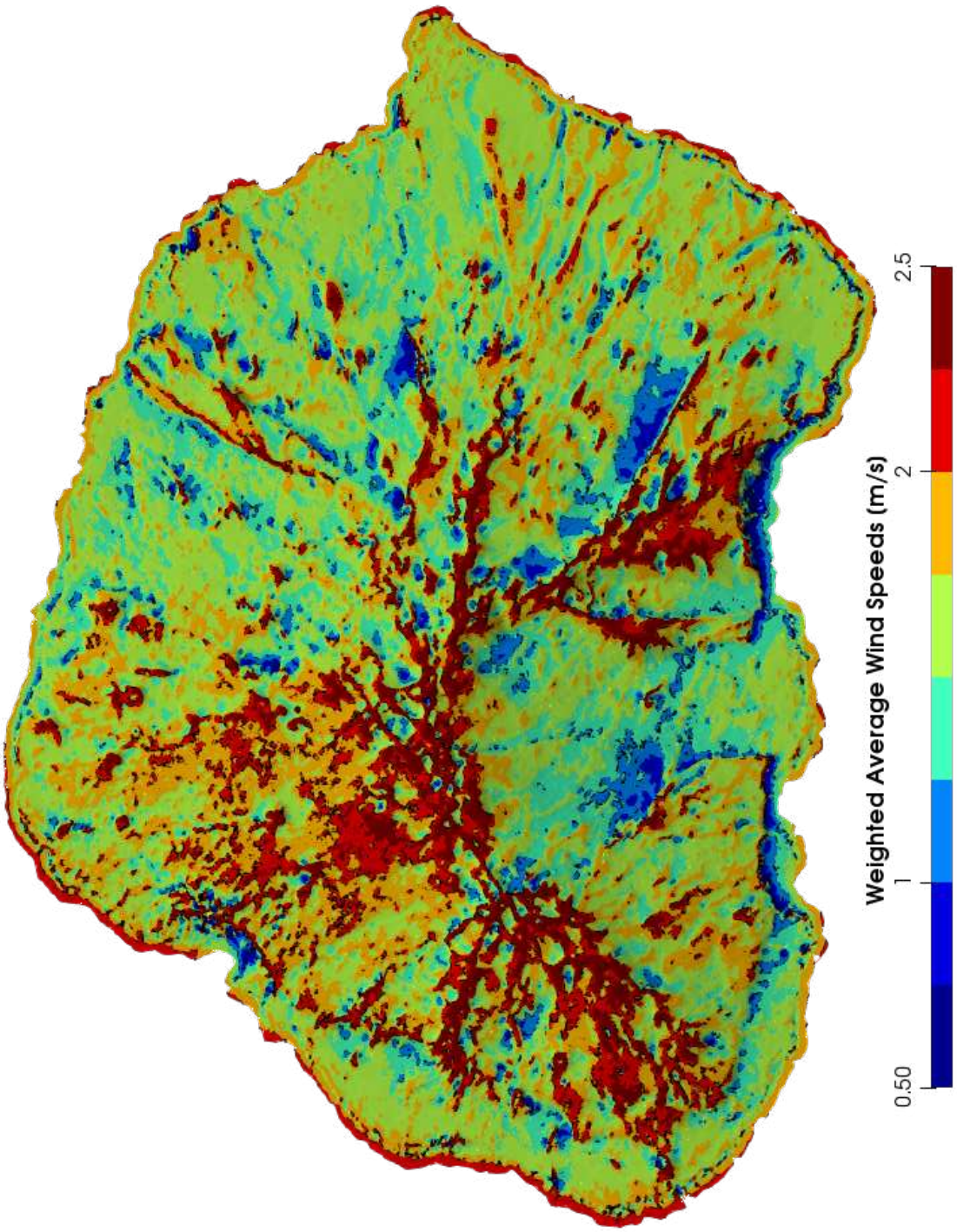

Figure 6.32: One metre iso-surface contour plot of weighted average wind velocity over MI, weighted by wind sector prevalence. The velocity colour scale has been clipped at 2.5 m/s to reveal more contrast. The maximum noted average velocity was 7.7 m/s

© University of Pretoria

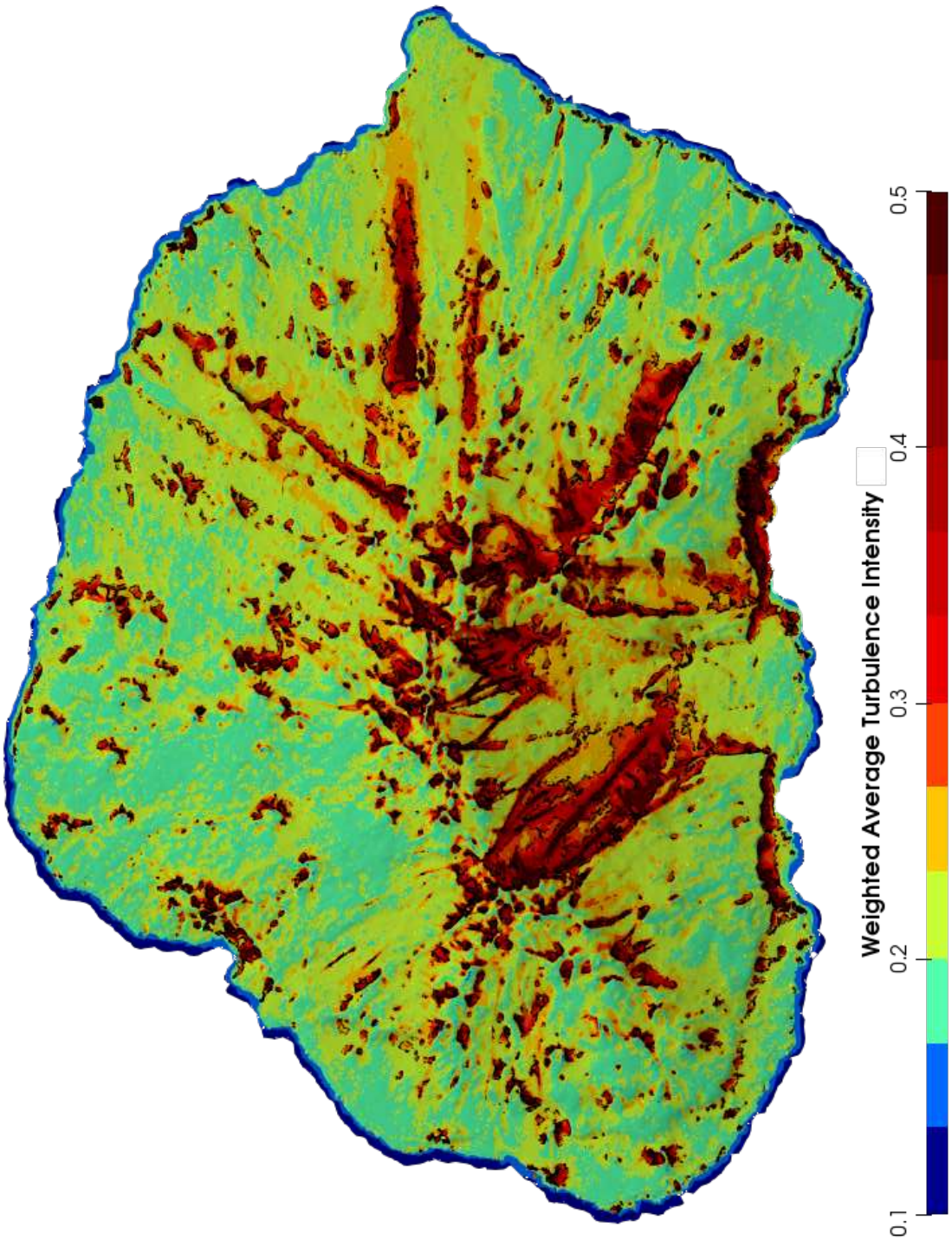

Figure 6.33: One metre iso-surface contour plot of weighted average wind turbulence intensity over MI, weighted by wind sector prevalence. The TI colour scale has been clipped to a value of 0.5 to add visual contrast

6.12 Summary

This Chapter gives an account of the simulation results and challenges as they were encountered throughout the project. Only three dominating wind directions were modelled and interrogated at first: west, north-west and south-west. After a thorough investigation and analysis of these three, the other remaining cardinal wind directions were added in.

© University of Pretoria

A so-called "full-scale" CFD model was designed to encompass a domain around MI and a vast part of its surroundings in order to fully capture any atmospheric phenomena. Interrogation of the full-scale model simulations revealed that island interactions could not be ignored since the wake from MI could definitely be intercepted by its neighbour under the right conditions, and vice versa. The simulation setup was further proved to be well-posed when an analysis of the experimental vs. simulated local friction velocity values showed good agreement. However, looking at the wind direction vectors showed that a small mistake had led to rather large error between the simulations and reality; an underestimation of the true strength of the Coriolis Effect. The Ekman spiralling as a result of the Coriolis force caused larger wind deflection than originally expected, thus resulting in the wind flow at surface levels having an entirely different heading to what was intended. The westerly and south-westerly wind validation cases did not seem too badly affected by the lapse in judgement but the north-westerly case suffered strong losses in accuracy.

After a full validation exercise, it was finally settled to accept these simulations. That being said, a healthy dose of caution is recommended when using these results in the future. An uncertainty of 35% is conservative when using these simulations to predict actual wind speed conditions. Similarly, the predicted wind direction can only be trusted within the bounds of a 35° prediction uncertainty. Further error analysis showed that the stations located on the south-eastern quadrant of the island had a higher agreement with simulations, making these locations good candidates for future studies. Predicting higher- or lower than average wind speeds is also possible using the current set of simulations. One only needs to factor the simulation results up or down by a suitable wind friction velocity value between the ranges of $u^* = 0.0 \rightarrow 0.3$ m/s. A conservative prediction uncertainty of 35% would still be applicable.

Unfortunately, attempts at simulating a much smaller "island-scale" domain did not produce any suitable results. The method of extracting surface profiles from the full-scale simulations and applying them as boundary conditions in the island-scale domain is believed to be sound, but the meshes were too different for the smaller domain simulations to converge correctly. The hidden nature of some of the settings in ANSYS Fluent led to challenges and complications during the mesh generation phase.

Finally, in terms of post-processing, all the wind direction simulations have been combined into a single wind velocity map. The map has been generated by weighting each of the simulations by the frequency of wind prevalence in the corresponding wind sector. A second turbulence intensity map has also been provided using similar techniques. These maps, as well as the individual wind maps showing all 16 cardinal wind directions, are believed to be helpful to many future biological studies on MI as well as any possible forays into wind energy generation on the island.

Any simulation data that were used in this chapter have since been inserted into a database for any future work.

© University of Pretoria

7 Conclusion

This Chapter concludes the study on modelling the wind patterns across Marion Island using CFD. The fine-scale wind simulations have been performed and validated, with varying degrees of success, in order to deliver a baseline CFD wind model that can be used in future biological and geographical studies on the island.

7.1 Objectives

On the whole, the original objectives of this study were to achieve a base-line predictive wind model for simulating wind patterns on MI and to compile any results into a format which would be useful to future researchers in the field, both of which have been achieved satisfactorily. Table 7.1 recounts the complete list of objectives given in Chapter 1.

Table 7.1: Full list of objectives achieved in the current study

Objectives	Achieved
• Review available literature on the subject of Atmospheric Boundary Layer (ABL) modelling.	✓
• Understand how other researchers in the field have approached similar problems and build on their insights to develop a strategy for modelling the atmosphere in ANSYS Fluent 2019R3.	✓
• Test various aspects of the CFD model independently such that an understanding of the interaction between program settings and their subsequent outputs can be ascertained	✓
• Test any CFD model settings on smaller and simpler problems first.	✓
• Identify any shortcomings in the developed model through performing case studies with published datasets and comparing the results to those of other researchers.	✓
• Find where the model can be improved or where caution should be taken to reduce the chance of producing invalid results.	✓
• Simulate the wind patterns on Marion Island using the CFD insights gained thus far.	✓
• Critically asses any results, comparing them with realistic measurements to validate the models.	✓
• Use the CFD results to generate useful colour maps of flow variables around the island.	✓
• Package any maps generated as a consequence of this study such that they may be used by researchers in future studies.	✓

© University of Pretoria

7.2 Wind Measurement

An experimental wind measurement campaign was executed to gather reliable data from 17 locations around MI and thus have a point of reference to compare and validate any future simulation results. The entire experimental dataset was vetted for erroneous readings and compiled into a database for ease of use. The campaign was subject to the following limiting factors:

- Measurement equipment was not authorised to stand more than one meter above ground level for fear of damaging sensitive fauna and flora in the environment.
- No wind measurements were available for locations out at sea, meaning that incoming wind boundary conditions had to be extrapolated from coastal stations.
- Harsh environmental factors were responsible for intermittent interruptions in the data-stream, making it all the more difficult to correlate experimental readings across large spatial and temporal scales.

From the outset it was clear that the chosen experimental layout would be inadequate for supplying a comprehensive set of validation statistics; the chaotic turbulence alone, at a height of 1m AGL, would prove enough to shake one's confidence in getting a clean experimental wind reading. However, the stations were placed exactly within the region of interest; only low-altitude wind patterns were important in this study since that is what future researchers would find most useful. Strong wind turbulence at near-ground level was a well-known risk beforehand. So although it would be difficult to validate a CFD simulation against realistic patterns due to the high wind measurement variability, if any simulation could predict even ball-park accurate values in the region of interest then it can be considered a success.

7.3 Modelling Strategy

After an in-depth literature review of the wind modelling discipline as well as some simulation experimentation on smaller example cases, a final wind modelling approach was settled upon to complete this study:

- Only the stable ABL was modelled since it was determined that the hyper-oceanic climate surrounding MI would dominate any other thermal effects relating to atmospheric stability.
- The standard RANS equations were chosen to model a time-averaged wind solution on the island to make the best use of computational resources. High frequency experimental measurement equipment was also not available to validate any would-be transient simulations.

© University of Pretoria

- A modified version of the k-ε turbulence closure scheme was used due to its simplicity and easy understanding. Other turbulence schemes were investigated but never fully implemented in this study.

- The Coriolis force was accounted for in the final simulation runs since it has a significant impact on atmospheric flows at the large scale seen here. It was regarded as negligible in the precursory investigations.

- Work in chapter 3 proved that the boundary inlet Equations presented by Richards and Norris (2011) would be adequate for the current application on MI. The goal of these Equations was to simulate a Horizontally Homogeneous Turbulent Surface Layer (HHTSL) that would propagate throughout the domain with as little degradation as possible.

- Boundary treatment of any wall surfaces was left to built-in ANSYS scalable wall functions.

Testing the full numerical setup on Bolund Island as a smaller proxy for MI showed that the chosen methods have some limitations. Particularly regarding turbulence modelling, the solver tends to under-predict TI as a result of the k-ε closure scheme assuming an isotropic state of turbulence. However, for the simplicity that it brings, this method was deemed to be suitable for the application and gave reasonable approximations of realistic wind patterns.

7.4 Simulation Findings

A full-scale simulation domain was built around MI and its nearby surroundings, including the neighbouring Prince Edward Island. The full-scale domain was intended to capture any mesoscale weather phenomena in the upper reaches of the atmosphere as well as fine-scale ground level activity down to a horizontal resolution of 30m. This task proved difficult and extremely time- and resource-consuming due to the range of orders of magnitude present in the problem. In this regard, it became abundantly clear that the chosen modelling methods are unsuitable for accurately simulating mesoscale weather phenomena without further input data. Focus was therefore concentrated on accurately predicting surface-flow phenomena.

Validation of the CFD results against measurements was successful but not entirely convincing. Depending on the simulated wind direction, some results were incredibly accurate while others had prediction error of up to 35%. Despite the high variability in results, an effort was made to find ways of classifying scenarios where the error could be expected to peak and thus avoid those situations if possible. Underestimating the impact of the Coriolis Effect on wind deflection was brought forward as a major contributor to error. However, it is not known at this stage what portion of the error can be attributed CFD modelling limitations and what can be attributed to faults in the experimental measurements as a result of the restrictions discussed. Although there is ample room for improvement, achieving wind predictions within an envelope of 35%

© University of Pretoria

error is a remarkable achievement that can still lead to numerous discoveries at a destination where reliable wind data have been non-existent until now.

7.5 Closing Thoughts

With all being said and done, there is still significant value in obtaining the CFD results despite the deficiencies. These results will be valuable as a foundation for upcoming work. The future of the MI wind project is packed with ideas and new proposals for moving forward from here; both, in the purely engineering focused discipline of modelling new climatic scenarios and pollution dispersal, as well as for the ecologically focused disciplines using said CFD models as a tool to assess the environmental impacts of wind on flora and fauna.

This project has highlighted where future CFD attempts can be improved in order to produce a compelling approximation of the realistic atmospheric phenomena occurring in the Marion Island territory. While error cannot be avoided when modelling such complex systems, it has been well quantified and discussed so that any further research may make informed judgements in future studies. The CFD simulations can certainly be interrogated and used by ecologists to draw worthwhile conclusions in their own work regarding wind impacts on the environment, provided that they apply a healthy dose of caution when accounting for prediction error.

© University of Pretoria

8 Future Work and Recommendations

This study is only the starting point, a first iteration, of a much larger project which will hopefully proceed over many years to come and span multiple academic disciplines. As such, there are many avenues for future work that have sprouted from here; the scope of this study simply could not cover everything. This section gives details for the engineering-specific aspects of this study which could benefit from extra attention in the future.

While modelling fluid dynamics interactions, a multitude of CFD simulation techniques have been developed through the years for treating different modelling scenarios; each with their various advantages and disadvantages. One aspect that remains unchanged across any study is that all computer simulated solutions need to be tested and verified against a reliable set of measured data. In this respect, there are a few recommendations which would substantially improve future validation exercises pertaining to modelling wind patterns across MI:

- Rather than placing a widespread fleet of stations over the island, emphasis should be made on building taller masts to retrieve wind data from higher altitudes. The turbulent wall interactions anywhere below 10 meters AGL are too chaotic to capture any meaningful wind measurements.

- 3D wind measurements would be preferable to the 2D measurements that were available to this study. Attempts were made to install 3D sensors during 2019 but the retrieved data were not yet comprehensive enough to be used much in this study.

- If permission to install sufficiently tall masts is not granted by the relevant environmental authorities in future discussions, a LIDAR sensor would be the perfect instrument for capturing 3D wind velocity and turbulence profiles from ground level all the way up to lower atmospheric heights. Although this suggestion is expensive, it need only be done at two or three locations around the island rather than at all 17 station locations currently in use.

- It would be helpful to have a station floating in the sea at a distance westward of MI. Whether it be placed on a permanent buoy or temporarily on the deck of a ship, the incoming wind data from this direction would be immensely helpful in calculating the simulated inlet wind conditions. Attempts were made in this study to retrieve the data captured by the meteorological team present on the SA Agulhas II (ship) whilst it was anchored near MI during the takeover weeks. However, this data was not useful at the time since the wind stations had not been installed on the island yet; there was no way to correlate the two bodies of data.

Towards the end of this study, attempts were made to drastically reduce domain size and focus on only simulating those parts of the MI that were important to the work at hand. While they

© University of Pretoria

did not go as well as expected, these types of island-scale simulations would be worth pursuing in the future. More effort could be put into generating a working mesh for these situations.

It is believed that the method of slicing the internal solution of a large-scale simulation and placing these flow values as boundary conditions at the inlet of a smaller scale simulation was a viable strategy. However, not enough information was available to make a final scrutiny possible in this study. If this "cut-and-paste" method of applying boundary conditions is verified to work well, future researchers would be able to go further in reducing domain size. This can happen incrementally until a point where wind patterns around lone geographical features could be modelled to the exclusion of the rest of MI and its surrounds; an exclusive simulation of Grey Headed Ridge, for example. These so called "landform-scale" simulations would make possible the detailed studies of individual bird nesting sites or plant seed dispersal activities down to an extremely fine scale.

Alternative turbulence modelling schemes were not given too much attention in this study after the modified k-ε modelling approach was found. The shortcomings of this approach were thoroughly discussed and understood by the time final simulations were being performed. However, there are dozens of other similarly applicable methods for accurately modelling turbulence in the ABL; some of which may even be better suited than the chosen k-ε closure scheme. It is suggested that future work pursue this venture; not only to find a better RANS turbulence closure scheme but also to perform transient turbulent simulations with the like of LES/DES. Turbulence scale-resolving simulations (SRS) such as these would provide rich topics for even more advanced studies down the line.

Finally, the topic of underestimating the effect of the Coriolis force needs to be addressed. To counteract the disagreements between CFD and experimental data under the circumstances noted in Section 6.6, there are various options available for further validation efforts:

- Using the difference between a full CFD simulation and its corresponding non-Coriolis counterpart, the wind deflection can be quantified as a result of numerically implementing the Coriolis effect. The deviation can then be added to any results as an adjustment factor to compensate for uncertainty.

- Keep the already extracted experimental dataset intact for a given case but compare the data to a CFD simulation from a *different* wind sector; one where the Coriolis spiralling has culminated in a surface level wind flow that falls within the same sector as the experimental dataset. As an example, compare the WNW wind simulation with the experimental results corresponding to an observed north-westerly surface wind. Since all 16 wind sectors have already been modelled and simulated to convergence, one would simply have to choose the best fitting CFD results to compare with the measured data.

- Conversely to the point above, the experimental data can be reinterpreted following the same procedure as outlined in Section 4.4 but with the additional allowance for deviation

© University of Pretoria

at the surface level caused by the Coriolis force. i.e. keep the CFD data intact for say a north-westerly simulation but compare the results against a new experimental dataset corresponding to surface winds on MI within the NNW sector.

- Finally, one could resort to performing a full-scale optimisation exercise to tweak the approaching wind at the applied boundary conditions until the simulated *surface level* winds follow a precise heading across MI. This would entail modifying the vertical boundary condition profiles into "reverse Ekman spirals" at any inlet faces and a similarly counter-rotated top boundary condition such that the surface level winds flow in a continuous direction unless otherwise acted upon.

The points mentioned here are by no means an extensive list of all the possible future work that could stem from this masters study. They are merely an engineering-biased view of what the author would have liked to pursue if time and budget had allowed for further research on this topic.

There are, of course, many more downstream applications for the generated simulation results to appear in. Ecological and geographical studies on MI are numerous, not to mention the interesting possibility of using wind data to aid the upcoming mouse eradication programme.

© University of Pretoria

References

Abkar, M. and Porte-Agel, F. (2015), 'Influence of atmospheric stability on wind-turbine wakes: A large-eddy simulation study', *Physics of Fluids* **27**(3), 1–20.

Aly, A. M. (2014), 'Atmospheric boundary-layer simulation for the built environment : Past , present and future', *Building and Environment* **75**, 206–221.

ANSYS (2013), 'ANSYS Fluent User ' s Guide', **15**(November), 724–746.

ANSYS (2018), 'ANSYS Fluent Theory Guide'.

ANSYS (2019), White paper: Ansys fluent mosaic technology automatically combines disparate meshes with polyhedral elements for fast, accurate flow resolution, Technical report, ANSYS Inc.

Balogh, M. and Parente, A. (2015), 'Realistic boundary conditions for the simulation of atmospheric boundary layer flows using an improved k-ϵ model', *Journal of Wind Engineering and Industrial Aerodynamics* **144**, 183–190.

Bechmann, A., Berg, J., Courtney, M. S., Hans, E. J., Mann, J. and Sørensen, N. N. (2009), *The Bolund Experiment : Overview and Background*, Vol. 1658.

Bechmann, A., Johansen, J. and Sørensen, N. N. (2007a), 'The Bolund Experiment -Design of Measurement Campaign using CFD.', *Risø National Laboratory Technical University of Denmark Roskilde, Denmark* **1623**(December).

Bechmann, A., Mann, J., Johansen, J., Sørensen, N. N. and Sørensen, J. N. (2007b), Large-eddy simulation of atmospheric flow over complex terrain, Technical report, Risø National Laboratory.

Berg, J., Mann, J., Bechmann, A., Courtney, M. and Jørgensen, H. E. (2011), 'The bolund experiment, part i: flow over a steep, three-dimensional hill', *Boundary-Layer Meteorology* **141**(2), 219.

Berge, E., Gravdahl, A. R., Schelling, J., Tallhaug, L. and Undheim, O. (2006), Wind in complex terrain. a comparison of wasp and two cfd-models, *in* 'Proceedings from EWEC', Vol. 27.

Blocken, B. (2014), 'Journal of Wind Engineering 50 years of Computational Wind Engineering : Past , present and future', *Journal of Wind Engineering and Industrial Aerodynamics* **129**, 69–102.

Blocken, B., Stathopoulos, T. and Carmeliet, J. (2007), 'Cfd simulation of the atmospheric boundary layer: wall function problems', *Atmospheric environment* **41**(2), 238–252.

Castro, F. A., Santos, C. M. S. and Palma, J. M. (2008), Parallelisation of the cfd code of a cfd-nwp coupled system for the simulation of atmospheric flows over complex terrain, *in*

© University of Pretoria

'International Conference on High Performance Computing for Computational Science', Springer, pp. 27–38.

Çengel, Y. A. and Ghajar, A. J. (2015), *Heat and mass transfer: fundamentals and applications*.

Chown, S. and Froneman, P. W. (2008), *The Prince Edward Islands: land-sea interactions in a changing ecosystem*, 1 edn, African Sun Media.

Crasto, G. (2007), 'Numerical simulations of the atmospheric boundary layer', *Universita degli Studi di Cagliari: Cagliari, Italy* .

Crutcher, H. L. (1957), 'On the standard vector-deviation wind rose', *Journal of Meteorology* **14**(1), 28–33.

DTU (2015), 'Ellipsys2d/3d - the numerical wind tunnel english', `http://www.the-numerical-wind-tunnel.dtu.dk/EllipSys`. (Accessed on 03/10/2018).

Garratt, J. R. (1994), *The atmospheric boundary layer*, Cambridge Univ. Press.

Gibson, M. and Launder, B. (1978), 'Ground effects on pressure fluctuations in the atmospheric boundary layer', *Journal of Fluid Mechanics* **86**(3), 491–511.

Hargreaves, D. M. and Wright, N. G. (2007), 'On the use of the k-ε model in commercial CFD software to model the neutral atmospheric boundary layer', *Journal of Wind Engineering and Industrial Aerodynamics* **95**(5), 355–369.

Jackson, P. and Hunt, J. (1975), 'Turbulent wind flow over a low hill', *Quarterly Journal of the Royal Meteorological Society* **101**(430), 929–955.

Juretić, F. and Kozmar, H. (2013), 'Computational modeling of the neutrally stratified atmospheric boundary layer flow using the standard k-ε turbulence model'.

Katul, G. G., Mahrt, L., Poggi, D. and Sanz, C. (2004), 'One-and two-equation models for canopy turbulence', *Boundary-Layer Meteorology* **113**(1), 81–109.

Koblitz, T. (2013), *CFD Modeling of Non-Neutral Atmospheric Boundary Layer Conditions*, Vol. 0019.

Launder, B. E. and Spalding, D. B. (1983), The numerical computation of turbulent flows, *in* 'Numerical Prediction of Flow, Heat Transfer, Turbulence and Combustion', Elsevier, pp. 96–116.

le Roux, P. C. (2008), Climate and climate change, *in* S. Chown and P. W. Froneman, eds, 'The Prince Edward Islands: land-sea interactions in a changing ecosystem, *Chapter 3*', 1 edn, African Sun Media, pp. 39–64.

Longo, S. (2012), 'Wind-generated water waves in a wind tunnel: Free surface statistics, wind friction and mean air flow properties', *Coastal Engineering* **61**, 27–41.

Manwell, J., McGowan, J. and Rogers, A. (2009), *Wind Energy Explained: Theory, Design and Application*, John Wiley & Sons.

Marshall, E. M. and Bakker, A. (2004), 'Computational fluid mixing', *Handbook of industrial mixing: science and practice* pp. 257–343.

© University of Pretoria

Meissner, C., Gravdahl, A. R. and Steensen, B. (2009), Including thermal effects in cfd simulations, *in* 'European Wind Energy Conference and Exhibition'.

Menter, F. R. (1994), 'Two-equation eddy-viscosity turbulence models for engineering applications', *AIAA journal* **32**(8), 1598–1605.

Monin, A. and Obukhov, A. (1954), 'Basic laws of turbulent mixing in the surface layer of the atmosphere', *Contrib. Geophys. Inst. Acad. Sci. USSR* **151**(163), e187.

NASA Worldview application (2000-2018), 'EOSDIS Worldview', `https://worldview.earthdata.nasa.gov/`. (Accessed on 2018-10-11).

O'Sullivan, J. P., Archer, R. A. and Flay, R. G. J. (2011), 'Journal of Wind Engineering Consistent boundary conditions for flows within the atmospheric boundary layer', *Journal of Wind Engineering and Industrial Aerodynamics* **99**(1), 65–77.

Parente, A., Gorlé, C., van Beeck, J. and Benocci, C. (2011), 'Improved k-ϵ model and wall function formulation for the RANS simulation of ABL flows', *Journal of Wind Engineering & Industrial Aerodynamics* **99**(4), 267–278.

Pearson, K. (1896), 'Vii. mathematical contributions to the theory of evolution.—iii. regression, heredity, and panmixia', *Philosophical Transactions of the Royal Society of London. Series A, containing papers of a mathematical or physical character* (187), 253–318.

Peña, A. and Gryning, S.-E. (2008), 'Charnock's roughness length model and non-dimensional wind profiles over the sea', *Boundary-Layer Meteorology* **128**(2), 191–203.

Richards, P. and Hoxey, R. (1993), Appropriate boundary conditions for computational wind engineering models using the k-ε turbulence model, *in* 'Computational Wind Engineering 1', Elsevier, pp. 145–153.

Richards, P. J. and Norris, S. E. (2011), 'Journal of Wind Engineering Appropriate boundary conditions for computational wind engineering models revisited', *Journal of Wind Engineering and Industrial Aerodynamics* **99**(4), 257–266.

Richards, P. J. and Norris, S. E. (2015), 'Journal of Wind Engineering Appropriate boundary conditions for a pressure driven boundary layer', *Journal of Wind Engineering and Industrial Aerodynamics* **142**, 43–52.

Roache, P. J., Ghia, K. N. and White, F. M. (1986), 'Editorial policy statement on the control of numerical accuracy'.

Schlatter, P. and Örlü, R. (2010), 'Assessment of direct numerical simulation data of turbulent boundary layers', *Journal of Fluid Mechanics* **659**, 116–126.

Schlichting, H. (1979), *Boundary-layer theory*, Springer.

Shih, T.-H., Liou, W. W., Shabbir, A., Yang, Z. and Zhu, J. (1995), 'A new k-*varepsilon* eddy viscosity model for high reynolds number turbulent flows', *Computers & Fluids* **24**(3), 227–238.

Smith, V. and Steenkamp, M. (1990), 'Climatic change and its ecological implications at a subantarctic island', *Oecologia* **85**(1), 14–24.

© University of Pretoria

Stull, R. B. (1988), Mean boundary layer characteristics, *in* 'An Introduction to Boundary Layer Meteorology', Springer, pp. 1–27.

Vasaturo, R., Kalkman, I., Blocken, B. and Wesemael, P. J. V. V. (2017), 'Large eddy simulation of the neutral atmospheric boundary layer: performance evaluation of three in flow methods for terrains with different roughness', *Journal of Wind Engineering & Industrial Aerodynamics* **173**(December 2017), 241–261.

Veron, F., Saxena, G. and Misra, S. (2007), 'Measurements of the viscous tangential stress in the airflow above wind waves', *Geophysical Research Letters* **34**(19).

Versteeg, H. K. and Malalasekera, W. (2007), *An introduction to computational fluid dynamics: the finite volume method*, Pearson Education.

Vladut, A. C., Cosoiu, C. I., Georgescu, A. M., Degeratu, M. and Damian, R. M. (2016), 'Wind Tunnel and Numerical Modeling of Atmospheric Boundary Layer Flow over Bolund Island', *Energy Procedia* **85**(November 2015), 603–611.

Wallace, J. M. and Hobbs, P. V. (2006), *Atmospheric science: an introductory survey*, Vol. 92, Elsevier.

Weber, R. O. (1999), 'Remarks on the definition and estimation of friction velocity', *Boundary-Layer Meteorology* **93**(2), 197–209.

White, A. A. and Bromley, R. (1995), 'Dynamically consistent, quasi-hydrostatic equations for global models with a complete representation of the coriolis force', *Quarterly Journal of the Royal Meteorological Society* **121**(522), 399–418.

White, F. M. (2011), 'Fluid mechanics, in si units'.

Wilcox, D. C. *et al.* (1998), *Turbulence modeling for CFD*, Vol. 2, DCW industries La Canada, CA.

Wood, N. (2000), 'Wind flow over complex terrain: A historical perspective and the prospect for large-eddy modelling', *Boundary-Layer Meteorology* **96**(1-2), 11–32.

Wu, J. (1975), 'Wind-induced drift currents', *Journal of Fluid Mechanics* **68**(1), 49–70.

Yakhot, V. and Orszag, S. A. (1986), 'Renormalization group analysis of turbulence. i. basic theory', *Journal of scientific computing* **1**(1), 3–51.

Yang, Y., Gu, M., Chen, S. and Jin, X. (2009), 'New inflow boundary conditions for modelling the neutral equilibrium atmospheric boundary layer in computational wind engineering', *Journal of Wind Engineering and Industrial Aerodynamics* **97**(2), 88–95.

Yeow, T. S., Cuerva, A., Conan, B. and Pérez-Álvarez, J. (2014), 'Wind tunnel analysis of the detachment bubble on Bolund Island', *Journal of Physics: Conference Series* **555**(1).

Zhang, X. (2009), *CFD simulation of neutral ABL flows*, Vol. 1688.

© University of Pretoria

A Commonly Used Roughness Lengths

Table A.1: Commonly used roughness lengths (Manwell *et al.*, 2009)

Terrain	z_0 [mm]
Very smooth, ice or mud	0.01
Calm open sea	0.2
Blown sea	0.5
Snow surface	3
Lawn grass	8
Rough pasture	10
Fallow field	30
Crops	50
Few trees	100
Many trees, hedges, few buildings	250
Forest and woodlands	500
Suburbs	1500
City centres with tall buildings	3000

© University of Pretoria

B A Brief Note on Dimensional Analysis

As an exercise, one could easily estimate a Reynolds number for flow around Marion Island using Equation 2.46 and the properties of air at a mean temperature of $T \approx 10°C$ (values adapted from (Çengel and Ghajar, 2015)). Based on the hill height of Marion Island as the characteristic length, $h \approx 1.2km$, there is virtually no hope of ever experiencing laminar wind patterns in that location:

$$Re = \frac{(1.246[kg/m^3]) \times (V_\infty[m/s]) \times (1.2 \times 10^3[m])}{(1.778 \times 10^{-5}[Pa.s])}$$

A freestream velocity of $V_\infty = 1.2 \times 10^{-2} m/s$ would be required in order to satisfy the laminar Reynolds number threshold; something unheard of in the Roaring Forties latitudes.

Note that the Reynolds number has no unit of measurement; it is completely dimensionless since it is a ratio of variables whose units cancel out. More than simply estimating flow regimes, non-dimensional parameters like the Reynolds number are commonly used to compare similar experimental datasets gathered from seemingly mismatched experimental cases.

Figure B.1 provides an illustrative example pulled from the Fluid Mechanics textbook (White, 2011) showing how non-dimensionalised parameters can compactly yet simply relay information. In this particular case, the Strouhal number contains size, velocity and frequency information regarding turbulent vortex shedding behind a bluff body (White, 2011). The Reynolds number, as discussed, contains fluid property information as well as flow speed and length-scale information. As a testament to the power of dimensional analysis, all the mentioned information can be plotted on the basic 2D axis shown in Figure B.1b. Furthermore, the non-dimensional data from multiple vortex shedding experiments can be reasonably compared even if completely different fluid conditions were present or varying sizes of bluff body were used to generate the data.

Although the concepts of vortex shedding and the Strouhal number are beyond the scope of the current project, Figure B.2 shows a satellite image of vortex shedding at atmospheric scales across MI, seen through a cloud topping (NASA Worldview application, 2000-2018). This is shown below to further cement the fact that dimensional analysis can be a powerful tool, applicable to analysing a vast majority of fluid dynamics problems despite glaring differences.

© University of Pretoria

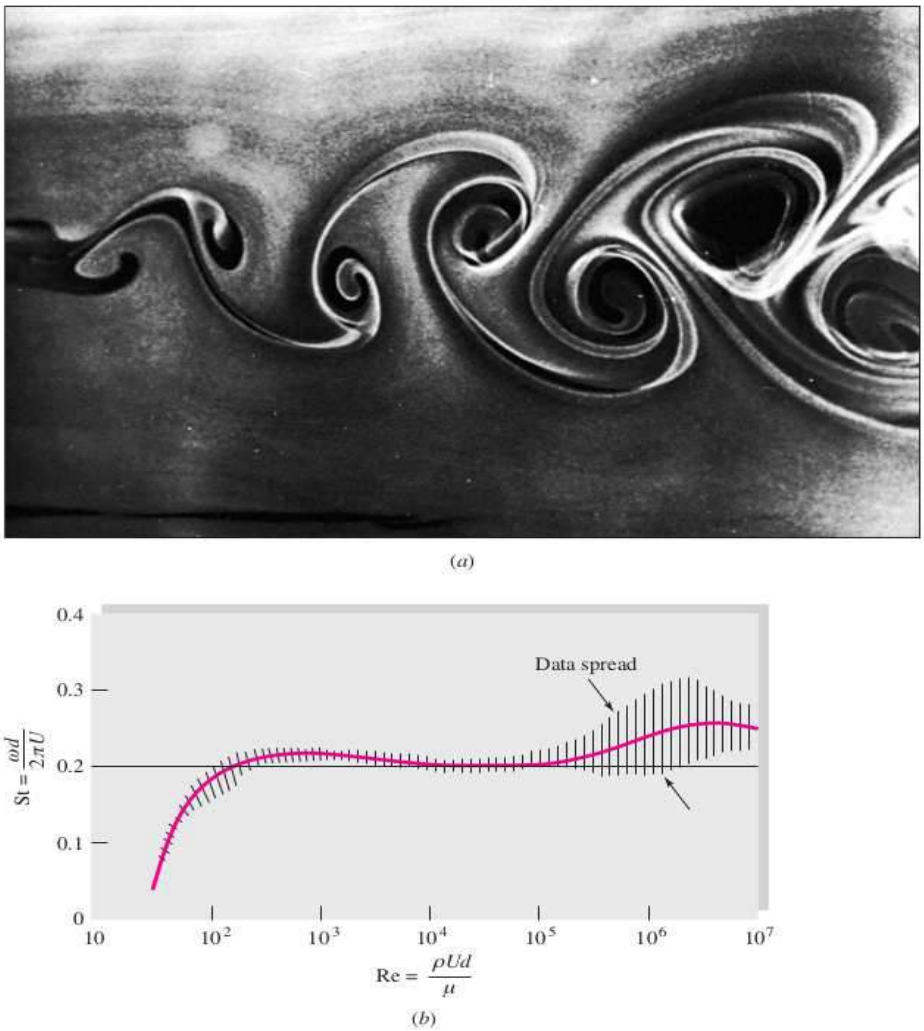

Figure B.1: A textbook example showing the use of non-dimensional quantities, *Re* and *St* numbers, to analyse size, frequency and speed of vortex shedding behind a cylinder bluff body (a) by plotting the experimentally determined shedding frequency data in non-dimensional coordinates (b). (White, 2011)

Figure B.2: On a day with the right wind conditions and cloud layer height over Marion Island, vortex shedding can be seen from satellite imagery above. *Imagery from the NASA Worldview application (2000-2018) operated by the NASA/Goddard Space Flight Center Earth Science Data and Information System (ESDIS) project*

© University of Pretoria

C Improved Parente *et al.* (2011) Wall Function UDF

UDF script for the improved wall function formulation used in the empty domain test:

```
#include "udf.h"
#include "math.h"
/* Model Constants*/
#define Cmu 0.03
#define vonKarman 0.4
#define Rho 1.225 // [kg/m3] density of air
#define z0 0.0005 // [m] sea aerodynamic roughness length
DEFINE_WALL_FUNCTIONS(Parente, f, t, c0, t0, wf_ret, yPlus, Emod){
 real ustar_ground, E_prime, yPlus_prime, zp, wf_value;
 real mu=C_MU_L(c0,t0);
 zp = 0.025; // [m] height of first cell centroid
 // constant for the empty domain mesh but this would be more complicated
 // to calculate for a complex terrain simulation

 ustar_ground = pow(C_K(c0,t0),0.5)*pow(Cmu, 0.25);
 E_prime = (mu/Rho)/(z0*ustar_ground);
 yPlus_prime = (zp+z0)*ustar_ground/(mu/Rho);
 switch (wf_ret){
 case UPLUS_LAM:
 wf_value = yPlus;
 break;
 case UPLUS_TRB:
 wf_value = log(E_prime*yPlus_prime)/vonKarman;
 /*wf_value = log(Emod*yPlus)/vonKarman; Standard Fluent*/
 break;
 case DUPLUS_LAM:
 wf_value = 1.0;
 break;
 case DUPLUS_TRB:
 wf_value = 1.0/(vonKarman*yPlus_prime);
 break;
 case D2UPLUS_TRB:
 wf_value = -1.0/(vonKarman*yPlus_prime*yPlus_prime);
 break;
 default:
 printf("Wall function return value unavailable\n");
 }
 return wf_value;
}
```


© University of Pretoria

D Raw Wind Data

Table D.1: Sample of raw daily averaged data retrieved from Marion Island wind station #6 (Cape Davis)

TOA5	CR300Series 6	CR300	9406	CR300.Std.07.00
TIMESTAMP	RECORD	StationName	LoggerBatt Min	LoggerBatt Max
TS	RN		Volts	Volts
2018-03-27	0	Marion ST6	13.08	13.83
2018-05-13	1	Marion ST6	12.71	15.63
2018-05-14	2	Marion ST6	12.62	12.72

LoggerBatt Avg	LoggerTemp Min	LoggerTemp Max	LoggerTemp Avg
Volts	Deg C	Deg C	Deg C
13.25	22.53	26.07	23.64
13.09	3.72	11.72	6.914
12.68	3.127	5.325	4.207

WSpeed 1M Min	WSpeed 1M Max	WSpeed 1M Std	WSpeed 1M AVE
meters/second	meters/second	meters/second	meters/second
0	0.17	0.011	0.013
0	40.69	2.972	4.796
0	17.65	2.34	6.711

WindDir 1M AVE	WindDir 1M Std	WSpeed 05M Min	WSpeed 05M Max
Deg	Deg	meters/second	meters/second
36.64	67.52	0	0.15
257.5	52.1	0	13.34
246.8	13.13	0	13.42

WSpeed 05M Std	WSpeed 05M AVE	WindDir 05M AVE	WindDir 05M Std
meters/second	meters/second	Deg	Deg
0.01	0.014	208.5	54.7
2.275	3.748	247.4	51.12
1.926	4.981	236.4	14.96

© University of Pretoria

E Wind Roses Across MI

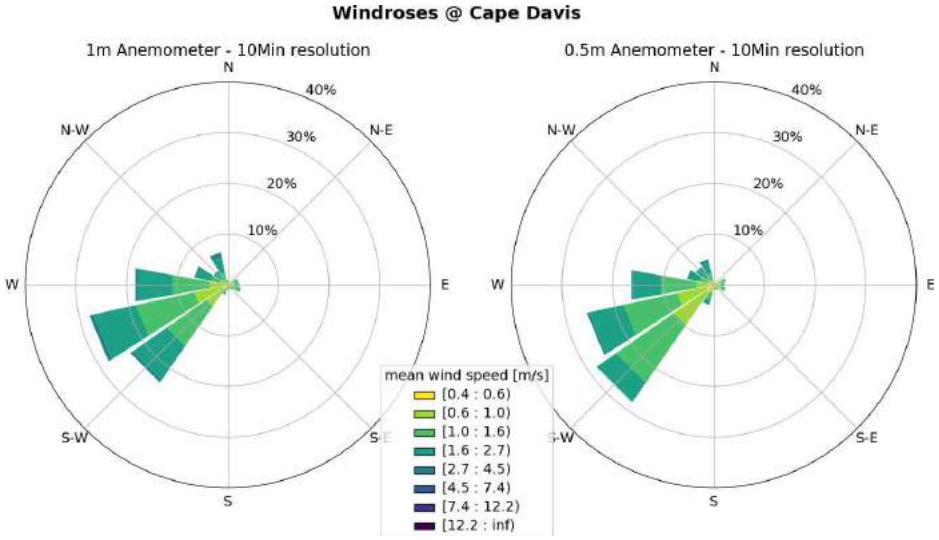

Figure E.1: Cape Davis wind rose diagrams

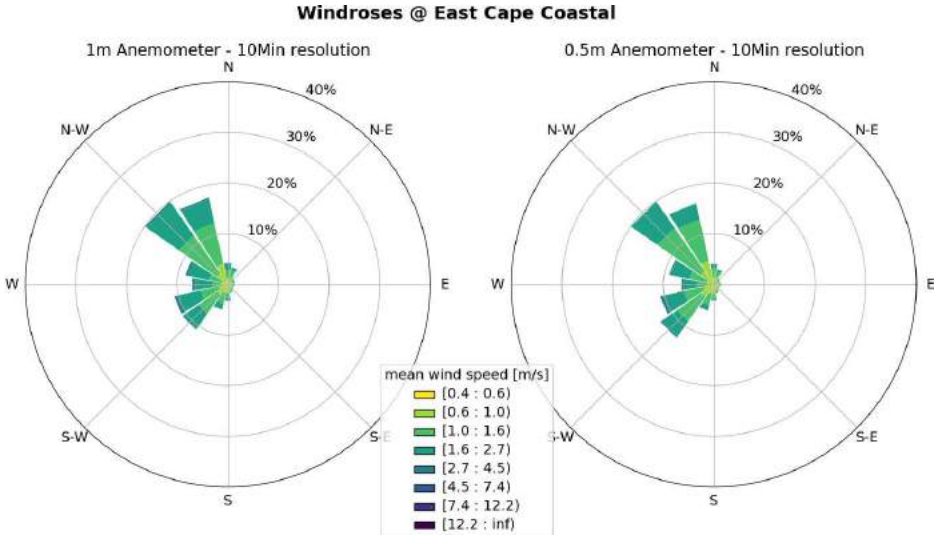

Figure E.2: East Cape Coastal wind rose diagrams

© University of Pretoria

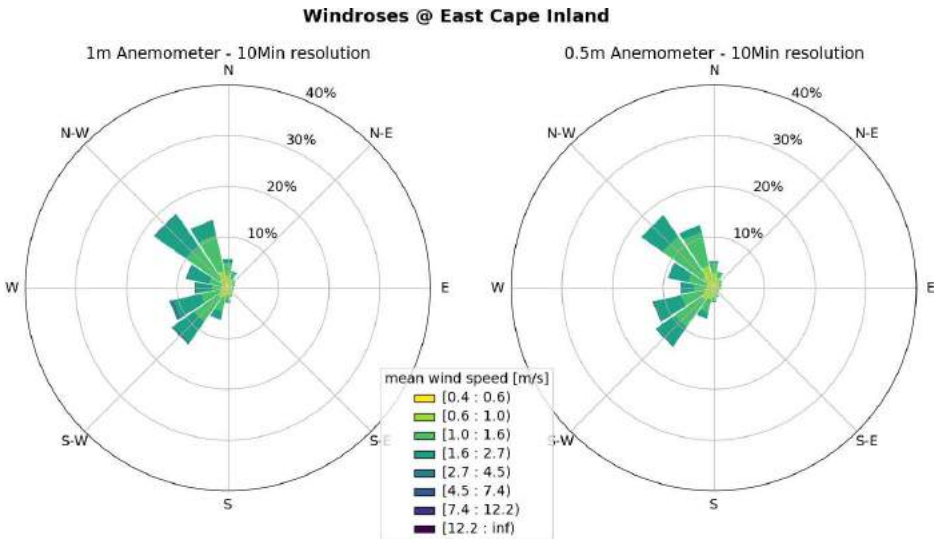

Figure E.3: East Cape Inland wind rose diagrams

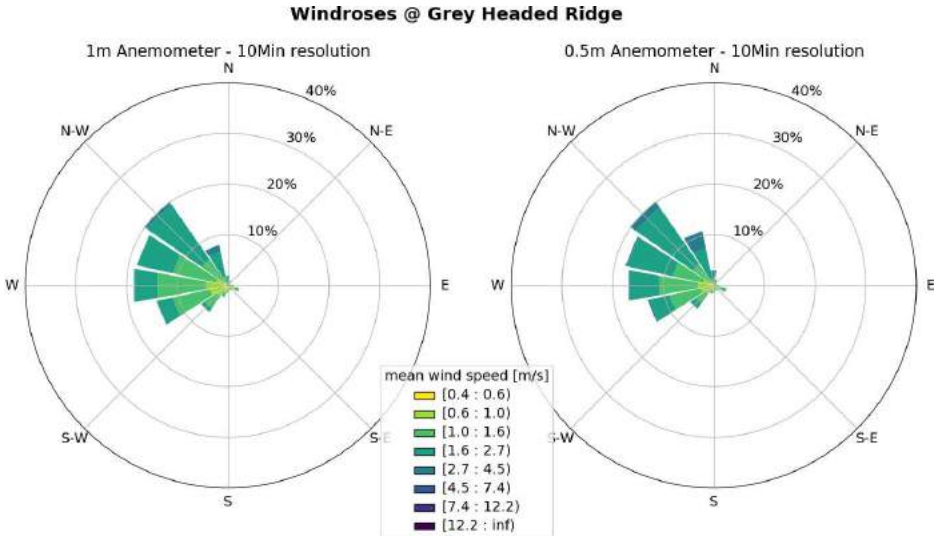

Figure E.4: Grey Headed Ridge wind rose diagrams

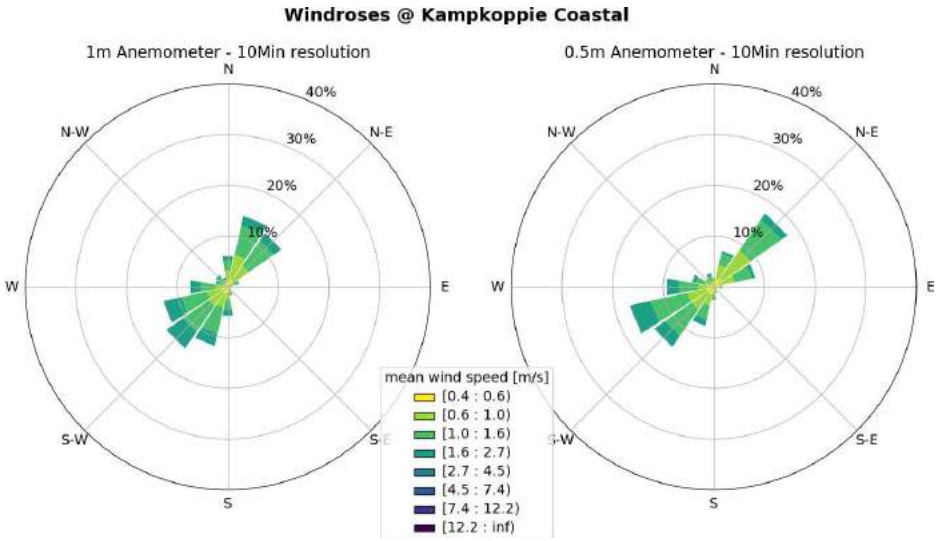

Figure E.5: Kampkoppie Coastal wind rose diagrams.

© University of Pretoria

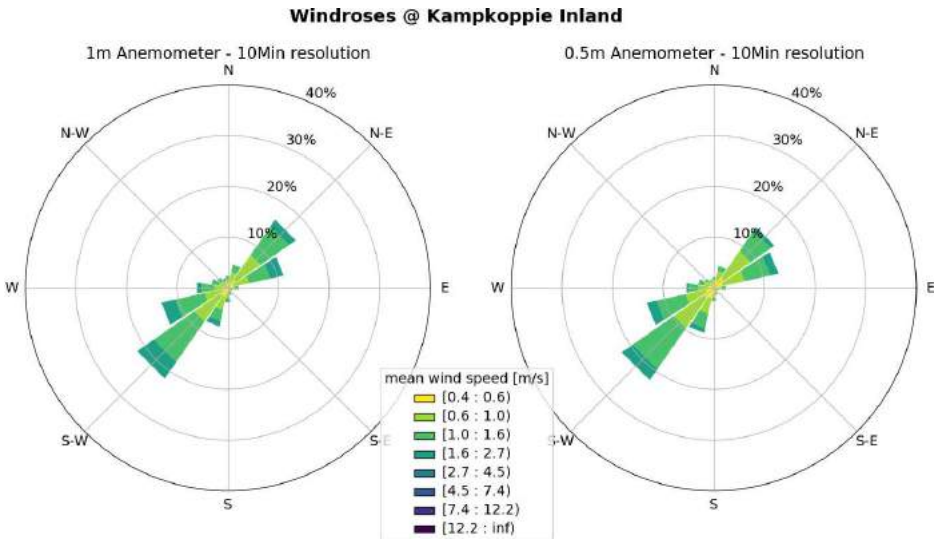

Figure E.6: Kampkoppie Inland wind rose diagrams.

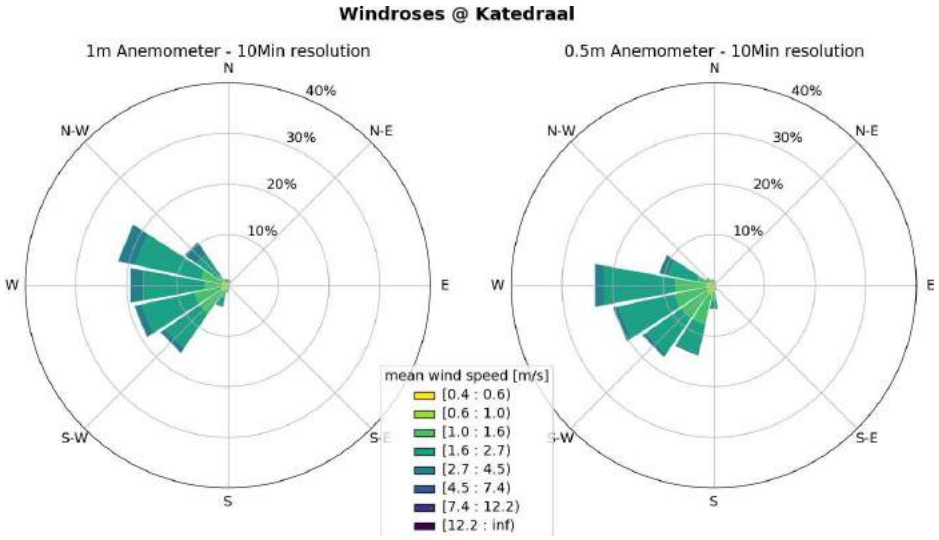

Figure E.7: Katedraal wind rose diagrams.

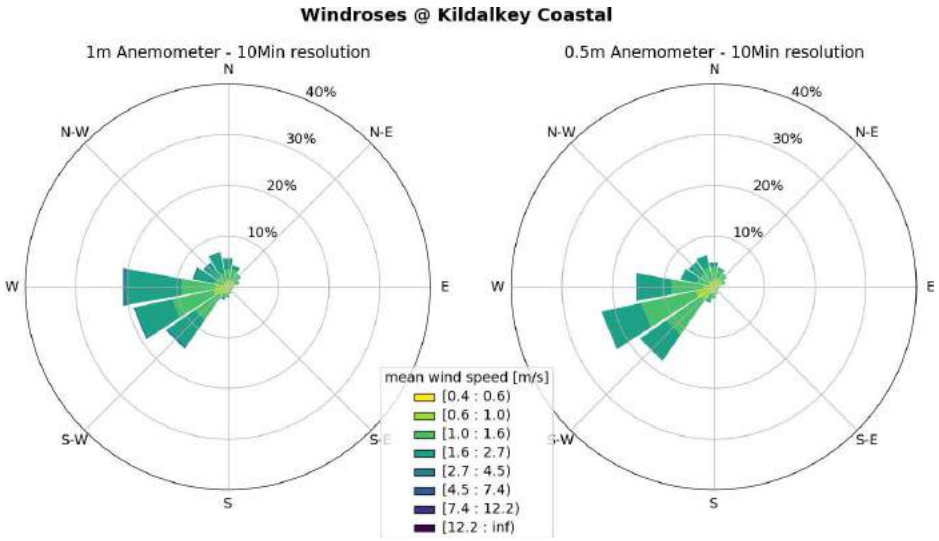

Figure E.8: Kildalkey Coastal wind rose diagrams.

© University of Pretoria

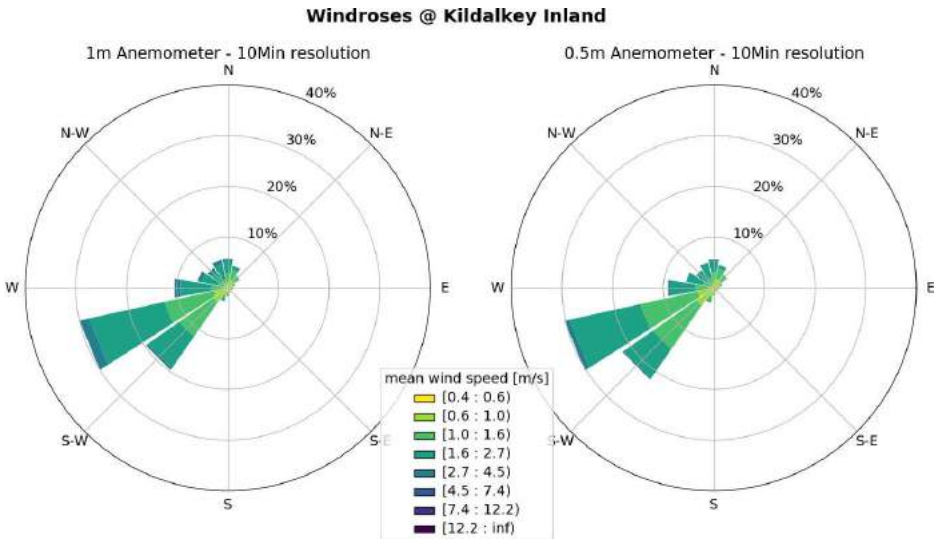

Figure E.9: Kildalkey Inland wind rose diagrams.

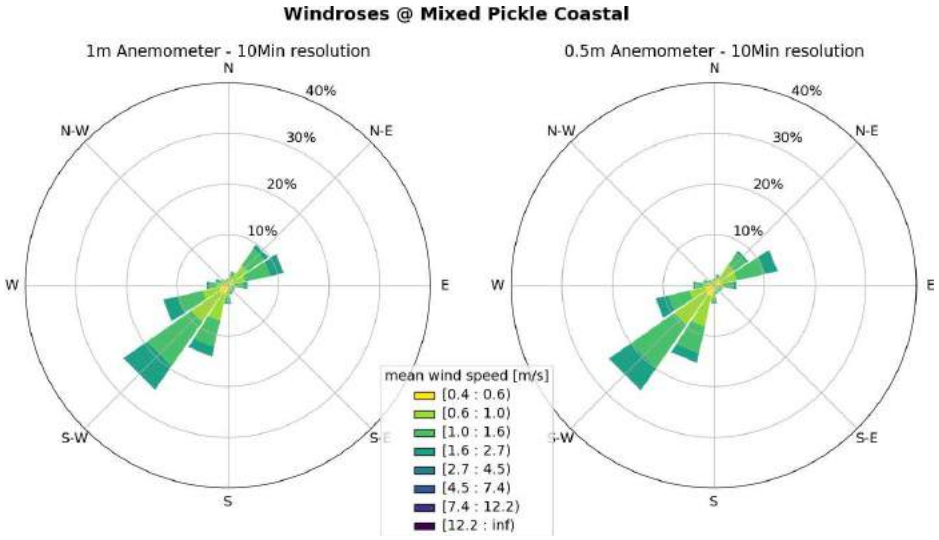

Figure E.10: Mixed Pickle Coastal wind rose diagrams.

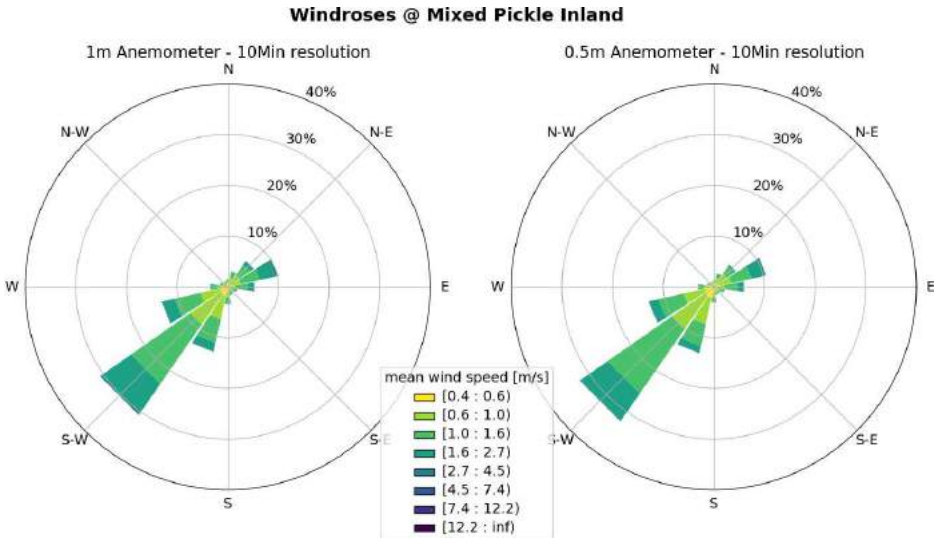

Figure E.11: Mixed Pickle Inland wind rose diagrams.

© University of Pretoria

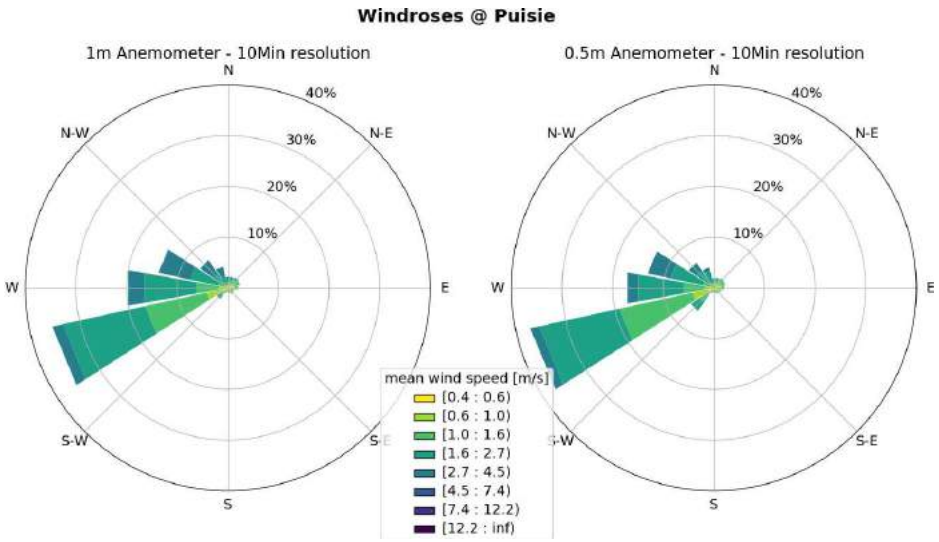

Figure E.12: Puisie wind rose diagrams.

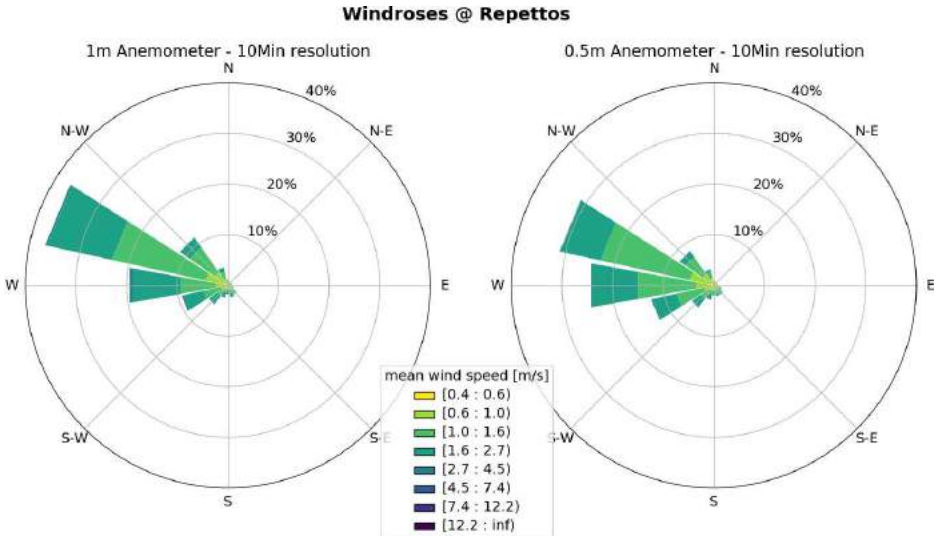

Figure E.13: Repettos wind rose diagrams.

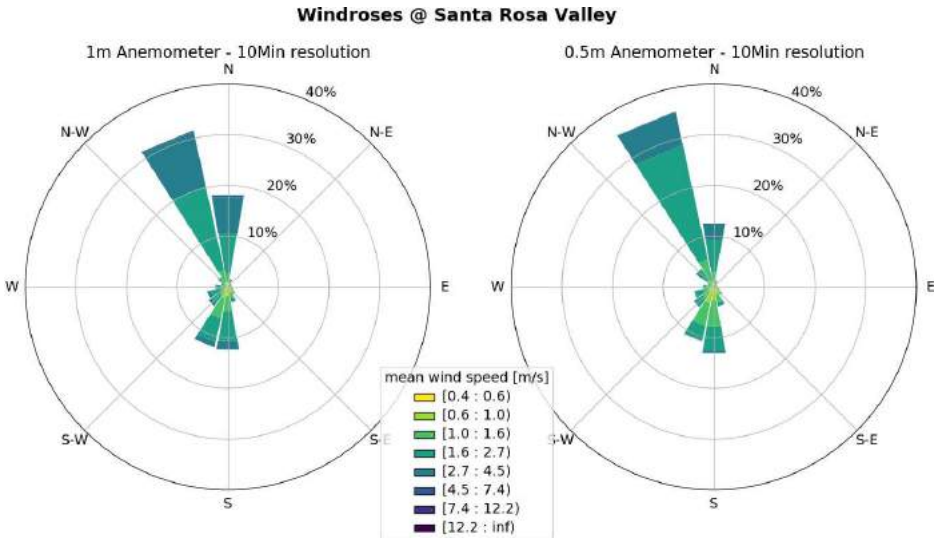

Figure E.14: Santa Rosa Valley wind rose diagrams.

© University of Pretoria

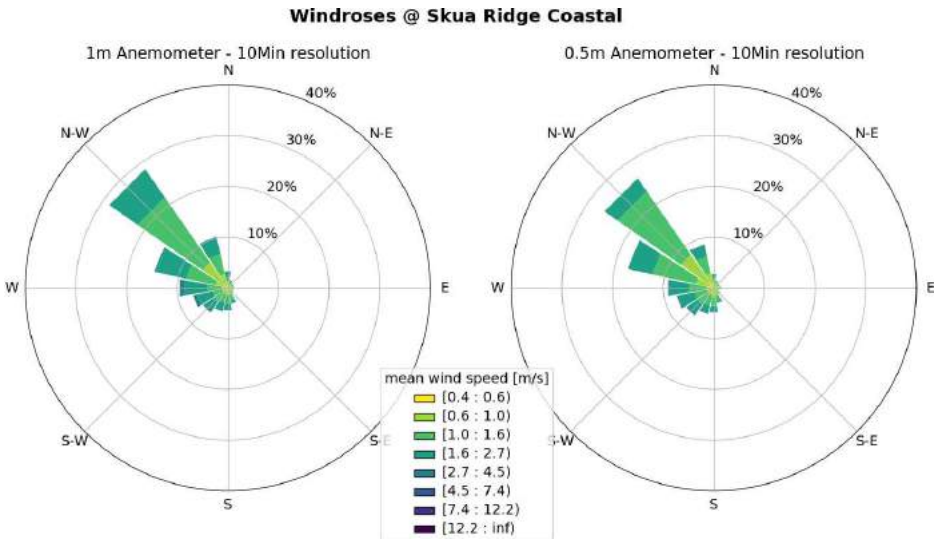

Figure E.15: Skua Ridge Coastal wind rose diagrams.

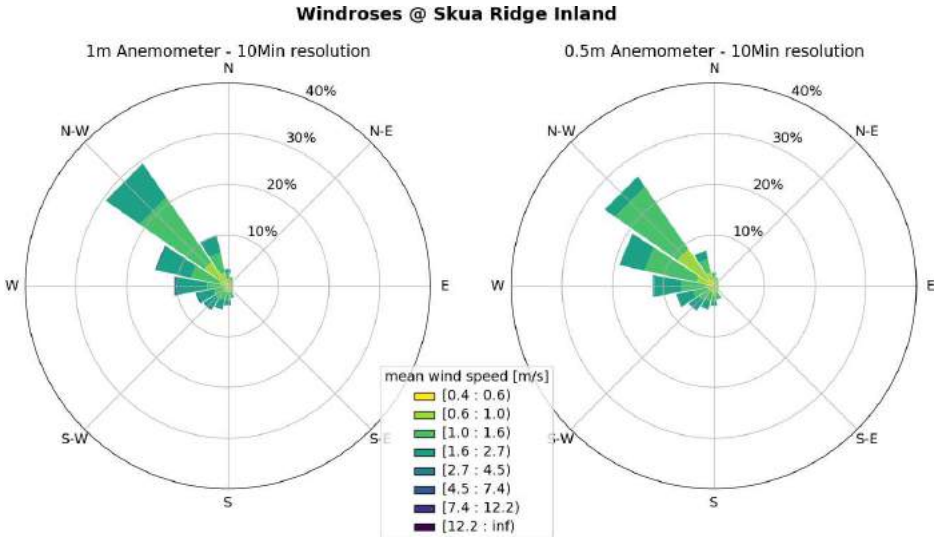

Figure E.16: Skua Ridge Inland wind rose diagrams.

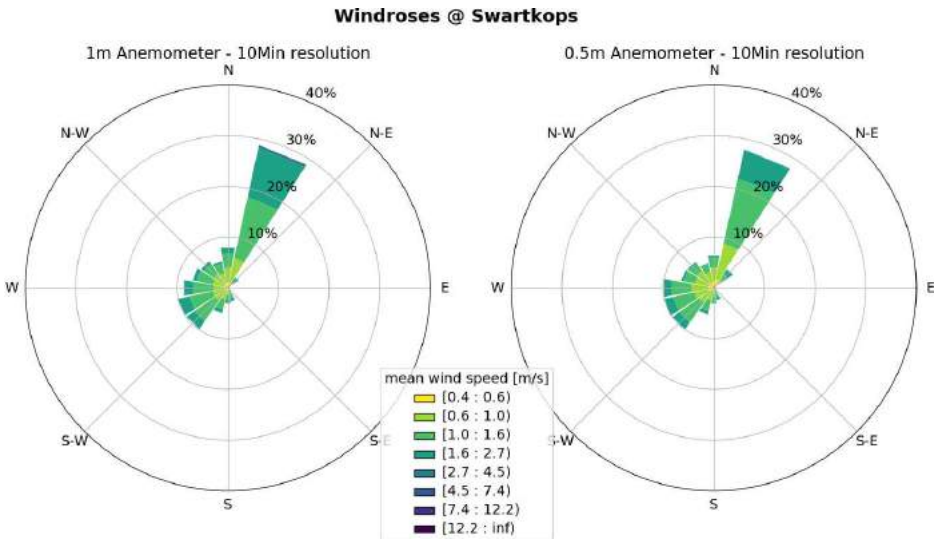

Figure E.17: Swartkops wind rose diagrams.

© University of Pretoria

F Mesh Generation Journals

Fluent Meshing journal used to generate the circle inner-domain around MI and PEI:

```
; Commented lines are preceded by a semi-colon.

; Import Marion Island STL geometry
/file/import/cad-geom
yes
"/mnt/lustre/users/kgoddard/Marion/MARION.stl"
y
m
cad-faceting
no

; Import PE Island STL geometry
/file/import/cad-geom
yes
"/mnt/lustre/users/kgoddard/Marion/PEI.stl"
y
m
cad-faceting
no

; These commands simplify the default geometry names
/file/import/cad-options/strip-file-name-extension-from-naming yes
/file/import/cad-options/strip-path-prefix-from-names yes

; Import cylindrical geometry body
/file/import/cad-geom
yes
"/mnt/lustre/users/kgoddard/Marion/Final/near_field.pmdb"
y
m
cad-faceting
yes
0
1500

; Define a variable for the horizontal cell sizing
(define res 50)

; Rename all geometry so it is easier to reference
/objects/rename-object pei pei_island
```


© University of Pretoria

```
/objects/rename-object marion marion_island

; Change boundary types (these are kept after meshing)
/boundary/manage/type (*interface*) interface
/boundary/manage/type (*top*) symmetry

; Material point
/material-point/create-material-point wind-zone 0 0 1000

; Global sizing controls
/size-functions/set-global-controls 12.5 1000 1.3

; Define scoped sizing controls
/scoped-sizing/create marion-cells soft face-zone y y marion* res 1.2
/scoped-sizing/create marion-cells2 hard face-zone y y marion* res 1.2
/scoped-sizing/create pei-cells soft face-zone y y pei* res 1.2
/scoped-sizing/create pei-cells2 hard face-zone y y pei* res 1.2
/scoped-sizing/create ground soft face-zone y y *sea* 100 1.1
/scoped-sizing/create surround soft face-zone y y top* 1000 1.3

; Compute sizing field
/scoped-sizing/compute

; Wrap all geometry into one surface mesh
; Boundary names and types are inherited from their parent geometries
/objects/wrap/wrap * () collectively atmosphere shrink-wrap wind-zone hybrid 1.
yes

; Compute domain volume region
/objects/volumetric-regions/compute atmosphere y '(wind-zone)

; Write intermediate surface mesh to file in case of disruptions
/file/write-mesh "/mnt/lustre/users/kgoddard/Marion/Final/final_wrap_50m.msh" yes
yes

; Quality control/improvement on surface mesh
/diagnostics/quality/general-improve objects '(*) skewness 0.85 30 10 yes

; Prisms/inflation layers
/mesh/scoped-prisms/create boundary-layer uniform 0.2 10 1.3 ...
                                  ... atmosphere fluid-regions only-walls
/mesh/poly/controls/cell-sizing size-field

```


© University of Pretoria

```
84 ; Mesh the interior domain with polyhedral cells
85 /mesh/auto-mesh atmosphere no scoped pyramids poly yes
86
87 ; Delete geometry artifacts and do final mesh checks
88 /mesh/prepare-for-solve yes
89
90 ; Write final domain mesh to file
91 /file/write-mesh "/mnt/lustre/users/kgoddard/Marion/Final/...
92 ____________________________________________...final_poly_50m.msh" yes
93 yes
94 exit y
```


© University of Pretoria

Fluent Meshing journal used to generate the outer-domain:

```
; Commented lines are preceded by a semi-colon.

; These commands simplify the default geometry names
/file/import/cad-options/strip-file-name-extension-from-naming yes
/file/import/cad-options/strip-path-prefix-from-names yes

; Import cylindrical geometry body
/file/import/cad-geom
yes
"/mnt/lustre/users/kgoddard/Marion/Final/near_field.pmdb"
y
m
cad-faceting
yes
0
1500

; Define domain dimension lengths
; "up" = upstream length [km]
; "down" = downstream length [km]
; "wide" = domain width [km]
; "high" = domain height [km]

(define up 50)
(define down 150)
(define wide 90)
(define high 6)

; Creat box geometry
/boundary/create-bounding-box '(*) wall ff 2000 absolute (* up -1000)...
                                        ...(* wide -500) 0 (* down 1000)...
                                        ...(* wide 500) (* high 1000) yes

; Rename box faces
/boundary/manage/name interface-near interface-far
/boundary/manage/name ff-zmax top-far
/boundary/manage/name ff-zmin sea-far
/boundary/manage/name ff-xmin inlet-wind
/boundary/manage/name ff-xmax outflow-wind
/boundary/manage/name ff-ymin south-face
/boundary/manage/name ff-ymax north-face

```


© University of Pretoria

```
; Create smaller boxes to control upstream-sizing and wake-sizing later on
/boundary/create-bounding-box '(*) wall wake 3000 absolute 0 -25000 0 ...
                                                    ...(* down 1000) 25000 3000 yes

/boundary/create-bounding-box '(*) wall ahead 3000 absolute (* up -1000)...
                                                    ...-30000 0 0 30000 3000 yes

; Material point
/material-point/create-material-point far-zone -35000 0 2000

: Global sizing controls
/size-functions/set-global-controls 125 2000 1.3

; Define scoped sizing controls
/scoped-sizing/create near-cells soft face-zone y y *interface-far* 150 1.3
/scoped-sizing/create ground soft face-zone y y *sea-far* 1000 1.3
/scoped-sizing/create wake-sizing boi face-zone y y wake* 500 1.3
/scoped-sizing/create ahead-sizing boi face-zone y y ahead* 250 1.3
/scoped-sizing/create sea-ahead soft face-zone y y ahead-zmin 100 1.3
/scoped-sizing/create inlet-size soft face-zone y y inlet-wind 250 1.3
;/scoped-sizing/create surrounds soft face-zone y y * 500 1.3
/scoped-sizing/create top-size hard face-zone yes no top-far 1000 1.3

; Compute sizing field
/scoped-sizing/compute

; Wrap all geometry into one surface mesh
/objects/wrap/wrap '(ff solid) collectively far-field shrink-wrap far-zone hybrid
yes

; Compute domain volume region
/objects/volumetric-regions/compute far-field y '(far-zone)

; Quality control/improvement on surface mesh
/diagnostics/quality/general-improve objects '(*) skewness 0.85 30 10 yes

; Prisms/inflation layers
/mesh/scoped-prisms/create boundary-layer uniform 0.2 10 1.3 ...
                                    ... far-field fluid-regions only-walls
/mesh/poly/controls/cell-sizing size-field

; Mesh the interior domain with polyhedral cells
/mesh/auto-mesh far-field no scoped pyramids poly yes
```


© University of Pretoria

```
86
87 ; Change boundary condition types
88 /boundary/manage/type '(inlet*) velocity-inlet
89 /boundary/manage/type '(outflow-* north-face* south-face*) outflow
90 /boundary/manage/type '(interface-*) interface
91 /boundary/manage/type '(top-*) symmetry
92
93 ; Delete geometry artifacts and do final mesh checks
94 /mesh/prepare-for-solve yes
95
96 ;/file/write-mesh "/mnt/lustre/users/kgoddard/Marion/Final/final_far.msh" yes
```


© University of Pretoria

G ANSYS Fluent Solver Settings

This Appendix chapter sheds further light on how the various inlet profiles and Fluent Solver settings were implemented in practice. Table G.1 gives the named expressions and their descriptions as they were used throughout the project. Named expressions are a valuable new feature found in Fluent 2019R1 and onwards which allow the user to specify algebraic formulae in the software without resorting to coding and compiling full UDF files in c++. One can see in this table how changing just the value of the **Utau** parameter (denoting surface-level friction velocity) would affect corresponding changes in all the successive inlet profiles.

Table G.1: ANSYS Named Expressions used in lieu of UDF's.

Name	Definition
Cmu	0.03
z0_l	0.015 [m]
z0_s	0.0005 [m]
K_l	**z0_l** * 2 * 9.9793
K_s	**z0_s** * 2 * 9.9793
Utau	0.13 [m s-1]
fc	2 * 0.00007292 * -0.72837096967 [s^-1]
zh	**Utau** / (5 * abs(**fc**))
Ugeo	**Utau**/0.4 * log((**zh**+**z0_s**) / **z0_s**)
Uin	IF(**Utau** / 0.4 * log((z+**z0_s**)/**z0_s**) <= **Ugeo**,**Utau** / 0.4 * log((z+**z0_s**) / **z0_s**) , **Ugeo**)
kin	IF(z<**zh** , (**Utau** * **Utau**) * (1/sqrt(**Cmu**)) * ((1-z/**zh**) * (1-z/**zh**)) , 0 [m^2 s^-2])
Epsin	**Utau** * **Utau** * **Utau** / (0.4 * (z+**z0_s**))

Name	Description
Cmu	Cmu parameter
z0_l	land roughness length
z0_s	sea roughness length
K_l	adjusted land sand grain roughness
K_s	adjusted sea sand grain roughness
Utau	Friction velocity
fc	Coriolis parameter
zh	ABL height
Ugeo	Geostrophic wind speed
Uin	inlet velocity magnitude profile
kin	inlet TKE profile
Epsin	inlet TDR profile

© University of Pretoria

A screenshot of the chosen viscous model dialogue box is given in Figure G.1. Pay special note to the modified model constants.

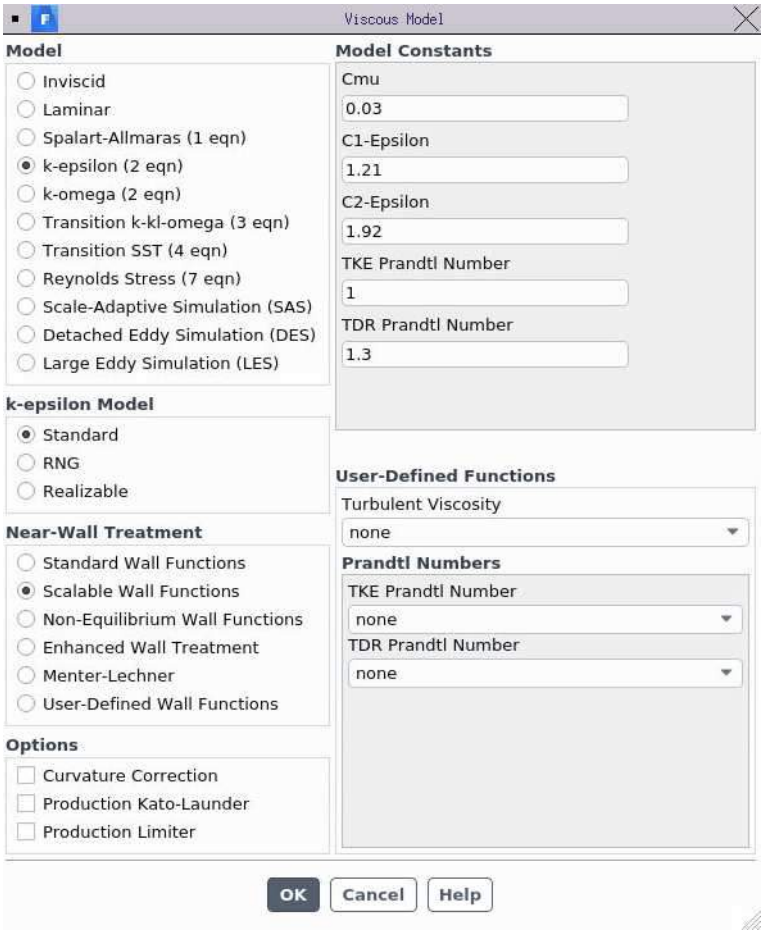

Figure G.1: Viscous model dialogue box showing the chosen k-ε turbulence model and its modified constants.

© University of Pretoria

The screenshots in Figures G.2 and G.3 show how the Coriolis force was implemented as a momentum source in the simulations. The fluid cell zone was modified to include momentum source terms (Figure G.2) and then the corresponding x- and y-momentum sources were prescribed algebraic named expressions as seen in Figure G.3.

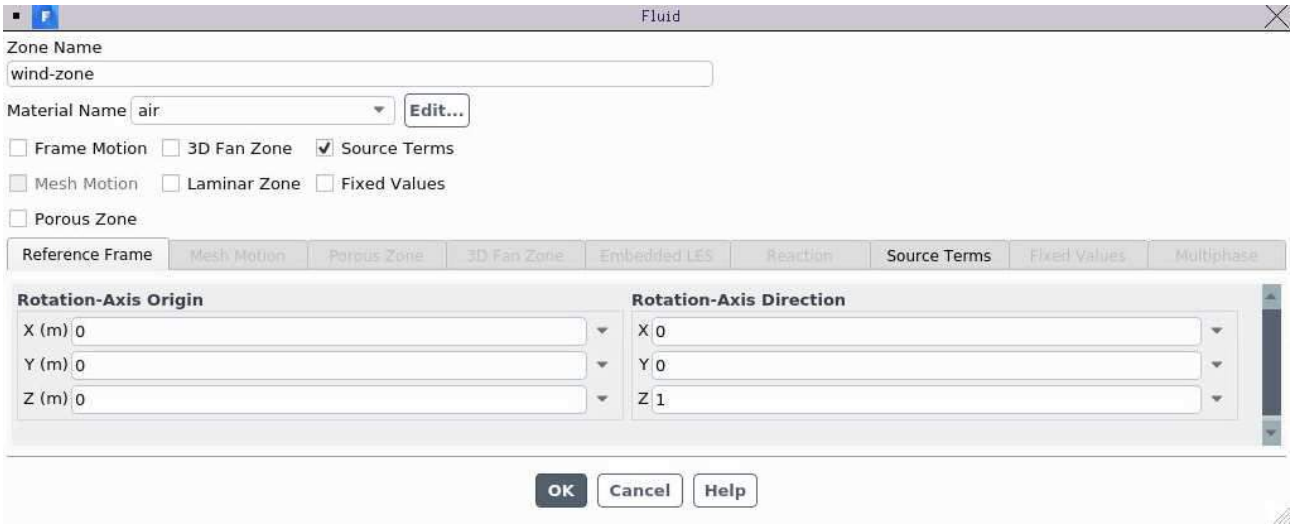

Figure G.2: Modified cell zone conditions to include user-defined momentum source terms.

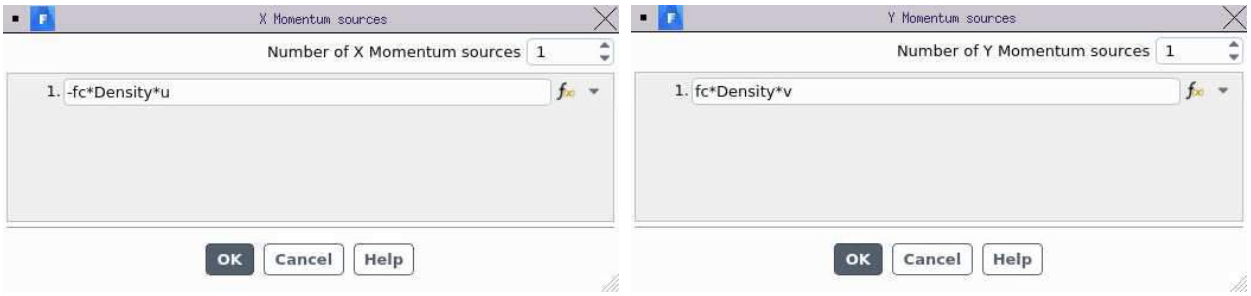

(a) **(b)**

Figure G.3: Coriolis force implemented as x-momentum (a) and y-momentum (b) source terms using algebraic expressions.

© University of Pretoria

H Grid Convergence

When performing CFD simulations, it is important to know whether or not the discretisation of the domain has caused any significant numerical error in the solution. It is generally accepted that finer meshes result in more accurate solutions. Thus, it is imperative to refine a mesh until the point where the CFD solution converges to an answer independent of cell sizing.

The Grid Convergence Index (GCI) method (Roache *et al.*, 1986) proceeds by taking successively finer CFD meshes to estimate the overall solution of a grid with infinitely small spacing. A grid refinement ratio, r, specifies how successive grids are related to one another; a ratio of $r = 2$ implies that the number of cells in a mesh has been doubled in each dimension. Note that exact integer values of r are not necessary, so long as $r > 1$ always. If successive solutions approach the same value, within the so-called asymptotic range, the grid convergence is valid and no further mesh refinement is necessary.

In the case of unstructured grids, it is not always possible to directly specify a constant refinement ratio, r. If one is unsure of the value of grid refinement ratio of a finer or coarser grid, an effective grid refinement ratio can be computed as

$$r_* = \left(\frac{N_1}{N_2}\right)^{1/D} \tag{H.1}$$

where N_1 denotes the number of cells in a finer grid, N_2 denotes the number of cells in a coarser grid and D specifies the number of dimensions in the domain. For the purpose of this discussion, r will refer to both the direct refinement ratio and the effective refinement ratios since they have equivalent uses in the equations to follow.

To sum up the overall accuracy of a given solution, certain performance parameters or solution variables need to be extracted. The CFD practitioner should take care not to use separation bubble lengths or flow transition points as parameters since these can fluctuate wildly under mesh refinement. Although there is no exact specification on what parameters to extract, integrated values across the entire domain or else stable points of interest within the domain are suggested since they are more indicative of the intent of a CFD simulation. For the purposes of this discussion, any extracted performance metrics will be denoted as f. f_3, f_2, and f_1 are the extracted metrics associated with successively finer meshes, with f_1 being the metric corresponding to the smallest grid spacing. p is then the order of convergence, calculated as

$$p = \ln\left(\frac{f_3 - f_2}{f_2 - f_1}\right) / \ln(r) \tag{H.2}$$

© University of Pretoria

Using the order of convergence and refinement ratio, Richard extrapolation (neglecting higher-order terms) can be used to estimate the performance parameter of a grid with zero spacing:

$$f_{h=0} = \frac{r^p f_1 - f_2}{r^p - 1} \tag{H.3}$$

The Grid Convergence Index of a mesh is described by Equation H.4:

$$GCI = \frac{F_s|\epsilon|}{r^p - 1} \tag{H.4}$$

where $F - s$ is a factor of safety and ϵ is the relative error between any two successive performance parameters:

$$\epsilon = \frac{f_2 - f_1}{f_1} \tag{H.5}$$

Thus, when three solutions are available, GCI_{12} and GCI_{23} can be calculated with a suggested safety factor of $F_s = 1.25$ (Roache *et al.*, 1986):

$$GCI_{12} = \frac{F_s|\frac{f_2 - f_1}{f_1}|}{r^p - 1} \quad \text{and} \quad GCI_{23} = \frac{F_s|\frac{f_3 - f_2}{f_2}|}{r^p - 1} \tag{H.6}$$

If the solutions lie within the asymptotic range, the calculated indices will follow the relationship:

$$GCI_{23} \approx r^p GCI_{12}$$

$$\therefore \frac{GCI_{23}}{r^p GCI_{12}} \approx 1 \tag{H.7}$$

In this case, mesh independence has been achieved.

© University of Pretoria

I Local Friction Velocity Plots

Contour plots for the local friction velocity, u_*, as simulated in the large-scale wind domain are given here. The local friction velocity was extracted from the CFD solutions and used to scale all data into a universal form for data comparison and validation against the experimentally gathered dataset.

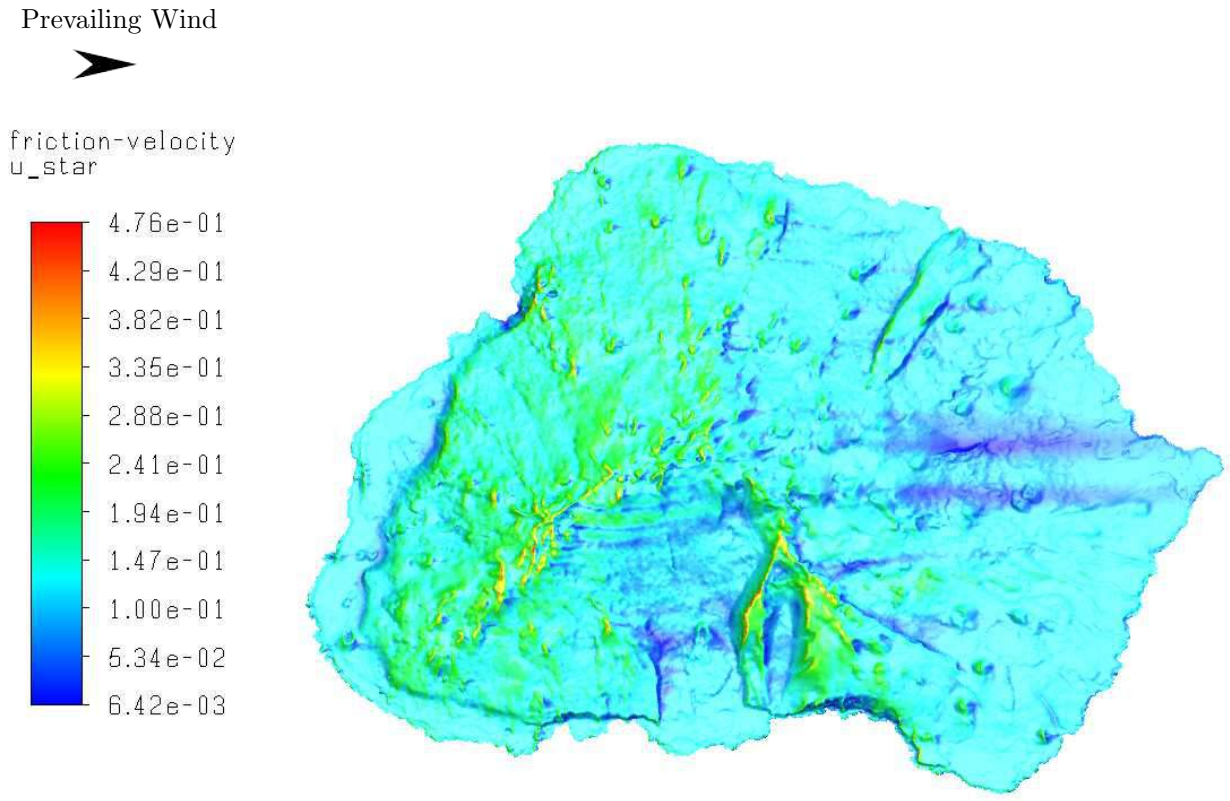

Figure I.1: Local friction velocity contours across MI for a Westerly prevailing wind.

© University of Pretoria

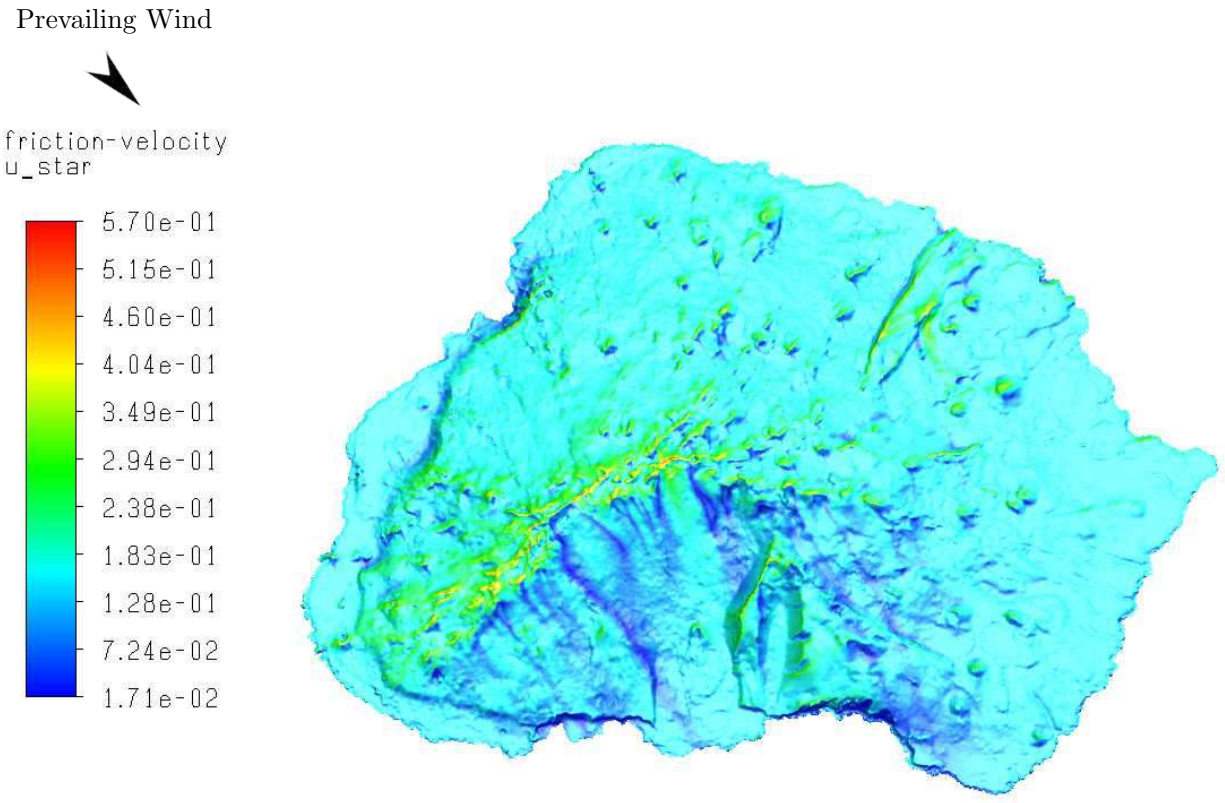

Figure I.2: Local friction velocity contours across MI for a North-Westerly prevailing wind.

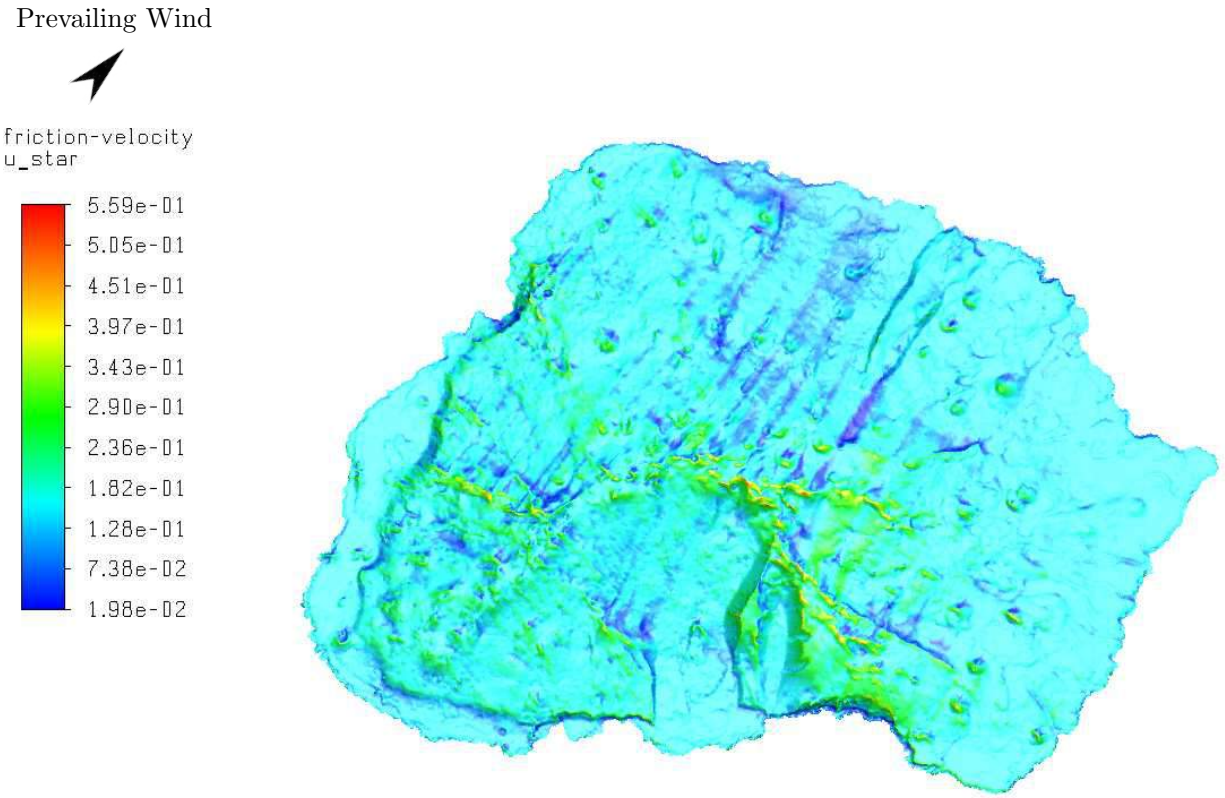

Figure I.3: Local friction velocity contours across MI for a South-Westerly prevailing wind.

© University of Pretoria

J Validation Data

Table J.1: Summarised raw experimental and CFD data for the Westerly wind case.

Site		Experimental Results				CFD Results				CFD Results (non-Coriolis)			
	Anem.	Magnitude [m/s]		Bearing [°]		Magnitude [m/s]		Bearing [°]		Magnitude [m/s]		Bearing [°]	
Station	Height [m]	Mean	Std Dev.	Mean	Std Dev.	Mean	Std Dev.	Mean	Std Dev.	Mean	Std Dev.	Mean	Std Dev.
Cape Davis	1	1.927	0.675	273.4	19.15	1.471	0.506	265.3	18.63	1.655	0.566	264.4	18.66
	0.5	1.817	0.629	262.9	19.06	1.736	0.497	265.5	14.96	1.956	0.555	264.6	14.94
East Cape Coastal	1	1.454	1.076	292.4	45.11	0.715	0.367	266.8	30.23	1.704	0.474	265.4	14.47
	0.5	1.269	1.033	291.7	49.64	0.761	0.395	266.9	30.58	1.961	0.446	265.6	11.47
East Cape Inland	1	1.381	1.087	287.9	49.45	0.789	0.347	266.8	24.89	1.648	0.488	266.9	15.39
	0.5	1.226	0.979	285.0	51.08	0.851	0.373	266.8	24.82	1.899	0.488	267.0	12.99
Grey Headed Ridge	1	1.381	0.846	291.9	37.67	1.512	0.480	263.6	17.20	1.817	0.569	264.6	16.76
	0.5	1.568	0.986	296.4	37.97	1.779	0.455	263.5	13.41	2.153	0.532	264.4	12.75
Kampkoppie Coastal	1	1.532	0.708	269.7	20.59	1.611	0.498	265.9	16.34	1.866	0.576	267.0	16.10
	0.5	1.451	0.681	278.6	24.34	1.909	0.458	266.0	12.11	2.225	0.524	267.2	11.71
Kampkoppie Inland	1	0.975	0.771	275.1	52.22	1.141	0.358	257.7	17.67	1.312	0.407	258.5	17.34
	0.5	0.869	0.692	271.9	52.41	1.306	0.366	257.8	15.54	1.508	0.414	258.6	15.10
Katedraal	1	1.911	1.179	273.2	35.34	1.210	0.383	262.1	17.32	1.639	0.485	260.7	16.21
	0.5	1.787	0.901	255.5	29.52	1.359	0.397	262.2	15.76	1.867	0.491	260.8	14.17
Kildalkey Coastal	1	1.510	0.977	276.9	37.47	1.100	0.391	268.9	18.76	1.399	0.458	270.4	16.83
	0.5	1.331	0.871	267.6	37.02	1.242	0.395	268.9	16.41	1.618	0.446	270.3	13.66
Kildalkey Inland	1	1.581	1.128	262.4	45.50	0.998	0.358	268.1	19.10	1.092	0.335	268.8	15.71
	0.5	1.434	1.025	260.2	45.66	1.102	0.379	268.1	18.18	1.248	0.343	268.9	13.73
Mixed Pickle Coastal	1	1.171	0.639	263.6	29.66	1.322	0.420	254.8	18.12	1.503	0.472	255.2	17.89
	0.5	1.109	0.603	259.7	30.71	1.547	0.408	254.7	14.76	1.762	0.457	255.0	14.47
Mixed Pickle Inland	1	1.144	0.641	254.0	33.49	1.264	0.395	252.0	17.96	1.410	0.439	251.3	17.95
	0.5	1.063	0.586	251.2	33.22	1.465	0.394	252.2	15.24	1.641	0.437	251.5	15.13
Puisie	1	2.107	1.113	274.0	29.32	1.618	0.542	262.9	18.41	1.798	0.600	262.8	18.35
	0.5	1.946	1.019	271.5	27.90	1.834	0.566	263.2	16.67	2.048	0.625	263.1	16.49
Repettos	1	1.762	0.748	290.9	24.08	0.749	0.310	292.6	24.43	1.003	0.365	281.8	20.85
	0.5	1.650	0.727	284.4	23.42	0.825	0.329	292.4	23.50	1.134	0.382	281.8	19.05
Santa Rosa Valley	1	1.657	1.907	333.8	174.85	0.589	0.434	263.2	47.34	0.632	0.498	247.8	48.14
	0.5	1.433	1.624	331.5	161.38	0.630	0.469	263.4	47.90	0.674	0.538	248.5	49.88
Skua Ridge Coastal	1	1.651	0.901	290.4	33.01	1.171	0.402	272.3	18.21	1.267	0.425	270.0	17.28
	0.5	1.461	0.807	287.0	33.29	1.337	0.407	272.2	15.73	1.471	0.423	269.9	14.35
Skua Ridge Inland	1	1.705	0.768	293.9	26.72	0.874	0.366	271.1	23.04	1.521	0.517	265.6	18.34
	0.5	1.484	0.610	285.9	22.61	0.966	0.383	271.1	21.52	1.770	0.509	265.6	15.05
Swartkops	1	1.277	0.610	294.8	28.40	1.356	0.401	271.6	15.10	1.568	0.458	270.6	14.70
	0.5	1.139	0.559	292.9	28.97	1.563	0.404	271.7	12.87	1.813	0.459	270.7	12.39

© University of Pretoria

Table J.2: Summarised raw experimental and CFD data for the South-Westerly wind case.

Site		Experimental Results				CFD Results				CFD Results (non-Coriolis)			
	Anem.	Magnitude [m/s]		Bearing [°]		Magnitude [m/s]		Bearing [°]		Magnitude [m/s]		Bearing [°]	
Station	Height [m]	Mean	Std Dev.	Mean	Std Dev.	Mean	Std Dev.	Mean	Std Dev.	Mean	Std Dev.	Mean	Std Dev.
Cape Davis	1	1.692	0.691	229.8	22.45	2.048	0.598	206.7	16.96	1.574	0.495	223.0	17.63
	0.5	1.417	0.603	224.9	24.24	2.411	0.543	207.4	12.96	1.853	0.468	223.8	14.24
East Cape Coastal	1	1.410	0.796	234.9	31.20	1.633	0.470	207.9	16.74	1.856	0.517	225.2	15.57
	0.5	1.357	0.771	233.5	30.96	1.870	0.455	207.6	14.06	2.121	0.494	225.1	13.11
East Cape Inland	1	1.430	0.787	230.0	29.23	1.566	0.453	205.5	16.79	1.479	0.429	222.3	16.35
	0.5	1.338	0.728	230.2	29.25	1.802	0.449	205.5	14.38	1.705	0.424	222.4	14.11
Grey Headed Ridge	1	1.390	0.580	243.3	24.66	1.889	0.614	221.4	18.33	1.942	0.624	233.4	18.44
	0.5	1.574	0.654	246.9	24.47	2.225	0.593	221.4	15.14	2.296	0.596	233.3	14.93
Kampkoppie Coastal	1	1.587	0.628	218.6	22.32	1.782	0.571	208.1	18.67	1.828	0.573	224.7	17.44
	0.5	1.519	0.595	231.6	22.72	2.079	0.546	208.0	15.22	2.135	0.542	224.6	14.27
Kampkoppie Inland	1	1.423	0.585	227.8	22.96	1.538	0.465	206.9	17.62	1.451	0.446	219.1	17.52
	0.5	1.299	0.539	226.1	22.81	1.768	0.471	207.1	15.43	1.667	0.453	219.2	15.55
Katedraal	1	1.935	0.855	224.2	24.07	1.825	0.575	190.6	17.54	1.319	0.420	210.3	18.51
	0.5	1.708	0.738	205.6	25.59	2.055	0.592	190.5	15.84	1.476	0.436	210.2	17.15
Kildalkey Coastal	1	1.817	0.638	232.2	20.25	1.387	0.440	209.3	18.47	1.838	0.582	223.5	17.72
	0.5	1.657	0.579	228.0	19.64	1.600	0.424	209.4	15.35	2.135	0.557	223.6	14.71
Kildalkey Inland	1	1.667	0.622	231.0	21.10	1.633	0.514	213.3	18.23	1.586	0.491	225.0	17.21
	0.5	1.557	0.576	229.3	20.64	1.889	0.525	213.3	16.10	1.836	0.499	224.7	15.23
Mixed Pickle Coastal	1	1.621	0.619	225.2	21.15	1.581	0.524	206.5	19.36	1.649	0.541	222.4	18.41
	0.5	1.569	0.610	223.1	21.39	1.844	0.514	207.1	16.17	1.930	0.530	222.7	15.50
Mixed Pickle Inland	1	1.581	0.612	225.2	21.39	1.672	0.495	205.9	17.21	1.586	0.481	220.6	17.19
	0.5	1.517	0.565	224.8	20.59	1.927	0.485	206.3	14.53	1.833	0.474	221.1	14.70
Puisie	1	1.797	0.602	242.1	19.40	1.811	0.590	228.5	18.36	1.923	0.600	236.7	18.06
	0.5	1.723	0.579	240.2	19.59	2.055	0.612	228.1	16.82	2.199	0.613	236.5	16.15
Repettos	1	1.534	0.909	240.8	32.96	1.191	0.396	190.5	18.64	1.005	0.373	225.2	20.40
	0.5	1.424	0.848	235.3	31.55	1.382	0.398	190.6	15.84	1.137	0.391	225.0	18.98
Santa Rosa Valley	1	1.808	1.217	191.2	41.02	1.675	0.522	189.2	17.16	1.572	0.551	200.0	20.44
	0.5	1.433	0.985	188.9	42.33	1.939	0.520	189.4	14.50	1.761	0.572	200.2	18.86
Skua Ridge Coastal	1	1.363	1.148	226.1	41.18	1.755	0.535	202.2	17.69	1.351	0.428	215.5	18.26
	0.5	1.280	1.046	221.0	43.27	2.008	0.528	202.4	15.12	1.547	0.428	216.1	15.94
Skua Ridge Inland	1	1.308	1.069	227.5	39.97	1.771	0.569	203.1	18.70	1.524	0.498	225.4	18.14
	0.5	1.187	0.937	225.6	39.70	2.061	0.550	203.3	15.39	1.778	0.486	225.5	15.32
Swartkops	1	1.366	0.585	229.8	24.14	1.678	0.476	205.4	16.44	1.468	0.417	219.3	16.24
	0.5	1.299	0.547	229.7	23.72	1.926	0.475	205.3	14.21	1.684	0.417	219.2	14.17

© University of Pretoria

Table J.3: Summarised raw experimental and CFD data for the North-Westerly wind case.

Site		Experimental Results				CFD Results				CFD Results (non-Coriolis)			
	Anem.	Magnitude [m/s]		Bearing [°]		Magnitude [m/s]		Bearing [°]		Magnitude [m/s]		Bearing [°]	
Station	Height [m]	Mean	Std Dev.	Mean	Std Dev.	Mean	Std Dev.	Mean	Std Dev.	Mean	Std Dev.	Mean	Std Dev.
Cape Davis	1	1.866	1.001	297.0	29.02	2.129	0.617	335.7	16.81	1.812	0.580	316.0	17.83
	0.5	1.769	0.918	285.0	30.42	2.536	0.537	335.1	12.12	2.163	0.542	315.4	14.09
East Cape Coastal	1	1.555	0.974	314.0	32.89	2.204	0.604	335.8	15.84	2.072	0.560	317.6	15.28
	0.5	1.421	0.881	311.7	33.31	2.598	0.543	335.8	11.92	2.438	0.502	317.6	11.73
East Cape Inland	1	1.457	1.058	308.6	38.72	1.554	0.470	340.9	17.42	1.522	0.461	317.6	17.06
	0.5	1.282	0.946	306.2	40.33	1.787	0.475	340.7	15.14	1.758	0.464	317.5	14.95
Grey Headed Ridge	1	1.518	0.809	299.7	30.10	0.822	0.458	335.5	32.97	1.510	0.472	294.6	18.21
	0.5	1.721	0.943	304.5	29.42	0.883	0.490	335.7	32.89	1.748	0.448	294.7	14.77
Kampkoppie Coastal	1	1.116	1.063	297.6	71.88	1.700	0.535	335.6	18.32	1.789	0.557	318.8	17.59
	0.5	1.024	0.995	307.7	75.24	2.014	0.496	335.6	14.17	2.140	0.506	318.5	13.47
Kampkoppie Inland	1	0.726	0.818	310.2	147.65	1.312	0.405	347.3	17.37	1.237	0.391	324.9	18.23
	0.5	0.613	0.715	307.2	145.80	1.508	0.410	347.0	15.08	1.420	0.399	324.8	16.21
Katedraal	1	2.067	1.322	284.0	39.34	1.403	0.579	333.9	24.26	1.695	0.537	322.5	18.15
	0.5	1.881	1.119	264.4	35.18	1.534	0.621	334.2	23.78	1.912	0.556	322.6	16.68
Kildalkey Coastal	1	1.419	1.107	293.4	47.04	1.391	0.469	354.4	18.34	1.173	0.386	315.8	18.26
	0.5	1.225	0.973	284.0	50.49	1.610	0.462	354.4	15.16	1.352	0.379	315.8	15.70
Kildalkey Inland	1	1.584	1.254	280.5	51.83	1.318	0.416	358.3	16.34	1.234	0.402	313.3	18.20
	0.5	1.404	1.142	278.1	54.33	1.509	0.426	357.9	14.36	1.415	0.415	313.5	16.45
Mixed Pickle Coastal	1	0.803	0.751	278.3	64.49	1.278	0.426	344.4	19.17	1.228	0.395	320.5	18.30
	0.5	0.744	0.680	272.7	61.56	1.520	0.414	344.4	15.34	1.445	0.382	320.7	15.13
Mixed Pickle Inland	1	0.762	0.783	273.3	68.36	1.300	0.396	348.4	16.99	1.165	0.359	323.3	17.68
	0.5	0.693	0.702	269.5	66.26	1.507	0.390	348.4	14.13	1.343	0.357	323.2	15.30
Puisie	1	2.333	1.280	288.4	33.18	1.125	0.361	332.6	18.71	1.205	0.407	322.2	19.29
	0.5	2.103	1.146	285.6	33.03	1.255	0.376	332.4	17.43	1.341	0.428	321.9	18.24
Repettos	1	1.717	0.597	297.3	20.34	1.845	0.535	337.9	16.75	1.688	0.512	321.6	17.34
	0.5	1.620	0.563	291.1	20.27	2.143	0.509	337.3	13.59	1.956	0.500	321.0	14.63
Santa Rosa Valley	1	2.222	1.467	336.8	41.31	0.931	0.347	13.1	21.49	0.488	0.369	313.7	37.59
	0.5	1.949	1.266	333.6	40.40	1.012	0.373	13.2	21.25	0.517	0.400	313.5	38.29
Skua Ridge Coastal	1	1.471	0.786	304.9	29.50	1.923	0.572	340.0	17.12	1.949	0.578	323.2	17.05
	0.5	1.295	0.701	301.8	30.56	2.226	0.542	340.3	13.80	2.261	0.546	322.9	13.91
Skua Ridge Inland	1	1.547	0.664	310.8	23.68	1.573	0.564	338.8	20.98	1.451	0.522	318.3	20.13
	0.5	1.307	0.552	302.6	24.33	1.840	0.563	338.7	17.71	1.689	0.523	318.7	17.50
Swartkops	1	1.145	0.735	319.7	34.77	1.697	0.501	340.8	16.97	1.691	0.499	322.0	16.91
	0.5	0.984	0.646	318.3	34.41	1.968	0.500	340.8	14.44	1.960	0.500	322.0	14.64

© University of Pretoria

K Combined Wind Velocity Profile plots

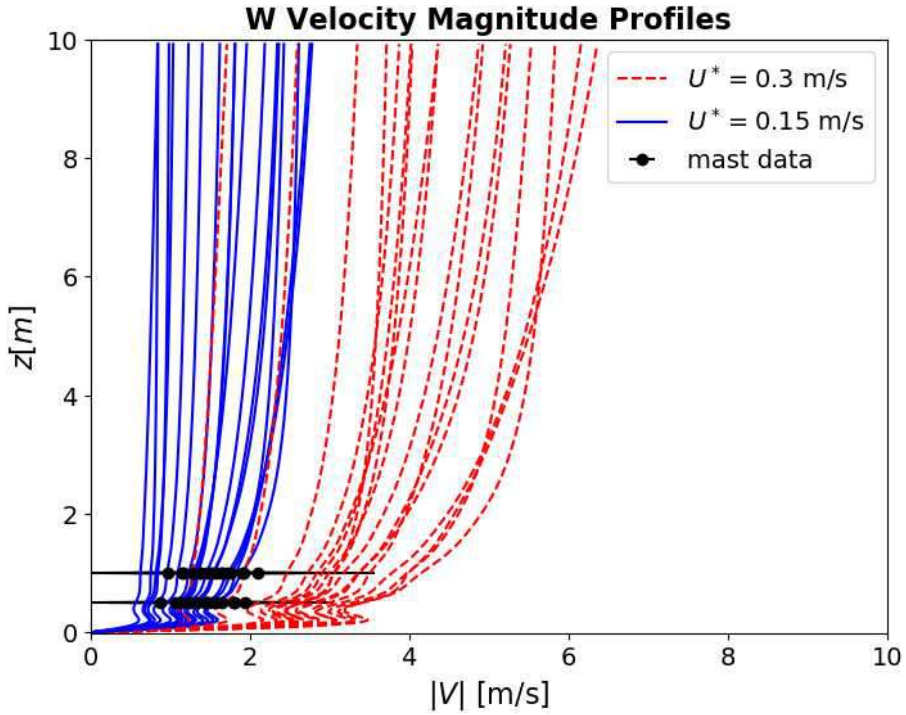

Figure K.1: Wind velocity profiles extracted at 17 locations from an average-speed (blue) and a high-speed (red) CFD wind simulation. This plot is specifically for a westerly wind flow direction over MI.

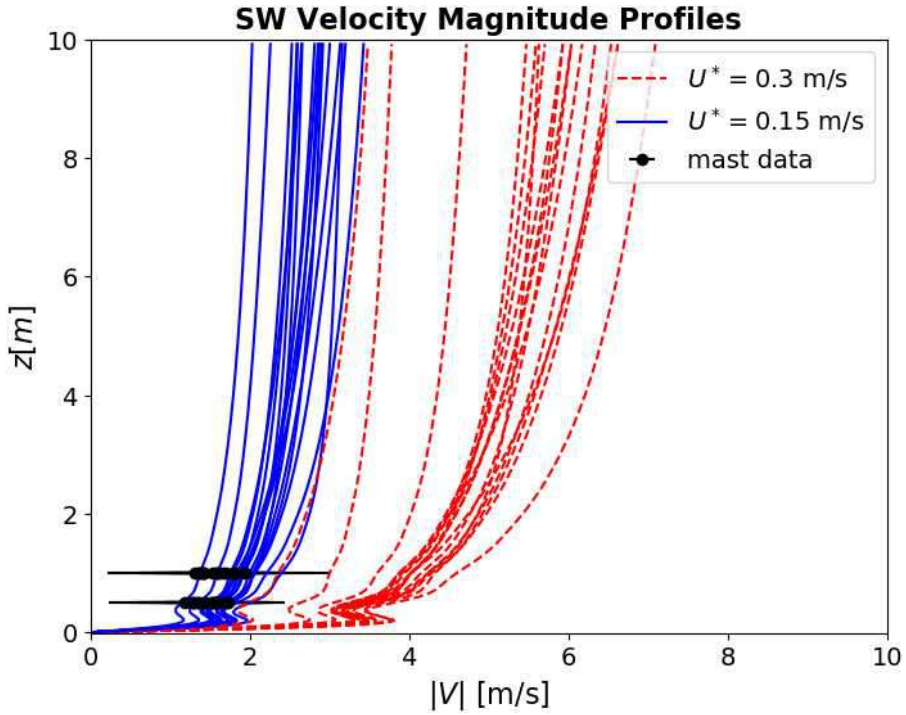

Figure K.2: Wind velocity profiles extracted at 17 locations from an average-speed (blue) and a high-speed (red) CFD wind simulation. This plot is specifically for a south-westerly wind flow direction over MI.

© University of Pretoria

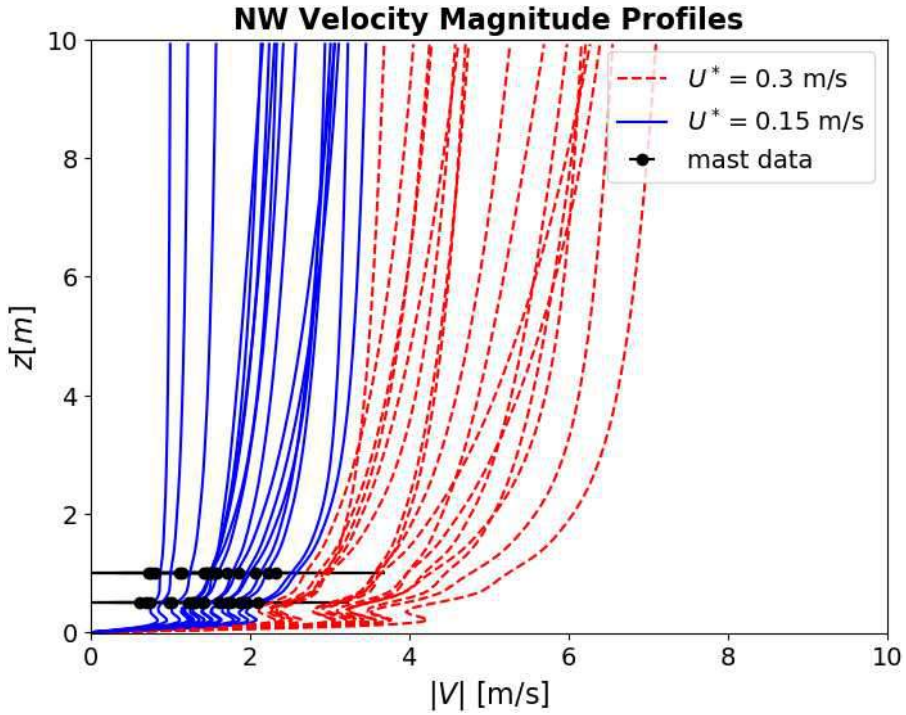

Figure K.3: Wind velocity profiles extracted at 17 locations from an average-speed (blue) and a high-speed (red) CFD wind simulation. This plot is specifically for a north-westerly wind flow direction over MI.

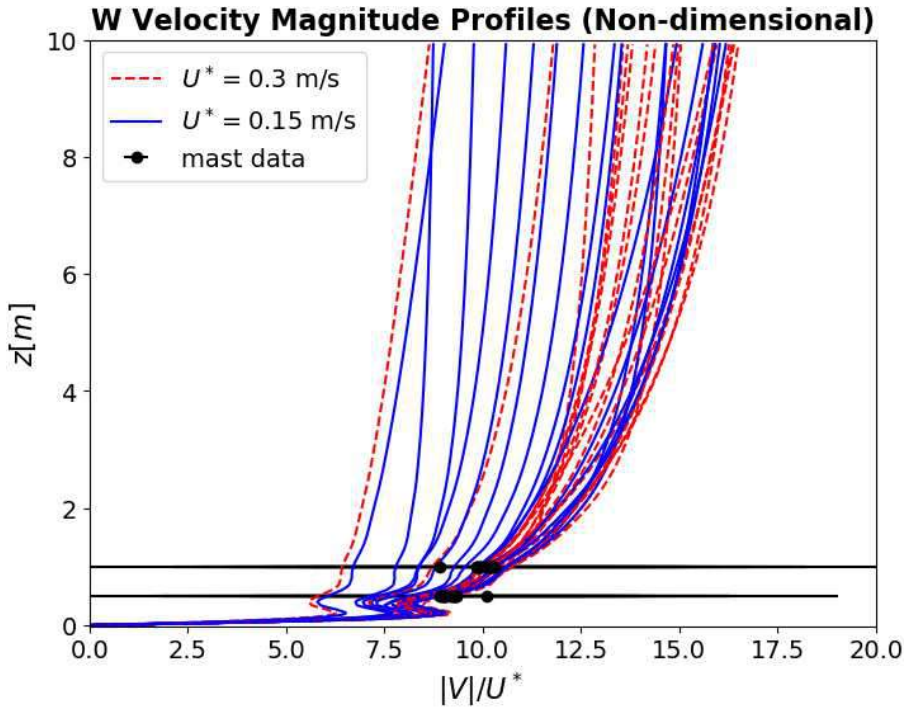

Figure K.4: Non-dimensional wind velocity profiles extracted from an average-speed (blue) and a high-speed (red) CFD wind simulation. The lines are densely overlapped after being cast into universal form. The overlapping is more pronounced at lower heights and becomes progressively more spread out with increased altitude. This plot presents the same data seen in Figure 6.25

© University of Pretoria

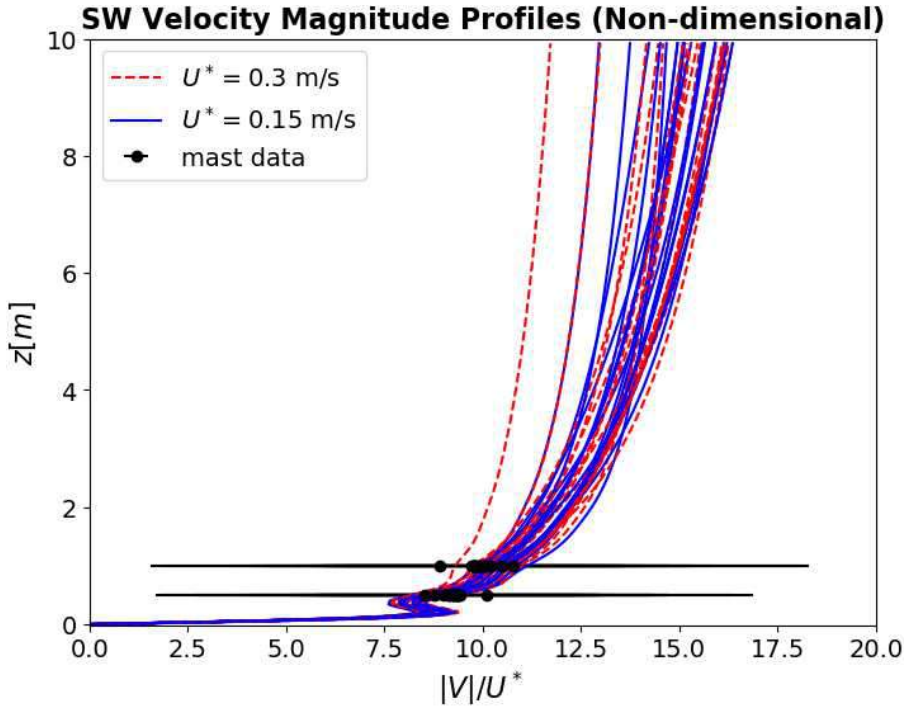

Figure K.5: Non-dimensional wind velocity profiles extracted from an average-speed (blue) and a high-speed (red) CFD wind simulation. The lines are densely overlapped after being cast into universal form. The overlapping is more pronounced at lower heights and becomes progressively more spread out with increased altitude. This plot presents the same data seen in Figure 6.25

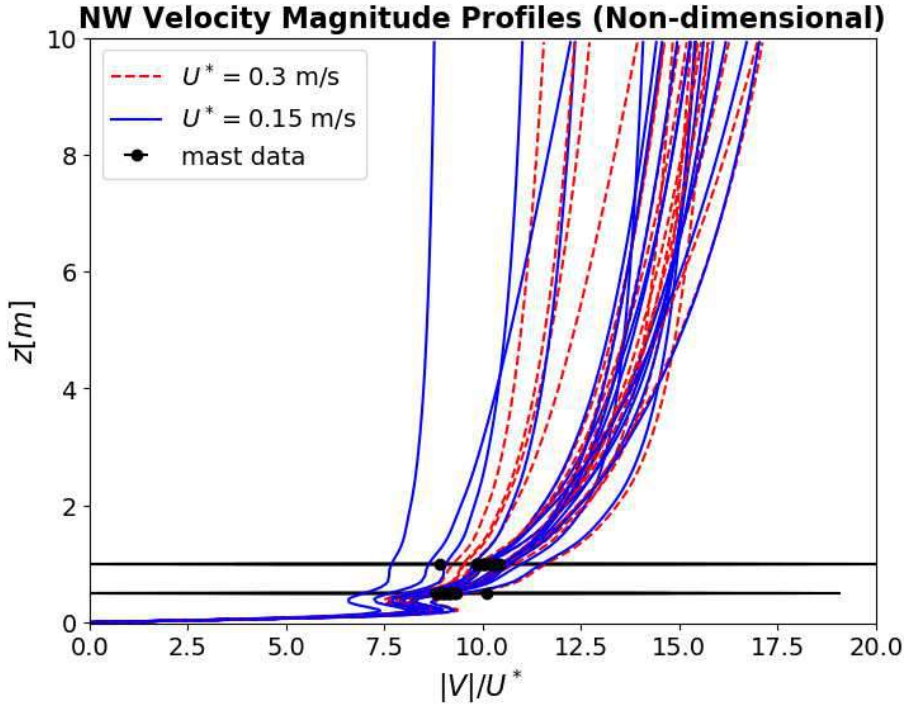

Figure K.6: Non-dimensional wind velocity profiles extracted from an average-speed (blue) and a high-speed (red) CFD wind simulation. The lines are densely overlapped after being cast into universal form. The overlapping is more pronounced at lower heights and becomes progressively more spread out with increased altitude. This plot presents the same data seen in Figure 6.25

© University of Pretoria

L Wind Velocity Maps (16 Directions)

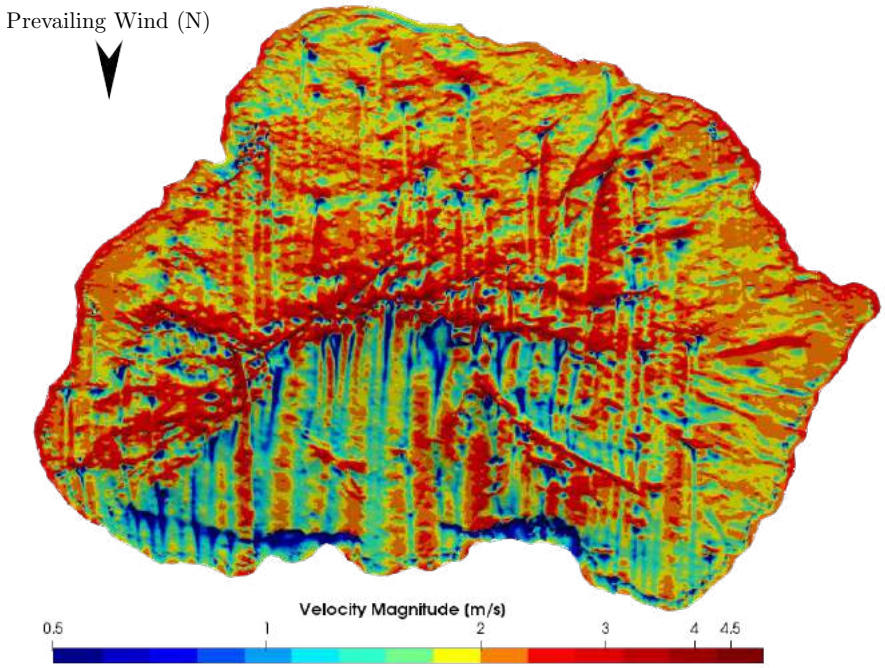

Figure L.1: NORTH: Wind velocity map at one meter AGL for MI subjected to a northerly prevailing wind.

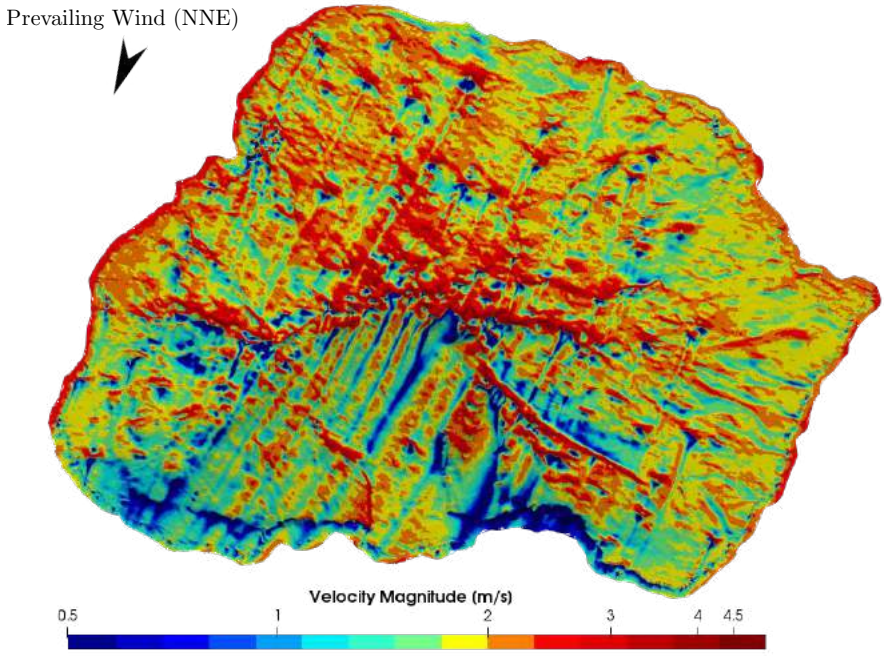

Figure L.2: NNE: Wind velocity map at one meter AGL for MI subjected to a north-north-easterly prevailing wind.

© University of Pretoria

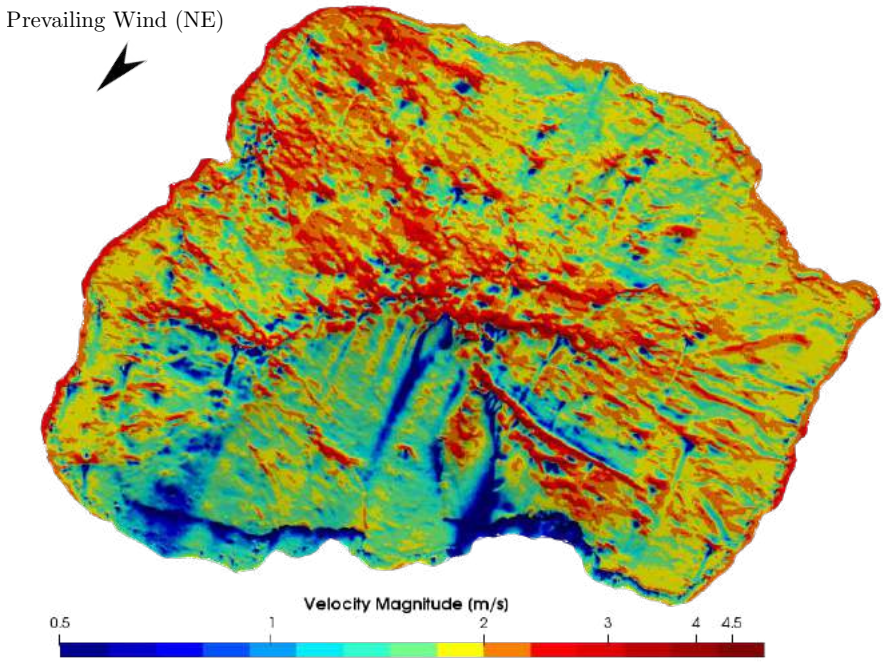

Figure L.3: NORTH-EAST: Wind velocity map at one meter AGL for MI subjected to a north-easterly prevailing wind.

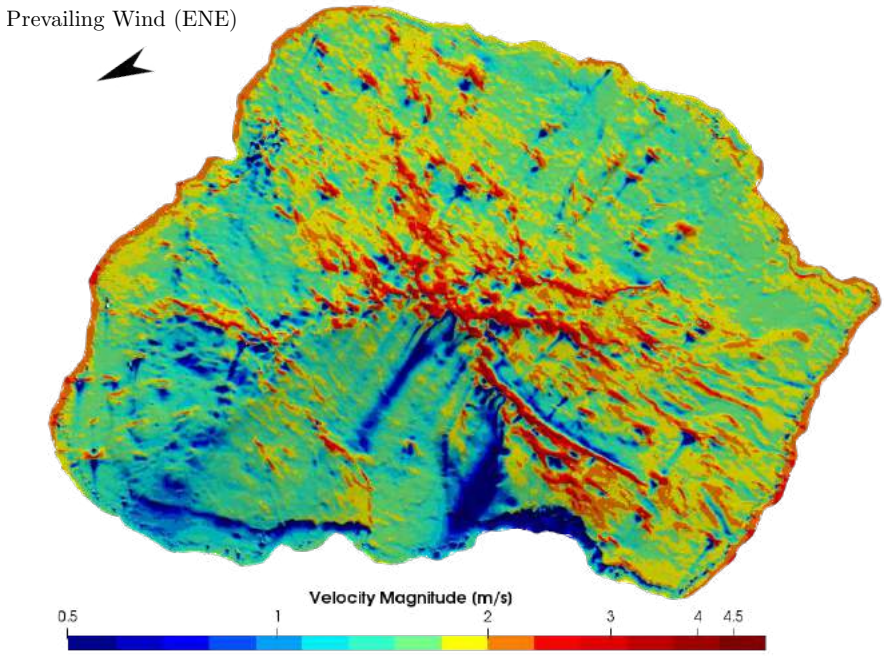

Figure L.4: ENE: Wind velocity map at one meter AGL for MI subjected to an east-north-easterly prevailing wind.

© University of Pretoria

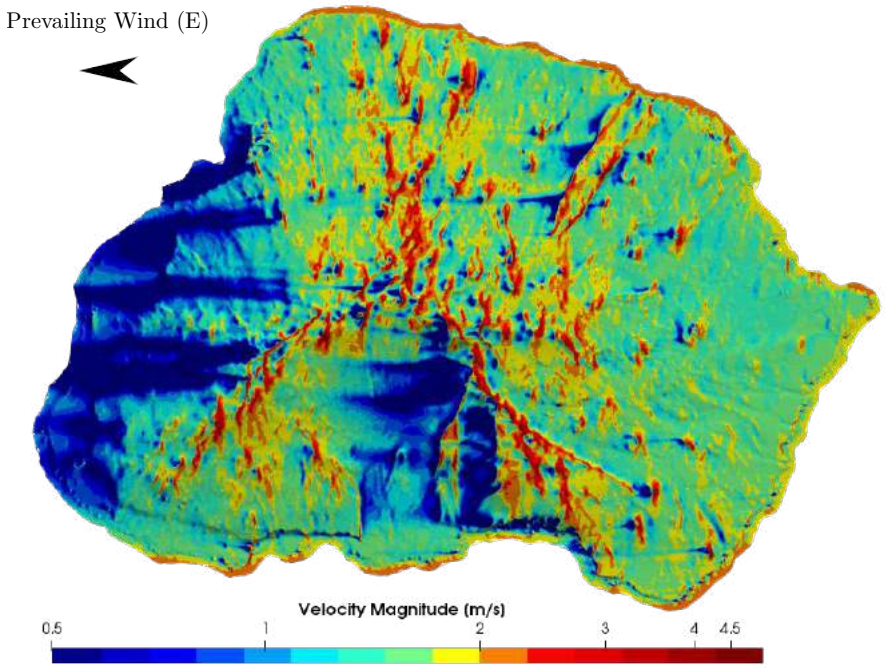

Figure L.5: EAST: Wind velocity map at one meter AGL for MI subjected to an easterly prevailing wind.

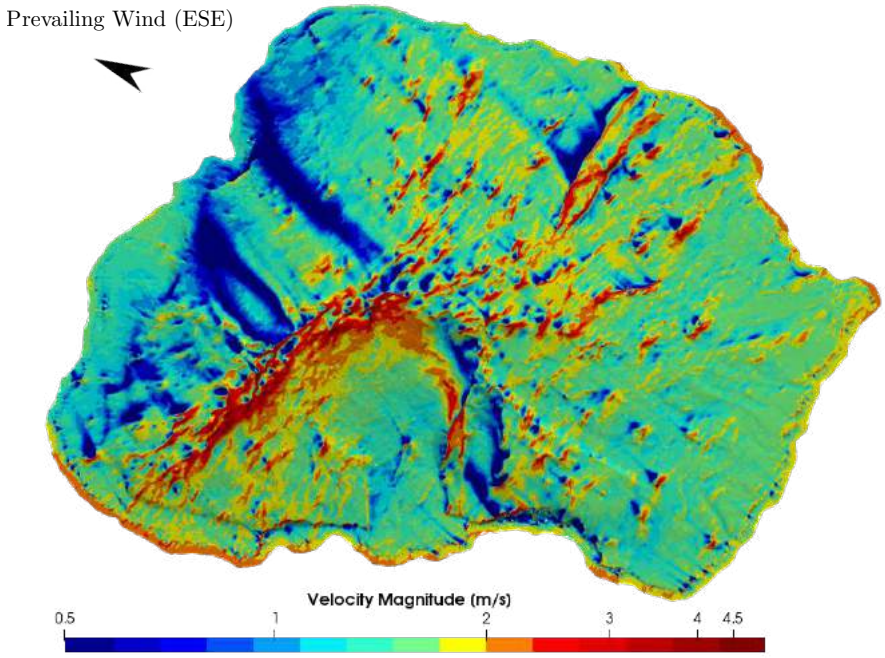

Figure L.6: ESE: Wind velocity map at one meter AGL for MI subjected to an east-south-easterly prevailing wind.

© University of Pretoria

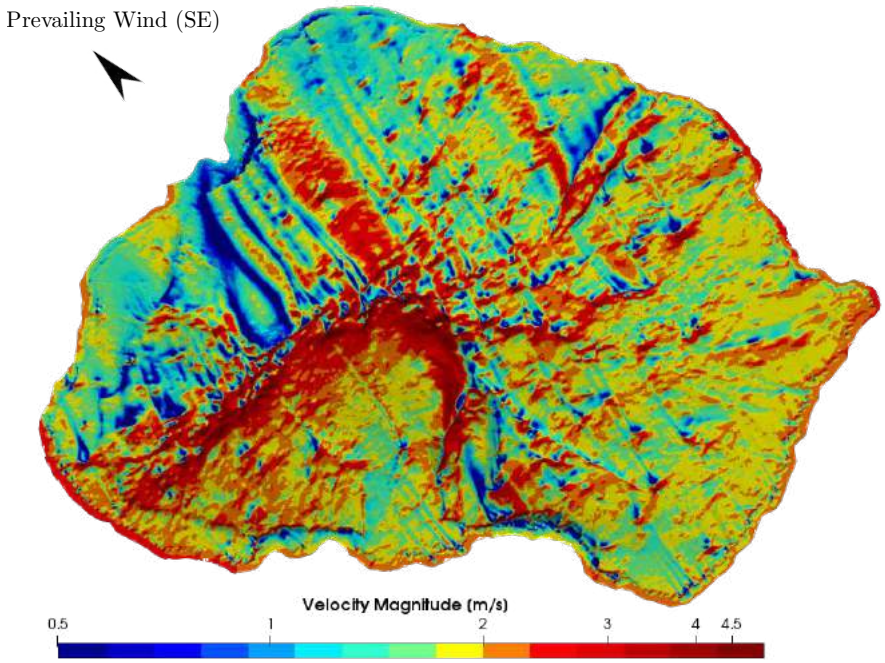

Figure L.7: SOUTH-EAST: Wind velocity map at one meter AGL for MI subjected to a south-easterly prevailing wind.

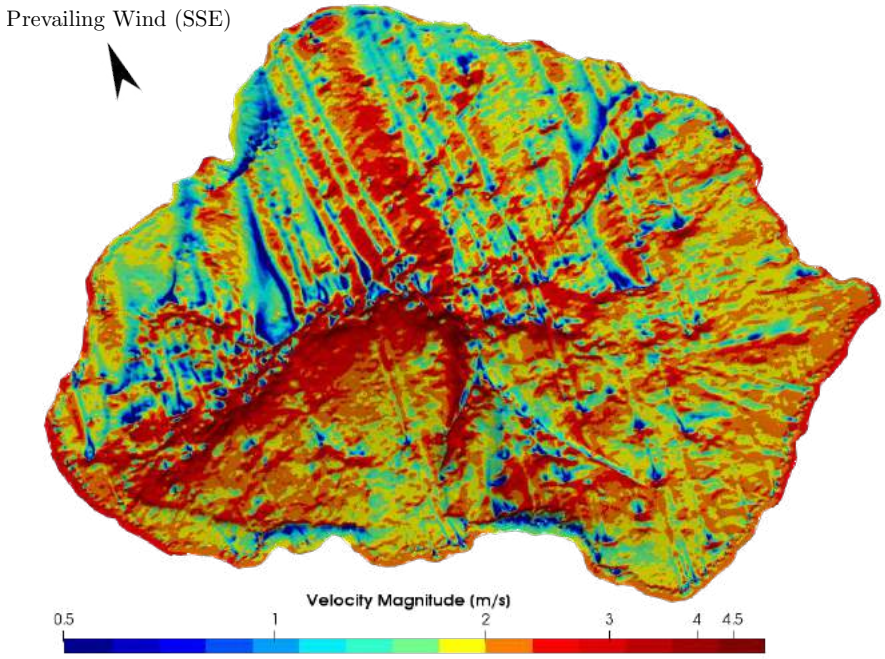

Figure L.8: SSE: Wind velocity map at one meter AGL for MI subjected to a south-south-easterly prevailing wind.

© University of Pretoria

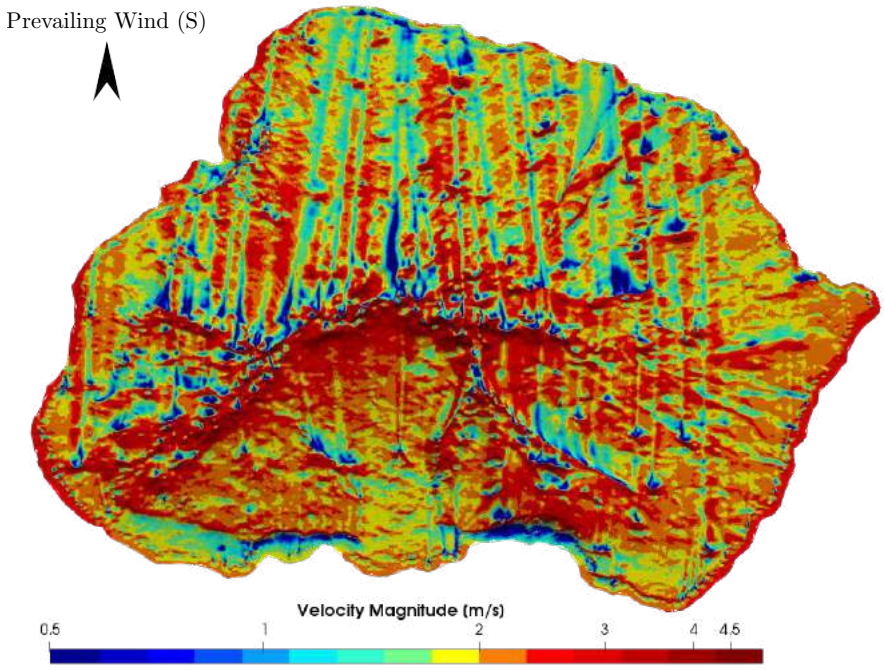

Figure L.9: SOUTH: Wind velocity map at one meter AGL for MI subjected to a southerly prevailing wind.

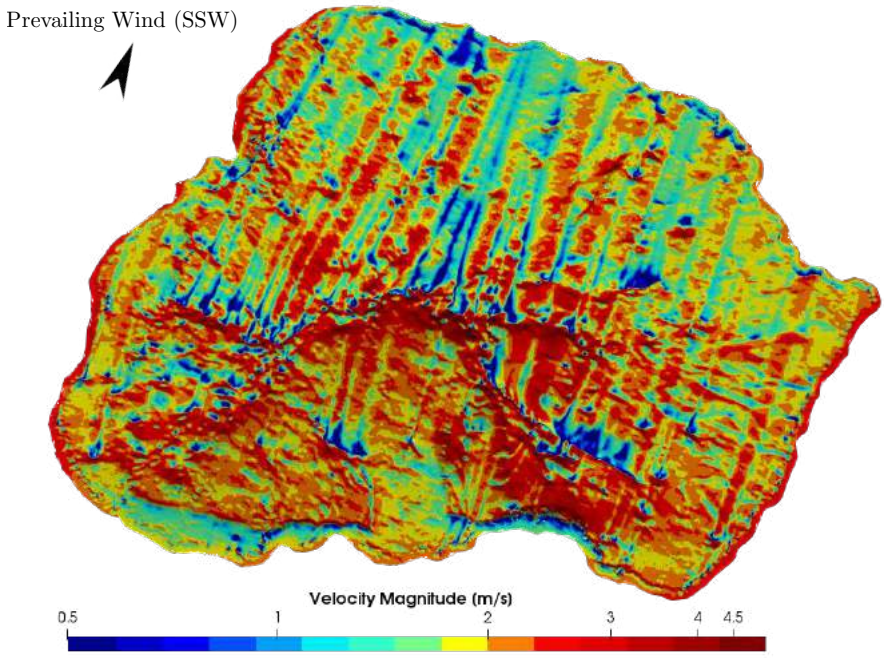

Figure L.10: SSW: Wind velocity map at one meter AGL for MI subjected to a south-south-westerly prevailing wind.

© University of Pretoria

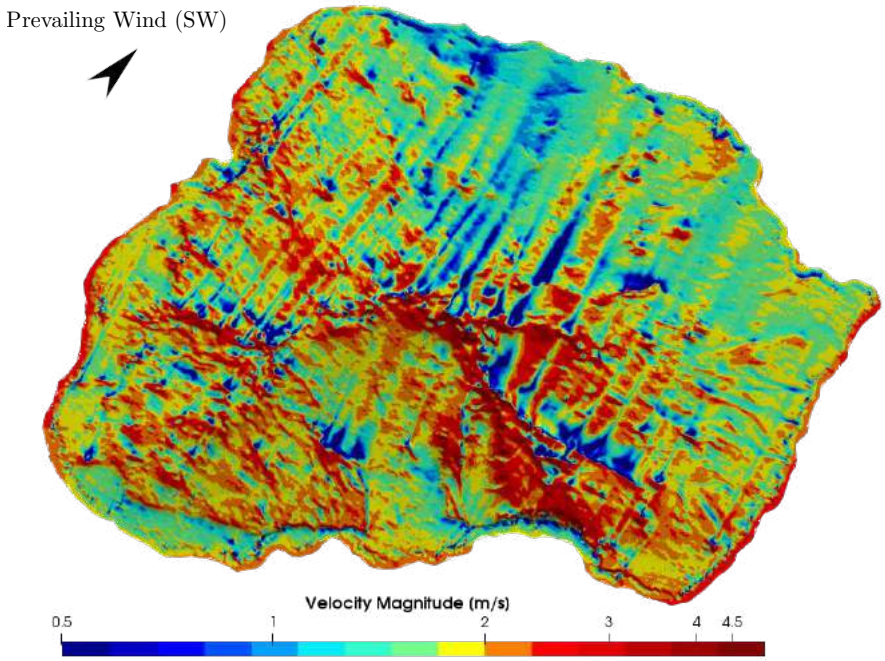

Figure L.11: SOUTH-WEST: Wind velocity map at one meter AGL for MI subjected to a south-westerly prevailing wind.

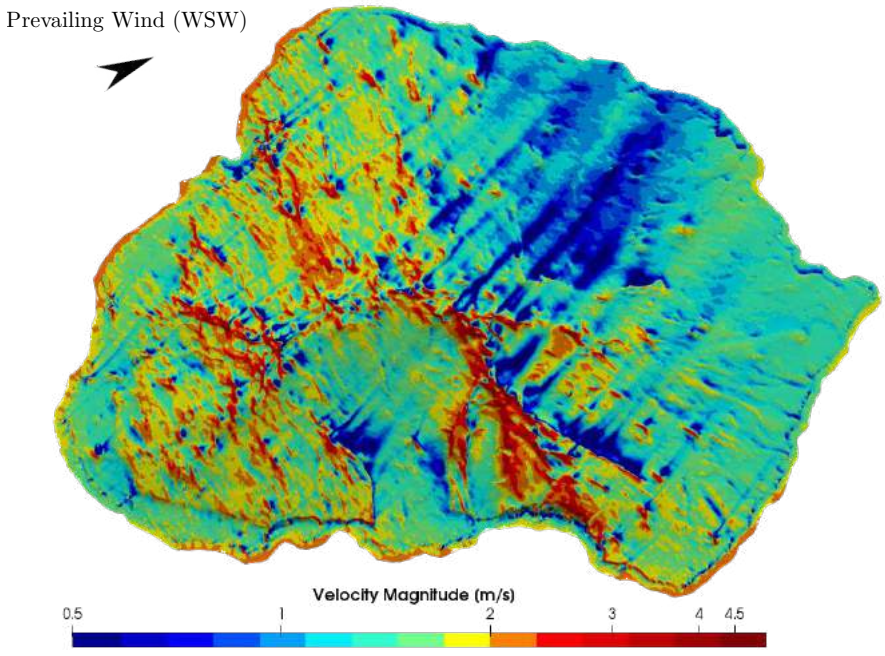

Figure L.12: WSW: Wind velocity map at one meter AGL for MI subjected to a west-south-westerly prevailing wind.

© University of Pretoria

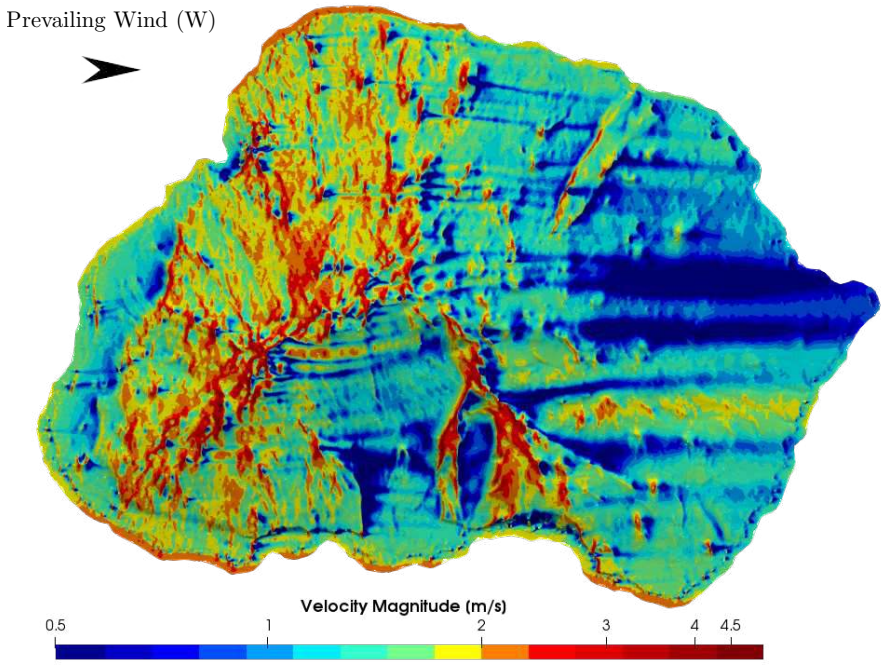

Figure L.13: WEST: Wind velocity map at one meter AGL for MI subjected to a westerly prevailing wind.

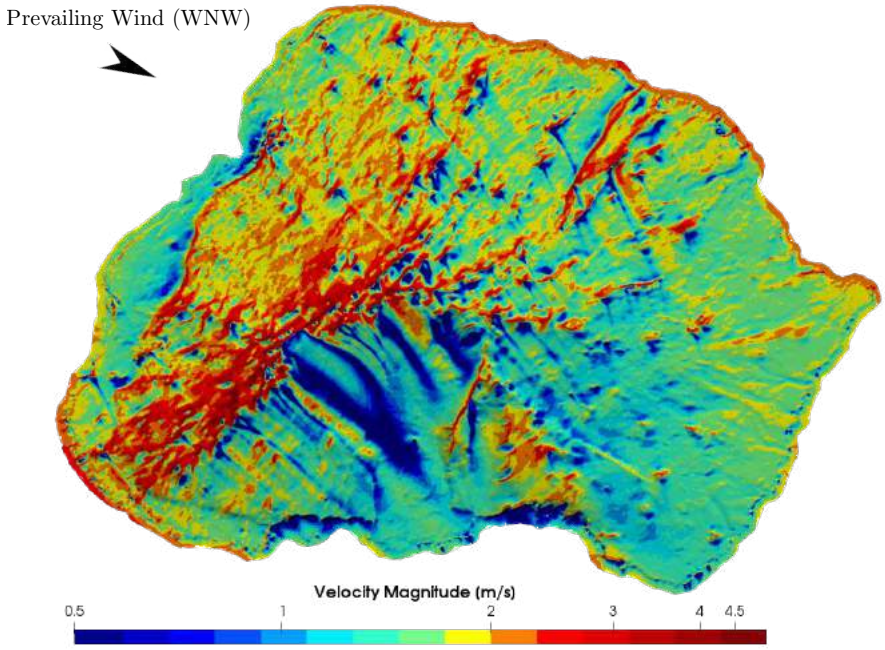

Figure L.14: WNW: Wind velocity map at one meter AGL for MI subjected to a west-north-westerly prevailing wind.

© University of Pretoria

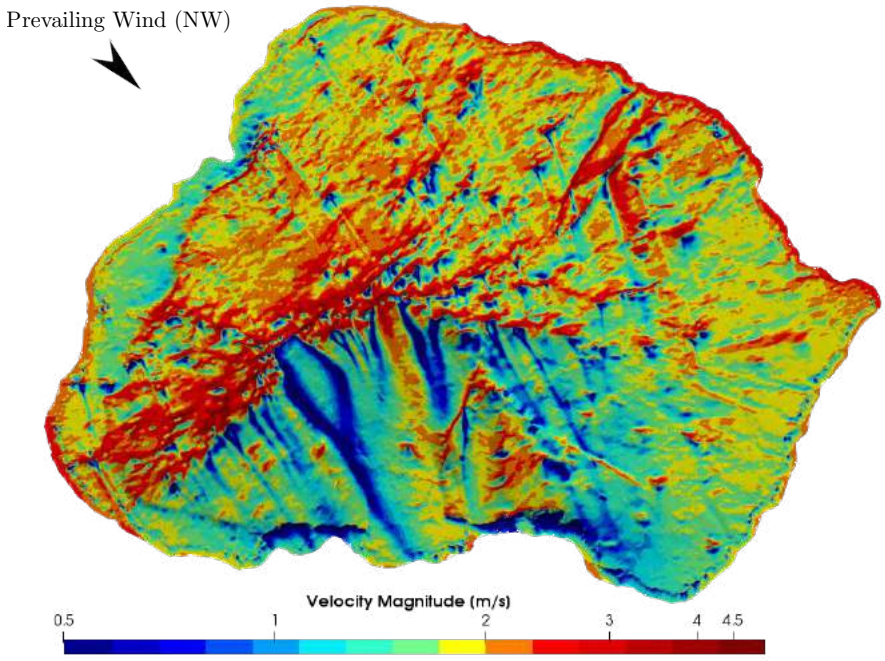

Figure L.15: NORTH-WEST: Wind velocity map at one meter AGL for MI subjected to a north-westerly prevailing wind.

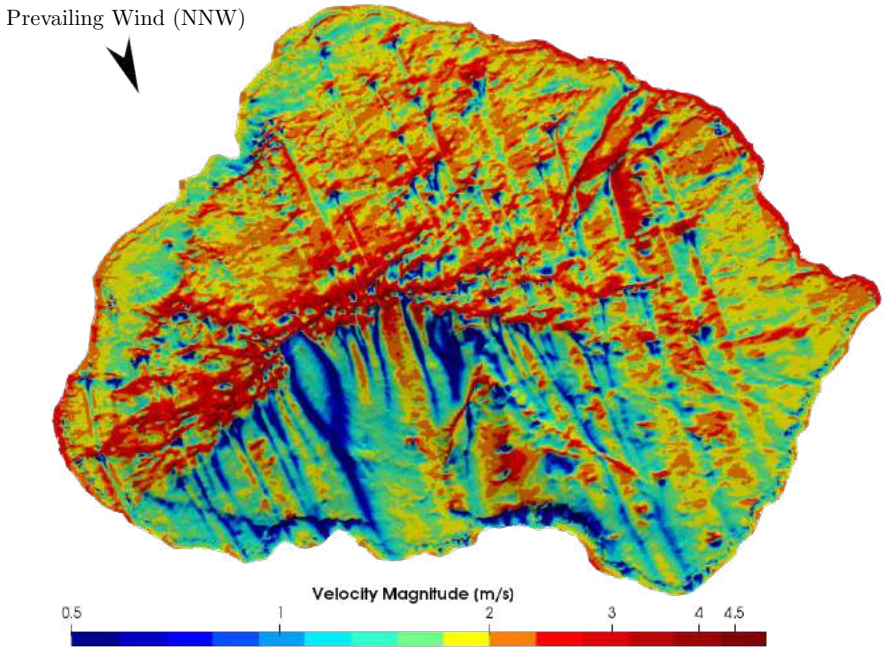

Figure L.16: NNW: Wind velocity map at one meter AGL for MI subjected to a north-north-westerly prevailing wind.

© University of Pretoria

M Wind Turbulence Maps (16 Directions)

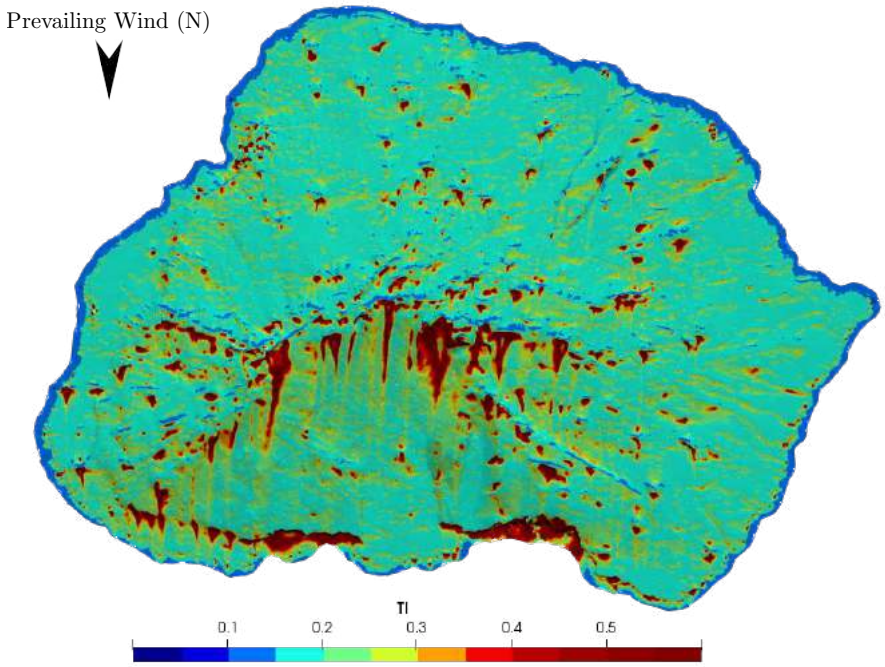

Figure M.1: NORTH: Wind turbulence intensity map at one meter AGL for MI subjected to a northerly prevailing wind.

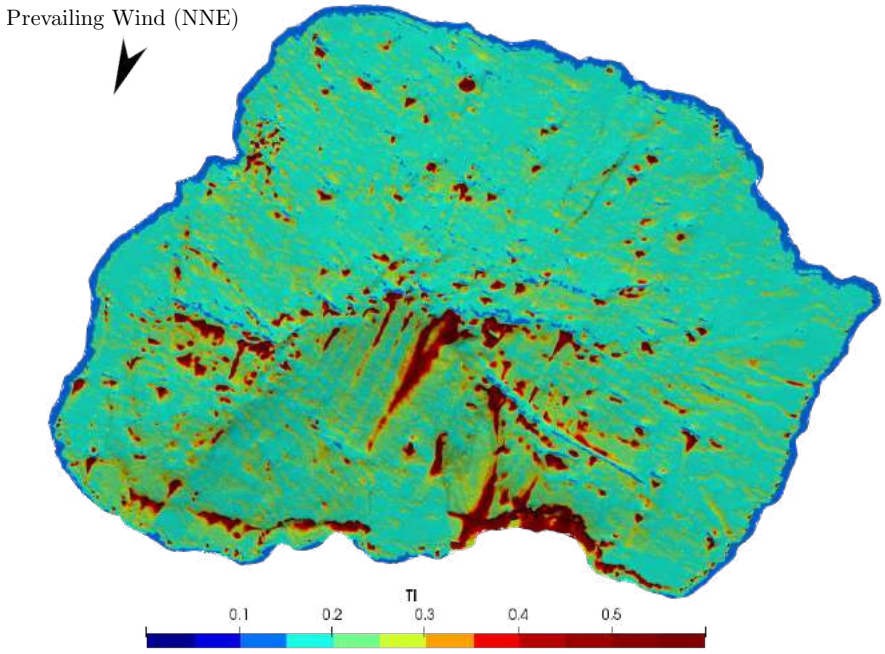

Figure M.2: NNE: Wind turbulence intensity map at one meter AGL for MI subjected to a north-north-easterly prevailing wind.

© University of Pretoria

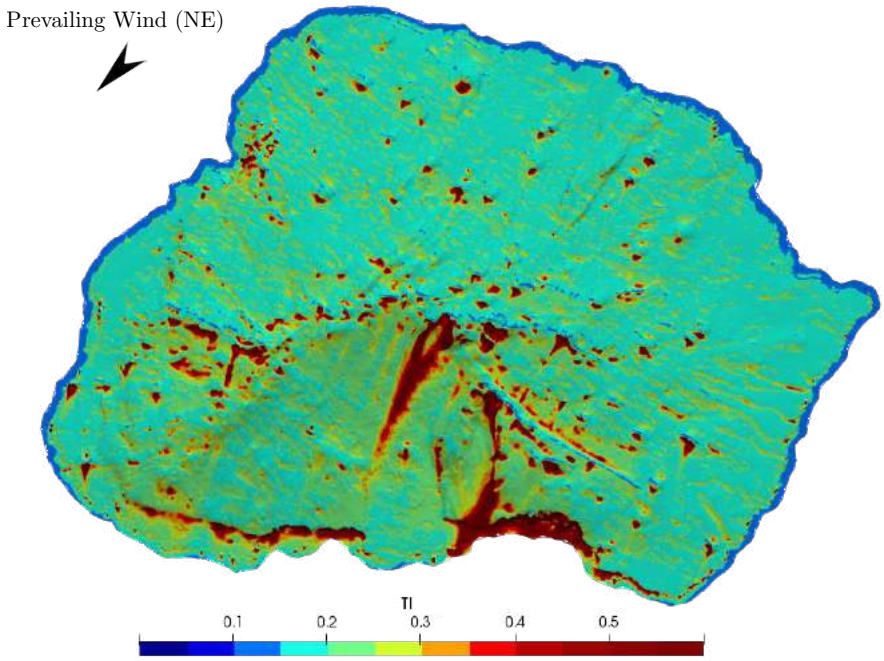

Figure M.3: NORTH-EAST: Wind turbulence intensity map at one meter AGL for MI subjected to a north-easterly prevailing wind.

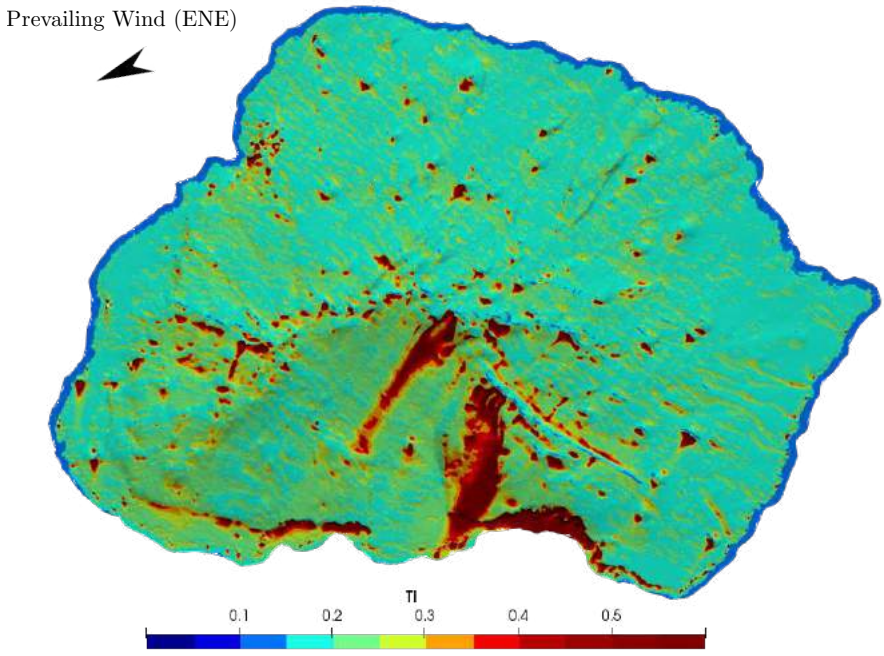

Figure M.4: ENE: Wind turbulence intensity map at one meter AGL for MI subjected to an east-north-easterly prevailing wind.

© University of Pretoria

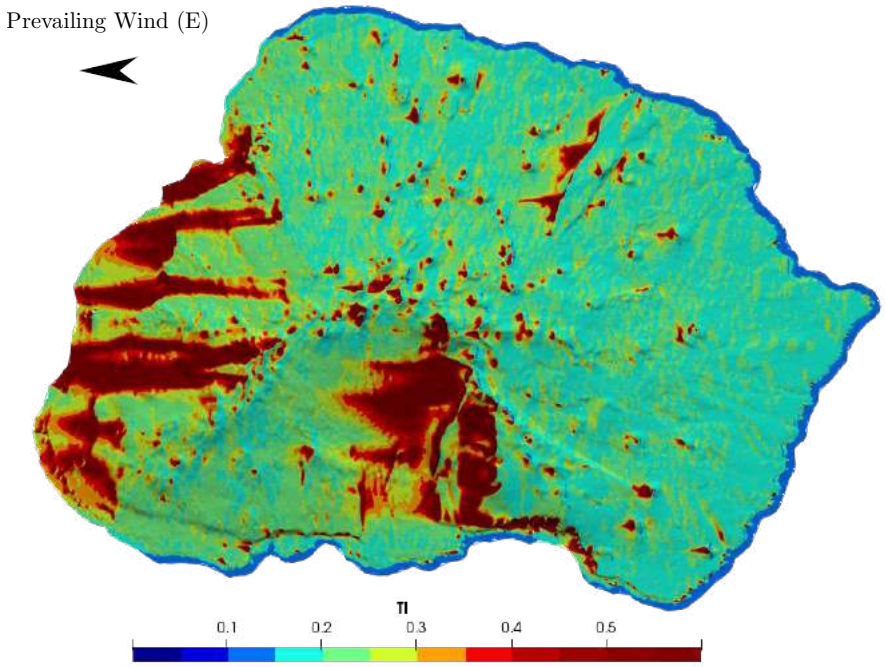

Figure M.5: EAST: Wind turbulence intensity map at one meter AGL for MI subjected to an easterly prevailing wind.

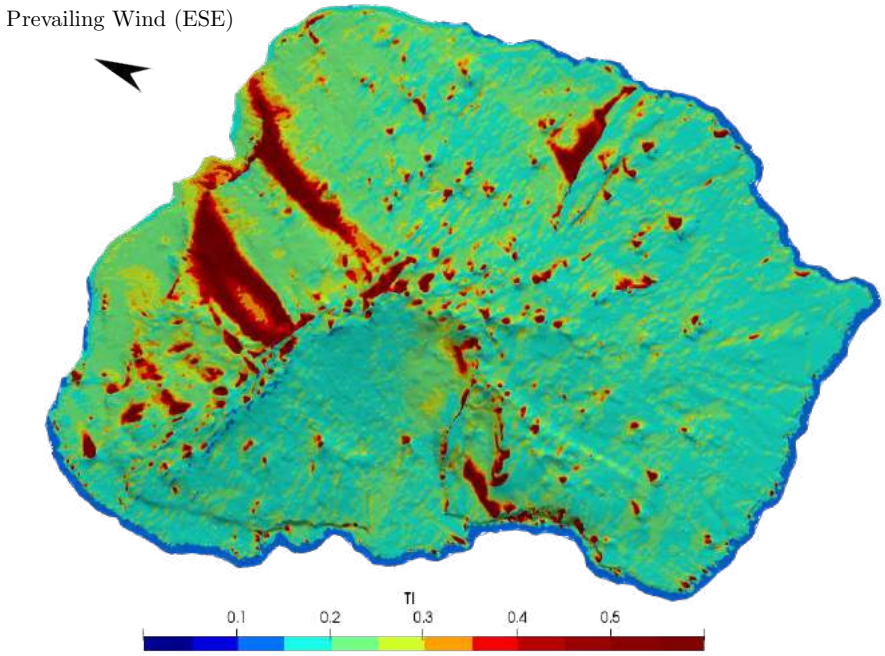

Figure M.6: ESE: Wind turbulence intensity map at one meter AGL for MI subjected to an east-south-easterly prevailing wind.

© University of Pretoria

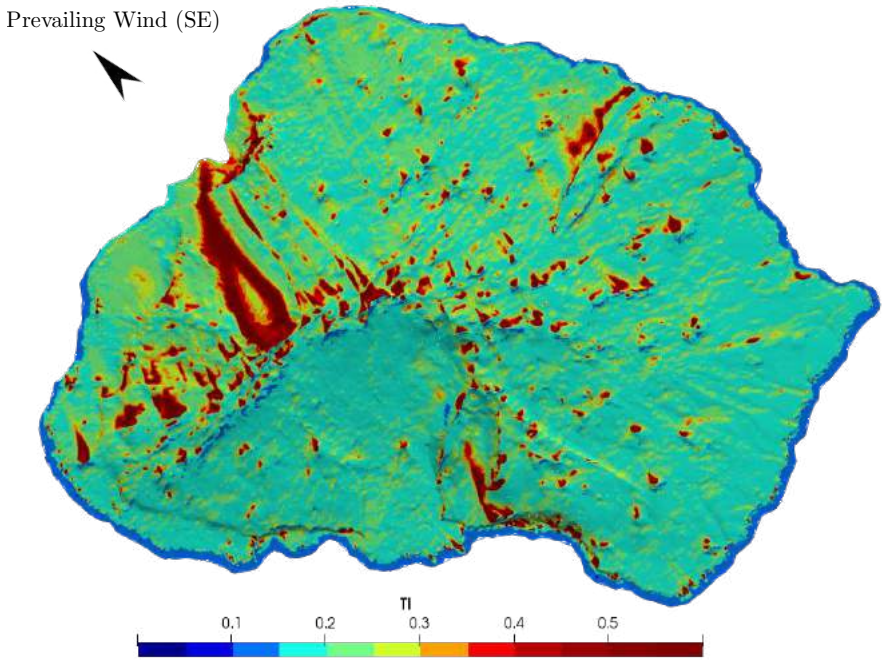

Figure M.7: SOUTH-EAST: Wind turbulence intensity map at one meter AGL for MI subjected to a south-easterly prevailing wind.

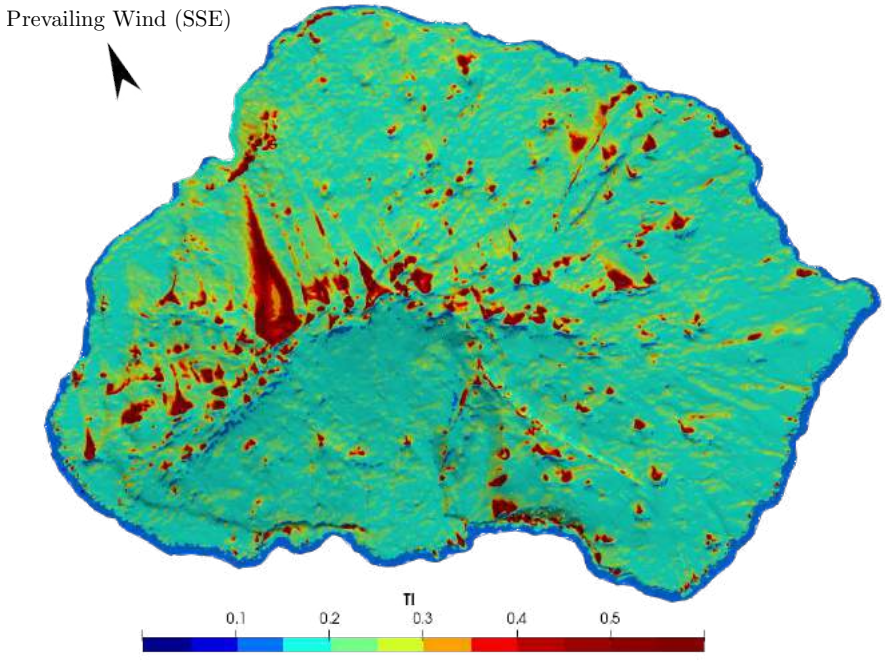

Figure M.8: SSE: Wind turbulence intensity map at one meter AGL for MI subjected to a south-south-easterly prevailing wind.

© University of Pretoria

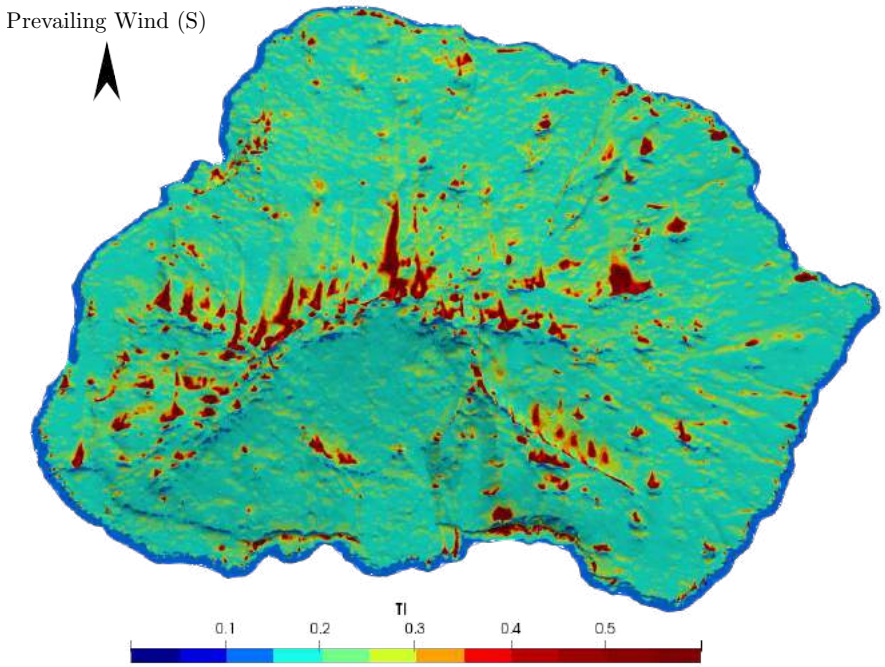

Figure M.9: SOUTH: Wind turbulence intensity map at one meter AGL for MI subjected to a southerly prevailing wind.

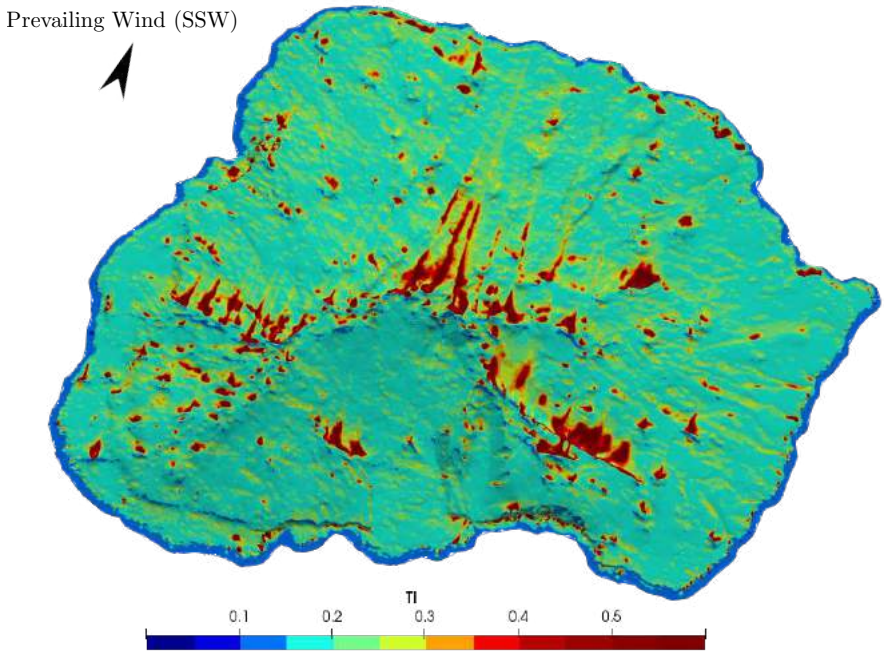

Figure M.10: SSW: Wind turbulence intensity map at one meter AGL for MI subjected to a south-south-westerly prevailing wind.

© University of Pretoria

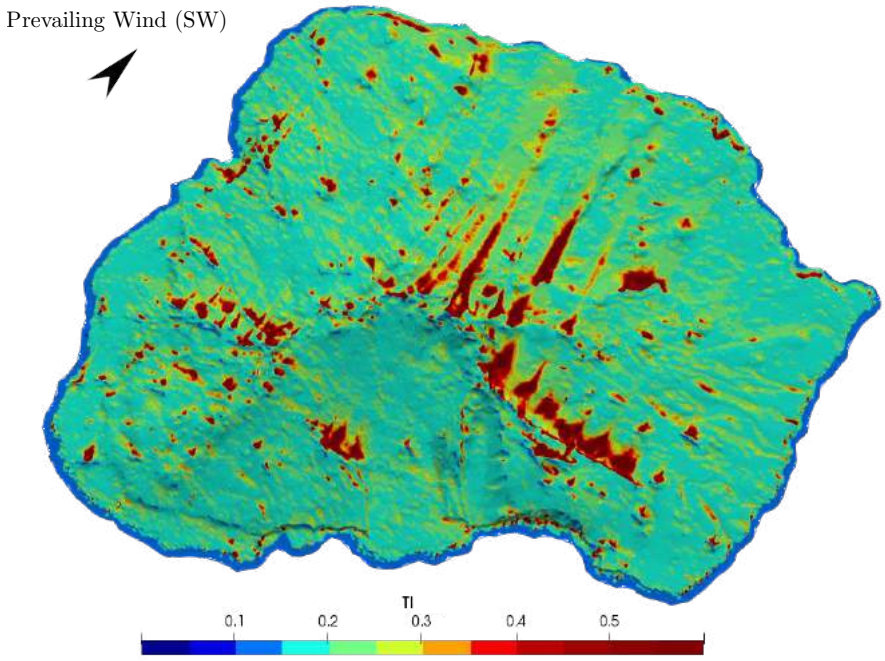

Figure M.11: SOUTH-WEST: Wind turbulence intensity map at one meter AGL for MI subjected to a south-westerly prevailing wind.

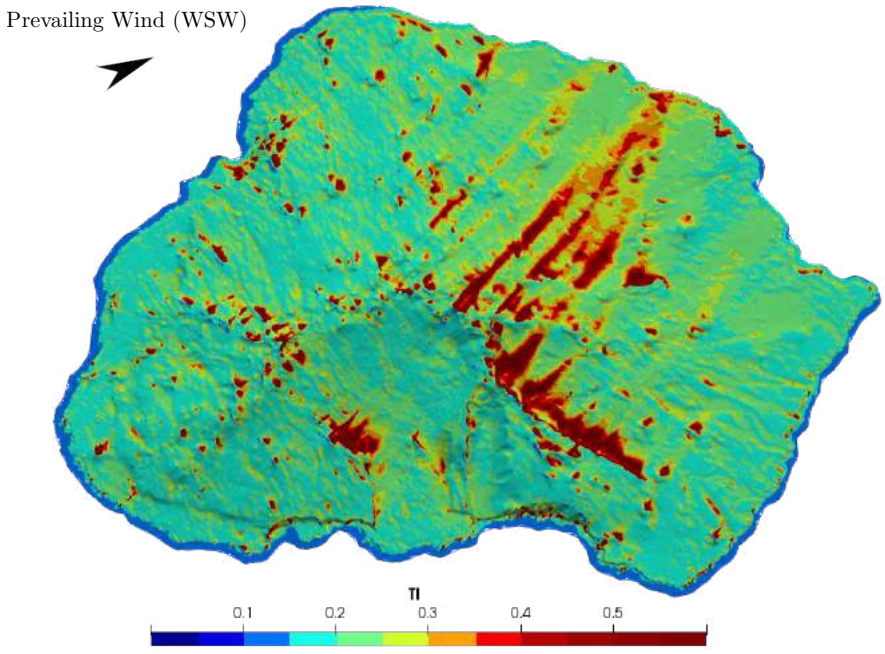

Figure M.12: WSW: Wind turbulence intensity map at one meter AGL for MI subjected to a west-south-westerly prevailing wind.

© University of Pretoria

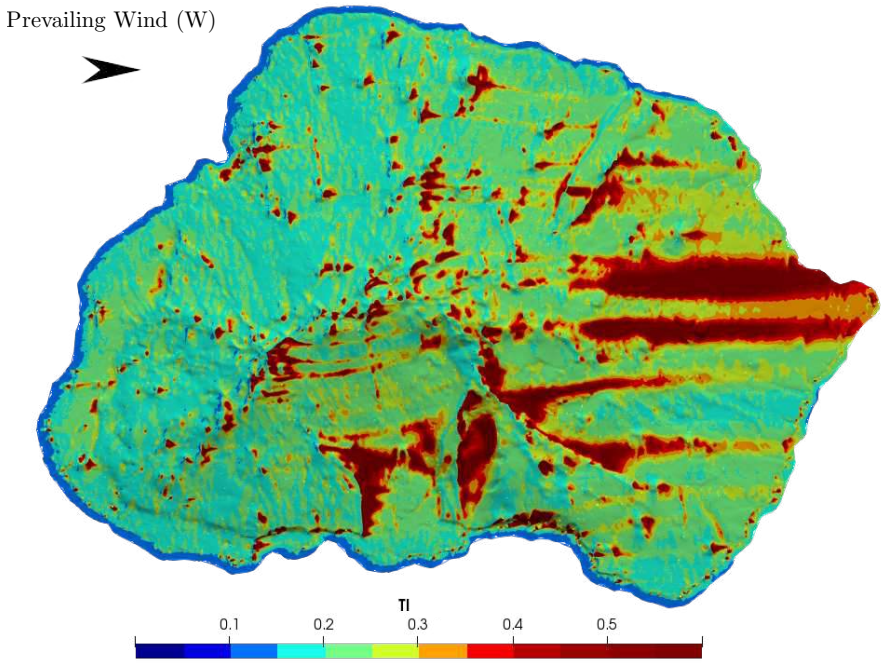

Figure M.13: WEST: Wind turbulence intensity map at one meter AGL for MI subjected to a westerly prevailing wind.

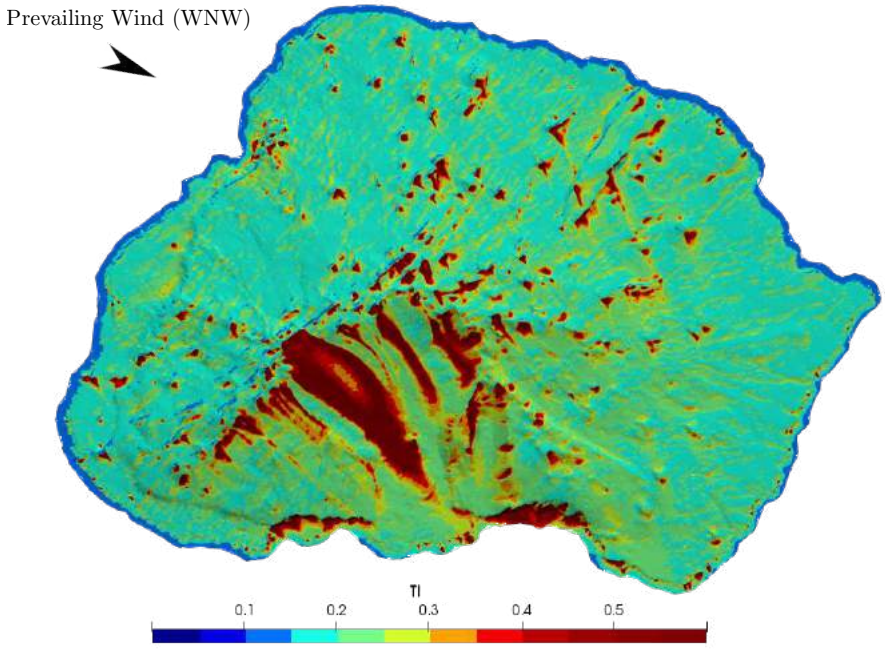

Figure M.14: WNW: Wind turbulence intensity map at one meter AGL for MI subjected to a west-north-westerly prevailing wind.

© University of Pretoria

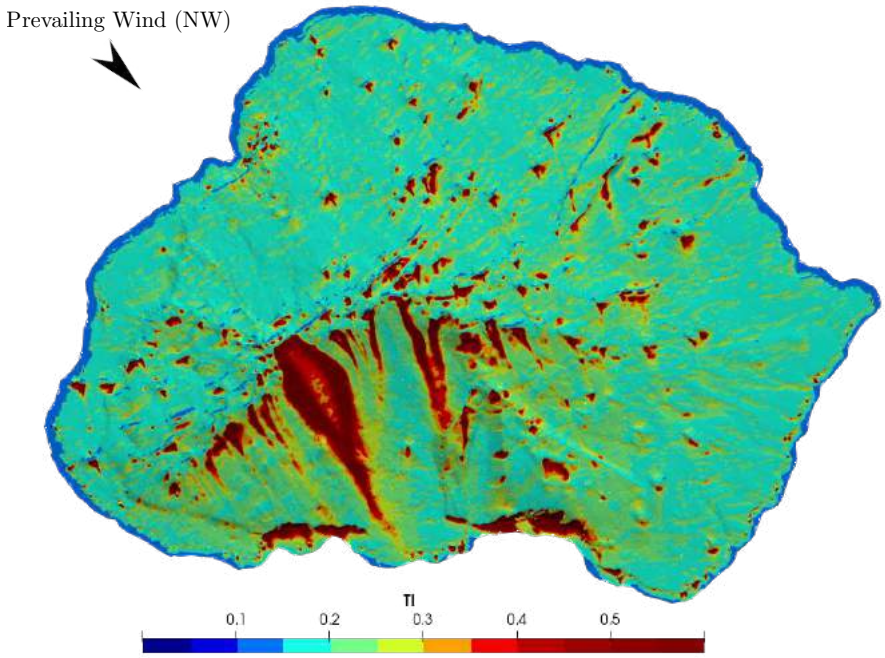

Figure M.15: NORTH-WEST: Wind turbulence intensity map at one meter AGL for MI subjected to a north-westerly prevailing wind.

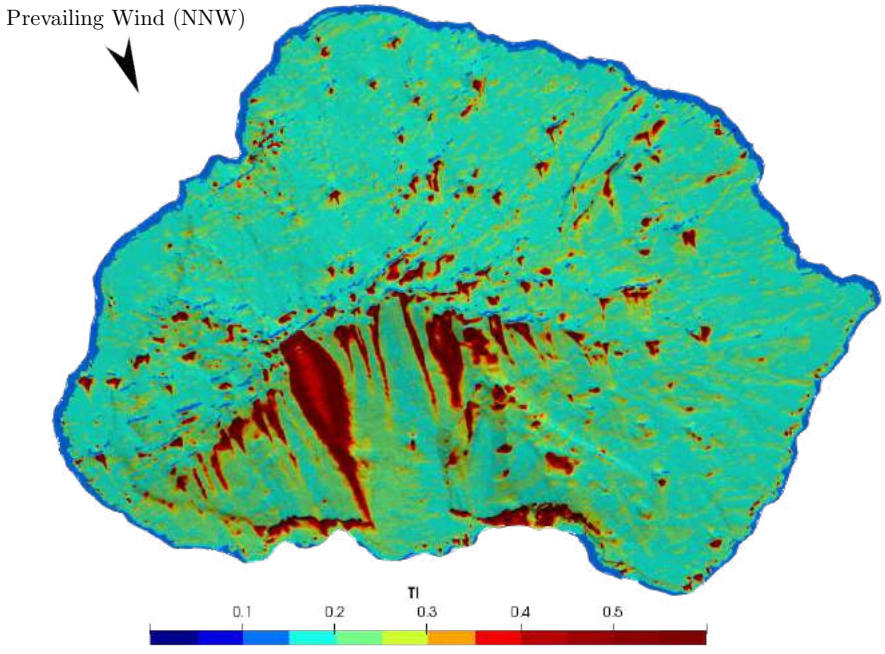

Figure M.16: NNW: Wind turbulence intensity map at one meter AGL for MI subjected to a north-north-westerly prevailing wind.

© University of Pretoria